



**HAL**  
open science

# Modelling and optimisation of metal foam integrated heat exchangers for power electronics cooling

Joseph Glass

► **To cite this version:**

Joseph Glass. Modelling and optimisation of metal foam integrated heat exchangers for power electronics cooling. Mechanical engineering [physics.class-ph]. Université Grenoble Alpes [2020-..], 2021. English. NNT : 2021GRALI007 . tel-03203080

**HAL Id: tel-03203080**

**<https://theses.hal.science/tel-03203080>**

Submitted on 20 Apr 2021

**HAL** is a multi-disciplinary open access archive for the deposit and dissemination of scientific research documents, whether they are published or not. The documents may come from teaching and research institutions in France or abroad, or from public or private research centers.

L'archive ouverte pluridisciplinaire **HAL**, est destinée au dépôt et à la diffusion de documents scientifiques de niveau recherche, publiés ou non, émanant des établissements d'enseignement et de recherche français ou étrangers, des laboratoires publics ou privés.

## THÈSE

Pour obtenir le grade de

### DOCTEUR DE L'UNIVERSITE GRENOBLE ALPES

Spécialité : **Mécanique des Fluides, Procèdes, Energétique**

Arrêté ministériel : 25 mai 2016

Présentée par

**Joseph GLASS**

Thèse dirigée par **Didier BOUVARD, Professeur, Grenoble INP,**  
et

Codirigée par **Yvan AVENAS, Maître de conférences, Grenoble  
INP, et Sébastien Ferrouillat, Maître de conférences, UGA**

Préparée au sein des **Laboratoires SIMaP, LEGI, et G2Elab**  
dans **l'École Doctorale I-MEP<sup>2</sup>**

## Modelling and Optimisation of Metal Foam Integrated Heat Sinks for Power Electronics Cooling

Thèse soutenue publiquement le **27 janvier 2021,**  
devant le jury composé de :

**M. Frédéric TOPIN,**

Maître de conférences HdR, Aix-Marseille Université, Rapporteur

**M. Frédéric LEFEVRE**

Professeur, INSA Lyon, Rapporteur

**M. Remy DENDIEVEL**

Professeur, Grenoble INP, Président du Jury

**M. Paul-Etienne VIDAL**

Maître de conférences HdR, Ecole Nationale des Ingénieur de Tarbes,  
Examineur

**M. Didier BOUVARD**

Professeur, Grenoble INP, Directeur de thèse

**M. Yvan AVENAS**

Maître de conférences HdR, Grenoble INP, Co-directeur de thèse, Invité

**M. Sébastien FERROUILLAT**

Maître de conférences, Université Grenoble-alpes, Co-encadrant, Invité



---

---

---

---

# ACKNOWLEDGEMENTS

---

I would like to express my sincere gratitude to my supervisors Didier Bouvard, Yvan Avenas and Sébastien Ferrouillat for their invaluable support and guidance throughout the duration of my PhD.

I would also like to thank Frédéric Girard, Florian Dumas and Sébastien Garcia for the large roles they played in the experimental aspects of this research project.

I am also thankful for the support and encouragement I received from my friends and family during this period.

Finally, I would like to thank my daughter Eloise, she is the reason for this undertaking, and is a constant motivation to me to do my best, to improve and to succeed.



---

---

# GENERAL INTRODUCTION

---

---

Several decades ago, power electronics (PE) emerged as an important discipline in the world of electrical engineering. It became far more prevalent in industrial, commercial, residential, aerospace and military environments in a wide range of applications, such as heating control, AC and DC supplies, electrochemical processes, machine drives and harmonic filtering [1]. PE is described as the application of solid-state electronics to the control and conversion of electric power. In modern systems, this is carried out with semiconductor switching devices such as diodes, thyristors, and power transistors. In recent years, there has been revolution in the use of PE converters as wide band gap materials such as Silicon Carbide (SiC) and Gallium Nitride (GaN) have begun to replace the standard Silicon (Si) semiconductors. With these new materials, more compact and efficient devices can be fabricated that are capable of offering switching speeds of up to ten times faster than their counterparts. Improvements are also seen in the breakdown voltage, the operating temperature, the current and the switching loss over Si devices with the same die size and thickness [2]. However, though higher switching speeds can lead to improved power density and efficiency of the converter, these devices also suffer from electromagnetic interference (EMI) issues. One method of overcoming these problems was to fundamentally redesign the conventional packaging structure of the switching cell. Power Chip-on-Chip (PCoC) is a structure developed at G2Elab that superimposes the components of the switching cell, which greatly reduces parasitic inductances, and improves the overall electromagnetic compatibility (EMC) behaviour of the power module. Unfortunately, all gains in terms of EMC by the PCoC structure are paid for by a less efficient thermal management. This work thus aims to propose a solution to the problem of modern PE packaging by offering a compact and efficient cooling strategy, using metal foam as a novel heat sink within a forced-convection liquid cooling environment. The potential advantages to heat transfer of metal foams arise from the possibility of an increased specific surface area over other heat sinks, such as microchannels, and from the tortuous structure of metal foam that generates flow turbulence and improves convective transfers within the coolant.

This work is a multidisciplinary endeavour carried out as a collaborated effort between G2Elab (power electronics, packaging and thermal management), LEGI (fluid mechanics, heat transfer, thermal and hydraulic modelling) and SIMaP (material engineering, sintering and microstructure characterisation) as part of the CoolPack project, funded by Univ. Grenoble Alpes. The resulting dissertation is organized as follows. Chapter 1 details the technological advancements in PE packaging and current cooling strategies, as well the characterisation and fabrication of metal foam. In Chapter 2, analytical models capable of predicting the thermal and hydraulic behaviour for metal foam and microchannel heat sinks are presented. In Chapter 3, the models are implemented into the software CADES to optimise the physical attributes of metal foam to maximises thermal performances whilst minimising the required hydraulic power. Finally, Chapter 4 contains a detailed look into the development of a new test bench and test section, capable of testing the thermal and hydraulic performances of small heat sinks.



---

# CHAPTER I

---

## INTRODUCTION TO POWER ELECTRONICS PACKAGING AND THERMAL MANAGEMENT

---

### Table of Contents

<b>1. INTRODUCTION.....</b>	<b>2</b>
<b>2. POWER ELECTRONICS PACKAGING.....</b>	<b>2</b>
<b>3. OVERVIEW OF COOLING STRATEGIES.....</b>	<b>7</b>
3.1 NATURAL AND FORCED CONVECTION.....	8
3.2 HEAT PIPES .....	10
3.3 LIQUID COOLED COLD PLATES .....	10
3.4 TWO PHASE DIRECT COOLING .....	11
3.4.1 Spray cooling .....	11
3.4.2 Jet impingement cooling.....	12
3.4.3 Immersion cooling.....	12
3.5 INTEGRATED MICRO HEAT SINKS .....	13
3.5.1 Single- and two-phase microchannels.....	13
3.5.2 Porous media cooling .....	14
<b>4. SUMMARY OF COOLING STRATEGIES .....</b>	<b>15</b>
4.1 CHOICE OF THERMAL MANAGEMENT STRATEGY.....	15
4.2 PROJECT AIMS .....	16
<b>5. METAL FOAMS .....</b>	<b>16</b>
5.1 CLASSIFICATION .....	17
5.2 MANUFACTURING TECHNIQUES.....	18
5.2.1 Homogeneous pore distribution .....	19
5.2.2 Non-homogenous pore distribution.....	21
5.3 FOAM MATERIAL .....	24
<b>6. COOLANT.....</b>	<b>24</b>
6.1.1 Types of Dielectric Coolant .....	25
6.1.2 Review of dielectric coolant thermal properties .....	26
<b>7. CONCLUSION .....</b>	<b>28</b>

## 1. Introduction

In this chapter, the main principles of the project and its background will be introduced. Due to the multidisciplinary nature of the work, it is not possible to enter into fine detail for every topic. Thus, only the most important aspects will be outlined here, accompanied by the most pertinent examples. In the following chapters, when the field of view has been narrowed, and the project aims and potential solutions have been proposed, a more detailed approach can be taken.

Chapter 1 begins with a recap of the recent evolution of power electronics (PE) packaging and how technological improvements have necessitated an increased focus on small scale, efficient cooling systems. This is followed by an overview of the most common types of coolers used with the PE industry, their applicability, and their advantages and disadvantages. This is concluded with the reasons why this project concentrates on the use of metal foams as a novel heat sink to be integrated within a PE package. Next, a close look at metal foams is taken, such as how they are characterised, the potential advantages they offer to PE cooling, and the most common manufacturing techniques. Also described is their thermal and hydraulic properties and how crucial parameters will be determined. This chapter is concluded with a description of the main aims of the project, and a look at the proposed solutions.

## 2. Power Electronics Packaging

Several decades ago, PE emerged as an important discipline in the world of electrical engineering. It became far more prevalent in industrial, commercial, residential, aerospace and military environments in a wide range of applications, such as heating control, AC and DC supplies, electrochemical processes, machine drives and harmonic filtering [1]. PE is described as the application of solid-state electronics to the control and conversion of electric power. In modern systems, this is carried out with semiconductor switching devices such as diodes, thyristors, and power transistors.

In recent years, there has been revolution in the use of power electronic converters as wide band gap materials such as Silicon Carbide (SiC) and Gallium Nitride (GaN) have begun to replace the standard Silicon (Si) semiconductors. This has allowed for the steady reduction in transistor size over the last forty years, as can be seen in Figure 1. This has resulted in two secondary effects, the first being an almost tenfold increase in power density, and also a significant increase in device temperatures as well. As for the energy that must be dissipated, this has increased from about 100 W/cm<sup>2</sup> to 400 W/cm<sup>2</sup>. With these new materials, more compact and efficient devices can be fabricated that are capable of offering switching speeds of up to ten times faster than their counterparts. Improvements are also seen in the breakdown voltage, the operating temperature, the current and the switching loss over Si devices with the same die size and thickness [2].

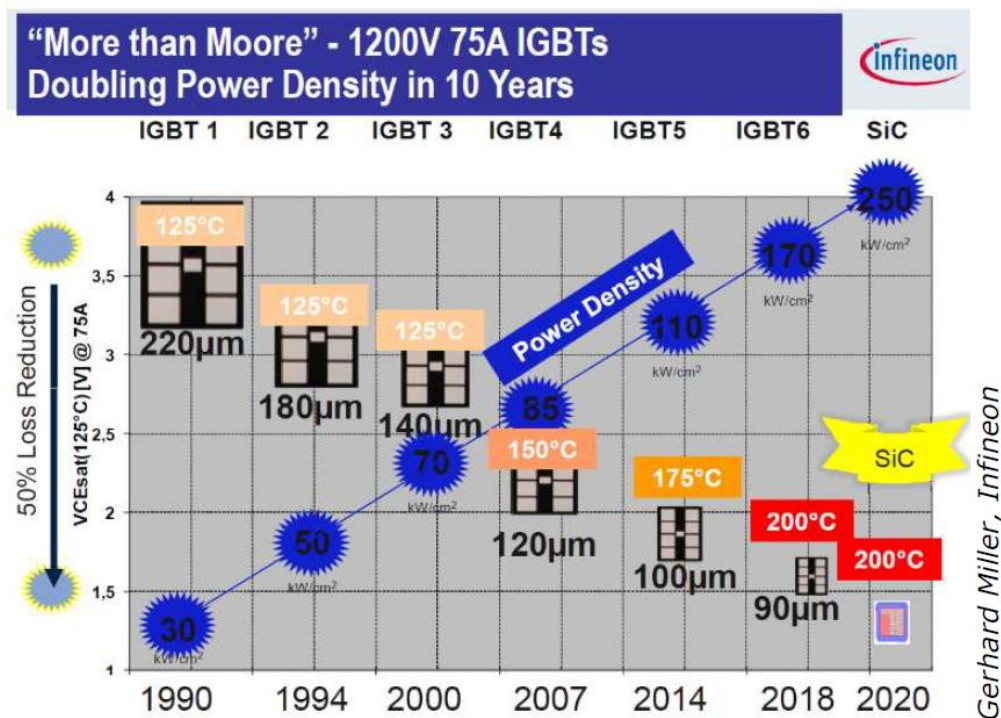


Figure 1: Increase in PE device power density compared with the reduction in transistor size over the last thirty years.

However, though higher switching speeds can lead to improved power density and efficiency of the converter, these devices also suffer from Electromagnetic Interference (EMI) issues. Most commonly, there is an increase in voltage ringing and overshoots due to the faster switching dynamics exciting resonant circuits, comprising leakage inductances and parasitic capacitances [3]. The cause of the problem can be explained, in part, by the inherent flaws within the design of the classic power module package. Figure 2 shows a diagram of a standard power module package:

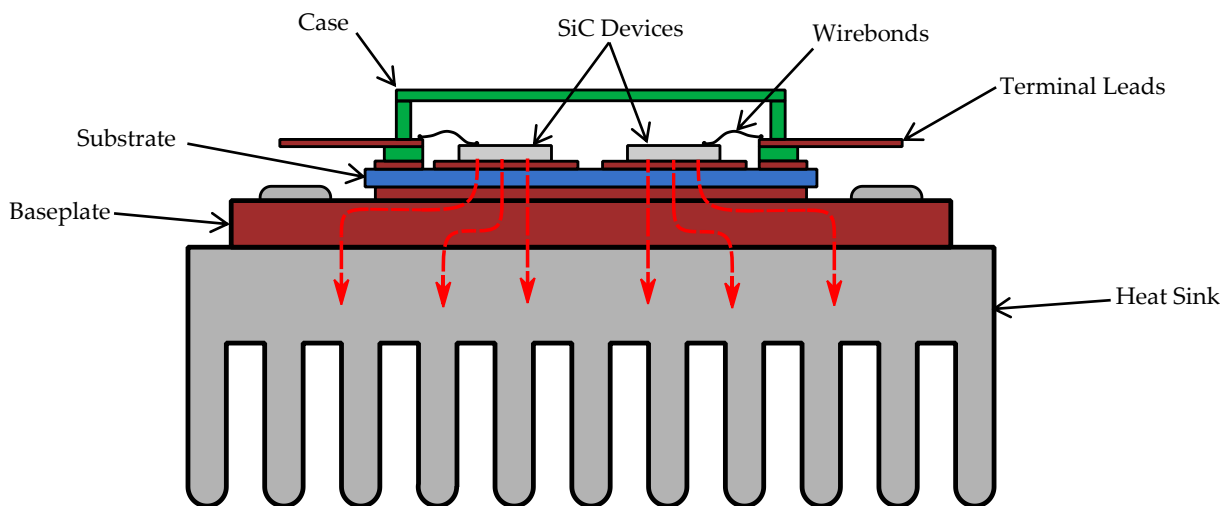


Figure 2: Cross-section of a classic power module.

The red arrows in Figure 2 describe the path of the heat flux from the chips to the heat sink. Not only is the above design unsuitable for dealing with the speed of modern power

modules, it also handicaps thermal management by limiting potential cooling to only a single side of the device. One method of overcoming switching speed issues was to fundamentally redesign the conventional packaging structure of the switching cell. Régnat [4] showed that the components of the switching cell could be superimposed on one another and sandwiched between the power inputs (+DC and -DC). This arrangement, proposed by G2Elab and called Power Chip-on-Chip (PCoC) (Figure 3), greatly reduces parasitic inductances, and improves the overall electromagnetic compatibility (EMC) behaviour of the power module. This is due to the three-dimensional nature of the design, which maximises the mutual magnetic coupling among the copper plates facing each other [5].

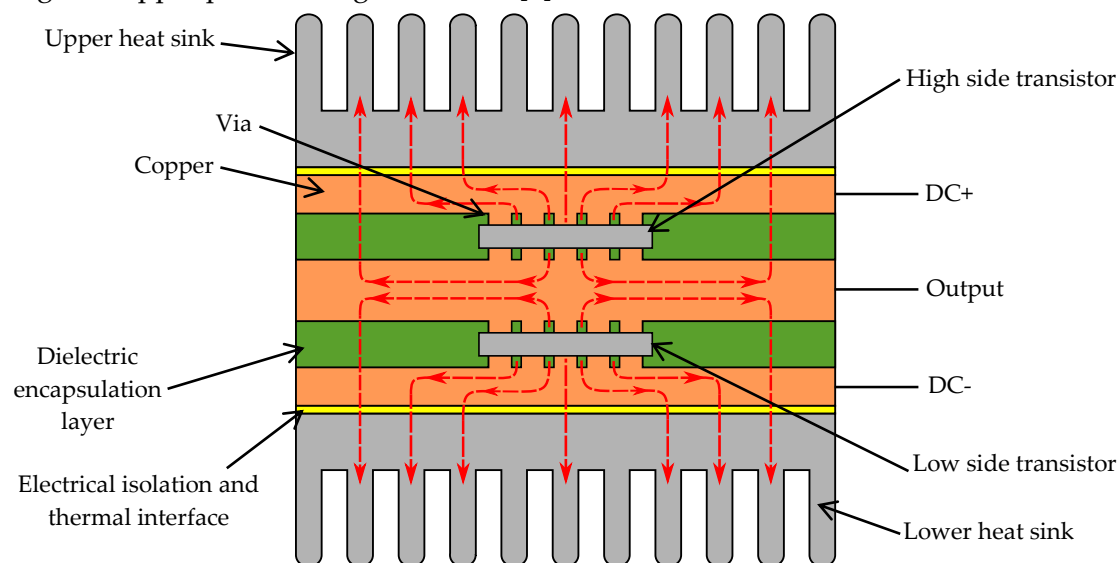


Figure 3: PCoC configured switching cell

To better understand the layout of the electronic components displayed in Figure 3, it can be viewed as an electrical diagram in Figure 4.

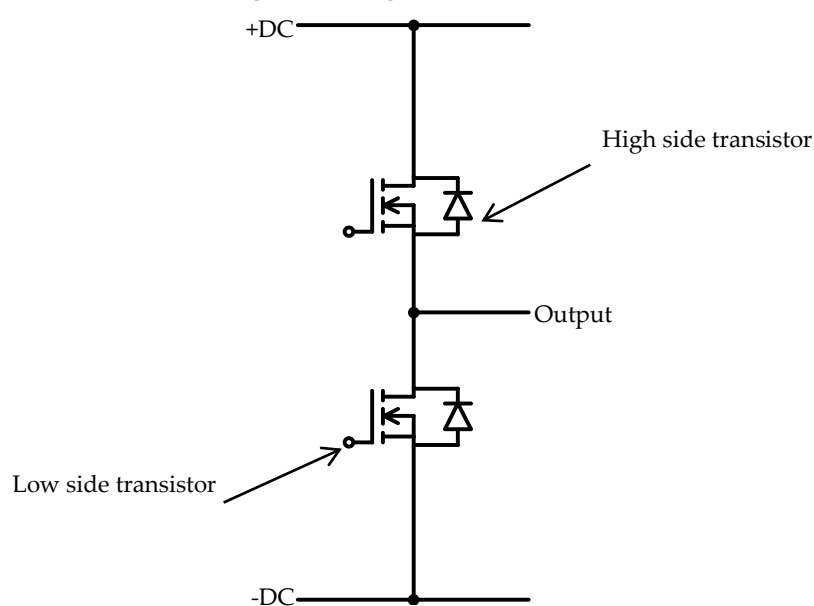


Figure 4: Electrical diagram of PCOC packaging design.

Unfortunately, all gains in terms of EMC by the PCoC structure are paid for by a less efficient thermal management; as the two chips are superimposed, normal double-sided cooling is not possible and there is a strong thermal coupling between them due to the intermediate copper. This makes it more difficult to remove heat from this region, between the high side and low side transistors. Equally problematic is that one of the chips is cooled by its front face, which does not allow for an optimal heat transfer (reduced heat exchange surface). By comparing Figure 3 with a package that has been designed with thermal management in mind (Figure 5), it is easier to see the thermal shortcomings.

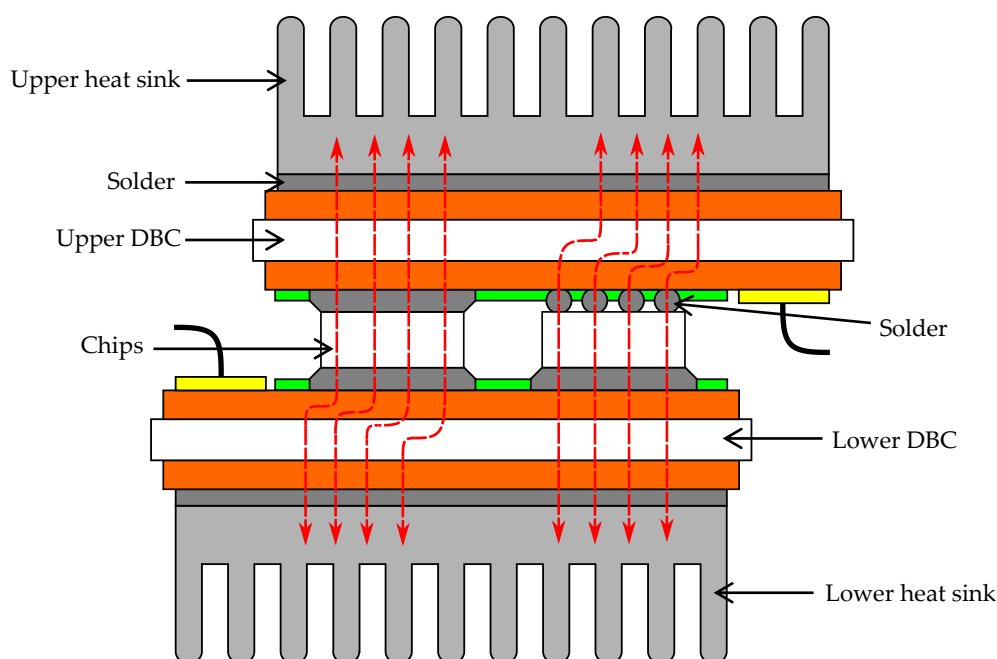


Figure 5: PE packaging for improved thermal management

Figure 5 places the chips in line with one another, as opposed to the stacking layout of PCoC. This results in a more even cooling, as both faces of the chips have a direct thermal link to the heat sinks. There is also no longer the central region between two chips where heat can recirculate. Therefore, the ideal PE package would offer the electromagnetic advantages of PCoC, and the thermal management seen in Figure 5. Unfortunately, to date no such package has been developed.

Thus, focus has shifted towards improving packages such as PCoC in order to make them a more viable solution to the EMC problem. One method of doing this is to integrate a cooling system, that utilises both conductive and convective heat transfer, as close to the chips as possible, in-between the high side and low side transistor, as seen in Figure 6.

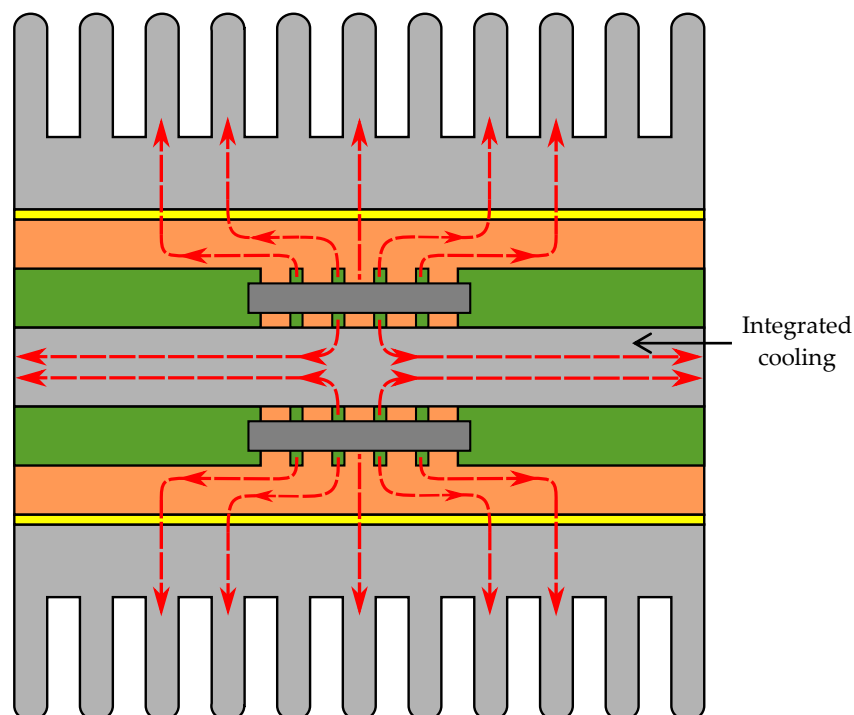


Figure 6: PCOC packaging design with integrated heat sink.

In the above diagram, the typical PCOC packaging seen in Figure 3 has been modified by replacing the interior copper plate with a cooling system. As with the design of Figure 5, the new design now provides double sided cooling to each of the chips. Though a clear improvement, there are certain constraints that must be taking into consideration when deciding which cooling system is the most appropriate,

- It must be electrically conductive to connect the two chips together.
- The overall size and thickness of the system must be small, so as to not increase the size of the power module. The modules size, and the distance between the stacked chips is predetermined to improve its EM behaviour. Thus the available space is of the order of 10mm wide, by 40mm long, with a height (distance between chips) of 5mm.
- Heat transfer rates must be very high to counteract the imposed space constraints just discussed. As has been seen in Figure 1, the energy that must be dissipated within modern PE models is upwards of  $400 \text{ W/cm}^2$ . This is thus the minimum that our system should be capable of dissipating.

The technological improvements in PE discussed in this section have been the driving force behind the increased focus on small scale, efficient cooling systems capable of mitigating the thermal deficiencies of modern PE packaging. As such, there exists today a multitude of possible cooling solutions that have a wide range of heat transfer rates, applications, advantages and disadvantages. In order to assess which solution is the most appropriate, a review of the most common options will be carried out in the following section.

### 3. Overview of Cooling Strategies

In this section, a general review of cooling solutions will be carried out. It is not possible to take a detailed look into all possible methods, so the focus will be on some of the most common and useful for this present study. Kang [6] carried out a review of different cooling technologies and how they have evolved to remove ever increasing levels of heat dissipation and to manage maximum temperatures within the PE device. He studied:

- Natural and forced air convection
  - Flat plate heat sink
- Heat pipes
- Liquid cold plates
- Two phase direct cooling
  - Immersion cooling
  - Spray cooling
  - Jet impingement cooling
- Integrated micro heat sinks
  - Micro-channel/pin-fin heat sinks
  - Porous media cooling

Natural air convection is one of the simplest methods of cooling, but also produces the lowest rates of heat transfer. This can be improved simply by adding a fan, converting the cooler into a forced convection heat sink. When higher heat flux densities are used, the shift to liquid forced convection is required, such as with liquid cold plates. Further improvements can then be achieved by utilising a phase change of the coolant such as with heat pipes. Then shifting to a direct cooling method, such as with spray and jet impingement cooling, contact thermal resistances can be reduced. Finally, by using micro heat sinks, the cooling solution can be integrated at the chip level, achieving much higher rates of heat transfer by reducing the hydraulic diameter.

A common method of characterising different cooling methods is to use the thermal time constant (TTC). This is a measurement of the time required for a thermistor to respond to the change in ambient temperature. When applied to cooling systems, typically a low TTC equates to a low maximum temperature [7]. This is because as the coefficient of heat transfer  $h$  increases, the TTC is decreased. Figure 7 shows the relationship between increasing cooling effectiveness and the thermal time constant of several cooling strategies.

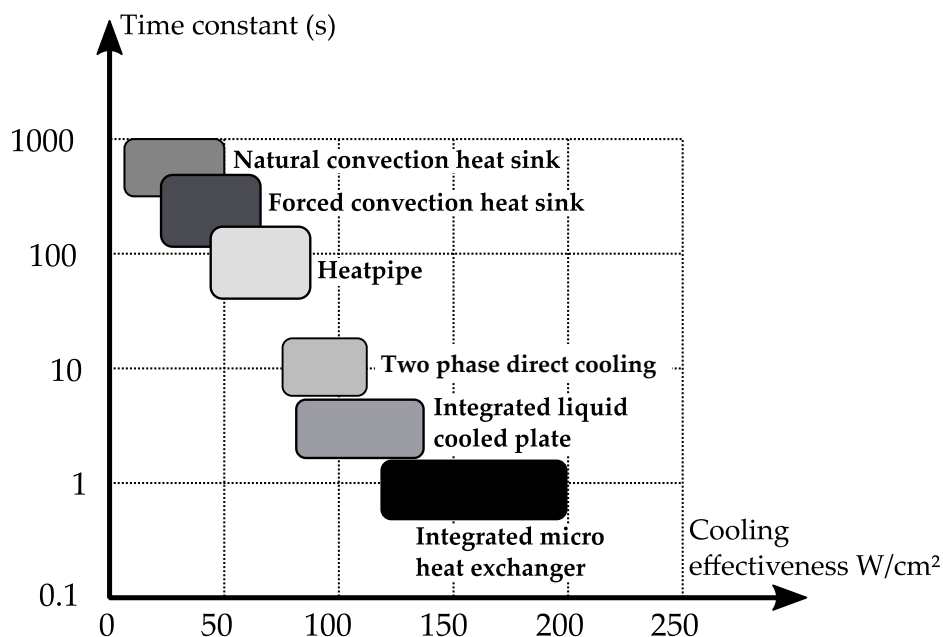


Figure 7: General cooling effectiveness and thermal time constant for common cooling strategies [7].

### 3.1 Natural and Forced Convection.

Natural convection heat sinks have no moving parts, and rely solely on buoyancy forces to generate movement within the fluid. Thermal expansion causes the fluid closest to the PE device to heat up, lowering its density. It then rises above the cooler, denser air, creating a circulation. Yu and Joshi [8] compared the performances of natural convection within horizontal enclosures containing heat sources flush mounted to an adiabatic board. Figure 8 shows the typical flow pattern that is expected with natural convection in a closed environment. The heat source is located at the centre of the lower horizontal surface.

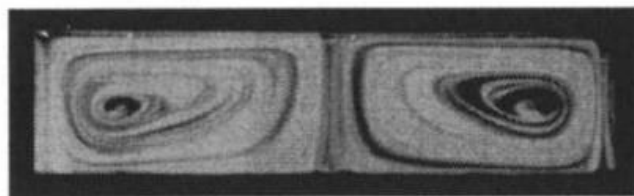


Figure 8: Flow pattern of natural convection in horizontal enclosure [8].

Natural convection heat sinks have the advantages of being low-cost, low-maintenance, energy-free and noise-free, however they are only suitable for low-power dissipating devices. In order to improve heat transfer, the introduction of finned surfaces is used extensively, which greatly increases the surface area of the heat sink. Baskaya *et al.* [9] carried out a systematic theoretical investigation on the effects of fin spacing, fin length, fin height, and temperature differences between the fin and the surroundings on the natural convection heat transfer from horizontal fin arrays. They showed that these parameters have a non-negligible effect on the overall heat transfer, and that an optimum performance cannot be found by only concentrating on one or two of them. They also confirmed the early work of Starner and McManus [10], who found that the incorrect application of fins can actually

reduce the overall heat transfer to below that of the flat base. This highlights the need for well-designed fins, with optimised geometries.

Through the simple addition of a fan, a natural convection heat sink can be converted into using forced convection, increasing heat transfer. Just like with natural convection, these heat sinks can use simple flat plates to remove heat from PE devices, as seen in Figure 9, or more complicated geometries, such as fin arrays.

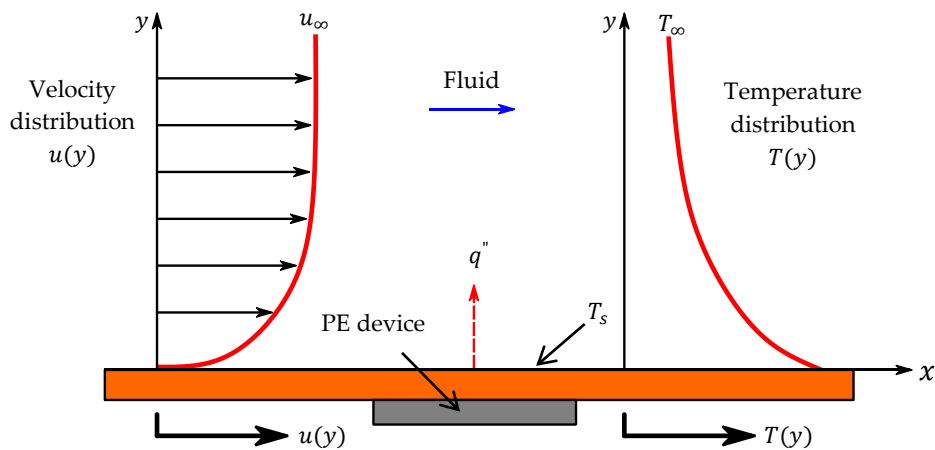


Figure 9: Forced convection flat plate heat sink assuming a steady, incompressible and laminar flow [11].

Kays and London [12] showed that the thermal resistance of a heat sink can be improved by increasing the mass flowrate, hence forced convection instead of natural. They also showed that improvements can be found by increasing the heat transfer coefficient at the surface of the heat sink, hence the use of smaller fin and flow channel dimensions, and by increasing the thermal capacity and thermal conductivity of the fluid, leading to the use of liquid coolants instead of gas, such as the system seen in Figure 10.

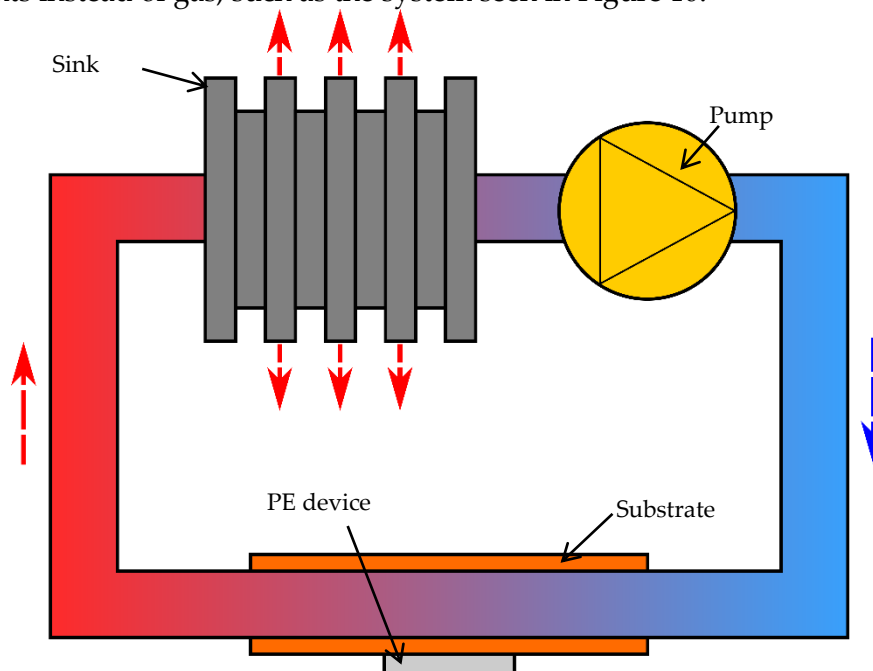


Figure 10: Pumping loop cooler.

## 3.2 Heat pipes

Heat pipes are a common form of indirect liquid cooling, meaning the chip is isolated from the cooling fluid. In contrast to direct cooling methods, such as immersion boiling, heat pipes rely on highly conductive thermal layers to transport the heat flux between the source and the coolant. This type of closed loop system requires little maintenance, and also makes it easier to keep the cooling fluid contaminate free. Heat pipes are sealed units, devoid of air, that are only partially filled with coolant. The coolant is specifically chosen such that it exists as both a fluid and a vapour over the operating temperature range. At the hot end of the pipe, the fluid evaporates and absorbs thermal energy. It then migrates to the cooler end of the pipe due to pressure differences, where it condenses back into a fluid, releasing thermal energy. Finally, it is absorbed into the wick and travels back to the hot end of the pipe due to capillary and/or gravity action. As heat pipes contain no mechanical moving parts they have the advantage of requiring very little maintenance. Unfortunately heat pipes are only capable of handling relatively small heat loads, around  $130 \text{ W/cm}^2$  [13].

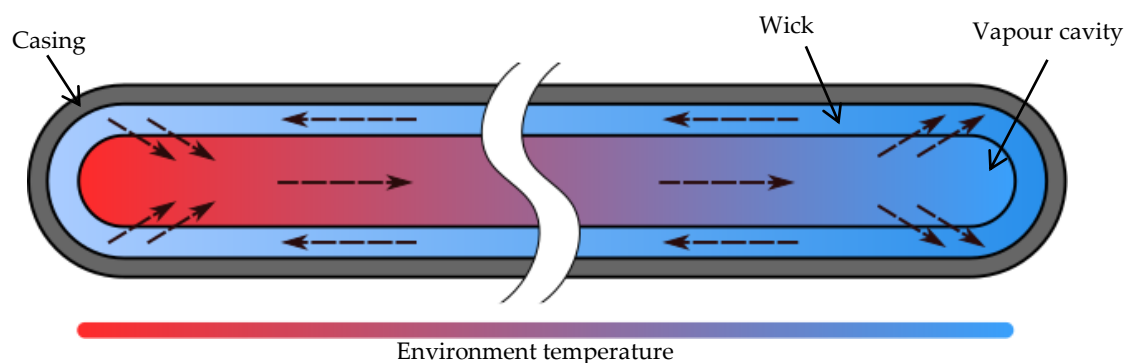


Figure 11 : Heat pipe cooling system.

## 3.3 Liquid cooled cold plates

Liquid cooled cold plates are able to provide localised cooling to power electronics by transferring the heat to the liquid that carried it away and in turn dissipates it to either the air, or another liquid [6]. Cold plates come in a large variety of configurations, but the identifying characteristic is having flow passages (tubes, channel, etc.) embedded within a metal substrate. One of the simplest designs is *Formed Tube Cold Plates*, where the coolant tubes are attached to the substrate by soldering, or by using a thermal epoxy [14]. However, its poor performance limits its use to low-power applications. Another example is *Machined Channel Cold Plates*, which has a greatly improved thermal performance. In this design, channels are directly machined into the substrate, and a cover is then soldered on top, forming the flow passages. Depending on the size of the channels, this method can be used in heat flux applications of over  $100 \text{ W/cm}^2$ .

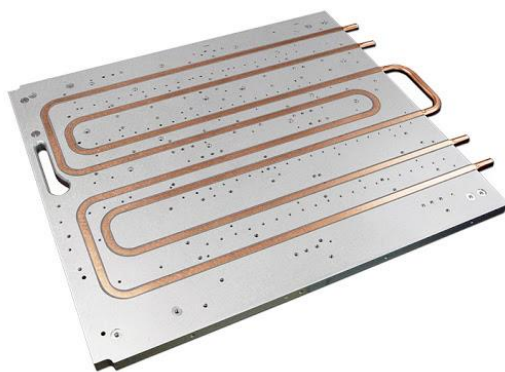


Figure 12: Channel passages machined into cold plate [14].

### 3.4 Two phase direct cooling

Two phase direct cooling removes the boundaries between the cooling fluid and the heat source, therefore reducing the number of contact thermal resistance layers and improving the overall heat transfer rates.

#### 3.4.1 Spray cooling

Spray cooling achieves high heat transfer coefficients by utilising the latent heat of vaporisation (Figure 13). A fluid is broken down into small droplets by either being injected through a nozzle at high pressures, or by using a high-speed air stream [15]. The drops then cling individually to the hot surface, creating a thin fluid film [16]. Heat transfer results from several mechanisms; convection occurs due to the impinging droplets, evaporation at the film surface, and nucleate boiling through the fluid film. Lin and Ponnappan [17] and Chen *et al.* [2] both carried out experiments using water as the working fluid and measured heat transfer rates of  $500 \text{ W/cm}^2$  and  $945.7 \text{ W/cm}^2$  respectively. Spray cooling has the advantage of providing uniform cooling over the surface of the heat source. However, the high complexity of the thermo-hydraulic behaviour of the spray makes it difficult to model and thus predict.

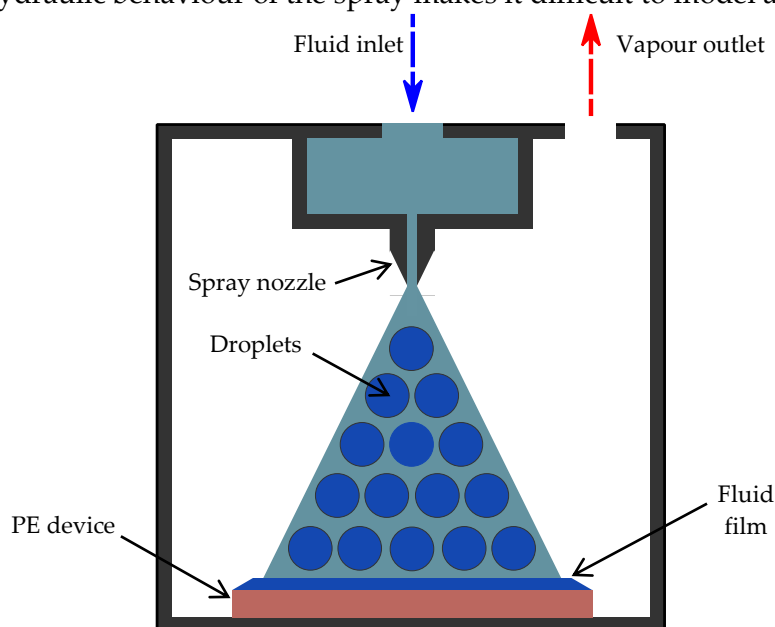


Figure 13: Spray cooling system

### 3.4.2 Jet impingement cooling

Through the use of a converging nozzle, jet impingement cooling delivers a constant, high velocity stream of fluid onto a heat surface (Figure 14). When enough heat is involved, bubbles begin to form and the process becomes a two-phase cooling system. This solution has garnered significant attention due to the possibility of high heat transfer coefficients. Silverman *et al.* [18] used liquid metal coolant to dissipate a heat flux of  $2000 \text{ W/cm}^2$  over an area of  $1 \text{ cm}^2$ . This is coupled with low manufacturing costs thanks to the use of inexpensive materials such as plastics, and convenient manufacturing techniques, like 3D printing. One of the main draw-backs, however, is that when only a single jet is used, two distinct fluid zones are formed; the first is the impingement zone, where the jet hits the surface, and the second begins where the liquid spreads out from the initial point of impact. This creates a non-uniform distribution of cooling, which could lead to failure inducing hotspots. Multi-jet coolers have subsequently become the focus of much research in order to address this issue [19], however this also increases implementation complexity as well as costs associated with the higher flowrates.

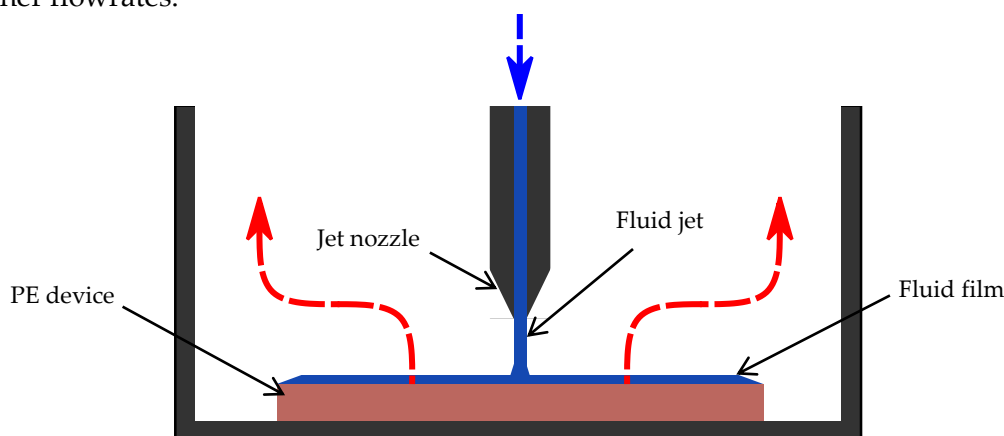


Figure 14: Jet impingement cooling system

### 3.4.3 Immersion cooling

Immersion cooling is a type of direct cooling that involves submerging the PE devices in a coolant pool (Figure 15). Direct liquid cooling is the process of bringing the surface of the chip in physical contact with the cooling fluid, eliminating less thermally efficient layers and thus reducing the overall thermal resistance [16]. It does, however, necessitate the use of a dielectric liquid, thus limiting choice of coolants that can be used. Immersion cooling is achieved through either natural convection, forced convection, or most commonly through nucleate boiling, which provides additional heat transfer through latent heat exchange, bubble induced mixing, and two-phase convection [16]. The highest rates of heat transfer are observed when forced convection is used [20], though this is accompanied with an increase in pressure loss, and thus the required pumping power. Though simple to implement, immersion cooling suffers from low heat transfer coefficients. They are also limited by the *Critical Heat Flux* (CHF), which denotes the departure from nucleate boiling where a thin vapour film can suddenly form along the heated surface, leading to a significantly lower rate of heat transfers and thus causes a large increase in the surface temperature.

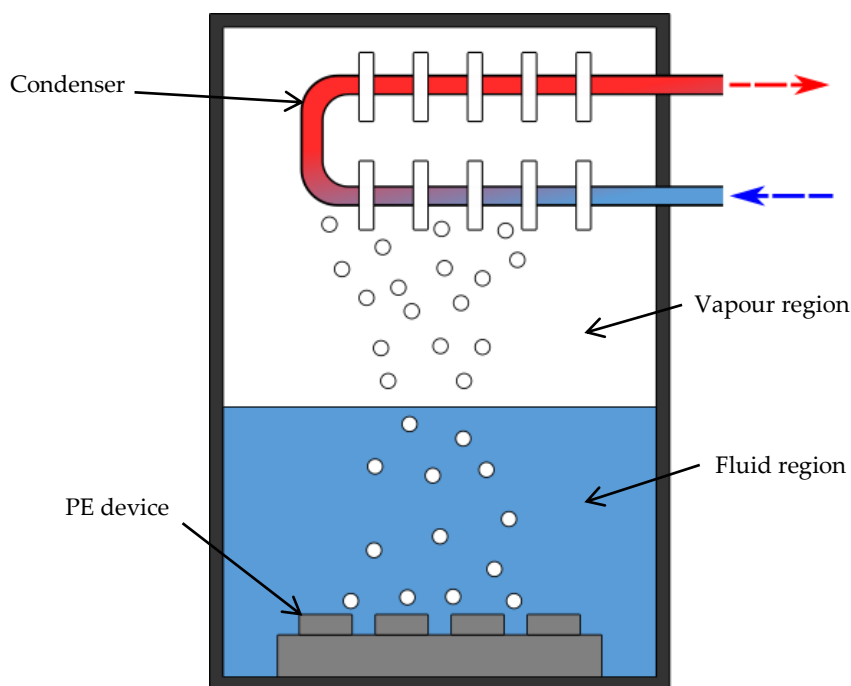


Figure 15: Direct cooling using pool boiling.

### 3.5 Integrated Micro Heat sinks

This category of cooling methods involves small heat sinks that are integrated just next to the PE device. Being small in size requires them to have very high heat dissipating potential in order to be a viable method.

#### 3.5.1 Single- and two-phase microchannels

Microchannel heat sinks have become an important fixture within the PE cooling industry. They use multiple flow channels with high surface-area-to-volume ratio, hereafter referred to as specific surface area. The channels are typically of the order of 1mm or smaller in diameter, and boast specific surface areas of around  $10^4 \text{ m}^{-1}$  or more [21]. They are therefore the typical choice of compact heat sink when very high rates of heat transfer, upward of  $750 \text{ W/cm}^2$  [22], are required. The excellent performance of microchannels does come at a cost however. High pressure losses, which increase with decreasing hydraulic diameter, are to be expected. Large temperature gradients along the length of the cooled surface have also been observed, due to the bulk temperature increase within the coolant. To enhance the performance of microchannel heat sinks further, two phase cooling can be used. This method utilises the latent heat of vaporisation of the coolant, and thus permits the use of lower fluid flowrates to achieve the same rate of heat transfer. This has the clear advantage of reducing the cost, weight and volume of the cooling system, as smaller pumps are required. Unfortunately, much like with spray cooling, the complexity of the thermal-hydraulic behaviour of the fluid means that correlations capable of accurately predicting performance are scarce [23].

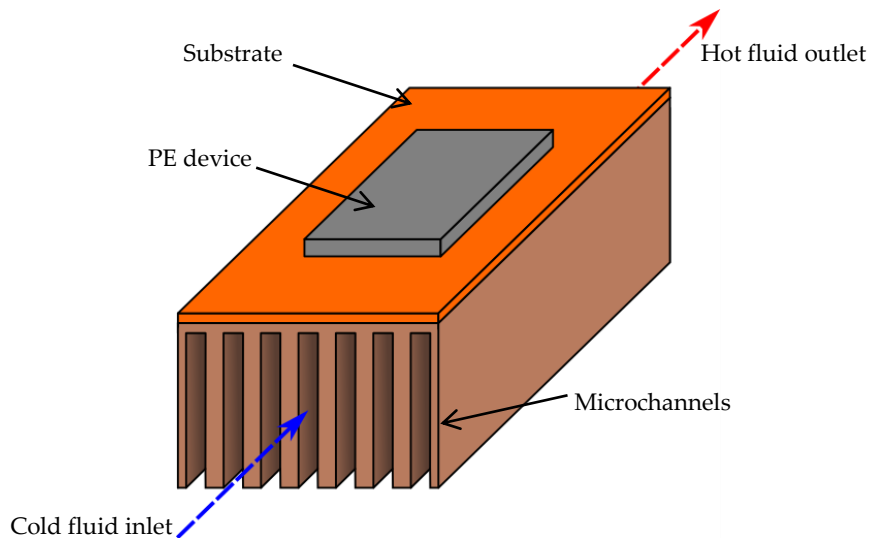


Figure 16: Microchannel heat sink

### 3.5.2 Porous media cooling

Similarly to microchannels, porous materials such as metal foams have the advantage of a drastically increased specific surface area, when compared with other cooling solutions. This makes them an ideal choice when high rates of heat dissipation are required and only limited space is available. Additionally, heat transfer is enhanced due to the tortuous structure of porous materials that generates flow turbulence and improves convective heat transfers within the coolant. There are also manufacturing advantages. For example, metal foams can be fabricated in large quantities, in sections with dimensions of an order of 1m, and can then simply be cut to the required size. It is also relatively simple to fabricate foams with geometrical features down to an order of  $10\mu\text{m}$ , this is considerably harder and more expensive to do with microchannels. However, much like the other high heat transfer rate options, the downside is the higher loss of pressure across the porous material. A much more detailed analysis of metals foams is carried out in Section 4 of this chapter.

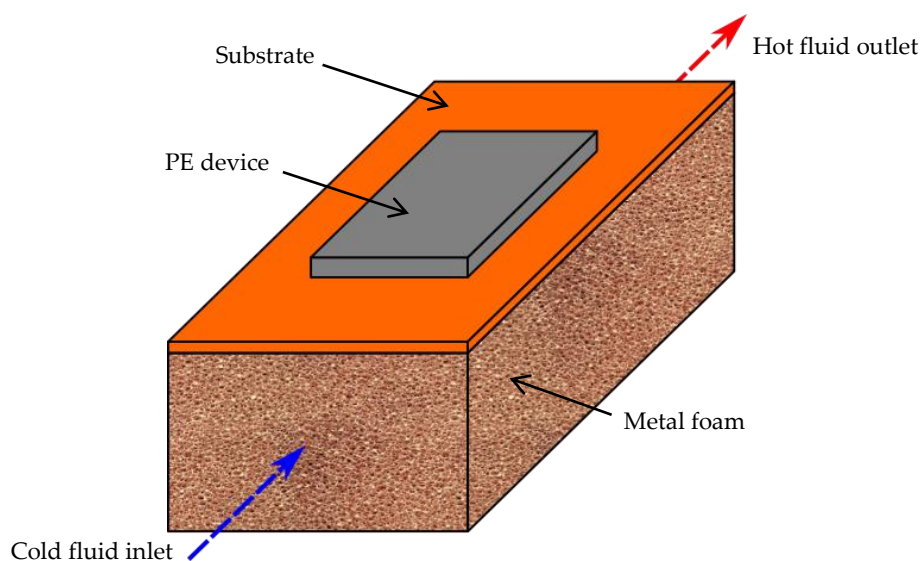


Figure 17: Metal foam heat sink

## 4. Summary of Cooling Strategies

By analysing the cooling options seen above, it seems that when attempting to improve heat transfer there are two strategies that are most commonly considered; the first is to focus on the coolant, such as using a phase change as with immersion boiling, and the second is to focus on the geometry of the heat sink, such as with liquid cold plates. Many solutions consider both these strategies, using multiple technologies in conjunction with one another. Micro heat sinks are an example of this, combining some kind of augmented geometry (microchannels, pin fins, metal foam etc.), with usually forced liquid or gas convection. By definition, this is one of the smallest solutions, thus suitable to be integrated within a power module, and Figure 7 shows that they offer the lowest TTC. It therefore seems to be the best option for improving the thermal management within a PCoC package. The question then becomes: which geometry (microchannels, pin-fins etc.) should be used? In order to answer this question, the aims must first be made clear. When considering the geometry of a heat sink, one must:

- Maximise overall heat transfer within the heat sink.
- Minimise pressure loss within the fluid, and thus the cost requirements of pumping the coolant.

In the case of microchannels, maximising heat transfer can be achieved simply by increasing the number of fins within the given volume of the heat sink. However, doing so will also reduce permeability and give rise to an increase in pressure loss. In order to achieve a balance between the two parameters, optimisation of the dimensions of the micro channels (fin width, channel width, number of channels etc.) must be carried out. As has been shown above, metal foams have the potential of offering even higher rates of heat transfer than microchannels, whilst fulfilling the other criteria of being small and, depending on the material, electrically conductive. It will also be shown in Chapter 3 that the internal geometry of metal foam can be optimised in much the same way as is done for microchannels. Coupled with the manufacturing advantages, this makes metal foams the ideal choice for a small, integrated heat sink. Therefore, this work has chosen to concentrate on metal foams as a novel replacement to the more common microchannel heat sinks for use within PE packaging. As a means of providing a well needed benchmark, microchannel heat sinks will also be considered. Both have very similar applications and also share many of the same design considerations. Microchannels are also well established within the literature, making finding appropriate models relatively easy.

### 4.1 Choice of thermal management strategy

In this work a novel cooling solution is proposed that can be implemented into the PCoC structure (Figure 3), and can potentially provide an adequate rate of heat transfer from the switching cells. The proposed idea, shown in Figure 18, integrates layers of metal foam heat sinks in between PE chips, replacing the copper substrate seen in Figure 3. This method would rely primarily on conductive heat transfer through the solid metal foam, and convective heat transfer within the liquid coolant.

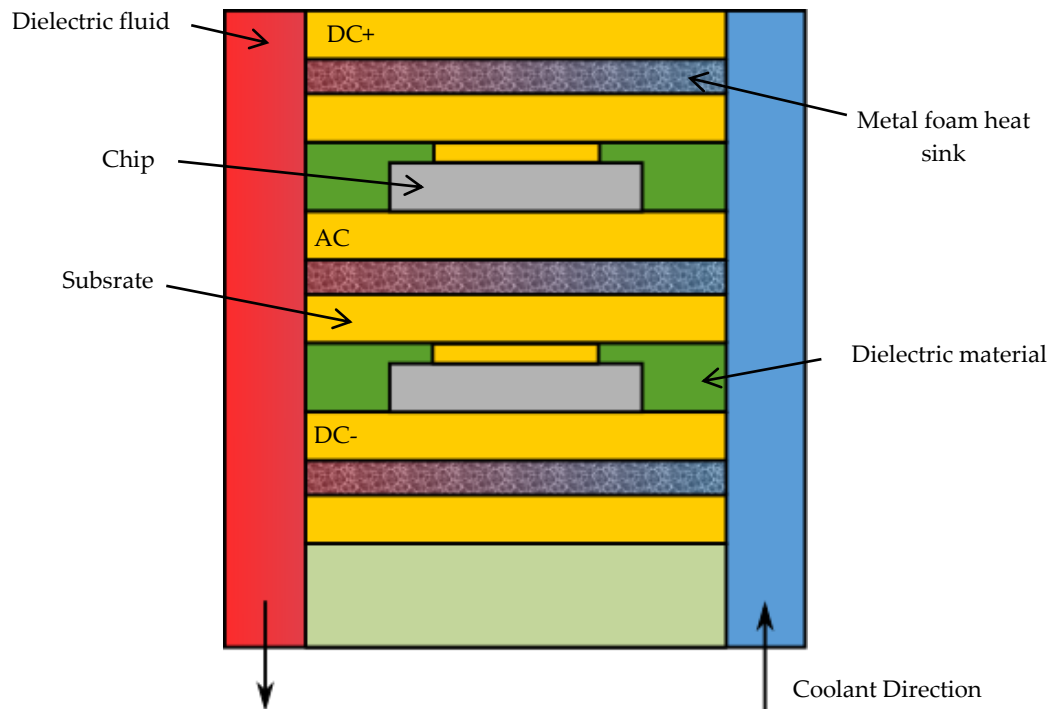


Figure 18: PCoC package with integrated micro heat sinks.

## 4.2 Project aims

So as not to simply trade better thermal management for increased input power, efficient cooling must occur whilst ensuring limited pressure losses. Therefore, the aims of this project are as follows:

- Develop an analytical model capable of predicting the thermal and hydraulic performance of flow through a metal foam heat sink.
- Compare the model with numerical simulations.
- Use the model to optimise the internal geometry of the metal foam to maximise heat transfer for a given pressure loss.
- Compare the performance of the optimised foam with that of optimised microchannels.
- Fabricate a test bench in order to validate the model experimentally.
- Simulate the combined PCoC package and integrated cooling system to determine overall thermal performance in an applied setting.

## 5. Metal Foams

The use of metal foams within heat sinks has increased drastically in recent years, as has the amount of research being carried out on this topic. These materials are typically lightweight, have low densities, high specific surface areas and good thermal properties. In order to integrate a metal foam heat sink into a power module, it is necessary to accurately predict heat transfer performances and pressure loss within the foam. To achieve this, it is necessary to understand exactly how metal foams are classified and characterised.

## 5.1 Classification

The broadest classification that can be applied to foam is whether it is open- or closed-celled (Figure 19). In open-cell foams, all the pores are interlinked, allowing a single, unbroken path to be drawn through the foam sample beginning and ending at any point. In contrast, closed-cell foams have completely isolated pores, thus no fluid can pass through.

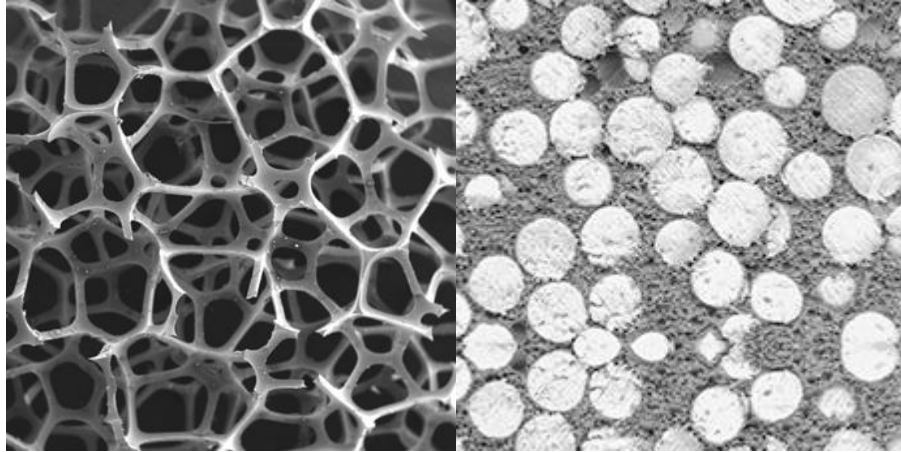


Figure 19: Open- (left) and closed- (right) celled metal foams.

As closed-cell foams are essentially impermeable, they are not suitable for heat sinks that employ convection heat transfer, and thus no further analysis will be carried out on them in this work. Only open-cell foams will be considered, and they can be further classified by their internal structure. Though typically stochastic in nature, metal foams are often represented by regular, repeating unit cells, which can range from the relatively simple cube, to the more sophisticated tetrakaidecahedron. Several examples can be seen in Figure 20.

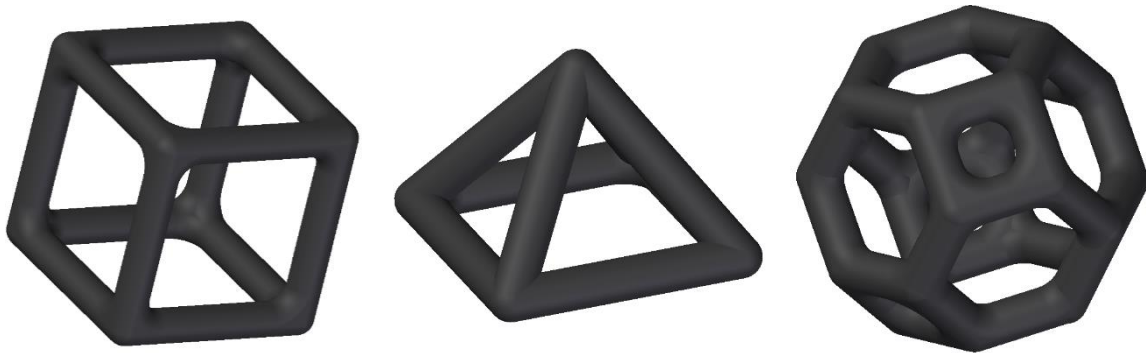


Figure 20: Examples of unit cells to represent metal foam. Cube (left), pyramid (centre), and tetrakaidecahedron (right).

Though some accuracy must clearly be sacrificed, the use of the above unit cells greatly simplifies numerical and analytical analysis by allowing the different physical aspects of foam to be more easily determined. These are as follows,

- Porosity ( $\epsilon$ ): the ratio of void volume to overall volume.
- Fibre diameter ( $d_f$ ): the average diameter of an individual solid fibre.

- Pore diameter ( $d_p$ ): the average diameter of the largest sphere that can fit within a unit cell.
- Specific surface area ( $A_{sf}$ ): the ratio of solid surface area to overall volume.
- Pore density ( $PPI$ , pores per inch): the average number of pores per inch within a given direction.

Of the above properties, it is the pore diameter that often requires further explanation, as it is not, as one might think, the diameter across the unit cell. Instead it is the diameter of the largest sphere that can be bounded by the cell, as shown in Figure 21.

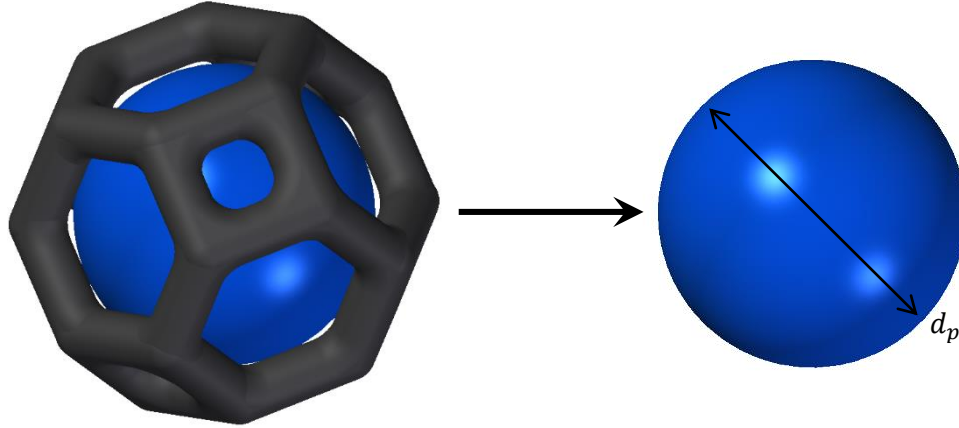


Figure 21: Visual representation of how the pore diameter of the tetrakaidecahedron is calculated.

Though the above parameters can be calculated experimentally (details in Chapter III), this is often difficult, time consuming and expensive, thus analytical models for a wide range of unit cells have been developed within the literature. This work, however, will only concentrate on those valid for the tetrakaidecahedron, as this geometry is commonly accepted to be the realistic when mimicking actual open foams. The following equations have been proposed [24], [25], [26]:

**Fibre diameter:**

$$d_f (m) = 1,18 \sqrt{\frac{1 - \varepsilon}{3\pi}} \left( \frac{1}{1 - e^{-\left(\frac{1-\varepsilon}{0,04}\right)}} \right) d_p \quad (1.1)$$

**Specific surface area:**

$$A_{sf} (m^{-1}) = \frac{3\pi d_f \left( 1 - e^{-\left(\frac{1-\varepsilon}{0,04}\right)} \right)}{(0,59d_p)^2} \quad (1.2)$$

**Pore density:**

$$PPI (pores/inch) = \frac{d_p}{0.0254} \quad (1.3)$$

## 5.2 Manufacturing Techniques

There are many different methods of manufacturing metals foams, each producing a final product with a wide range of properties. They can be broadly split into two groups, those that produce a homogenous pore distribution, and those who produce a pore distribution that

is non-homogenous. As mentioned previously, there are several advantages when fabricating a metal foam heat sink. Namely the features of metal foams are dependent upon the scale of the metal powder used within the fabrication process, and thus it is easier to produce a foam with pore size and fibre size of the order of  $10\ \mu\text{m}$ .

### 5.2.1 Homogeneous pore distribution

#### *Vapour deposition*

This process first requires medical grade polyurethane foam as a framework, offering a quasi-uniform pore size. The foam is reticulated and then pyrolysed, resulting in a low-density reticulated vitreous carbon (RVC) skeleton that can be later machined into a range of predetermined shapes [27]. Then, by using chemical vapour deposition, commercially pure tantalum is deposited throughout the RVC framework. Thus, it is the cellular density and pore geometry of the polyurethane foam that determines the pore size and homogenous structure of the metal foam. The porosity is controlled by the duration of the CVD process, and is approximately 75–85%, with an average pore size of about 550 microns.

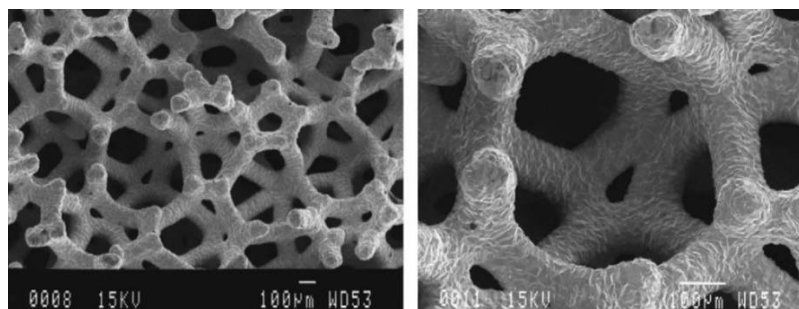
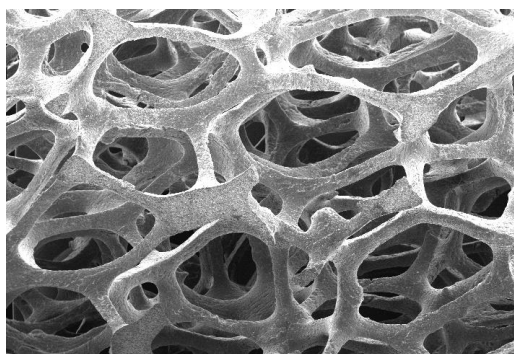


Figure 22: An example of foam produced by vapour deposition [27].

#### *Investment casting*

Much like vapour deposition, this method uses another material to first create the desired template, in this case, an open-celled polymer foam. The polymer is coated with a mould casting slurry (typically a ceramic powder) which is then dried, embedded in casting sand and baked. This hardens the mould and also decomposes the polymer. The mould is then filled with a molten metal and allowed to cool. After removal of the mould material, what remains is the metal allowing in the shape of the original polymer foam [28]. The majority of the metal foams available on the market use this manufacturing method, such as Duocel, which is used in the experimental validation section of this work in Chapter 4. The final properties of the metal foam are completely controlled by the initial polymer template, with a typically porosity around 90%.



*Figure 23: An example of foam produced by investment casting.*

#### *Additive manufacturing*

Also known as 3D printing, this novel manufacturing process has been used to create porous metals with controlled size, shape and distribution of the porosity. The advantage of additive manufacturing is the almost limitless complexity of the structures that can be produced, straight from a computer model, with no need for tooling. Various additive manufacturing techniques has been developed for metallic and ceramic materials. We describe below only one of them, called binder-jetting. This method is able to create a foam inside a cavity that contains a metal or ceramic powder bed supported by the moving piston. The printing is operated layer by layer. An organic binder material is used to selectively adhere the particles at the location where matter is required. When one layer is made, the piston is lowered, and another layer of powder particles is distributed. This process is repeated until the foam is of the required depth. The binder is then consolidated using an initial heat treatment, allowing any unbounded powder is removed. Finally, a secondary heat treatment removes the binder, and the remaining powder is sintered (see the definition of sintering in the following section).

This manufacturing method has the potential of producing foams with the widest range of properties, as they are only dependant on the initial computer design (Figure 24). However, the scale of physical features (fibres, pores) that can be fabricated is limited by current 3D printing technology, the smallest being of the order of  $100\mu\text{m}$ , larger than other methods.

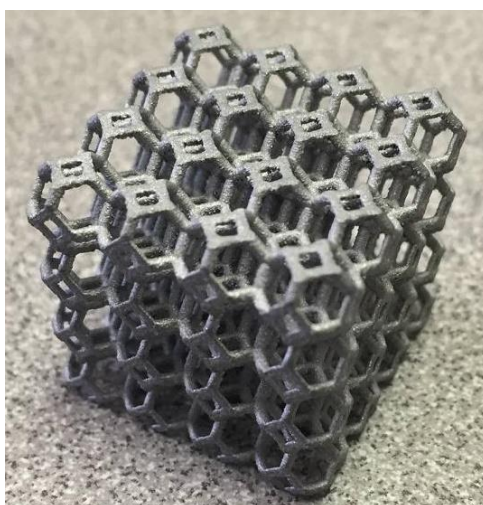


*Figure 24: An example of foam produced by additive manufacturing.*

## 5.2.2 Non-homogenous pore distribution

### *Replication*

This approach, used by Li et al. [29], is a three step procedure for fabricating highly porous titanium and titanium alloy. Polyurethane foams are submersed in a titanium slurry, containing 70% Ti-6Al-4V powder, 20% H<sub>2</sub>O and 10% ammonia solution. The solution is added to improve the rheological properties of the slurry. By drying and repeating the process several times, all of the polyurethane foam struts are eventually coated with the metal powder. The polyurethane scaffold is then thermally removed, and the remaining metal powders are sintered, producing a reticulated open-cell foam with hollow titanium struts (Figure 25). This method is unique in that it produces a foam with three separate porosities,

- the porosity on the surface of the hollow struts,
- the porosity at the core of the hollow struts previously occupied by the polyurethane foam, and,
- the open porosity between struts.

The properties of the finally product are heavily dependent on the rheological properties of the slurry. The foam produced by Li et al. [29] had a porosity of about 88%.

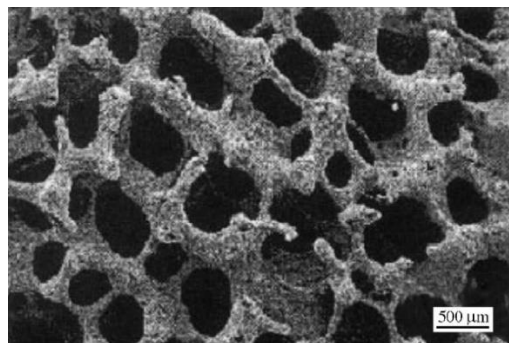


Figure 25: An example of foam produced by replication [27].

### *Powder sintering*

By far the most common methods for fabricating porous materials, sintering is the process of binding powder particles at temperatures much lower than the fusion temperature of the metal [30]. Instead, the particles are joined together by atom diffusion, creating a strong bond at contact points, whilst maintaining a relatively constant pore size, as can be seen in Figure 26. Powders are first compacted with a binder, added to hold the particles together. This ensures a greater area for mass transport between the particles in the solid-state diffusion process [31].

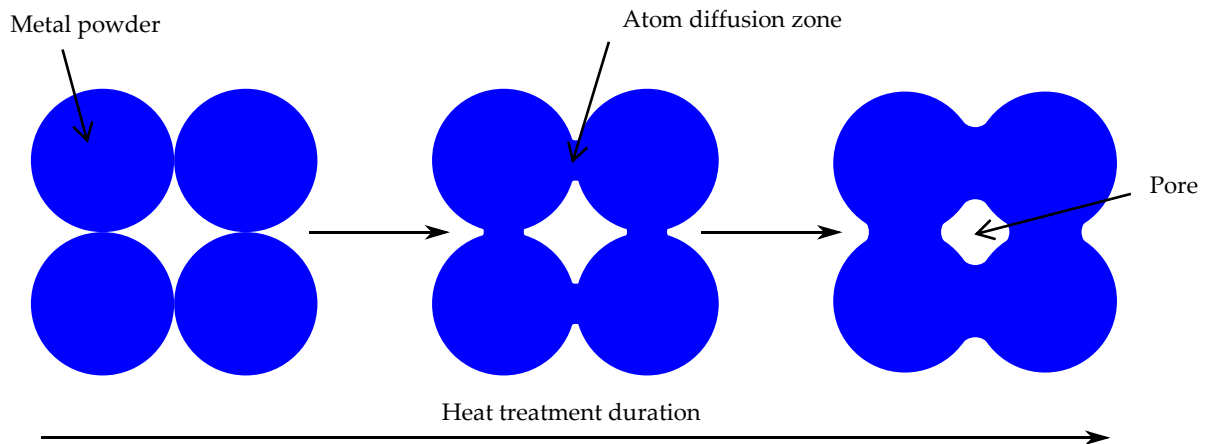


Figure 26: Sintering of metal powders.

Porosity is controlled by several process variables, including compacted powder density, sintering temperature and time, and alloying additions. The pore size and shape are dictated by the size and shape of the powder used. For spherical powder particles the porosity is limited to 50% and the shape of the pores is highly non-spherical [31].

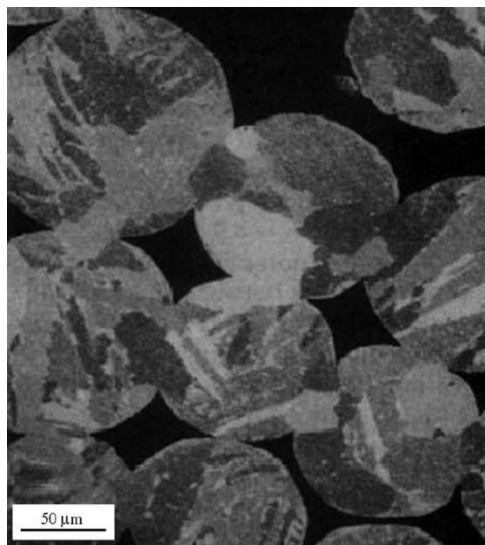


Figure 27: An example of foam produced by powder sintering [27].

#### Space Holder Method

The space holder method is a fabrication process based on sintering, which includes an additional step that can greatly increase the porosity of the final product. The first step is to create a mixture of metal powder and a space holder material (potassium carbonate, salt), which is then compacted, as before. The mixture is then subjected to a low temperature heat treatment, or pre-sintering, used to create an initial, albeit weak bond between the metal particles. Then, depending on the space holder material, an additional, higher heat treatment is used to remove it, as can be seen in Figure 28. In the case of salt, the second heat treatment is ignored and instead the sample is submerged in water until all of the salt has dissolved. Finally, a last heat treatment further sinters the metal powder, finishing the process.

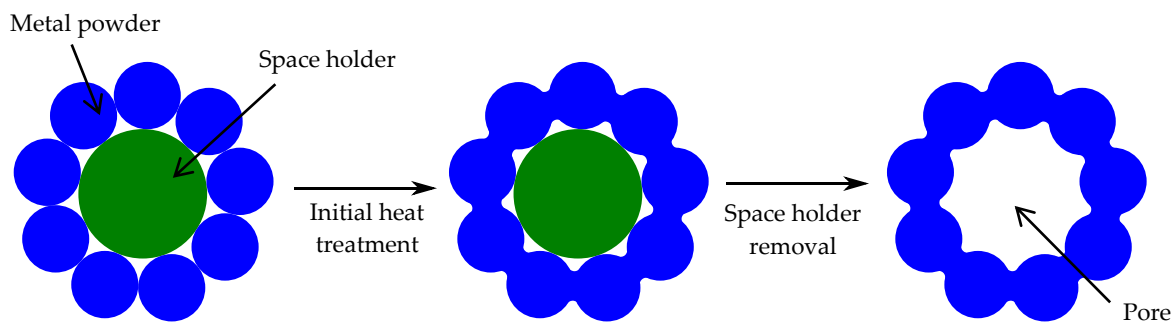


Figure 28: Space holder method determines pore size.

This method provides a foam with a close to homogenous pore structure and primary porosity levels of around 60–80%. There is also a secondary porosity between the individual powder particles, as seen in the previous section. By choosing the size, shape and quantity of the space holder used, this process gives the manufacturer greater control over the physical and mechanical properties of the foam.

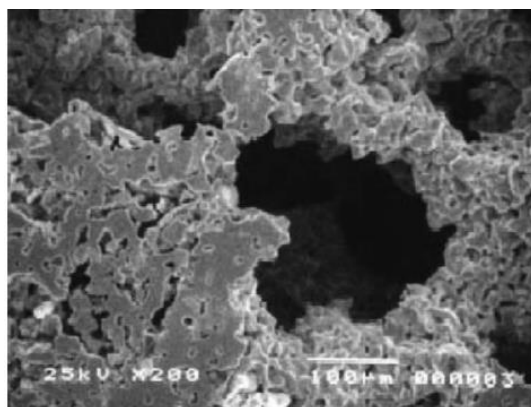


Figure 29: An example of foam produced by space holder method [27].

Lost carbonate sintering is a type of space holder method used to produce Versarien® foam [32], another commonly available foam on the market (Figure 30). It uses copper powder, potassium carbonate powder as the space holder, and ethanol as the binder. The mixture is compressed and placed within a VTS vacuum furnace where it then undergoes a three step heat treatment. The first step removes the ethanol binder at a relatively low temperature. Then the temperature is increased so as to partial sinter the copper particles. Finally, the temperature is increased again, decomposing the potassium carbonate and finishing the sintering process.

Similarly to the space holder method, the foams that are produced have two distinct porosities, controlled by the size of the potassium carbonate powder, and the size of the copper powder respectively. The Versarien® foam produced by this method has a porosity of 63%.

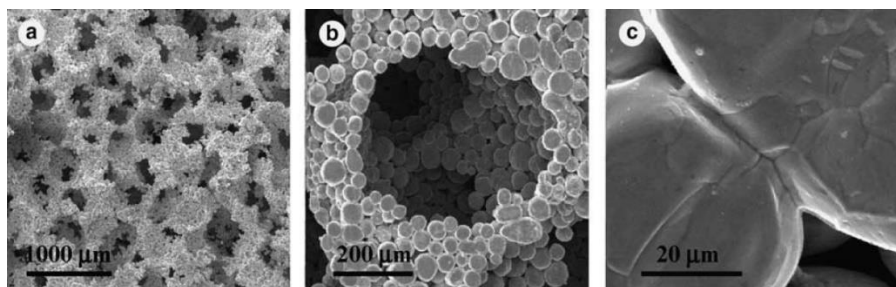


Figure 30: An example of foam produced by lost carbonite sintering [32].

### 5.3 Foam material

The metal foams will be made of copper due to its excellent thermal conductivity. Copper is also regularly used to make metal foams in several of the manufacturing methods introduced earlier (powder sintering, rapid prototyping, space holder, lost carbonate sintering) making it the ideal choice. A comparison of the thermal conductivities of metals common used in heat sink design can be seen in Figure 31.

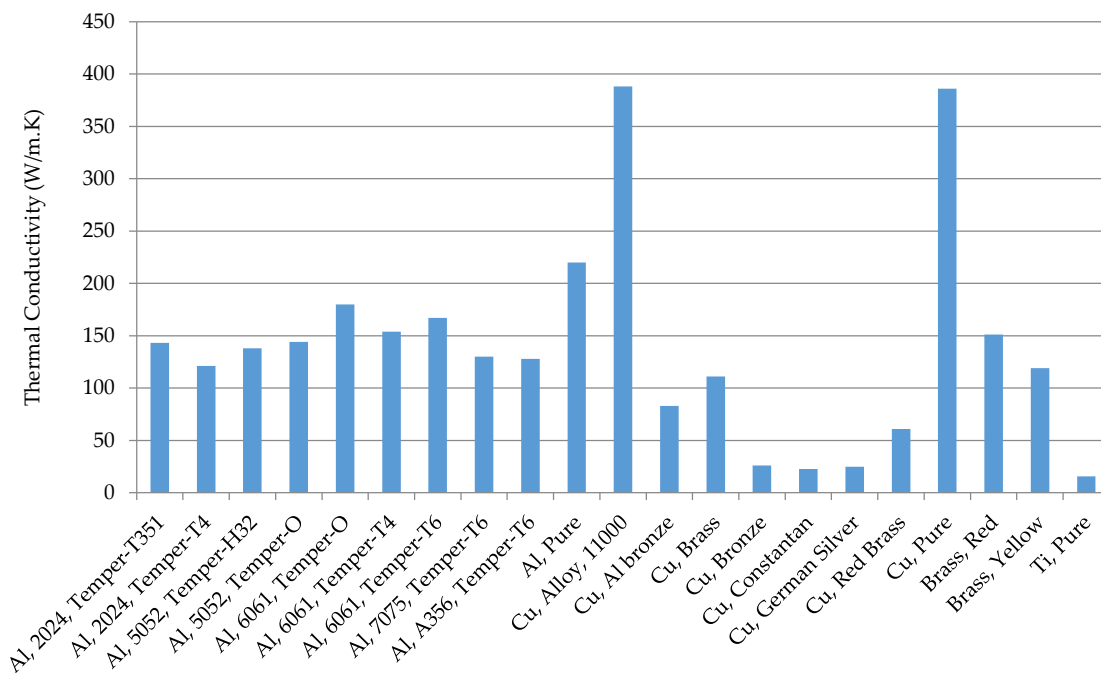


Figure 31: Thermal conductivities of common metals used to make foam.

## 6. Coolant

Each layer of metal foam is traversed by a heat transfer fluid, providing double-sided cooling to each chip. Because of the high currents used with a PE device, and the relatively small distance between each chip, it is necessary to use a dielectric liquid to prevent a voltage short. A review was therefore carried out to determine which of the many available fluids would be the most effective coolant.

A dielectric liquid is a dielectric material in a liquid state, that can prevent, or rapidly quench electric discharges, and is used as an insulator in high voltage application [33]. The

parameter used to describe how effective as an insulator a dielectric liquid is, is its *dielectric strength*. Other desirable features of a coolant used in a PE environment are:

- high thermal stability;
- non-flammable;
- low toxicity;
- chemical inertness against heat sink materials;
- good heat transfer properties.

### 6.1.1 Types of Dielectric Coolant

#### *Mineral Oil*

“Mineral oil” is a term applied to a broad range of distillates primarily made from petroleum. Most often, mineral oil is the liquid by-product of refining crude oil to make gasoline and other petroleum products. Mineral oils have good dielectric properties and are one of the most common used liquids, being very readily available. Unfortunately, they are typically highly viscous and do not biodegrade easily.

#### *Silicate Ester*

A silicate is a compound containing an anionic silicon compound and an ester is a chemical compound derived from an acid (organic or inorganic) in which at least one –OH (hydroxyl) group is replaced by an –O–alkyl (alkoxy) group. Synthetic ester fluids have suitable dielectric properties and are more readily biodegradable than mineral oil and hydrocarbon fluids. Due to their high cost compared with other less-flammable fluids, synthetic esters are mainly used in specialty applications such as traction and mobile transformers. Synthetic esters also have excellent thermal stability and good low-temperature properties. Natural esters, such as vegetable oil and seed oil, have good thermal properties coupled with a low cost and a low environmental impact. However, they often have higher viscosities than other synthetic liquids.

#### *Poly-alpha-olefin (PAO)*

A PAO is any of a class of polymers produced from a simple olefin as a monomer. These fluids are characterised by being able to remain oily and viscous, even at lower temperatures. While having some of the desirable characteristics of a liquid coolant for electronics, PAOs are flammable and not compatible with several plastic and rubber components. Their specific heat and thermal conductivity properties are also inferior to that of water based fluids.

#### *Fluorocarbon/hydrocarbon*

Among the non-aqueous fluids, a popular cooling media in electronics is the fluorinated compounds. Typically employed fluorinated compounds, such as perfluorocarbons (i.e. FC-77), hydrofluoroethers (HFEs) and perfluorinated polyethers exhibit many good characteristics. They are dielectric, non-flammable, non-toxic, and with a low freezing point and viscosity. But the cost of these compounds is very high and their specific heat and thermal conductivity are much lower than those of water based fluids. Despite their poorer thermal properties as compared to water, perfluorocarbons are particularly suitable for direct contact cooling due to their high electrical resistivity.

### Silicone Oil

Another class of popular coolants derived from chemistry is dimethyl- and methyl phenyl-poly (siloxane), more commonly known as silicone oil. Since this is a synthetic polymeric compound, the molecular weight as well as the thermo-physical properties can be adjusted. These liquids can be used at temperatures as low as  $-100^{\circ}\text{C}$  and as high as  $400^{\circ}\text{C}$ , with an excellent service life in closed systems in the absence of oxygen. They are non-toxic and have low viscosity, however their very low surface tension gives these fluids the tendency to leak around pipe-fittings.

#### 6.1.2 Review of dielectric coolant thermal properties

When choosing a dielectric liquid, it is important outline what makes a good coolant. As previously stated, the dielectric strength of the liquid is crucial, and all of the coolants included in this analysis are suitably insulating. Following this, the thermal properties must be assessed, with the ideal liquid having a:

- high density  $\rho$ , thermal conductivity  $k_f$  and specific heat capacity  $C_p$  to improve heat transfer;
- low viscosity  $\mu$  to reduce the required pumping power.

Therefore a performance parameter  $P_{th}$  was used as a means of testing the different coolants that were available on the market:

$$P_{th} = \frac{\rho k_f C_p}{\mu} \quad (1.4)$$

The results of the analysis can be seen in Table 1. The coolants have been colour coded to differentiate each family of liquid. Figure 32 shows the  $P_{th}$  values of each of the coolants.

Transformer Oil
Mineral Oil
Silicone Oil
Ester-based Oil
Pao
Fluorocarbon/hydrocarbon

TABLE 1:

Dielectric coolant parameters

Coolant	Liquid Density ( $\text{kg.m}^{-3}$ ) at $25^{\circ}\text{C}$	Dynamic Viscosity ( $\text{Pa.s}$ ) at $25^{\circ}\text{C}$	Thermal Conductivity ( $\text{W.m}^{-1}.\text{K}^{-1}$ ) at $25^{\circ}\text{C}$	Specific Heat Capacity ( $\text{KJ.kg}^{-1}.\text{K}^{-1}$ ) at $25^{\circ}\text{C}$	$P_{th}$ ( $\text{W}^2.\text{m}^{-4}.\text{K}^{-2}.\text{Pa}^{-1}$ )
Water	997	8.90E-04	0.607	4.810	3.27E+06
Trafosynth	912	7.10E-03	0.130	2.000	3.34E+04
Paratherm NF	880	2.71E-02	0.108	1.825	6.38E+03
Clearco PSF 0,65cSt	760	4.94E-04	0.100	1.717	2.64E+05
Clearco PSF 1cSt	818	8.18E-04	0.100	1.717	1.72E+05
Clearco PSF 1.5cSt	851	1.28E-03	0.100	1.717	1.14E+05

Coolanol 20	887	2.31E-03	0.117	1.970	8.87E+04
Coolanol 25R	893	4.91E-03	0.129	1.840	4.32E+04
Midal eN	915	6.41E-02	0.178	1.860	4.73E+03
Spectrasyn 2	798	3.99E-03	0.140	2.300	6.44E+04
Synfluid 2	798	4.07E-03	0.142	2.219	6.18E+04
FC-3283	1820	1.37E-03	0.066	1.100	9.68E+04
FC-40	1855	4.08E-03	0.065	1.100	3.25E+04
FC-43	1860	4.65E-03	0.065	1.100	2.86E+04
FC-70	1940	2.33E-02	0.070	1.100	6.42E+03
FC-72	1680	6.38E-04	0.057	1.100	1.65E+05
Novec 649	1600	6.40E-04	0.059	1.103	1.63E+05
Novec 7500	1614	1.24E-03	0.065	1.138	9.61E+04
Novec 7700	1797	4.49E-03	0.065	1.030	2.68E+04
Paratherm LR	760	1.52E-03	0.150	2.010	1.51E+05

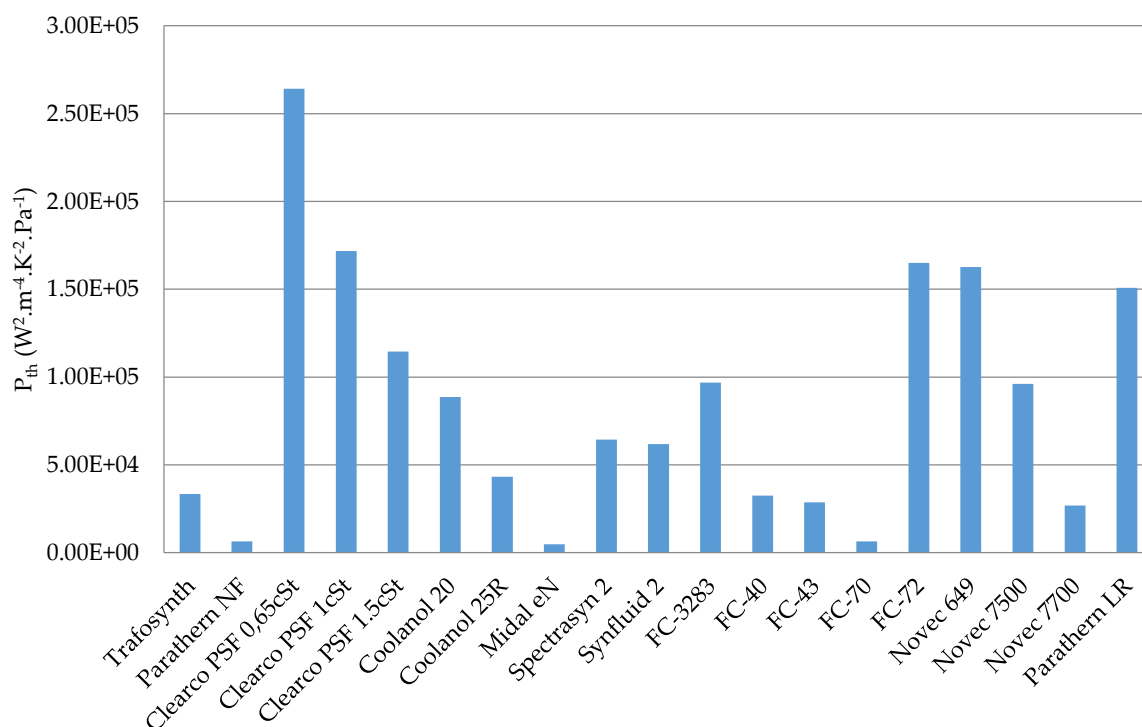


Figure 32: Performance parameter of different dielectric liquids.

The top performer is the silicon oil Clearco PSF 0,65cSt, followed by Clearco PSF 1cSt. Unfortunately, both of these fluid have very low flash points,  $-1^{\circ}C$  and  $37^{\circ}C$  respectively, which was deemed too great a safety hazard. The next two high performing coolants are the fluorocarbons FC-72 and Novec 649. Again however, these fluid each come with a crucial drawback having boiling points of  $56^{\circ}C$  and  $49^{\circ}C$  respectively, which places their region of applicability outside of the operational conditions of this project. So finally the fifth highest performing coolant was chosen, Paratherm LR. It is an aliphatic-hydrocarbon based heat transfer fluid designed for use in closed-loop, liquid-phase heating and cooling systems up to  $232^{\circ}C$  in electric and steam heaters and down to a  $-50^{\circ}C$  surface temperature in direct-expansion sinks. It is a very stable liquid, not reacting when coming in contact with water,

and also inert enough that the presence of chemical coatings, oils and other mechanical residues does not affect its operational lifetime.

## 7. Conclusion

In this chapter, the basic concepts of PE and its packaging have been introduced. It has been explained how the technological advancements, leading to improved EMC behaviour, had an overall negative effect on the thermal management of the packaging. This has led to the need for efficient small scale cooling solutions, that can be integrated into modern PE packaging. Therefore, as part of the broader context of this work, the most pertinent of the currently available cooling strategies, and their advantages and disadvantages, have also been presented. This review of the literature helped to decide the solution proposed by this study, which involves sandwiching layers of metal foam heat sinks in between PE chips. In theory, this solution would maintain the EMC advantages of the PCoC packaging design, whilst also providing adequate cooling, thus making the PCoC layout more viable. As part of the proposed solution metal foams were described in detail, how they are classified, examples of their physical properties and some of the most common fabrication methods. The material of the foam heat sink and the liquid coolant were also discussed. By carrying out studies of the scientific literature, it was found that copper, with its very high thermal conductivity, is the most appropriate choice of material. This decision is reinforced by the fact that several of the manufacturing techniques can use copper. In a similar manner it was found that Paratherm LR provides the highest thermal conductivity, and lowest viscosity whilst also having a higher enough dielectric strength. After deciding this principle factors of the cooling strategy proposed in this work, it was then possible to layout the specific aims of the project which fall roughly into three categories: Analytical model, optimisation, experimental validation.

In the next chapter the proposed solution will be described in detail and simplified down into a model that will be tested. The geometry of the heat sinks, the imposed boundary conditions and the choice of dielectric liquid will also be discussed. Following this, the analytical model, its origins and its derivation will be presented in depth. This will be followed by comparisons with numerical simulations, the problems that arose during validation, and the eventual solution thanks to the use of a *Space Mapping* (SM) algorithm.

## 8. Bibliography

- [1] B. K. Bose, "Power Electronics- A Technology Review," *Proceedings of the IEEE*, vol. 80, no. 8, 1992.
- [2] C. Chen, F. Luo and Y. Kang, "A Review of SiC Power Module Packaging: Layout, Material System and Integration," *Transactions on Power Electronics and Applications*, vol. 2, no. 3, 2017.
- [3] D. Garrido-Diez and I. Baraia, "Review of Wide Bandgap Materials and their Impact in New Power Electronics," in *IEEE International Workshop of Electronics, Control, Measurement, Signals and their Application to Mechatronics*, Donostia-San Sebastian, 2017.
- [4] G. Régnat, "Onduleur à Forte Intégration Utilisant des Semi-Conducteurs à Grand Gap," Université Grenoble-Alpes, 2016.

- [5] E. Vagnon, P. O. Jeannin, J. C. Cr ebier and Y. Avenas, "A Bus-Bar-Like Power Module Based on Three-Dimensional Power-Chip-on-Chip Hybrid Integration," *IEEE Transactions on Industry Applications*, vol. 46, no. 5, 2010.
- [6] S. Kang, "Advanced Cooling for Power Electronics," in *International Conference on Integrated Power Electronics Systems (CIPS)*, 2012.
- [7] L. Meysenc, M. Jylhakallio and P. Barbosa, "Power Electronics Cooling Effectiveness Versus Thermal Inertia," *Transactions on Power Electronics*, vol. 20, no. 3, 2005.
- [8] E. Yu and Y. K. Joshi, "Natural Convection Air Cooling of Electronic Components in Partially Open Compact Horizontal Enclosures," *IEEE Transactions on Components and Packaging Technologies*, vol. 23, no. 1, pp. 14-22, 2000.
- [9] S. Baskaya, M. Sivrioglu and M. Ozek, "Parametric Study of Horizontal Natural Convection Heat Transfer from Horizontal Rectangular Fins," *International Journal of Thermal Science*, vol. 39, pp. 797-805, 2000.
- [10] K. E. Starner and H. N. McManus, "An Experimental Investigation of Free-Convection Heat Transfer from Rectangular Fin-Arrays," *Journal of Heat Transfer*, vol. 85, no. 3, pp. 273-278, 1963.
- [11] F. Incropera, D. Dewitt, T. Bergman and A. Lavine, *Fundamentals of Heat and Mass Transfer*, 6th ed.
- [12] W. M. Kays and A. L. London, *Compact Heat Exchangers*, Third Edition, New York: McGraw-Hill Inc., 1984.
- [13] Y. F. Maydanik, "Loop Heat Pipes," *Applied Thermal Engineering*, vol. 25, no. 5-6, pp. 635-657, 2005.
- [14] S. G. Kandlikar and C. N. Hayner, "Liquid Cooled Cold Plates for Industrial High-Power Electronic Devices- Thermal Design and Manufacturing Considerations," *Heat Transfer Engineering*, vol. 30, no. 12, pp. 918-930, 2009.
- [15] K. A. Estes and I. Mudawar, "Optimizing and Predicting CHF in Spray Cooling of a Square Surface," *Journal of Heat Transfer*, vol. 118, no. 3, pp. 672-679, 1996.
- [16] A. Iradukunda, D. Huitink and F. Luo, "A Review of Advanced Thermal Management Solutions and the Implications for Integration in High Voltage Packages," *IEEE Journal of Emerging and Selected Topics in Power Electronics*, vol. 8, no. 1, pp. 256-271, 2020.
- [17] I. Lin and R. Ponnappan, "Heat Transfer Characteristics of Spray Cooling in a Closed Loop," *International Journal of Heat and Mass Transfer*, vol. 46, pp. 3737-3746, 2003.
- [18] I. Silverman, A. L. Yarin, S. N. Reznik, A. Arenshtam, D. Kijet and A. Nagler, "High Heat-Flux Accelerator Targets: Cooling with Liquid Metal Jet Impingement," *International Journal of Heat and Mass Transfer*, vol. 49, no. 17-18, pp. 2782-2792, 2006.
- [19] A. Bhunia and C. L. Chen, "On the Scalability of Liquid Microjet Array Impingement Cooling for Large Area Systems," *Journal of Heat Transfer*, vol. 133, no. 6, 2011.
- [20] I. Mudawar, D. Bharathan, K. Kelly and S. Narumanchi, "Two-Phase Spray Cooling of Hybrid Vehicle Electronics," *IEEE Transactions on Components and Packaging Technologies*, vol. 32, no. 2, pp. 501-512, 2009.
- [21] M. G. Khan and A. Fartaj, "A Review on Microchannel Heat Sinks and Potential Applications," *International Journal of Energy Research*, vol. 35, pp. 553-582, 2010.

- [22] D. B. Tuckerman and R. F. W. Pease, "High-Performance Heat Sinking for VLSI," *IEEE Electron Device Letters*, Vols. EDL-2, no. 5, pp. 126-129, 1981.
- [23] J. Lee and I. Mudawar, "Two-Phase Flow in High-Heat-Flux Microchannel Heat Sink for Refrigeration Cooling Applications: Part II-Heat Transfer Characteristics," *International Journal of Heat and Mass Transfer*, vol. 48, no. 5, pp. 941-955, 2005.
- [24] S. Y. Kim, J. W. Paek and B. H. Kang, "Flow and Heat Transfer Correlations for Porous Fin in a Plate-Fin Heat Sink," *Journal of Heat Transfer*, vol. 122, pp. 572-578, 2000.
- [25] C. Zhao, T. Kim, T. Lu and H. Hodson, "Thermal Transport Phenomena in Porvair Metal Foams and Sintered Beds," University of Cambridge, 2001.
- [26] W. Lu, T. Zhang and M. Yang, "Analytical Solution of Forced Convective Heat Transfer in Parallel-Plate Channel Partially Filled with Metallic Foams," *International Journal of Heat and Mass Transfer*, vol. 100, pp. 718-727, 2016.
- [27] G. Ryan, A. Pandit and D. P. Apatsidis, "Fabrication Methods of Porous Metals for use in Orthopaedic Applications," *Biomaterials*, vol. 27, no. 13, pp. 2651-2670, 2006.
- [28] M. F. Ashby, A. G. Evans, N. A. Fleck, L. J. Gibson, J. Hutchinson and H. N. Wadley, *Metal Foams: A design Guide*, Woburn, MA: Butterworth-Heinemann, 2000.
- [29] J. P. Li, S. H. Li, K. Groot and P. Layrolle, "Preparation and Characterization of Porous Titanium," *Key Engineering Materials*, Vols. 218-220, no. 14, pp. 51-54, 2001.
- [30] R. M. German, *Sintering Theory and Practice*, New York, NY: John Wiley and Sons, Inc., 1996.
- [31] S. Ashman and S. G. Kandlikar, "A Review of Manufacturing Processes for Microchannel Heat Sink Fabrication," in *Fourth International Conference on Nanochannels, Microchannels and Minichannels*, Limerick, 2006.
- [32] J. M. Baloyo, "Porous Metals with Novel Structure for Optimum Heat Exchange Performance," University of Liverpool, Liverpool, 2016.
- [33] J. C. Maxwell, *Electricity and Magnetism*, London: Clarendon Press, 1873.

---

# CHAPTER 2

---

## MODELLING METAL FOAMS TO PREDICT THERMAL AND HYDRAULIC PERFORMANCES

---

### Table of Contents

1. INTRODUCTION.....	32
2. METAL FOAM HEAT SINK.....	32
2.1 HEAT SINK SCHEMATICS.....	32
<i>Thermal boundary conditions</i> .....	33
<i>Hydraulic boundary conditions</i> .....	33
3. MODELLISATION .....	33
3.1 GOVERNING EQUATIONS.....	34
3.2 EFFECTIVE THERMAL CONDUCTIVITY .....	36
3.2.1 Experimental determination .....	36
3.2.2 Pore-scale analysis.....	39
3.2.3 Analytical Models .....	41
3.3 INTERFACIAL HEAT TRANSFER COEFFICIENT .....	46
3.3.1 Pore-scale analysis.....	46
<i>Cube cell geometry and meshing</i> .....	47
<i>Cube cell boundary conditions</i> .....	49
<i>Cube cell results</i> .....	49
<i>Tetraikaidcahedral cell geometry and meshing</i> .....	50
<i>Tetraikaidcahedral cell boundary conditions</i> .....	52
<i>Tetraikaidcahedral cell results</i> .....	52
3.3.2 Analytical correlations.....	53
3.4 PERMEABILITY AND INERTIAL RESISTANCE FACTOR.....	55
3.4.1 Pore-scale simulations .....	55
3.4.2 Analytical Correlations.....	57
3.5 REMARKS .....	57
4. ANALYTICAL MODEL .....	57
4.1 MICROCHANNEL MODEL.....	59
4.2 METAL FOAM MODEL .....	64
4.3 MODEL SUMMARY .....	65
5. MODEL VALIDATION.....	67

5.1	COMPARISON WITH THE LITERATURE .....	67
5.2	MACRO-SCALE SIMULATIONS .....	69
	<i>Geometry</i> .....	69
	<i>Meshing</i> .....	70
	<i>Results</i> .....	70
6.	CONCLUSION .....	74

## 1. Introduction

In this chapter the heat sink proposed in Chapter 1 will be described in greater detail and simplified down into a model that can be analysed both analytically and numerically. The geometry of the heat sink, the imposed boundary conditions, and the mechanisms of heat transfer present will also be discussed. The different methods of modelling metal foams in order to predict thermal and hydraulic performances will then be explained. Following this, a means of deriving an analytical model, as well as the assumptions required to do so, will be laid out for both a typical microchannel, and a novel metal foam heat sink. Validation will be performed, first by testing the models ability to reproduce experimental data from the literature, and then by direct comparison with numerical simulations.

## 2. Metal Foam Heat Sink

### 2.1 Heat sink schematics

The problem that will be analysed within this work is defined by simplifying the proposed solution shown in Figure 17. As the metal foam filled channels are all identical, only a single channel will be analysed initially. This will reduce the overall complexity of the analytical model and the numerical simulations that will be seen later in this chapter. To simplify further, though Figure 17 shows that a heat flux will be imposed on both faces of some of the foam filled channels, in this analysis, a heat flux will only be imposed on the upper surface of the channel. Finally, the heat flux will be imposed uniformly over this surface, as if the chip spans the entire surface of the substrate. Therefore, the heat sink is simplified to the case study shown in Figure .

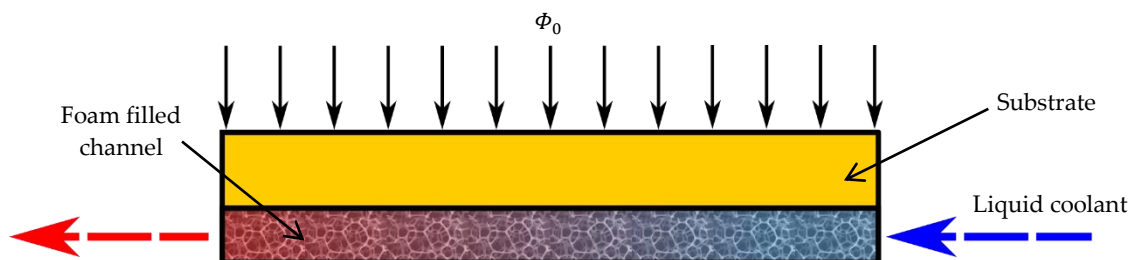


Figure 33: Simplified diagram of proposed metal foam filled heat sink

The metal foam is fixed to a substrate, that experiences a uniform heat flux  $\Phi_0$  on its upper surface. Cooling is achieved via the forced convection of a coolant that traverses the metal foam. A detailed, 3D schematic of this case study can be seen in Figure 34.

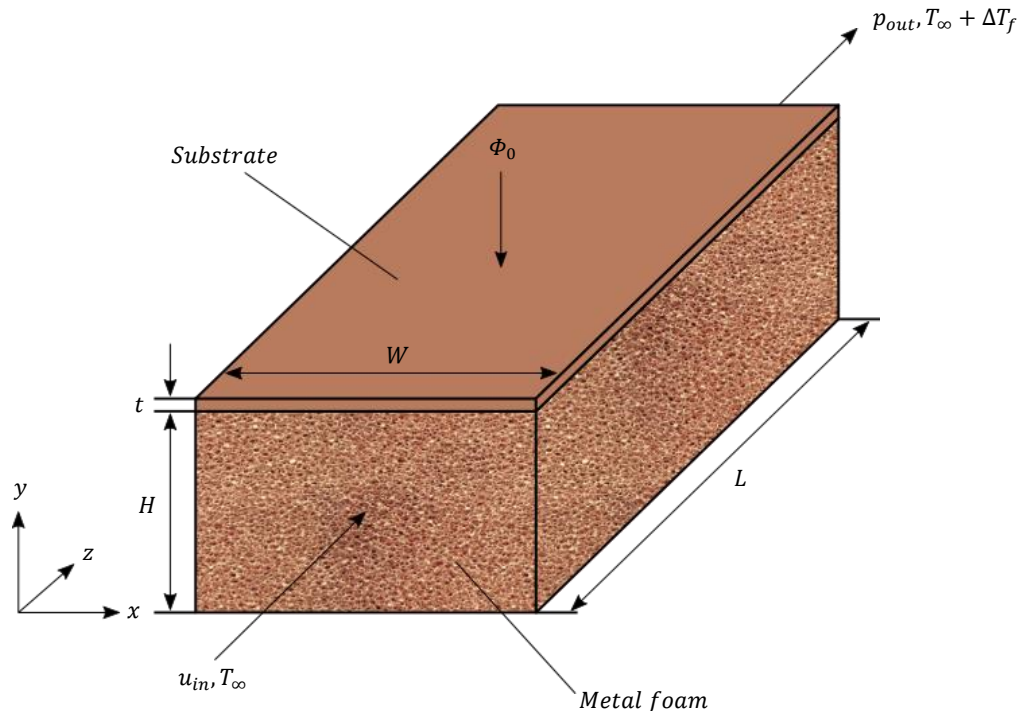


Figure 34 : 3D schematic diagram of metal foam heat sink for use in simulations and experimentation.

In Figure 34, though only a single arrow has been used to denote  $\Phi_0$ , it is still a uniform heat flux over the entire surface of the heat sink. The foam section has a height of 5mm, a width of 10mm and a length of 40mm. The thickness of the copper plate is 2mm.

#### *Thermal boundary conditions*

As previously stated, a uniform heat flux is applied evenly over the surface of the substrate. The sides and base of the channel are adiabatic, thus the only boundaries that permit the transfer of heat are the inlet, the outlet and the surface of the substrate. Flow enters the heat sink with an initial temperature of  $T_\infty$ .

#### *Hydraulic boundary conditions*

Flow enters the heat sink with a uniform velocity  $u_{in}$  in the  $z$ -axis. The inlet and outlet are at  $z = 0$  and  $z = L$  respectively. The sides and base of the channel are solid walls thus there is no mass transfer across these boundaries, and flow tangential to the walls obeys the no-slip condition. The flow leaves the heat sink at the outlet with a fixed pressure  $p_{out}$  which will be used in conjunction with the inlet velocity to determine the pressure at the inlet.

### 3. Modelisation

The section outlines the numerous method of modelling both the thermal and hydraulic performances of metal foam heat sinks.

### 3.1 Governing equations

Due to the high level of complexity associated with the micro structure of metal foams, it is not possible to model samples at the macro scale in realistic detail. As such, volume-averaged equations have been developed, capable of calculating the global thermal and hydraulic performances. This means that a section of porous material (packed beds, tube banks, foam) comprised of two distinct phases is instead considered to be a single, homogenous block. The advantage of this method is that it requires significantly less computing power; however certain local information is inaccessible, for example the local surface temperatures of the solid phase. These volume-averaged equations are presented below:

**Porous media energy equation:**

$$\underbrace{\rho_f C_p \nabla \vec{u} T}_{\text{Convection term}} - \underbrace{k_{eff} \nabla^2 T}_{\text{Conduction term}} + S_f^h = 0 \quad (2.5)$$

where  $\rho_f$  is the fluid density,  $C_p$  is the fluid specific heat capacity,  $\vec{u}$  is the velocity vector,  $T$  is the average temperature,  $k_{eff}$  is the effective thermal conductivity and  $S_f^h$  is the fluid enthalpy source term, which would be equal to zero in this study. Equation (2.5) makes the assumption of *Local Thermal Equilibrium* (LTE) between the solid and fluid phases of the porous medium. Hence only a single energy equation is solved, and the individual thermal conductivities are replaced by an effective thermal conductivity. However, due to the nature of heat transfer within metal foams, the solid and fluid phase temperatures are not the same. Ranut et al. [34] studied forced convection in a rectangular channel filled with graphite foam at the macro scale. They considered that the *Local Thermal Non-Equilibrium* (LTNE) between foam and coolant exists, and thus proposed a two-equation energy model. It was assumed that the foam micro structure was homogenous, and the flow was assumed to be steady, laminar and incompressible. The research validated the need for a two-energy equation approach, citing substantial errors when only a single equation was used. Thus, instead of assuming the porous zone as a single homogenous block, as before, now it is assumed to be both a fluid zone, and a completely solid zone, that exist coincidentally with each other.

**Solid energy equation:**

$$\underbrace{k_{eff,s} \nabla^2 T_s}_{\text{Conduction in solid phase}} - \underbrace{h_{sf} A_{sf} (T_s - T_f)}_{\text{Convection between phases}} = 0 \quad (2.6)$$

**Fluid energy equation:**

$$\underbrace{\rho_f C_p \nabla \vec{u} T_f}_{\text{Convection term}} - \underbrace{k_{eff,f} \nabla^2 T_f}_{\text{Conduction in fluid phase}} - \underbrace{h_{sf} A_{sf} (T_s - T_f)}_{\text{Convection between phases}} = 0 \quad (2.7)$$

where  $T_s$  and  $T_f$  are the solid and fluid temperatures respectively. The above equations include several material parameters that are required to close the model:

- Instead of using a single effective thermal conductivity, there is now an effective thermal conductivity for each phase,  $k_{eff,s}$  and  $k_{eff,f}$ .
- The interfacial (local) heat transfer coefficient,  $h_{sf}$ , which defines the way heat is exchanged between the solid and the fluid by convection when they are at different temperatures.

The LTNE model has been used extensively within the literature to better understand the thermal performance of porous materials. Tassou *et al.* [35] carried out a study of the forced convection heat transfer characteristics in high porosity open-cell metal-foam filled pipes. They presented an analytical model of heat transfer derived from the LTNE equations. Their model was validated against numerical calculations and they were able to assess the impact of certain foam physical features (porosity, pore density, channel size, height of foam etc.) on heat transfer performance. They found that at a constant fluid flowrate, the Nusselt number increased with decreasing porosity, or increasing pore density, especially when the thermal conductivity of the solid is much higher than the fluid. Boyd & Hooman [36] presented a 3D numerical simulation of an air-cooled metal foam heat sink with potential application in thermal management of fuel cell systems. They analysed air flowing through a foam filled channel, with empty inlet and outlet sections, and with a constant heat flux applied to the top and bottom. They found that increasing the velocity of the coolant increased the heat transfer coefficient, but that the rate of improvement eventually levelled off, such that higher velocities provided negligible benefits. For Reynolds numbers based on the hydraulic diameter of the channel ranging from 2200 to 4000, they found Nusselt numbers of 31 to 45. Jiang *et al.* [37] studied flow and convection heat transfer in a plate channel filled with metallic or non-metallic particles using both the local thermal equilibrium model and a non-local thermal equilibrium model. They mentioned in their paper that if one could analyse the contributing factors of the thermal resistances within a metal foam heat sink, then it would be possible to optimise the structure of the foam. Lu *et al.* [26] also studied the problem of heat transfer within parallel plate, this time partially filled with metal foam. They showed that performance was higher than traditional, non-foam filled plates. They found that thermal performance is improved by increasing either the pore density, the Reynolds number, or by decreasing the porosity.

As with the energy equations, macro-scale models have been developed to describe the hydraulic behaviour of flow through a porous medium, again relying on the assumption of a homogeneous material. The hydraulic behaviour of flow through a porous material is described by the well-known conservation of mass and Navier-Stokes equations:

### Conservation of Mass

$$\frac{\partial \rho_f}{\partial t} + \nabla \rho_f \vec{u} = 0 \quad (2.8)$$

### Navier-Stokes

$$\underbrace{\frac{\partial \vec{u}}{\partial t}}_{\text{Variation}} + \underbrace{(\vec{u} \cdot \nabla) \vec{u}}_{\text{Convection}} = - \underbrace{\frac{1}{\rho_f} \nabla p}_{\text{Internal source}} + \underbrace{\nu \nabla^2 \vec{u}}_{\text{Diffusion}} - \underbrace{S_i}_{\text{External source}} \quad (2.9)$$

where  $\vec{u}$  is the velocity vector,  $t$  is time,  $p$  is pressure,  $\nu$  is the kinematic viscosity, and  $S_i$  is the external momentum source. As this volume-averaged approach neglects the tortuous

micro geometry of the foam, the calculated pressure loss would be considerably underestimated. To address this, Darcy [38] proposed the following equation:

$$\frac{\Delta p}{L} = \frac{\mu_f}{K} u_s \quad (2.10)$$

where  $L$  is the length of the porous region,  $\mu_f$  is the fluid dynamic viscosity,  $K$  is the permeability of the foam, and  $u_s$  is the superficial velocity. The superficial velocity must be used as the actual velocity within the foam is very difficult to determine; it is the average velocity that the fluid would have, were it travelling down an empty channel with the same volumetric flowrate. This equation predicts a linear relationship between the pressure loss and the superficial velocity. Later, Forchheimer [39] studied flow through porous materials at elevated Reynolds numbers. He found the appearance of inertial losses due to turbulent effects, and thus he proposed an extension to Darcy's equation:

$$\frac{\Delta p}{L} = \frac{\mu_f}{K} u_s + C_2 \frac{1}{2} \rho_f u_s^2 \quad (2.11)$$

Thus,  $S_i$  in equation (2.9) becomes:

$$S_i = \frac{\mu_f}{K} u_s + C_2 \frac{1}{2} \rho_f u_s^2 \quad (2.12)$$

As with the LTNE model, certain material parameters are required to complete equation (2.12).

- The permeability,  $K$ , which defines the amount with which the fluid flow is impeded by the foam structure.
- The inertial resistance factor,  $C_2$ , which measures the additional pressure losses caused by inertia.

Both these parameters are only dependent upon the geometry of the porous material. Thus, the question becomes, how to determine  $k_{eff,s}$ ,  $h_{sf}$ ,  $K$  and  $C_2$ ?

## 3.2 Effective thermal conductivity

In metal foam heat sinks, comprised of both a solid and liquid phases, and a unique microstructure, the effective thermal conductivity of the solid phase  $k_{eff,s}$  must be considered to estimate the temperature gradients within the solid phase. It is a physical quantity that takes into account the effective conductivity of both the constitutive material, and the material architecture [40]. It can be determined in a multitude of different ways, by either performing experiments, analysing foam at the pore-scale, or by using pre-existing analytical models.

### 3.2.1 Experimental determination

The effective thermal conductivity of foam can be determined experimentally using the steady state method [41] outlined in Figure 35.

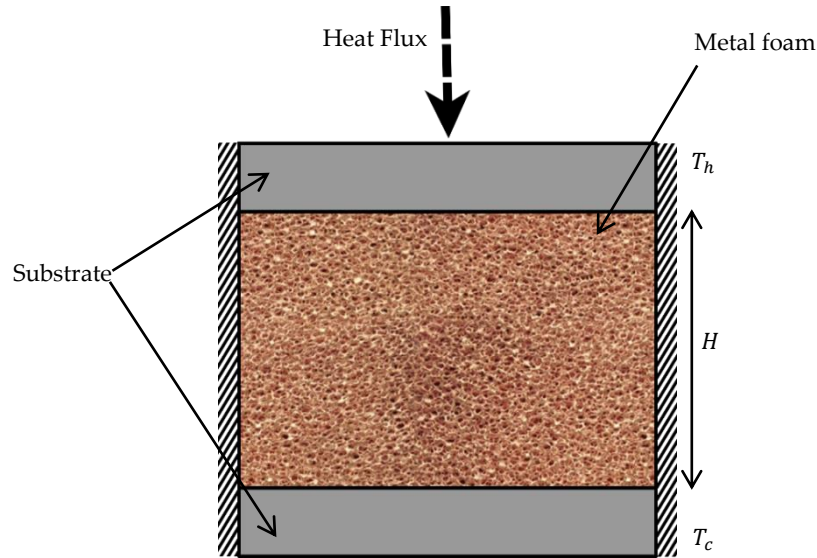


Figure 35: Steady state method of experimentally determining the effective thermal conductivity of metal foam sample [41].

In order to establish a one-dimensional temperature gradient across the metal foam sample, the upper surface of the upper substrate, and the lower surface of the lower substrate are held at a high temperature ( $T_h$ ) and a low temperature ( $T_c$ ) respectively. When the experiment has reached a steady state,  $k_{eff}$  can be calculated through the application of Fourier's Law:

$$q'' = k_{eff} \frac{\Delta T}{H} \quad (2.13)$$

where  $\Delta T$  is the temperature difference across the foam sample, and  $H$  is the height of the foam. Figure 36 shows experimental data from the literature for high porosity Duocel™ copper foams saturated with a range of fluids from Yao et al. [42] and Xiao et al. [43].

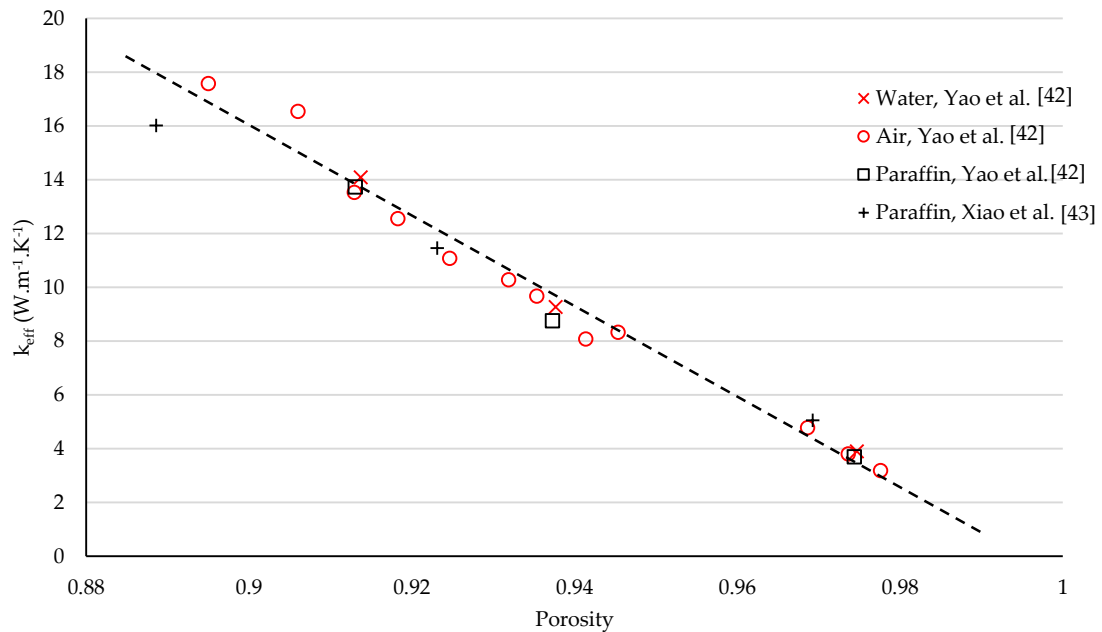


Figure 36: Experimental determination of effective thermal conductivity of copper foam saturated with air, water and paraffin.

The results in Figure 36 highlight the relatively small importance of the choice of coolant when the thermal conductivity of the solid phase is much larger. It is clear that the factor affecting  $k_{eff}$  the most is the porosity, and that at elevated porosities there is not a large deviation from a linear trend line. Figure 37 shows similar results for Duocel<sup>™</sup> aluminium foam from Calmidi & Mahajan [41], Sadeghi et al. [44] and Phanikumar & Mahajan [45].

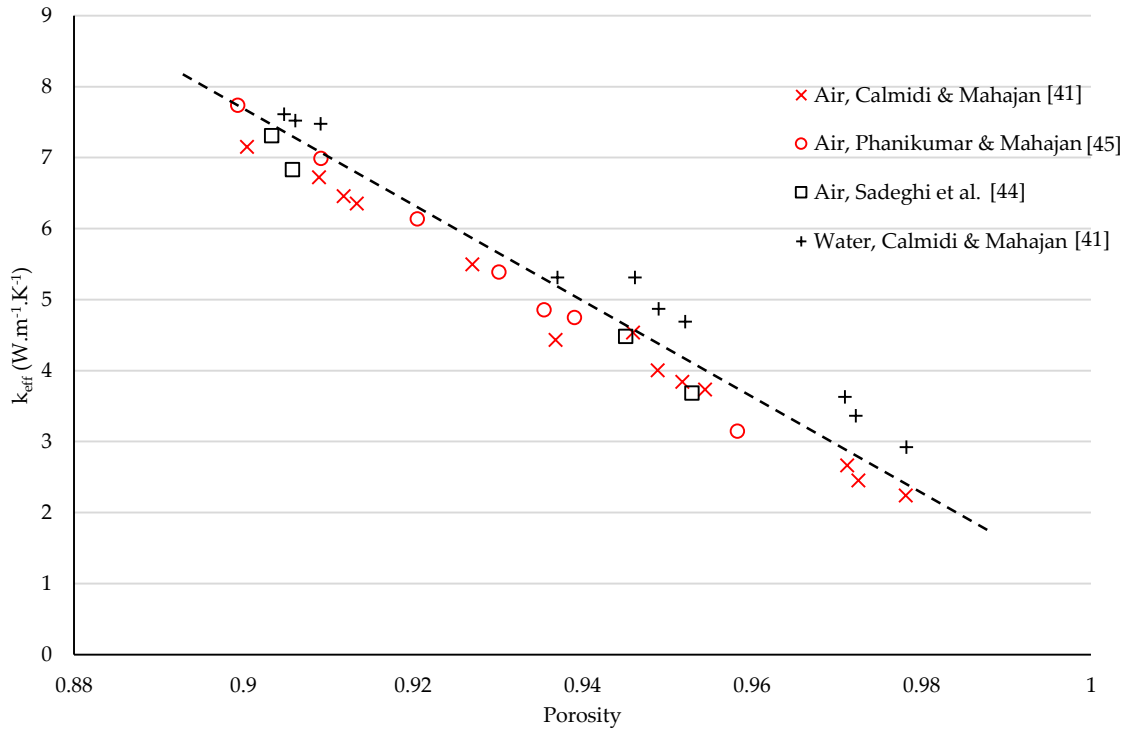


Figure 37: Experimental determination of effective thermal conductivity of aluminium foam saturated with air and water.

The results from Figure 36 and Figure 37 suggest that the use of the dielectric fluid Paratherm<sup>™</sup> LR, instead of the thermally superior water has a small impact on the overall effective thermal conductivity of the heat sink. Finally, Solorzano *et al.* [46] studied the effective thermal conductivity of foams made from the aluminium alloy AlSi7. They included a larger range of porosities than the other works seen here, from 0.5 to 0.8, and used the experimental data to assess the validity of several analytical models. In this study, foams were fabricated using the powder sintering technique.

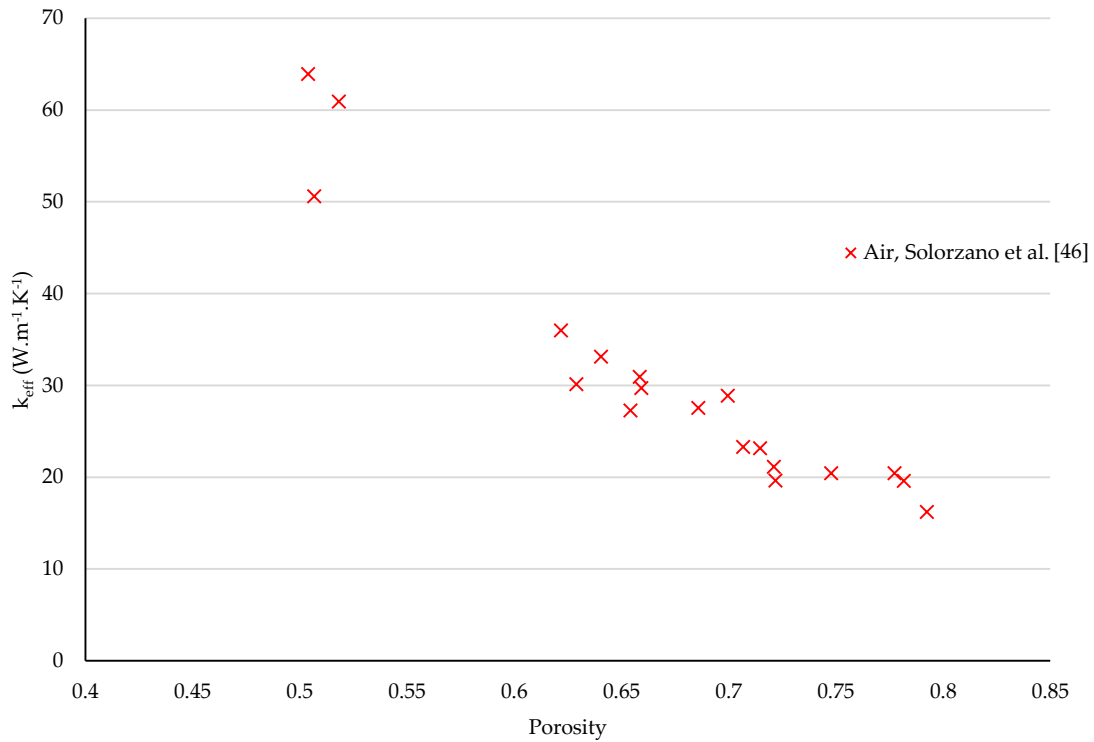


Figure 38: Experimental determination of  $k_{eff}$  of AlSi7 foam saturated with air.

### 3.2.2 Pore-scale analysis

Pore-scale simulations are carried out using small sections of foam, allowing the determination of local results. These values are then applied over the whole foam sample by assuming the geometry is homogenous. Ranut *et al.* [34] showed that the effective thermal conductivity can be ascertained by considering a small cube of foam, saturated by a fluid, as can be seen in Figure 39.

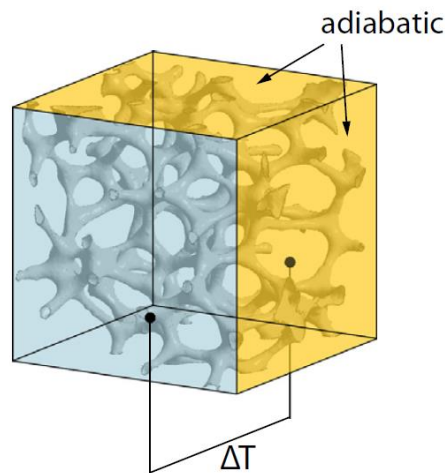


Figure 39: Computational domain used in CFD simulation for the prediction of  $k_{eff}$  [34].

The 3D foam structure was devised through the use of X-Ray microtomography on real aluminium foam. By applying an arbitrary temperature difference across two faces of the cube, and considering the remaining lateral faces adiabatic, it was possible to solve the energy

equations for both the fluid and the solid simultaneously. The momentum equation was not solved as the fluid was considered motionless. Ranut *et al.* [34] carried out simulations for both air and water and the fluid medium, the results of which can be seen in Figure 40.

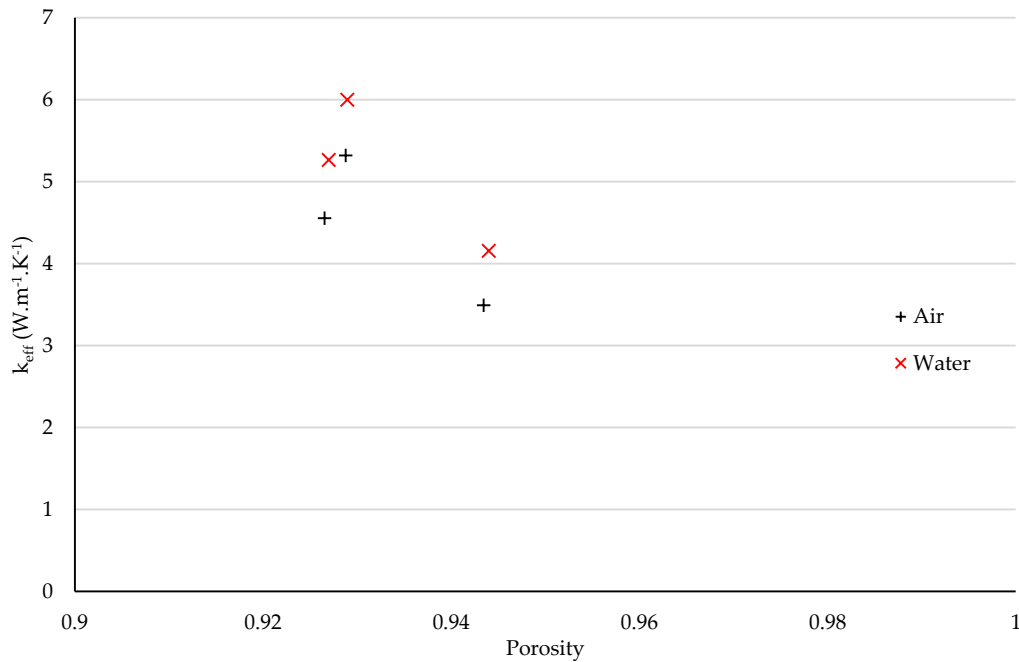


Figure 40: Numerical calculation of  $k_{eff}$  of aluminium foam [34].

The results in Figure 40 again show that the overall effective thermal conductivity is not greatly affected by the choice of fluid. Zafari *et al.* [47] also applied the same method in their study, simulating both aluminium and copper foam cubes, using air as the fluid medium. Their results, shown in Figure 41, obviously evidence the major effect the choice of the solid phase has on  $k_{eff}$ .

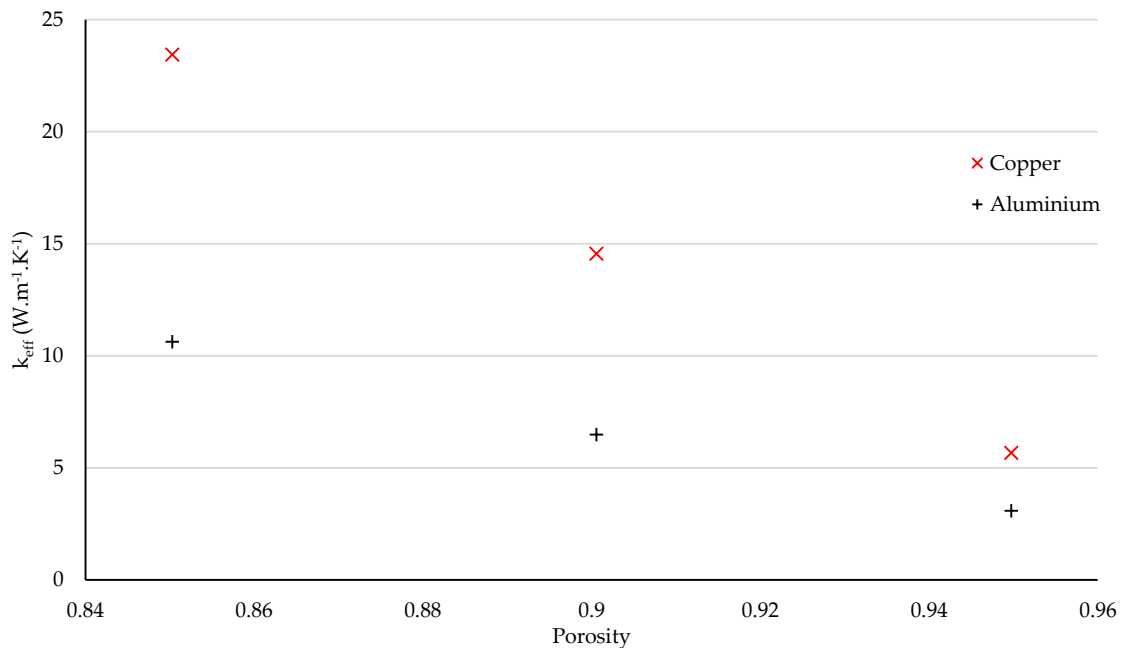


Figure 41: Numerical calculation of the  $k_{eff}$  of copper and aluminium foam [47].

Both the results shown in Figure 40 and Figure 41 were achieved using realistic foam geometries found from X-ray microtomography. Though this obviously aids in the accuracy of the study, it also limits the range of geometrical parameters that can be tested, hence why both of these studies only looked at highly porous foams. Wang & Pan [48], however, used a random generated-growth method instead, meaning they were able to produce theoretical 3D foam samples with a much greater range of porosities. Instead of using real materials within their study, they simply applied a thermal conductivity of  $100 \text{ W} \cdot \text{m}^{-1} \text{K}^{-1}$  to the solid phase, and  $1 \text{ W} \cdot \text{m}^{-1} \text{K}^{-1}$  to the fluid phase. The results of their study can be seen in Figure 42,

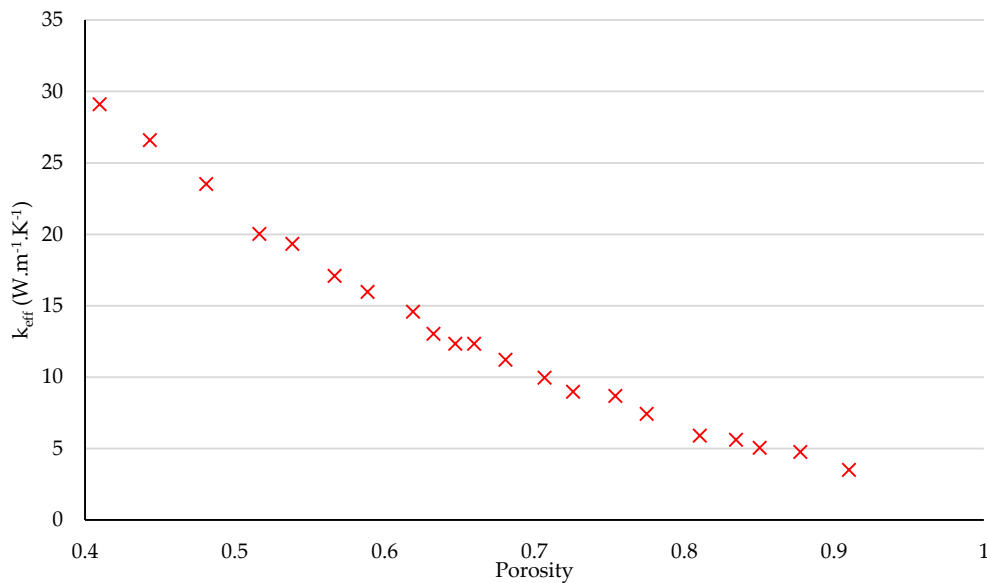


Figure 42: Numerical calculation of  $k_{eff}$  [48].

Though the results in Figure 42 cannot be directly compared with other results that use real world materials, they can be used as a benchmark for testing the analytical models shown in the next section.

### 3.2.3 Analytical Models

Determining  $k_{eff,s}$  can be achieved by using a model for the overall effective thermal conductivity, and then neglecting the conductive heat transfer within the fluid. This is valid when the thermal conductivity of the solid phase is significantly higher than for the fluid phase. Wiener [49] developed a simple model by considering the two phases to be either in parallel, or series with each other:

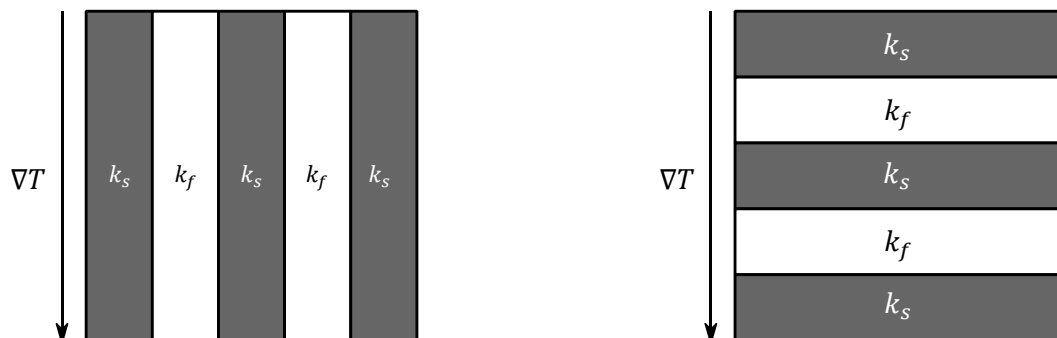


Figure 43: Models of  $k_{eff}$  in parallel (left) and series (right).

Weiner [49] assumed that the effective thermal conductivity could be calculated using the volume fraction of the phases, and by modelling it as a series of layers either parallel or perpendicular to the temperature gradient. Thus, he derived the following equations:

$$k_{eff} = \varepsilon k_f + (1 - \varepsilon)k_s \quad \text{-Parallel} \quad (2.14)$$

$$k_{eff} = \frac{k_f k_s}{\varepsilon k_s + (1 - \varepsilon)k_f} \quad \text{-Series} \quad (2.15)$$

Though capable of predicting the upper and lower limits, these models are too simple to accurately calculate the effective thermal conductivity of a porous material. Maxwell [33] proposed a more sophisticated equation by considering low concentration spherical inclusions without any interaction in a homogenous matrix. The upper limit of  $k_{eff}$  was obtained by embedding lower conductivity particles in a high conductivity matrix:

$$k_{eff} = k_s + \frac{\varepsilon}{\frac{1}{k_f - k_s} + \frac{1 - \varepsilon}{3k_s}} \quad (2.16)$$

and the lower limit was obtained when higher conductivity particles are embedded in a low conductivity matrix:

$$k_{eff} = k_f + \frac{1 - \varepsilon}{\frac{1}{k_s - k_f} + \frac{\varepsilon}{3k_f}} \quad (2.17)$$

A more relevant model to this work was proposed by Yang *et al.* [50], who used a unit cell analysis based on the tetrakaidecadron with realistic node sizes at the fibre intersections. They studied aluminium foams saturated in both air and water at high porosity ranges ( $\varepsilon \geq 0.8$ ). Their worked showed good agreement with the existing experimental data, having a *Mean Squared Error* (MSE) of just 0.48, and they also confirmed that fibre shape and pore size have little influence on the effective thermal conductivity of the bulk porous media. Their models is as follows:

$$k_{eff} = \frac{1 - \varepsilon}{\left(1 - e + \frac{2e}{2\alpha}\right) \left(3(1 - e) + \frac{3}{2}\alpha e\right)} k_s + k_f \varepsilon \quad (2.18)$$

where  $e$  is the node thickness to fibre length ratio, and  $\alpha$  is the node to fibre cross-sectional area ratio, with values derived from experimental measurements of 0.3 and 1.5 respectively. The final model to be looked at is the Bruggemann model, revised by Collishaw and Evans [51]:

$$1 - \varepsilon = \left(\frac{k_f - k_{eff}}{k_f - k_s}\right) \left(\frac{k_s}{k_{eff}}\right)^{1/3} \quad (2.19)$$

This model has the advantage of being validated by experimental data at lower porosities ( $\sim 0.45$ ) by Solorzano *et al.* [46].

By cancelling out  $k_f$  in the above equations, and plotting the results for a range of porosities using copper ( $k_s = 387.6 \text{ W/m.K}$ ) as the solid phase, an idea of the expected values of  $k_{eff,s}$  can be obtained. As the lower limit models from Weiner [49] and Maxwell [33] assume that thermal conduction occurs only in the fluid phase, which is clearly not the case, the predicted results are far too low and can be ignored. The upper limit models may also be an over estimation, evidenced by the fact that they both produce a higher result than the more intricate models from Yang [50] and Collishaw and Evans [51]. The results calculated from the above models, as well as several other models from the literature, can be seen in Figure 44.

Unfortunately it must also be noted that Yang *et al.* [50] questioned the validity of their model at porosities lower than those included in their analysis, stating that at decreased porosities, the cell fibres may be thicker for a given pore size. Heat transfer along a thickened fibre would then violate the 1D conduction assumption that they had made. Therefore, though this model shows a highly level of accuracy at predicting  $k_{eff}$ , its limited range of effectiveness makes it inappropriate for this work.

To better assess the validity of the models, they were compared with the results calculated from pore-scale simulations shown in Figure 42 and the experimental data from Figure 38. To make the comparison, all the results were normalised by dividing the effective thermal conductivity by the respective solid phase thermal conductivity. The results of this can be seen in Figure 45. As was assumed, the two analytical models from Weiner [49] and Maxwell [33] seem to over predict the effective thermal conductivity. Whereas the Bruggemann model aligns closely with experimental results, even at lower porosities. It will therefore be the chosen model within this work. Finally, Figure 46 shows the same results but only at elevated porosities (>90%).

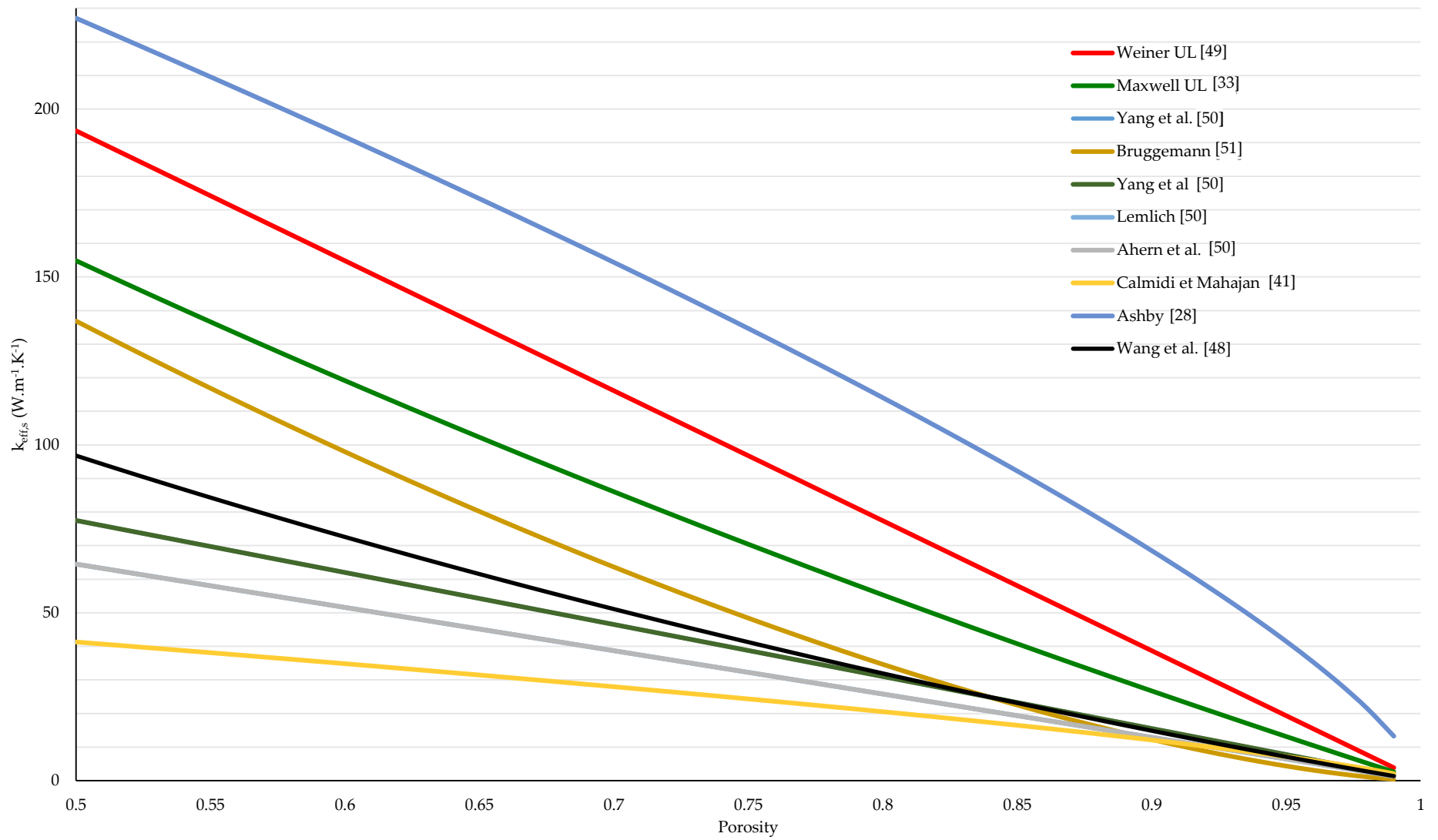


Figure 44: Various models of solid phase  $k_{eff}$  of open celled copper foams for a range of porosities.

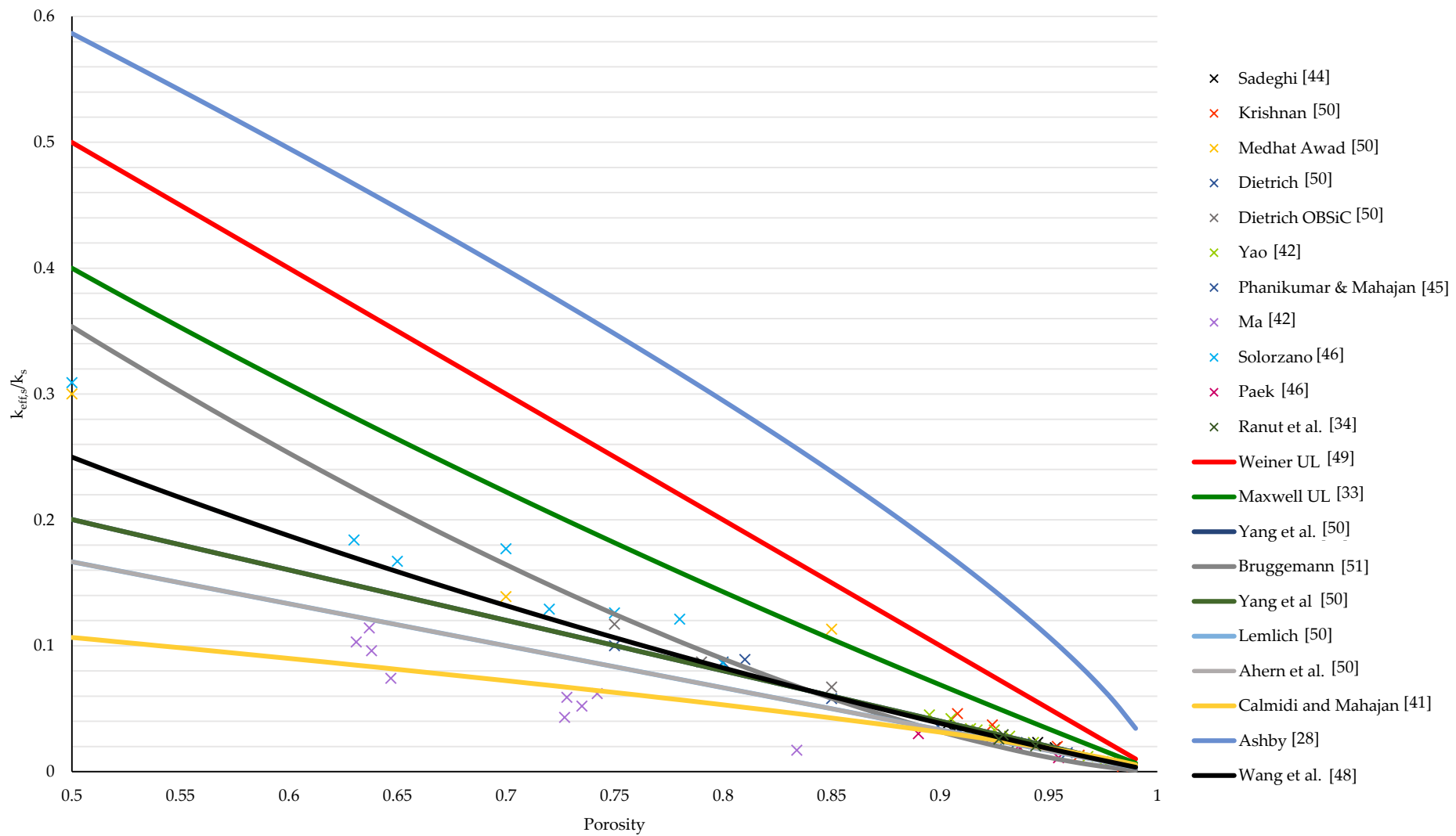


Figure 45: Comparison of normalised  $k_{eff}$  determined by experimentation (cross) and analytical models (line).

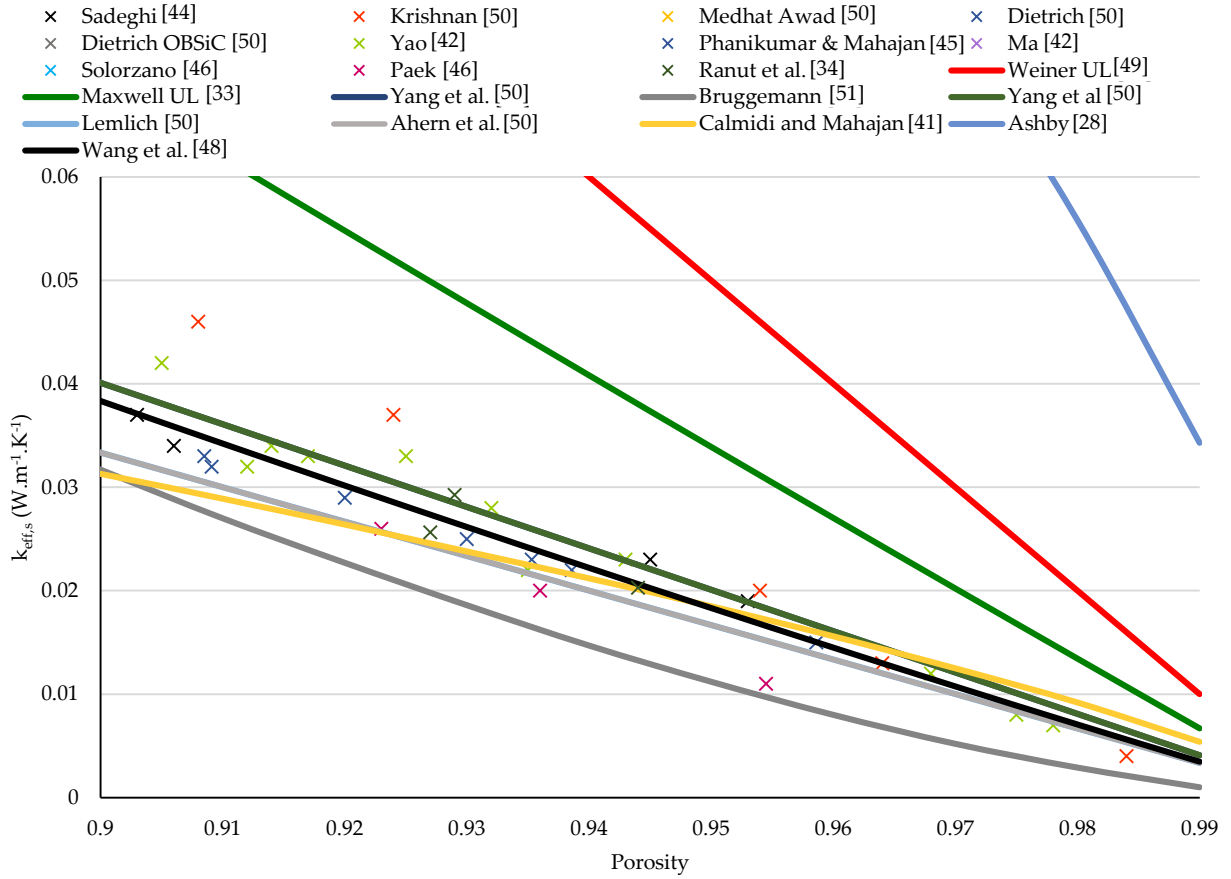


Figure 46: Comparison of normalised  $k_{eff}$  determined by experimentation (cross) and analytical models (line) at elevated porosities (>90%).

### 3.3 Interfacial heat transfer coefficient

The interfacial heat transfer coefficient can be difficult to determine as it is a function of the many flow characteristics (thermal properties of the fluid, flow regime, flow rate, surface rugosity). It is also very difficult to determine experimentally, as the local fluid and solid temperatures are inaccessible without also disturbing the fluid flow. As such,  $h_{sf}$  is typically calculated either by performing pore-scale simulations, or by adapting analytical correlations developed from experimental data of some other porous structure (i.e. packed beds, packed tubes).

#### 3.3.1 Pore-scale analysis

Calculating  $h_{sf}$  from pore-scale simulations is performed in a similar way to calculating  $k_{eff}$ : a computational domain is defined that contains a small section of foam micro geometry. The major difference is that in this case the fluid phase is not static, and is instead given a constant flow rate. Wu *et al.* [52] chose to study the  $h_{sf}$  of ceramic foam. They represented the micro geometry as idealised packed tetrakaidecahedron structures and used the three-dimensional *Reynolds-Averaged Navier–Stokes* (RANS) equations to solve the flow and temperature fields. They studied air with a range of inlet velocities and a fixed surface temperature, and calculated  $h_{sf}$  by applying *Newton's law of cooling*:

$$h_{sf} = \frac{q''}{(T_s - T_f)} \quad (2.20)$$

They studied porosities from 0.66 to 0.93 and found that the local heat transfer coefficient  $h_{sf}$  ranged from  $150 \text{ W.m}^{-2}\text{.K}^{-1}$  to  $450 \text{ W.m}^{-2}\text{.K}^{-1}$  for inlet velocities ranging from  $1 \text{ m.s}^{-1}$  to  $4 \text{ m.s}^{-1}$ . Ranut *et al.* [34] used *X-ray Computed Microtomography* ( $\mu$ -CT) to precisely describe the microstructure of the aluminium foam. Numerical simulations were carried out using air as the coolant, and either a fixed surface temperature, or a fixed surface flux. Two foams with different pore densities (10 PPI and 40 PPI) were purchased for use in this study, and the two others (20 PPI and 30 PPI) were estimated using linear interpolation. They found that  $h_{sf}$  varied from  $15 \text{ W.m}^{-2}\text{.K}^{-1}$  to  $280 \text{ W.m}^{-2}\text{.K}^{-1}$  for a Reynolds number, based on the nominal pore diameter, ranging from 1 to 100. Nie *et al.* [53] also presented a method for the accurate representation of metal foams at the pore scale. They created 3D models using *Laguerre-Voronoi Tessellations* (LVT). This method generates cylindrical struts based on the random packing of spheres within a volume. They performed numerical simulations for a wide range of pore densities (10 PPI to 50 PPI), of porosities (70% to 95%), and of Reynolds numbers (100 to 100000). In this case, the characteristic length used was  $1/A_{sf}$ . They found that  $h_{sf}$  increased with increasing Reynolds number, and also with increasing porosity at constant pore density.

In this work two separate foam geometries have been simulated. Firstly, a less realistic, but significantly simpler, cube based unit cell, then following this, the more complex tetrakaidehedra unit cell. In each case, the governing equations are the standard conservation of momentum, mass, and solid and fluid energy equations.

#### *Cube cell geometry and meshing*

The first foam geometry test was constructed but creating a repeating pattern of cube unit cells, as can be seen in Figure 47. Also highlighted are the definitions of  $d_f$  and  $d_p$  for this kind of unit cell.

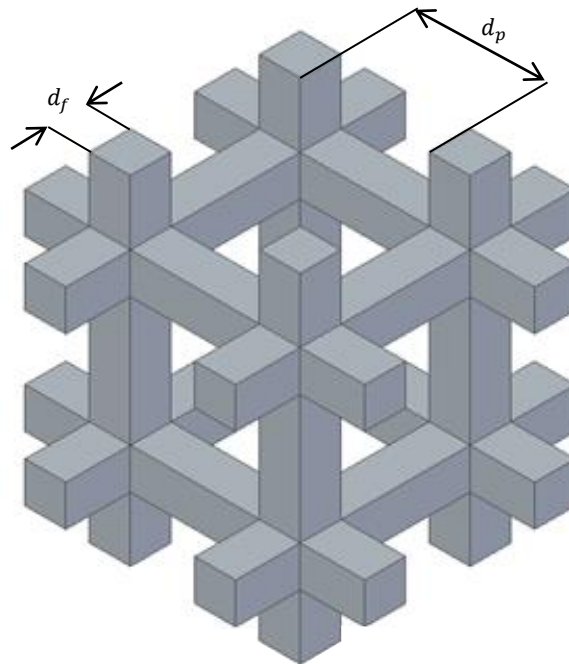


Figure 47: Cube unit cell

These individual cells can then be packed together in order to create a repeating pattern that represents the foam geometry, as can be seen in Figure 48.

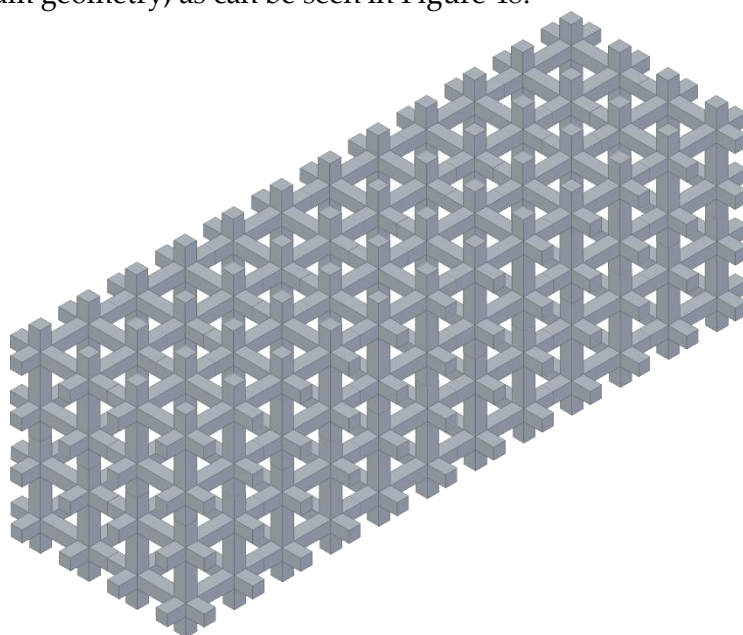


Figure 48: Packed cube cells.

Computational time is then reduced by cutting the packed structure along lines of symmetry, greatly reducing complexity without losing any flow or thermal information. The final computational domain is shown in Figure 49.

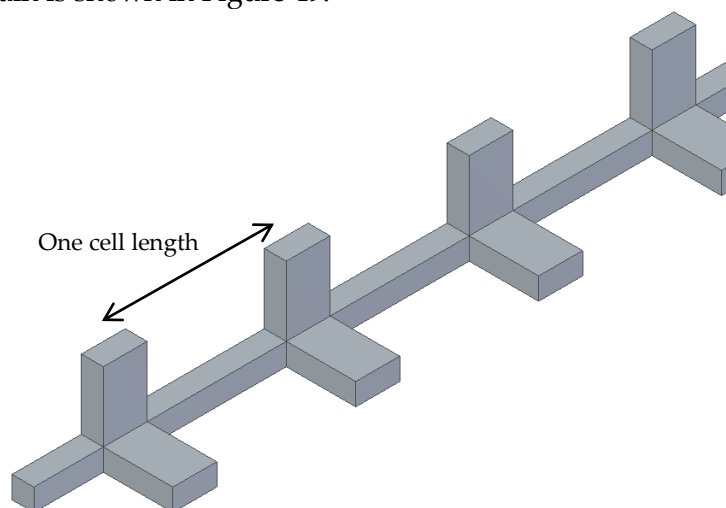


Figure 49: Cube cell computation domain.

Due to the relative simplicity of this structure, meshing was achieved using only square cells, with 5 layers of inflation at the solid/fluid interface. A mesh independence study was carried out by measuring the pressure drop, as well as the average velocity at the outlet. The results showed that a mesh containing roughly 500,000 elements was fine enough, and reducing the element size further provided a negligible improvement to the accuracy of the simulations.

*Cube cell boundary conditions*

A velocity-inlet condition was used at the fluid entrance, and a pressure-outlet, with a fixed pressure of 101325 Pa, was defined at the outlet. A fluid was defined in Ansys that had all the same corresponding parameters as Paratherm™ LR. The velocity of the fluid at the inlet was fixed at  $0.065 \text{ m} \cdot \text{s}^{-1}$  as it corresponds on a macro scale to an increase in fluid temperature of 20 K when using a flux of 100 W. All the strut surfaces were defined as non-slip, non-penetrating walls, with a surface flux density that equates to a total flux of 100 W. It was also assumed that the flow was one-dimensional, and that the average streamline runs parallel along the length of the computational domain. Thus, the four exterior sides of the computational domain are defined as symmetrical boundary conditions. By varying either the pore diameter, or the fibre diameter, a range of different porosities were generated. The parameters of all the different foams that were tested are shown in Table 2.

TABLE 2:

Cube cell foam parameters

Fixed pore diameter					
Porosity	0.76	0.81	0.86	0.90	0.93
Fibre diameter (mm)	0.08	0.07	0.06	0.05	0.04
Pore diameter (mm)	0.17	0.17	0.17	0.17	0.17
Specific surface area (1/m)	10444.8	9676.8	8755.2	7680	6451.2
Fixed fibre diameter					
Porosity	0.65	0.70	0.75	0.85	0.95
Fibre diameter (mm)	0.06	0.06	0.06	0.06	0.06
Pore diameter (mm)	0.19	0.18	0.21	0.31	0.64
Specific surface area (1/m)	8755.2	9839.7	8458.9	5397.5	1895.2

*Cube cell results*

Simulations of each foam were carried out, and flow and thermal information was recorded for comparison. The local heat transfer coefficient was then calculated using equation (2.20). The results show that both the pore diameter and fibre diameter have a strong influence on  $h_{sf}$ . When the fibre diameter is fixed, the increased porosity is achieved by increasing the pore size which results in a decreased PPI. As has been shown by Ranut *et al.* [34],  $h_{sf}$  decreases with decreasing PPI, and the results shown confirm this trend. Alternatively, when the pore diameter is fixed, the porosity is increased by decreasing the diameter of the solid fibres. The results show that this caused an increase in  $h_{sf}$  which coincides with the work carried out by Nie *et al.* [53].

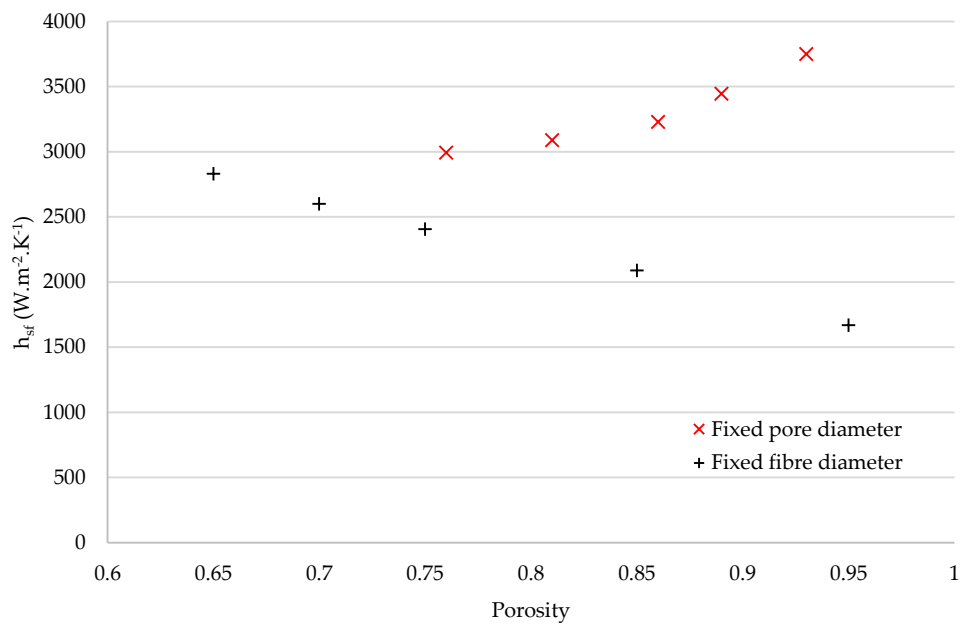


Figure 50: Local heat transfer coefficient for cube cell foams using Paratherm LR as coolant.

#### Tetrakaidecahedral cell geometry and meshing

The second foam geometry test was constructed by creating a repeating pattern of tetrakaidecahedral unit cells. As previously shown, it is well agreed upon within the literature that the tetrakaidecahedron best represents the micro geometry of open celled foam. This can be seen in Figure 50. Also highlighted are the definitions of  $d_f$  and  $d_p$  for this kind of unit cell.

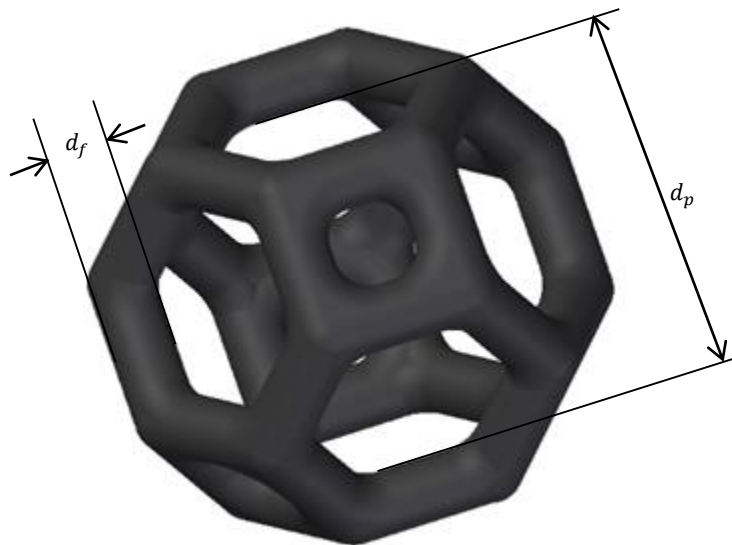


Figure 51: Tetrakaidecahedral unit cell.

As before, the individual cells can be packed together to make up the foam geometry, as can be seen in Figure 52.

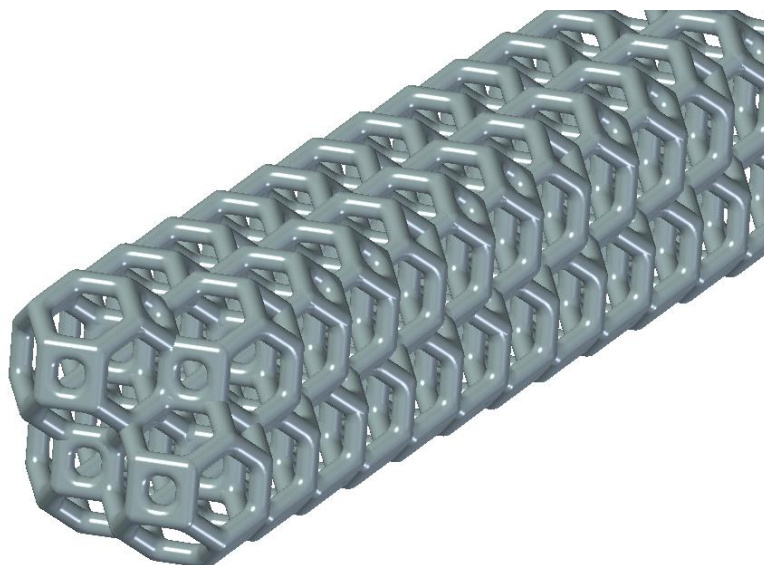


Figure 52: Packed tetrakaidecahedra.

Then, in order to reduce computational requirements, the packed cells can be cut in such a way that all of the boundaries that are parallel to the flow are symmetrical (Figure 53).

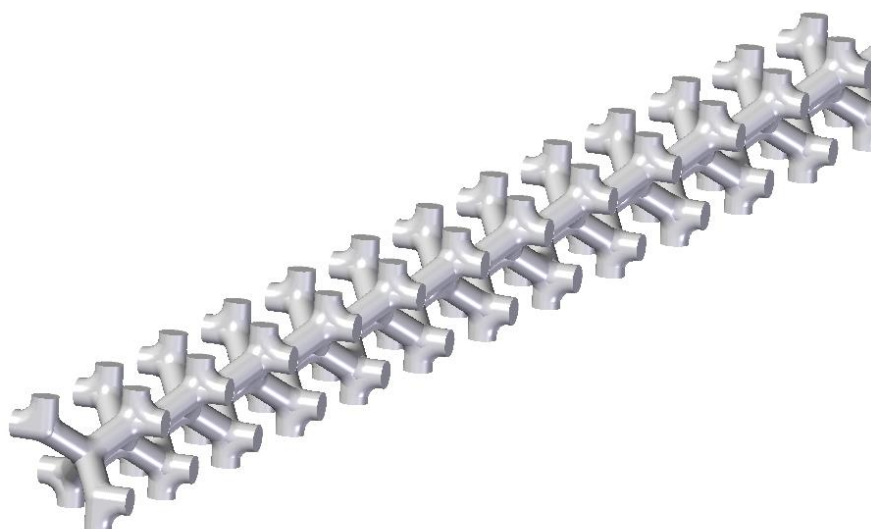


Figure 53: Tetrakaidecahedral cell computational domain.

Thus, the computational domain consists of a thin channel filled with foam with the following properties:

TABLE 3

Tetrakaidecahedral foam parameters	
Porosity	0.91
Fibre diameter (mm)	0.397
Pore diameter (mm)	2.82
Specific surface area (1/m)	1304

The values of the properties were chosen to correspond with the real Duocel<sup>tm</sup> foam that is readily available on the market, and which was used during the experimentation section of this work (see Chapter 4). As the flow paths within packed tetrakaidehedra are can be highly tortuous depending on the porosity, a very fine mesh is required in order to accurately simulate the hydraulic behaviour. The mesh used within this study consisted of tetrahedral elements, as well as 5 inflation layers at the surface of the struts. Figure 54 shows the mesh used on the surface of the foam.

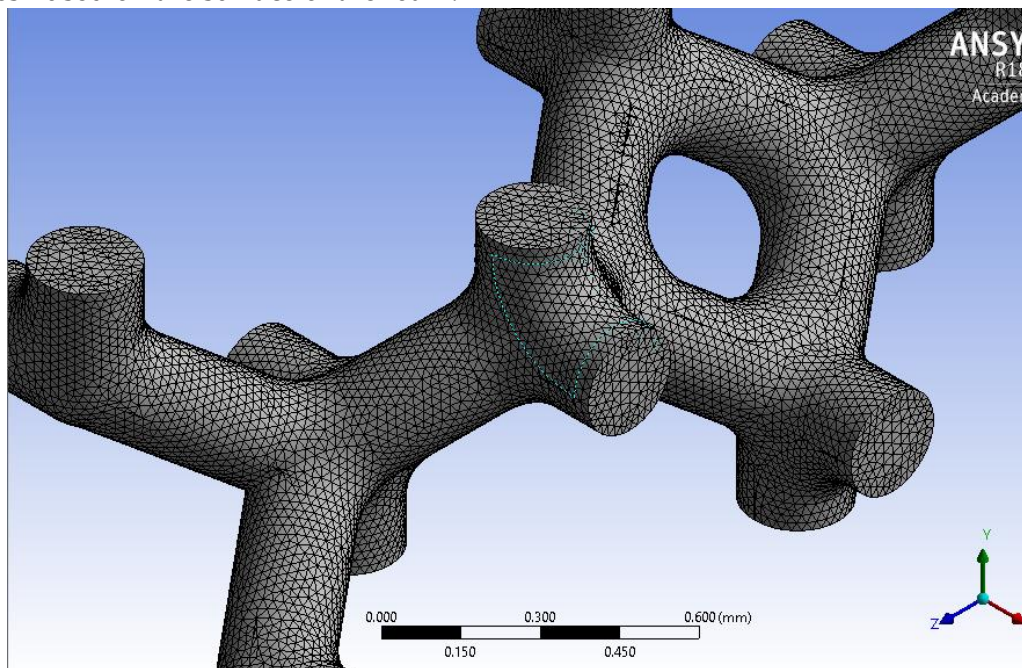


Figure 54: Surface mesh.

A mesh independence study was carried using the same method as before. This time a mesh containing roughly 9000000 elements was required, with finer meshes producing negligible improvements to accuracy.

#### *Tetrakaidehedral cell boundary conditions*

As before, a velocity-inlet condition was used at the fluid entrance, and a pressure-outlet, with a fixed pressure of 101325 Pa, was defined at the outlet. All the strut surfaces were defined as non-slip, non-penetrating walls. It was also assumed that the flow was one-dimensional, and that the average streamline runs parallel along the length of the computational domain. Thus, the four exterior sides of the computational domain are defined as symmetrical boundary conditions.

#### *Tetrakaidehedral cell results*

As with the cube cell simulation,  $h_{sf}$  was determined by applying equation (2.20). As is expected, the results show a steady increase in  $h_{sf}$  with increasing fluid velocity.

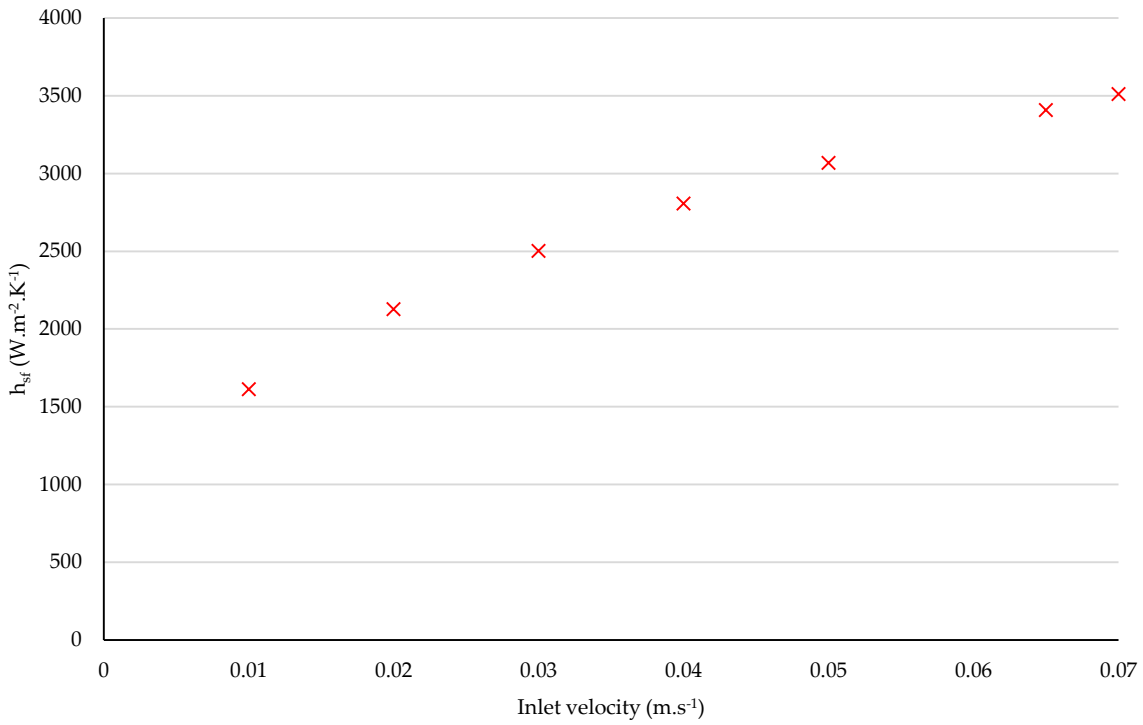


Figure 55:  $h_{sf}$  of tetrakaidecahedral foam with 0.91 porosity using Paratherm LR as coolant.

### 3.3.2 Analytical correlations

Analytical correlations of  $h_{sf}$  are based on the relationship between three dimensionless numbers: The local Nusselt number, the local Reynolds number, and the Prandtl number:

$$Nu_l = \frac{h_{sf} l}{k_f} = f(Re_l, Pr) \quad (2.21)$$

The Nusselt number is the ratio of the convective thermal resistance to the conductive thermal resistance, the Reynolds number is the ratio of the inertial forces to the viscous forces, and the Prandtl number is the ratio of the momentum diffusivity to the thermal diffusivity. As this is a correlation for calculating local information the characteristic length scale  $l$  must reference this fact. Kakac *et al.* [54] proposed a correlation for cross-flow within staggered tube banks using the tube diameter as the characteristic length. Later, Zhang *et al.* [26] showed that this correlation could be used in the case of metals foams by exchanging the tube diameter with the fibre diameter  $d_f$ . However, due to the fact that the cross section of the fibres become non-circular at higher porosities, a shape factor  $d = (1 - e^{-(1-\varepsilon)/0.04})d_f$  was introduced. Zhang *et al.* [26] successfully applied equation (2.22) to foams with porosities as low as 70% without loss of accuracy. However, in their article they failed to mention whether it could be applied to porosities lower than this, and as such, consideration must be taken.

$$Nu_d = \frac{h_{sf} d}{k_f} = \begin{cases} 0.76 Re_d^{0.4} Pr^{0.37}, & (1 \leq Re_d \leq 40) \\ 0.52 Re_d^{0.5} Pr^{0.37}, & (40 \leq Re_d \leq 10^3) \\ 0.26 Re_d^{0.6} Pr^{0.37}, & (10^3 \leq Re_d \leq 10^5) \end{cases} \quad (2.22)$$

where  $Re_d = \rho_f u d / \mu_f$  and  $Pr = C_p \mu_f / k_f$ .

Equation (2.22) assumes that the flow through the foam section is fully developed, and thus  $h_{sf}$  does not depend upon the length of the heat sink. This assumption was verified, using the pore scale simulations shown previously, by calculating the rate of change of the fluid velocity,  $\partial u_z / \partial z$ , along the length of the foam samples,  $z$ . The results, using both the cube cell and tetrakaidehedra geometries, can be seen in Figure 56 and Figure 57.

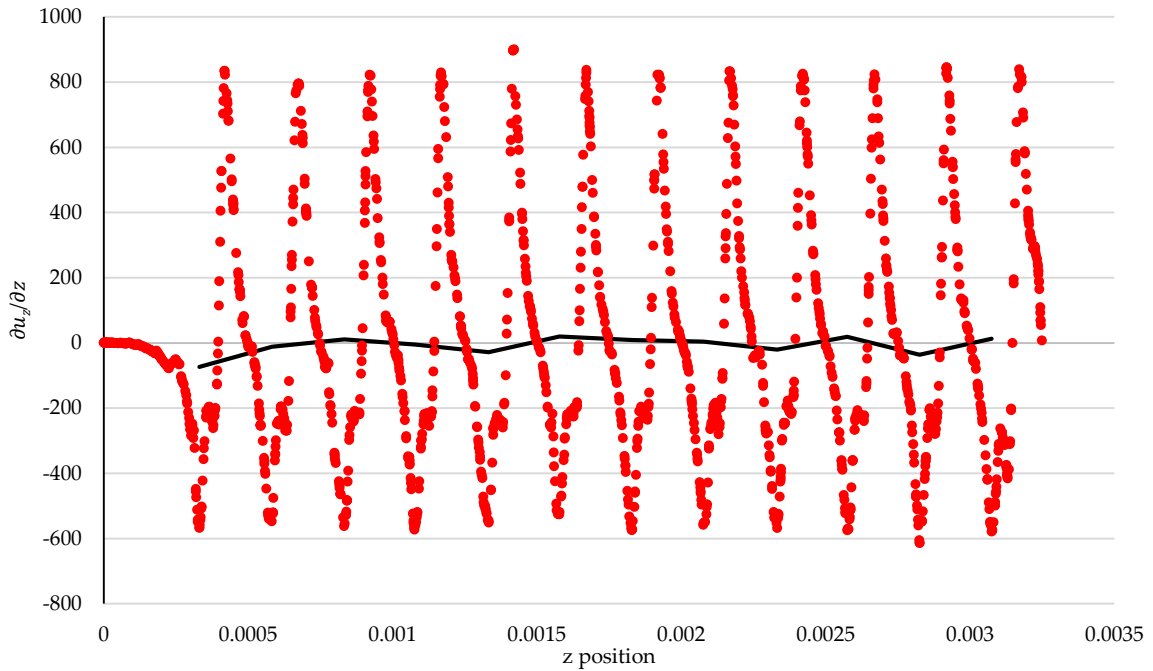


Figure 56:  $\partial u_z / \partial z$  of water through a cube cell geometry of porosity 91%.

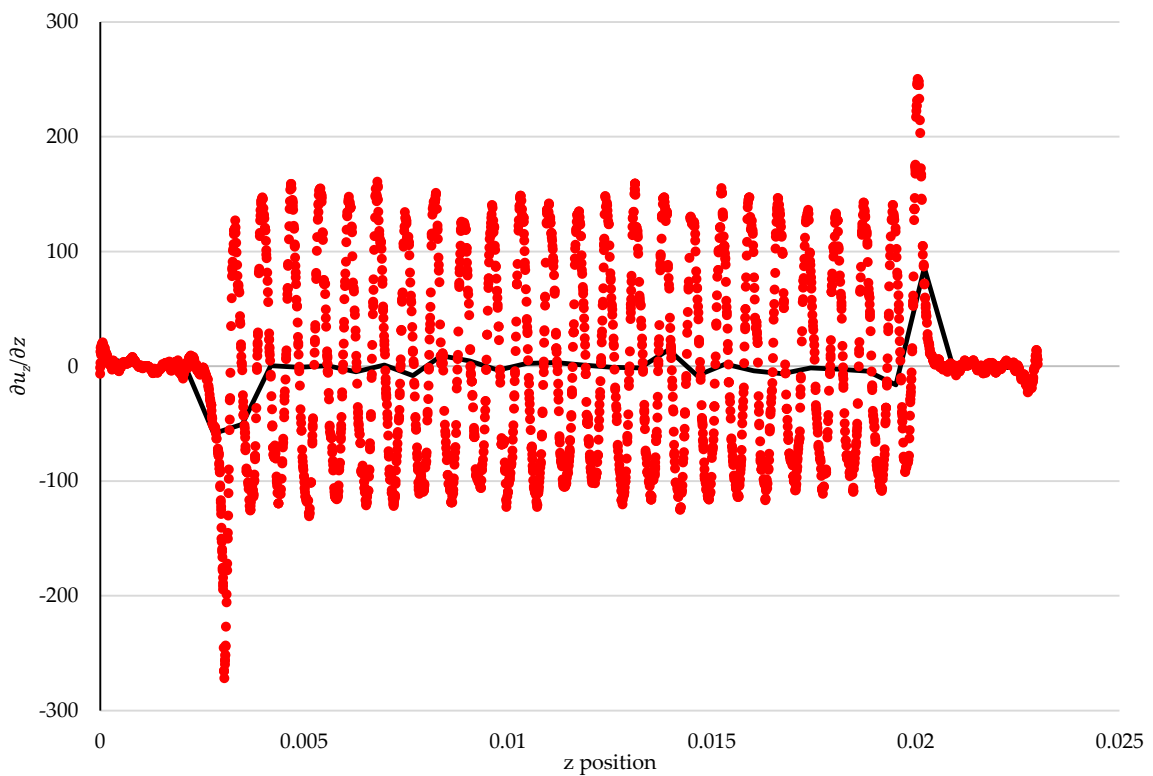


Figure 57:  $\partial u_z / \partial z$  of water through a tetrakaidehedra cell geometry of porosity 91%.

In Figure 56 and Figure 57, the red points indicate the exact values of  $\partial u_z / \partial z$  at each position along the length of the foam. The initial flat region in both graphs represents the entrance region, void of any foam. As expected, the results show a cyclic nature corresponding with the individual cells. The black lines show the cell averaged values of  $\partial u_z / \partial z$ , which give a clearer picture of the overall flow behaviour. In both cases, the averaged flow is initially disturbed as it enters the porous zone, after which it becomes very stable again two cell lengths later. This validates the assumption of a fully developed flow required to use equation (2.22), thus the next step is to determine if it can accurately predict  $h_{sf}$  calculate numerically in the previous section.

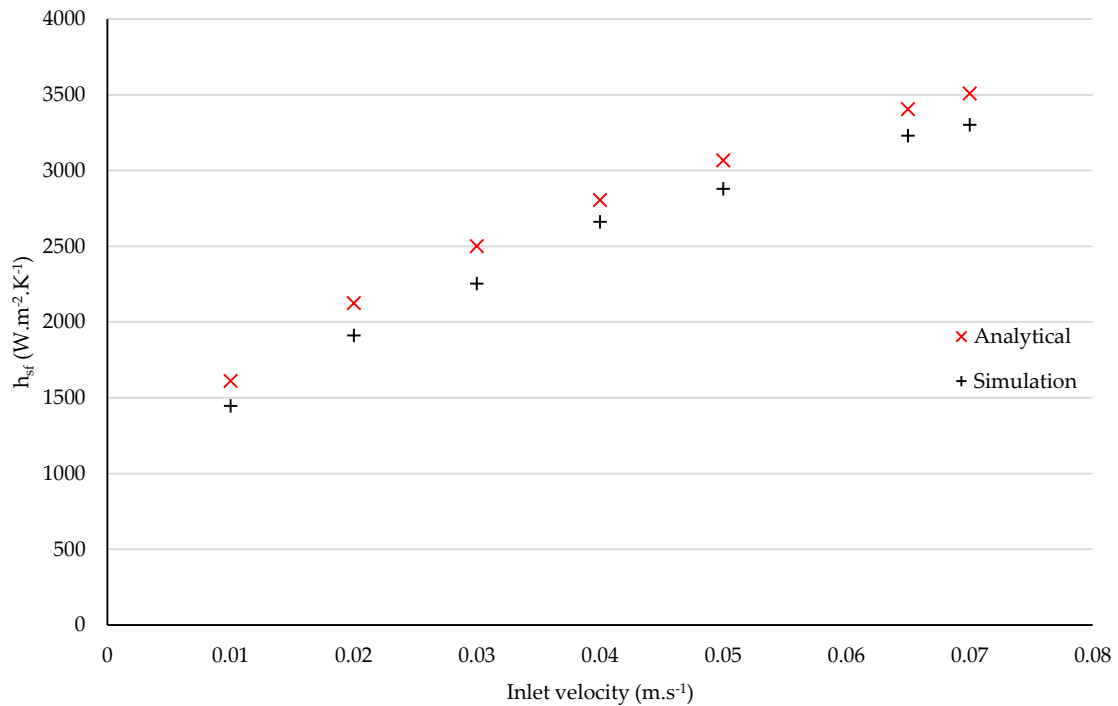


Figure 58: Comparison of  $h_{sf}$  calculated analytically and through numerical simulations of tetrakaidecahedral foam with 0.91 porosity using Paratherm LR as coolant.

The results show a good agreement between the analytical model and the numerical simulations, with an average deviation of 8%.

### 3.4 Permeability and inertial resistance factor

#### 3.4.1 Pore-scale simulations

When determining  $K$  and  $C_2$  using pore-scale simulations, or experimentation, the exact same method is used: pressure loss is measured across the porous material at a range of superficial velocities. This will lead to a pressure gradient profile as seen in Figure 59.

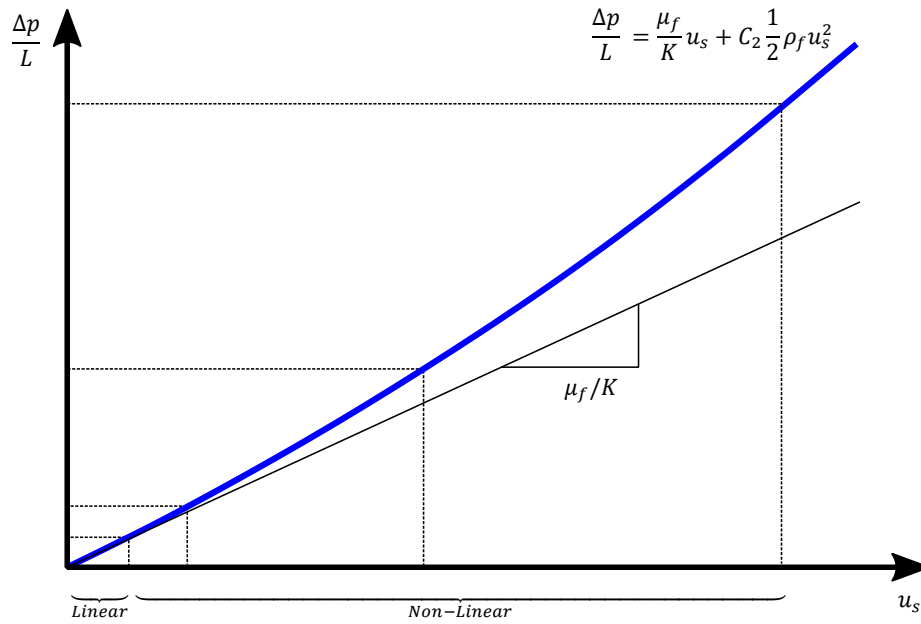


Figure 59: A typical pressure loss/velocity profile [40].

$K$  is determined by analysing the linear portion of the pressure gradient profile, at low Reynolds numbers where inertial losses can be neglected.  $C_2$  can then be calculated by fitting the Darcy-Forchheimer equation to the experimental data using a least square method.

Once again examples can be taken from the cube cell simulations carried out in this work. As only laminar flow was studied, no value for  $C_2$  was calculated. The calculated permeabilities of the cube cell foams can be seen in Figure 60.

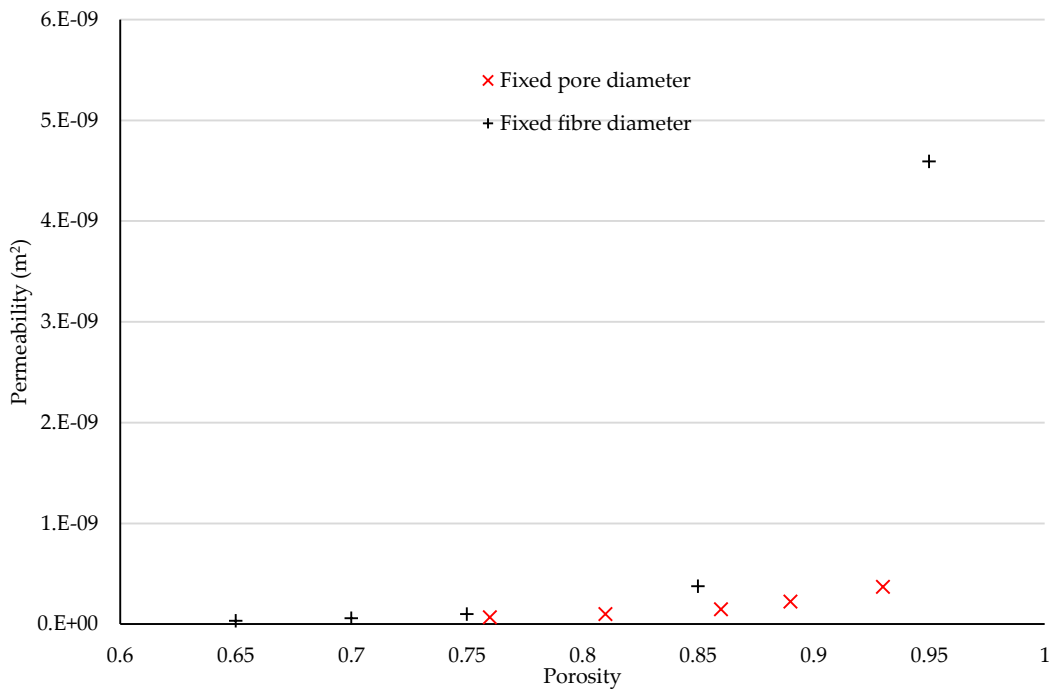


Figure 60: Permeability of cube cell foams.

The results show that varying the diameter of the pores has a greater influence on permeability than varying the diameter of the foam fibres. As anticipated, in both cases an increased porosity resulted in an increased permeability, as there is less solid matter to impede the fluid flow.

### 3.4.2 Analytical Correlations

Calmidi [55] proposed an equation to calculate  $K$  based on the porosity, pore size and fibre size of the foam:

$$\frac{K}{d_p^2} = 0.00073(1 - \varepsilon)^{-0.224}(d_f/d_p)^{-1.11} \quad (2.23)$$

Inayat *et al.* [56] proposed the following to calculate  $C_2$  based on the Hagen-Poiseuille equation, assuming that metal foams can be considered as a bundle of tangle tubes [56]:

$$C_2 = \frac{\tau^2}{\varepsilon^2 D_h} \quad (2.24)$$

where  $\tau$  is the tortuosity of open celled foams and  $D_h$  is the hydraulic diameter, defined as follows:

$$\tau = 1 + 1.2175 \frac{1 - 0.971(1 - \varepsilon)^{0.5} (1 - \varepsilon)}{(1 - \varepsilon)^{0.5} \varepsilon} \quad (2.25)$$

$$D_h = \frac{4\varepsilon}{A_{sf}(1 - \varepsilon)} \quad (2.26)$$

It was deemed unnecessary to compare these analytical models with the numerical simulations shown in Figure 59 for two reasons

### 3.5 Remarks

This section has described the multitude of ways that the four unknown parameters ( $k_{eff,s}$ ,  $h_{sf}$ ,  $K$  and  $C_2$ ) required to close the volume-averaged, macro-scale models, can be determined. It has been decided that within this work, the analytical approach will be used for the following reasons:

- The analytical models shown in this chapter are all well used within the literature, and have been validated experimentally.
- It is the simplest method, allowing for the immediate calculation of the required parameters.
- As one of the aims of this project is to develop an analytical model capable of predicting global heat transfer performance, it makes sense that each of the parameters used within the model can be calculated analytically.
- Analytical models also make the task of optimisation the foam properties far simpler.

## 4. Analytical Model

In this section an analytical model will be developed that is capable of calculating the total thermal resistance of the metal foam heat sink shown in Figure 34, as well as the pressure

loss in the working fluid. This is achieved by simplifying the local governing equations shown earlier in this chapter. In order to calculate the total thermal resistance  $R_{tot}$ , the heat sink must be simplified down into a resistance network. This is typically achieved by representing the heat sink as an equivalent electric circuit, as shown in Figure 61.

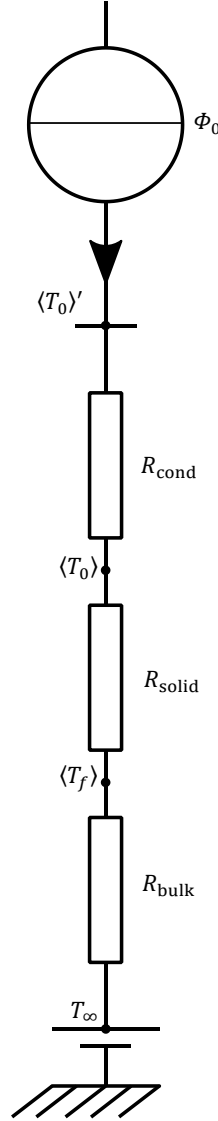


Figure 61: Equivalent electrical resistance network of heat sink.

In Figure 61,  $\langle T_0 \rangle'$  refers to the average temperature of the surface of the heated plate and  $\langle T_0 \rangle$  is the temperature at the interface between the heated plate and the foam. As  $R_{cond}$  is considered to be sufficiently small, the difference between  $\langle T_0 \rangle'$  and  $\langle T_0 \rangle$  can be neglected and  $\langle T_0 \rangle'$  will no longer be referred to.  $\langle T_f \rangle$  is the temperature of the fluid, and  $T_\infty$  is the temperature of the fluid at the inlet of the heat sink. It can therefore be seen that there are three separate thermal resistances working in series:

- The conductive thermal resistance  $R_{cond}$  as the flux travels through the depth of the heated plate (neglected for the optimisation process).

- The combination of the conductive thermal resistance as the energy moves in the downwards  $y$  direction through the solid phase, and the convective thermal resistance between the solid and the fluid,  $R_{solid}$ .
- The thermal resistance due to the bulk temperature rise in the fluid  $R_{bulk}$  in the  $z$  direction.

Thus, the total thermal resistance can be calculated by:

$$R_{tot} = R_{solid} + R_{bulk} \quad (2.24)$$

There is also a thermal resistance at the interface between the metal foam and the copper plate that must be considered. This will be addressed in chapter 4. As mentioned in Chapter 1, analytical models for microchannel heat sinks are commonplace within the literature, and in this work the same procedure is used to derive a model for a metal foam heatsink. The results of the two models will then later be compared. Thus, the derivation of a microchannel model will first be described, and afterwards the necessary modifications required to apply the method to metal foam will then be explained.

#### 4.1 Microchannel model

The first step is to present a geometry with the same external dimensions as the one seen in Figure 34.

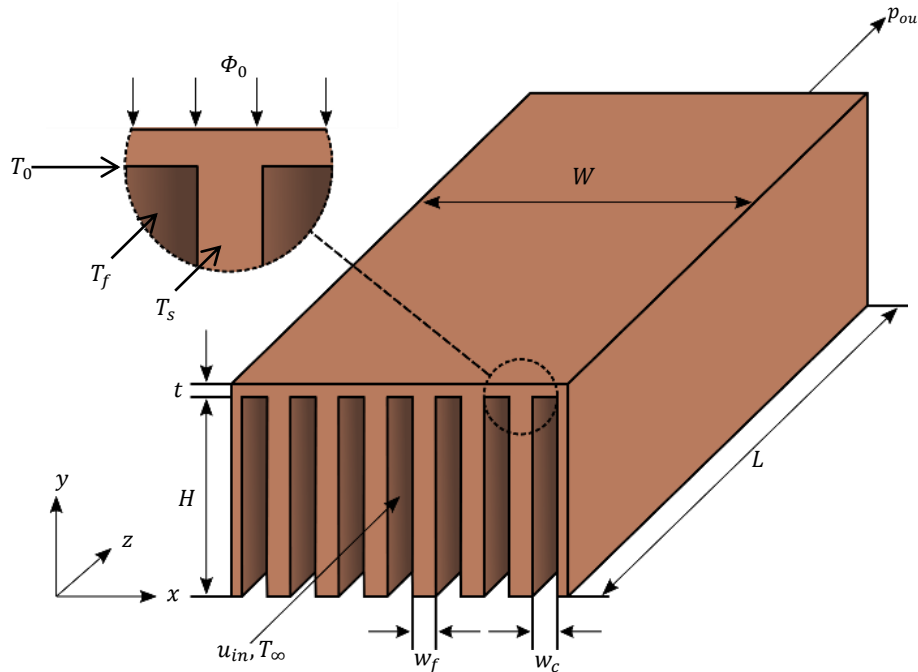


Figure 62: 3D schematic diagram of microchannel heat sink.

The microchannel heat sink seen in Figure 62 has the same exterior dimensions as the metal foam heat sink shown before ( $H=5\text{mm}$ ,  $W=10\text{mm}$ ,  $L=40\text{mm}$ ,  $t=2\text{mm}$ ). The channel width  $w_c$ , and fin width  $w_f$ , are parameters of the heat sinks that are varied in order to optimise performance, much like the fibre and pore diameters of the metal foam heat sink. The equations that govern the heat transfer and fluid flow through the microchannel heat sink are

the equations for the conservation of mass and momentum as seen before, and the volume-averaged two-equation energy model [57]:

**Solid energy equation:**

$$\nabla^2 T_s - \frac{2h_{sf}}{k_s w_f} (T_s - T_f) = 0 \quad (2.25)$$

**Fluid energy equation:**

$$\rho_f C_p \nabla \vec{u} T_f - k_f \nabla^2 T_f = 0 \quad (2.26)$$

This set of equations assumes a steady, incompressible and laminar flow and neglects radiation heat transfers. The microchannel analytical model used within this paper was taken from Liu *et al.* [58], and is derived by simplifying Equation (2.25) using the following assumptions:

- the fluid inlet velocity is uniform;
- the heated plate is thin enough so that the conduction heat transfer along its length (the  $z$  direction) is negligible;
- the variation in fluid temperature in the  $y$  direction is negligible when compared to the difference in temperature between the solid and fluid phases;
- the temperatures across the width of the fins (the  $x$  direction) can be averaged (thin fin assumption).

The third assumption neglects the variation in fluid temperature in the  $y$  direction, which relies on the height of the channels being sufficiently small and the convection heat transfer within the fluid being high enough. The fourth assumption states that the solid temperatures are constant in the  $x$  direction. Thus, it can be written that:

$$\frac{d^2(T_s(y, z))}{dy^2} = \frac{d^2(T_s(y, z) - T_f(z))}{dy^2} \quad (2.27)$$

Substituting equation (2.27) into (2.25) gives:

$$\frac{d^2(T_s(y, z) - T_f(z))}{dy^2} = \frac{2h_{sf}}{k_s w_f} (T_s(y, z) - T_f(z)) \quad (2.28)$$

The term on the right hand side contains the parameters describing the microchannel, which are conventionally replaced by the parameter  $m^2$ :

$$m^2 = \frac{2h_{sf}}{k_s w_f} \quad (2.29)$$

Thus:

$$\frac{d^2(T_s(y, z) - T_f(z))}{dy^2} = m^2 (T_s(y, z) - T_f(z)) \quad (2.30)$$

Equation (2.30) is a 2nd order differential equation and can be solved to give a solution of the following form:

$$(T_s(y, z) - T_f(z)) = ae^{my} - be^{-my} \quad (2.31)$$

Two boundary conditions are required to find the values of the parameters  $a$  and  $b$  in equation (2.31):

1. When  $y = H$ ,  $T_s = T_0$  ( $T_0$  is the temperature at the base of the fins).

2. When  $y = 0$ ,  $\frac{dT_s}{dy} = 0$  (the tips of the fins are considered adiabatic, thus the heat transfer is negligible).

Applying the two boundary conditions will lead naturally to the following equation:

$$(T_s(y, z) - T_f(z)) = (T_0(z) - T_f(z)) \frac{\cosh(m(H - y))}{\cosh mH} \quad (2.32)$$

Liu and Garimella [58] showed that the boundary condition at the base of the fin is typically described in one of two different ways, depending on the assumptions made:

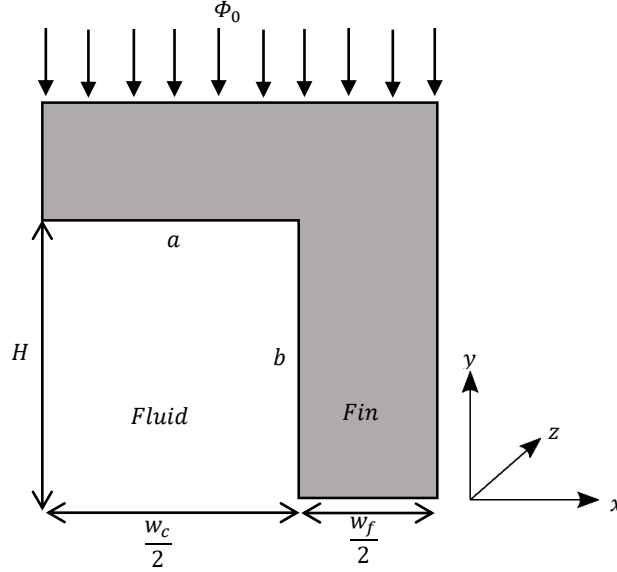


Figure 63: Schematic diagram of heat flux applied to a microchannel.

$$\Phi_0 = -k_s A \left. \frac{dT_s}{dy} \right|_{y=H} \quad (2.33)$$

$$\frac{(w_c + w_f)}{w_f} \Phi_0 = -k_s A \left. \frac{dT_s}{dy} \right|_{y=H} \quad (2.34)$$

where  $A$  is the surface area of the heated region of the heat sink. Equation (2.33) states that the imposed heat flux flows evenly into both the fluid and the fin, whilst equation (2.34) states that all the heat flux travels down the base of the fin. As neither of these two extremes can be considered accurate, Liu and Garimella [58] proposed the following compromise:

$$\frac{2\eta\alpha}{2\eta\alpha + 1} \frac{(w_c + w_f)}{w_f} \Phi_0 = -k_s A \left. \frac{dT_s}{dy} \right|_{y=H} \quad (2.35)$$

where  $\alpha = H/w_c$  is aspect ratio of the fin and  $\eta$  is the fin efficiency given by:

$$\eta = \frac{\tanh(mH)}{mH} \quad (2.36)$$

Liu & Garimella [58] demonstrated that their boundary condition was able to calculate the heat flux through the base of the fin to within 10% of the value found by numerical simulation. The definition of  $(T_s - T_f)$  in equation (2.32) can then be substituted in equation (2.35):

$$\begin{aligned} \frac{2\eta\alpha}{2\eta\alpha + 1} \frac{(w_c + w_f)}{w_f} \Phi_0 &= k_s A (T_0(z) - T_f(z)) \left. \frac{d \frac{\cosh(m(H-y))}{\cosh mH}}{dy} \right|_{y=H} \\ &= k_s A (T_0(z) - T_f(z)) m \tanh mH \end{aligned} \quad (2.37)$$

Rearranging equation (2.37) gives:

$$T_0(z) = T_f(z) + \frac{\Phi_0}{k_s m A \tanh mH} \frac{2\eta\alpha}{2\eta\alpha + 1} \frac{(w_c + w_f)}{w_f} \quad (2.38)$$

$T_0$  is an important parameter, and by assuming a negligible conductive thermal resistance through the thickness  $t$  of the top surface in Figure 62, and thus a constant solid temperature, it can be taken as the temperature of the chip that provides the heat flux  $\Phi_0$ . This is a valid assumption as the top surface, being solid copper, has a very high thermal conductivity.  $T_0$  can also be averaged over the heat surface and can then be used as a means of validating both the microchannel and metal foam models, as well as a way of making comparisons between the two. To average  $T_0$ , the average fluid temperature within the heat sink must be determined. This can be found from an energy balance:

$$\Phi_0 = \rho C_p Q (T_f(L) - T_\infty) \quad (2.39)$$

where  $Q$  is the volumetric flowrate. By assuming that the heat flux is imposed uniformly, and thus that the fluid temperature increases linearly along the length of the channel, the average fluid temperature can be calculated by:

$$\langle T_f \rangle = T_f \Big|_{z=L/2} = T_\infty + \frac{\Phi_0}{2\rho C_p Q} \quad (2.40)$$

The factor 2 in equation (2.40) is used in calculating the average fluid temperature. The definition of  $\langle T_f \rangle$  can then be substituted into equation (2.38):

$$\langle T_0 \rangle = T_\infty + \frac{\Phi_0}{2\rho C_p Q} + \frac{\Phi_0}{k_s m A \tanh mH} \frac{2\eta\alpha}{2\eta\alpha + 1} \frac{(w_c + w_f)}{w_f} \quad (2.41)$$

where  $\langle T_0 \rangle$  is the average temperature at the base of the fins across the whole heat sink. The temperature profiles of  $T_0$  and  $T_f$  along the length of the channel can be seen in Figure 64, which mirrors the equivalent electrical resistance diagram shown in Figure 61. It can be seen clearly that, when  $T_f$  is assumed to increase linearly, the average fluid temperature  $\langle T_f \rangle$  can be found at the point  $z = L/2$ .

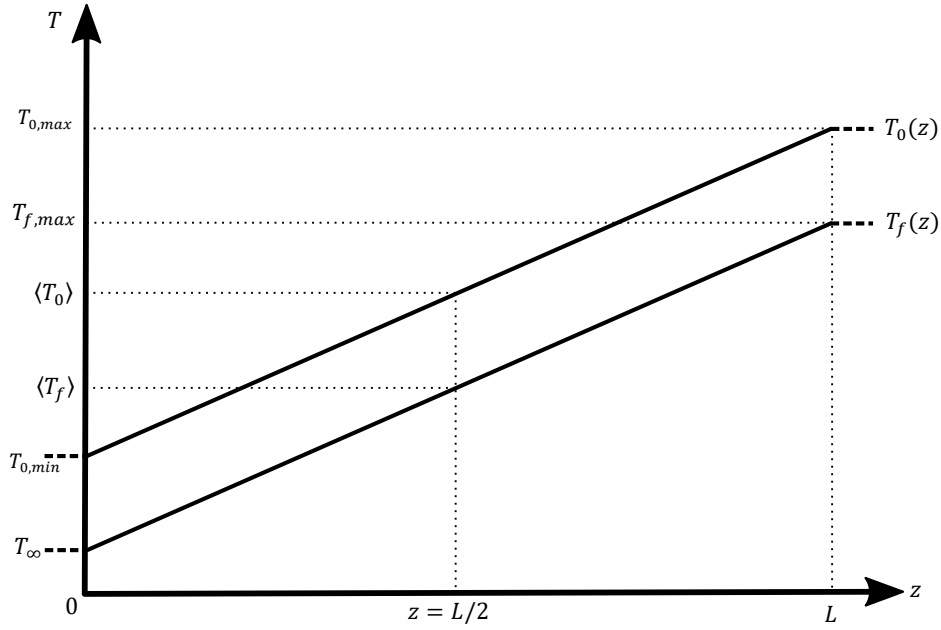


Figure 64: Temperature profiles along the length of the channel.

By using the definition of thermal resistance  $R = ((T_0) - T_{\infty})/\Phi_0$ , an equation for the total thermal resistance of the microchannel heat sink can then be derived:

$$R_{tot} = \frac{1}{2\rho C_p Q} + \frac{1}{k_s m A \tanh mH} \frac{2\eta\alpha}{2\eta\alpha + 1} \frac{(w_c + w_f)}{w_f} \quad (2.42)$$

In order to complete the model, the interfacial heat transfer coefficient and the hydraulic behaviour of the flow must also be calculated. In this work equations were taken from Harms et al. [59]. They presented correlations for the Nusselt number and friction factor  $f$  for both simultaneously developing, and fully developed flows within a microchannel. To determine which equations should be used, the length of the channel  $L$  must be compared with the thermal length  $(1/D_h Re Pr)$  and hydraulic length  $(1/D_h Re)$ . When  $L$  is significantly larger, the flow can be considered fully developed, both thermally and hydraulically. As varying  $w_c$  and  $w_f$  will affect the entrance lengths, and thus whether or not the flow is fully developed, both correlations must be available for use. The Nusselt correlations are as follows:

#### Fully developed

$$Nu_{fd} = 8.235(1 - 1.883\alpha + 3.767\alpha^2 - 5.814\alpha^3 + 5.361\alpha^4 - \alpha^5) \quad (2.43)$$

#### Simultaneously developing

$$Nu = 3.35(L^*)^{-0.13} \alpha^{0.12} Pr^{-0.038}, \quad 0.013 \leq L^* \leq 0.1 \quad (2.44)$$

$$Nu = 1.87(L^*)^{-0.3} \alpha^{0.056} Pr^{-0.036}, \quad 0.0005 \leq L^* \leq 0.013 \quad (2.45)$$

where  $L^*$  is the ratio between  $L$  and the thermal length ( $L^* = L/D_h Re Pr$ ). The interfacial heat transfer coefficient can then be calculated using:

$$h = \frac{Nu k_f}{D_h} \quad (2.46)$$

where  $D_h$  is the microchannel hydraulic diameter given by [58]:

$$D_h = \frac{2w_c H}{w_c + H} \quad (2.47)$$

And finally the pressure drop across a microchannel heat sink can be calculated as follows:

$$\Delta P = \frac{\rho u_m^2}{2} \left( f \frac{L}{D_h} \right) \quad (2.48)$$

where  $u_m$  is the average velocity of the fluid as it passes through the microchannels, and  $f$  is the friction factor, given by:

### Fully developed

$$(fRe)_{fd} = 96(1 - 1.3553/\alpha + 1.9467/\alpha^2 - 1.7012/\alpha^3 + 0.9564/\alpha^4 - 0.2537/\alpha^5) \quad (2.49)$$

### Simultaneously developing

$$fRe = \left( \left( \frac{3.2}{(L^+)^{-0.57}} \right)^2 + (fRe)_{fd}^2 \right)^{0.5}, \quad L^+ < 0.05 \quad (2.50)$$

where  $L^+$  is the ratio between  $L$  and the hydraulic length ( $L^+ = L/D_h Re$ ). Thus, the thermal resistance and associated pressure drop can be calculated for any microchannel, traversed by any coolant. In Chapter 3, it will be shown that this equation can be used to minimise the total thermal resistance for a given pressure drop.

## 4.2 Metal foam model

In this section, the procedure to derive an analytical model for microchannels will be applied to metal foam heat sinks. It must be noted that the principle assumption required for the derivation of this model, is that the change in temperature of the fluid through the height of the heat sink is negligible. This, along with the other assumptions previously outlined, means that equation (2.27) can be substituted into the LTNE solid energy equation presented earlier in this chapter. This gives:

$$\frac{d^2(T_s(y, z) - T_f(z))}{dy^2} - \frac{h_{sf} A_{fs}}{k_{eff,s}} (T_s(y, z) - T_f(z)) = 0 \quad (2.51)$$

This is similar to equation (2.28), but crucially, the parameters that define a microchannel ( $h$ ,  $k_s$  and  $w_f$ ) are replaced with the parameters that define metal foam ( $h_{sf}$ ,  $k_{eff,s}$  and  $A_{sf}$ ). Hence, in order to simplify this equation, a new parameter can be used,  $m_{fo}^2$ :

$$m_{fo}^2 = \frac{h_{fs} A_{fs}}{k_{eff}} \quad (2.52)$$

where the subscript  $fo$  is used to denote this refers to foam, and to differentiate from the microchannel model shown earlier. Therefore, equation (2.51) becomes:

$$\frac{d^2(T_s(y, z) - T_f(z))}{dy^2} - m_{fo}^2 (T_s(y, z) - T_f(z)) = 0 \quad (2.53)$$

Equation (2.53) can be solved as before, however this time the boundary condition at the base of the foam is as follows:

$$\Phi_0 = -k_{eff,s}A \left. \frac{d(T_s(y,z) - T_f(z))}{dy} \right|_{y=H} \quad (2.54)$$

Thus the equation for  $\langle T_0 \rangle_{fo}$  can be determined:

$$\langle T_0 \rangle_{fo} = T_\infty + \frac{\Phi_0}{2\rho C_p Q} + \frac{\Phi_0}{k_{eff,s} m_{fo} A \tanh m_{fo} H} \quad (2.55)$$

And finally, the total thermal resistance is:

$$R_{tot,fo} = \frac{1}{2\rho C_p Q} + \frac{1}{k_{eff,s} m_{fo} A \tanh m_{fo} H} \quad (2.56)$$

A new term can now be defined: the foam efficiency  $\eta_f$ . Similar to the fin efficiency in microchannels, this parameter takes into consideration the fact that the temperature of the foam is not uniform in the  $y$  direction. It is the ratio between the actual heat that has been transferred, and the heat that would have been transferred were the foam to be at uniform temperature:

$$\eta_{fo} = \frac{k_{eff,s}A \left. \frac{d(T_s(y,z) - T_f(z))}{dy} \right|_{y=H}}{h_{fs} A_{fo} (T_0(z) - T_f(z))} \quad (2.57)$$

where  $A_{fo}$  is the surface area of the metal foam in contact with the coolant. Rearranging equation (2.57) gives:

$$\eta_{fo} = \frac{\tanh(m_{fo}H)}{m_{fo}H} \quad (2.58)$$

This can then be substituted in equation (2.56):

$$R_{tot,fo} = \frac{1}{2\rho C_p Q} + \frac{1}{k_{eff,s} m_{fo}^2 A H \eta_{fo}} \quad (2.59)$$

### 4.3 Model summary

The following outlines the principle equations of the metal foam analytical model.

#### Energy

##### Thermal Resistance

$$R_{tot,fo} = \frac{1}{2\rho C_p Q} + \frac{1}{k_{eff,s} m_{fo}^2 A H \eta_{fo}}$$

$R_{tot,fo}$ : foam total thermal resistance

$\rho$ : fluid density

$C_p$ : fluid specific heat

$Q$ : fluid flow rate

$k_{eff,s}$ : solid phase effective thermal conductivity

$A$ : top plate surface area of heat sink

$H$ : height of heat sink

$\eta_{fo}$ : foam efficiency

## Energy

### Interfacial heat transfer coefficient

$$\frac{h_{sf}d}{k_f} = \begin{cases} 0.76Re_d^{0.4}Pr^{0.37}, & (1 \leq Re_d \leq 40) \\ 0.52Re_d^{0.5}Pr^{0.37}, & (40 \leq Re_d \leq 10^3) \\ 0.26Re_d^{0.6}Pr^{0.37}, & (10^3 \leq Re_d \leq 10^5) \end{cases}$$

$h_{sf}$ : interfacial heat transfer coefficient

$d$ : shape factor relating to fibre diameter

$k_f$ : fluid thermal conductivity

$Re$ : Reynolds number

$Pr$ : Prandtl number

### Effective solid thermal conductivity

$$1 - \varepsilon = \left( \frac{k_f - k_{eff}}{k_f - k_s} \right) \left( \frac{k_s}{k_{eff}} \right)^{1/3}$$

$\varepsilon$ : porosity

$k_s$ : solid thermal conductivity

$k_{eff}$ : effective thermal conductivity

### Specific surface area

$$A_{sf} \text{ (m}^{-1}\text{)} = \frac{3\pi d_f \left( 1 - e^{-\left(\frac{1-\varepsilon}{0.04}\right)} \right)}{(0.59d_p)^2}$$

$A_{sf}$ : specific surface area

$d_f$ : fibre diameter

$d_p$ : pore diameter

## Hydraulic

### Pressure loss

$$\frac{\Delta p}{L} = \frac{\mu_f}{K} u_s + C_2 \frac{1}{2} \rho_f u_s^2$$

$\Delta p$ : pressure difference across heat sink

$L$ : heat sink length

$\mu_f$ : fluid dynamic viscosity

$K$ : foam permeability

$u_s$ : fluid velocity

$C_2$ : inertial coefficient

## Hydraulic

### Permeability

$$\frac{K}{d_p^2} = 0.00073(1 - \varepsilon)^{-0.224}(d_f/d_p)^{-1.11}$$

### Inertial coefficient

$$C_2 = \frac{\tau^2}{\varepsilon^2 D_h}$$

$\tau$ : tortuosity

$D_h$ : hydraulic diameter

### Tortuosity

$$\tau = 1 + 1.2175 \frac{1 - 0.971(1 - \varepsilon)^{0.5}}{(1 - \varepsilon)^{0.5}} \frac{(1 - \varepsilon)}{\varepsilon}$$

## 5. Model Validation

Model validation was performed by first attempting to replicate experimental results from the literature. After this, the overall performance of the heat sink is compared with macro scale simulations.

### 5.1 Comparison with the literature

In order to get a sense of the effectiveness of the proposed model, preliminary comparisons were carried out with several different sources from the literature. The most common method of comparing thermal performance with in the literature is to use the average Nusselt number, calculated from the following equation:

$$Nu = \frac{hL}{k_f} \quad (2.60)$$

where  $L$  is the length of the porous region and  $h$  is the average heat transfer coefficient given by:

$$h = \frac{1}{AR_{tot,fo}} \quad (2.61)$$

Hetsroni et al. [60], Noh et al. [61], and Bayomy et al. [62] carried out studies on samples of ERG aluminium metal foams ( $\varepsilon = 0.9$ , 40 PPI, and  $d_p \approx 0.001m$ ), with water as the working fluid. The overall Nusselt numbers of their systems were determined experimentally, as a function of the Reynolds number. The results of their work, as well as the predictions made by the model proposed in this study can be seen in Figure 65. The analytical model proposed in this work seems to predict well the experimental data from the literature. Ten percent errors bars were included to quantify the models performance. At Reynolds numbers above 900, the majority of the experimental data points are encapsulated by the error bars.

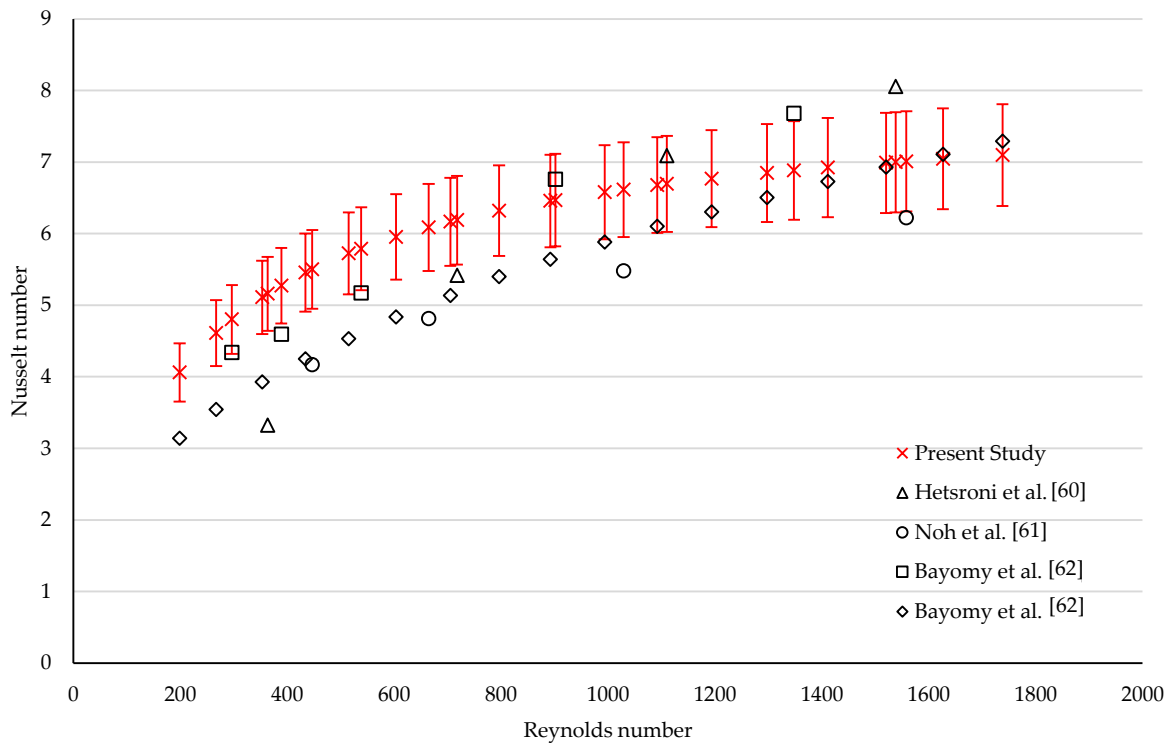


Figure 65: Variation of overall Nusselt number with Reynolds number.

This model was also tested for its ability to predict hydraulic behaviour. These results can be seen in Figure 66. Similarly, ten percent error bars were used as a means of assessing the models performance. In this case, all the experimental data points rest within the ten percent limit.

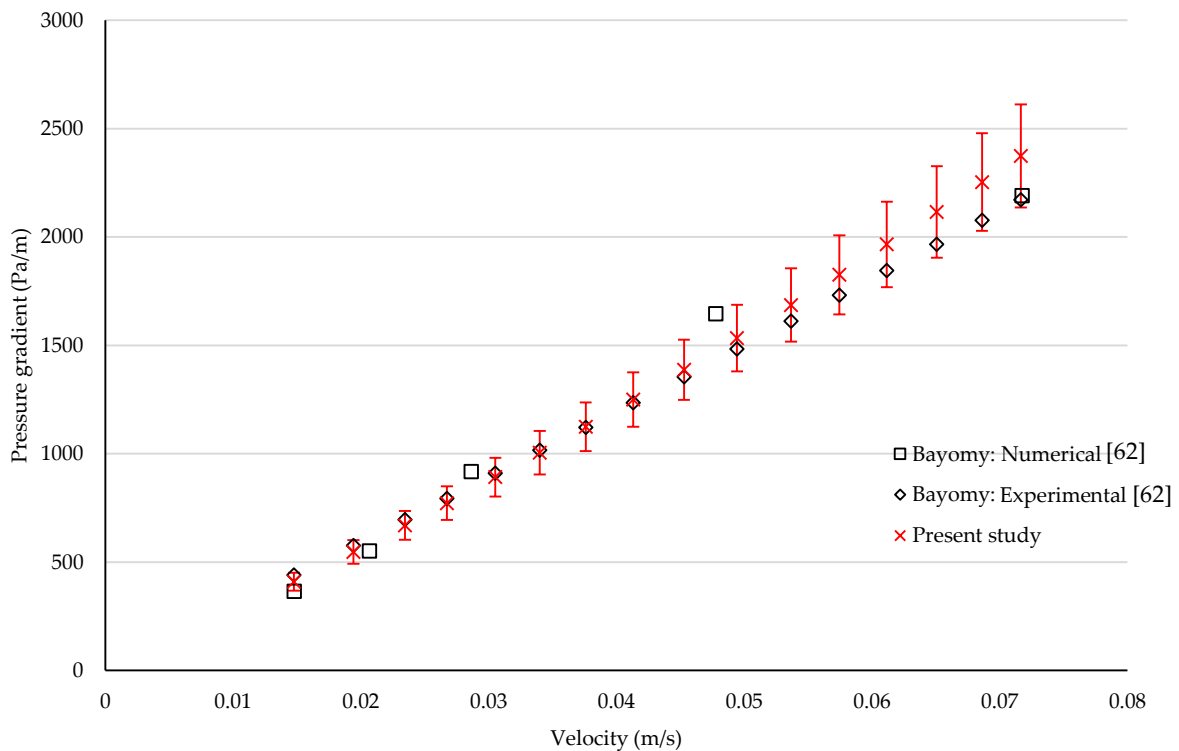


Figure 66: Variation of pressure gradient with fluid velocity.

Once again, a good agreement is seen between the analytical model of this a work, and the experimental data from Bayomy et al [31]. The next step is to validate the model further by directly comparing model predictions with numerical simulations. Thus, the model can be tested under the very specific conditions chosen for this work.

## 5.2 Macro-scale simulations

The Ansys FLUENT porous media model solves the LTNE energy equations and the Darcy-Forchheimer momentum equations outlined in the beginning of this chapter. It is used for a wide variety of single phase and multiphase problems, including flow through packed beds, filter papers, perforated plates, flow distributors, tube banks, and open celled foams. When the model is used, a cell zone is defined in which the porous media model is applied. When solving the two energy equations shown earlier in this chapter (equations 2.6 and 2.7), a dual cell approach is used. As such, a solid zone that is spatially coincident to the porous fluid zone is defined, and only interacts with the fluid with regards to heat transfer.

### Geometry

A geometry based on Figure 34 was made using the built-in software in Ansys Workbench, and can be seen in Figure 67.

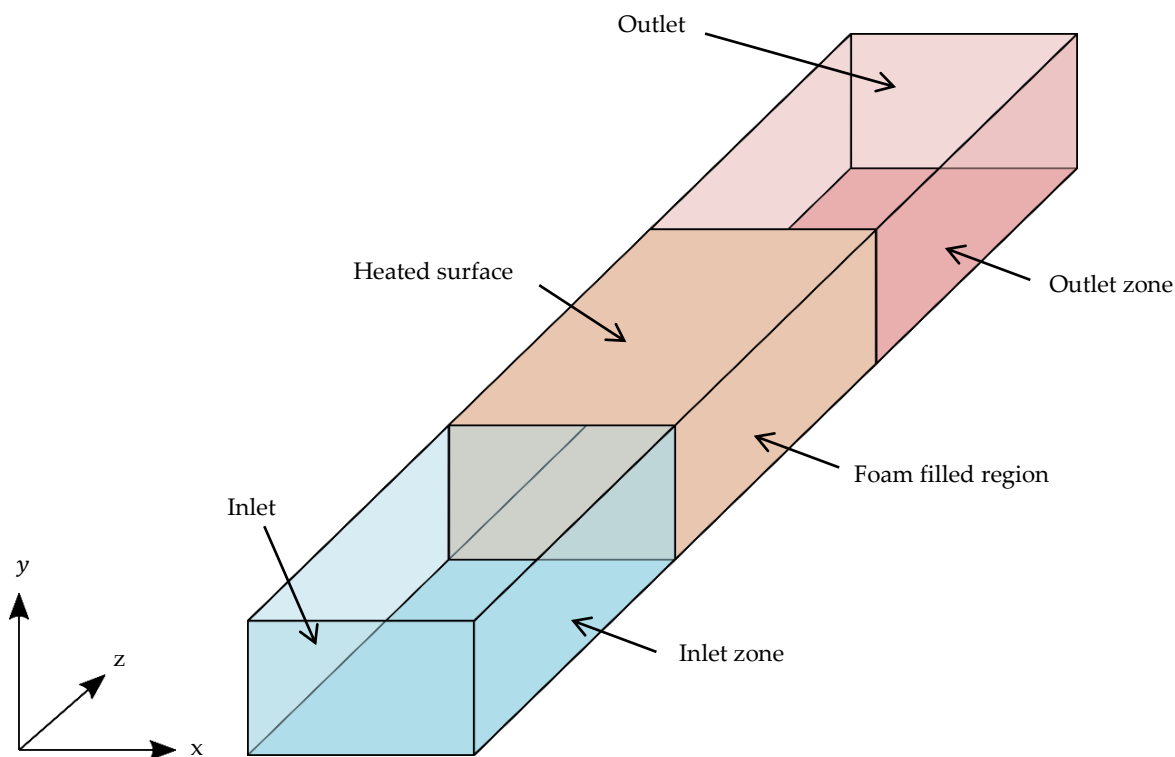


Figure 67: Simulated volume of metal foam filled channel.

Initially, in order to avoid entry and exit effects on the flow, an inlet and an outlet zone were attached to the foam filled region. However, simulations showed that the results were unaffected, so these regions were removed so as to reduce computing time. The foam filled region was also cut in half along the z axis, as this is a line of symmetry.

### Meshing

Meshing was achieved using roughly 4000000 quad elements and an edge sizing function was implemented to increase mesh density at the connection between the foam and the heated surface. Mesh independence was achieved by reporting the average heated surface temperature, as well as the average velocity at the outlet, and systematically reducing the maximum face size until the difference between results dropped to below  $10^{-3}$ . Figure 68 shows how the control volume was meshed at the interface between the porous zone and the heated surface.

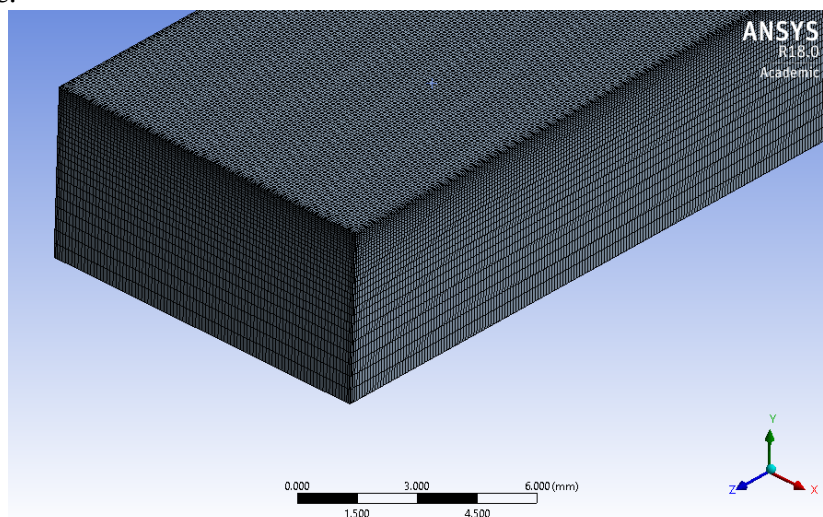


Figure 68: Meshing of foam filled channel.

### Results

Parametric simulations were performed for a wide range of porosities, spanning from 20% to 95%. To test the limits of the model, the foam fibre diameter was held fixed at three different values (300, 155 and  $10\mu\text{m}$ ) considered to represent current fabrication figures. The porosity was then varied by adjusting the pore diameter, using equation (2.27). A volumetric flow rate of  $3.25 \times 10^{-6} \text{m}^3/\text{s}$  ( $u_{in} = 0.065 \text{m/s}$ ) was chosen as it corresponds to an increase in fluid temperature of 20 K when using a flux of 100 W. Table 4 shows the values of the important foam parameters (pore diameter, specific surface area, effective thermal conductivity), calculated from the previously described analytical models in section 3.

TABLE 4:

Input parameters for simulated foams

<b>Fibre diameter = 10<math>\mu</math>m</b>			
Porosity	Pore diameter (mm)	$A_{sf}$ (1/m)	$k_{eff}$ (W.m <sup>-1</sup> .K <sup>-1</sup> )
0.2	0.029	320000	281
0.3	0.031	280000	235
0.4	0.034	240000	193
0.5	0.0347	200000	155
0.6	0.041	160007	119
0.7	0.048	120066	86
0.8	0.058	80542	55
0.9	0.076	43577	26
0.95	0.083	28031	13
<b>Fibre diameter = 155<math>\mu</math>m</b>			
Porosity	Pore diameter (mm)	$A_{sf}$ (1/m)	$k_{eff}$ (W.m <sup>-1</sup> .K <sup>-1</sup> )
0.2	0.45	20645	281
0.3	0.48	18064	235
0.4	0.52	15483	193
0.5	0.57	12903	155
0.6	0.64	10323	119
0.7	0.74	7746	86
0.8	0.90	5196	55
0.9	1.17	2811	26
0.95	1.29	1808	13
<b>Fibre diameter = 300<math>\mu</math>m</b>			
Porosity	Pore diameter (mm)	$A_{sf}$ (1/m)	$k_{eff}$ (W.m <sup>-1</sup> .K <sup>-1</sup> )
0.2	0.87	10666	281
0.3	0.93	9333	235
0.4	1.01	8000	193
0.5	1.10	6666	155
0.6	1.23	5333	119
0.7	1.42	4002	86
0.8	1.73	2684	55
0.9	2.27	1452	26
0.95	2.49	934	13

As with the pore-scale simulations, a fluid was defined in Ansys that had all the same corresponding parameters as Paratherm™ LR. To make comparisons between the numerical simulations and the analytical model, the parameter  $\Delta T$  was defined as follows:

$$\Delta T = \langle T_0 \rangle - T_\infty \quad (2.62)$$

Figure 69, Figure 70, and Figure 71 show the effects of porosity on  $\Delta T$  for foams with fibre diameters of  $300\mu\text{m}$ ,  $155\mu\text{m}$  and  $10\mu\text{m}$  respectively. The analytical model shows good agreement with the numerical simulations for the first two diameters, with an average deviation in results of 5.03% and 7.61% respectively. In the case of the foams with fibre diameter of  $10\mu\text{m}$ , a greater disparity was seen between the model and the simulations, with an average deviation of 28.23%. This is because, in this case, the assumption that the fluid temperature is constant in the y direction no longer holds true. For the model to be valid, the difference in fluid temperature at  $y=0$  and  $y=H$  must be sufficiently small in comparison to the difference between the fluid and solid temperatures. However, the results show that by increasing the local heat transfer coefficient, as occurs when the fibre diameter is reduced, this is no longer the case. Thus the effectiveness of the model is limited to metal foams whose local heat transfer coefficients are not so high as to undermine this assumption.

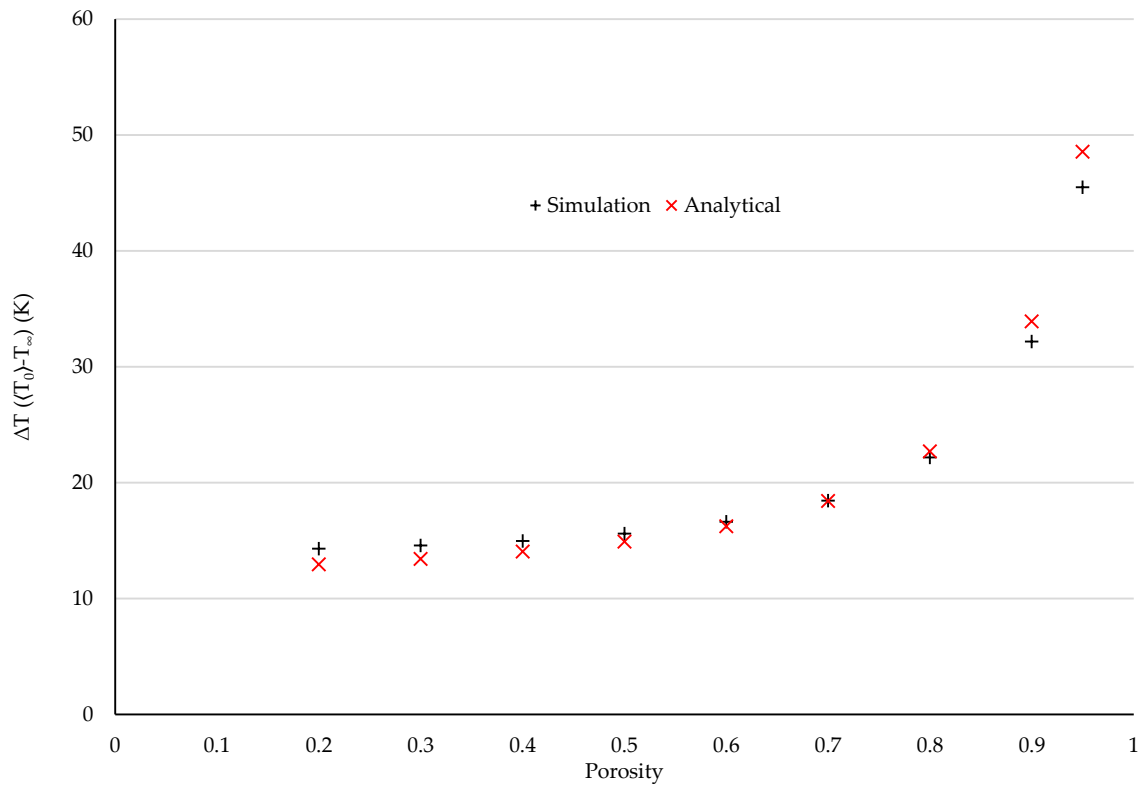


Figure 69: Effects of porosity on  $\Delta T$  for metal foams with porosities 20-95% and fibre diameter  $300\mu\text{m}$ .

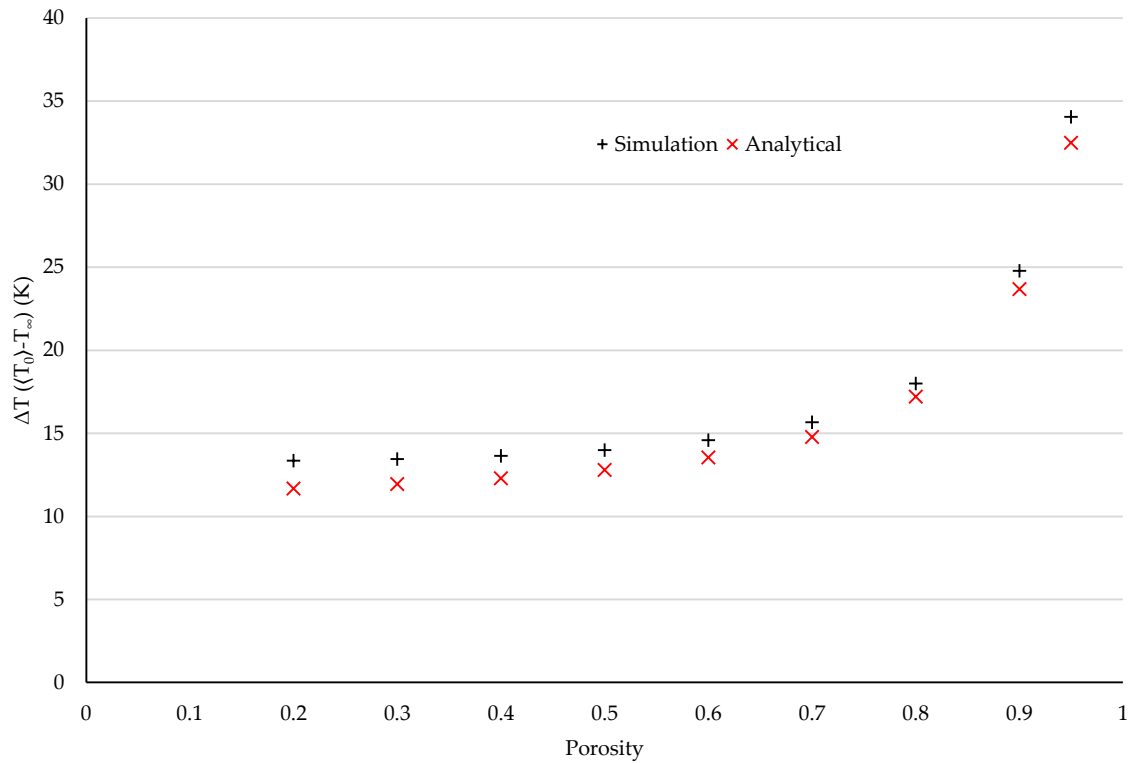


Figure 70: Effects of porosity on  $\Delta T$  for metal foams with porosities 20-95% and fibre diameter 155  $\mu\text{m}$ .

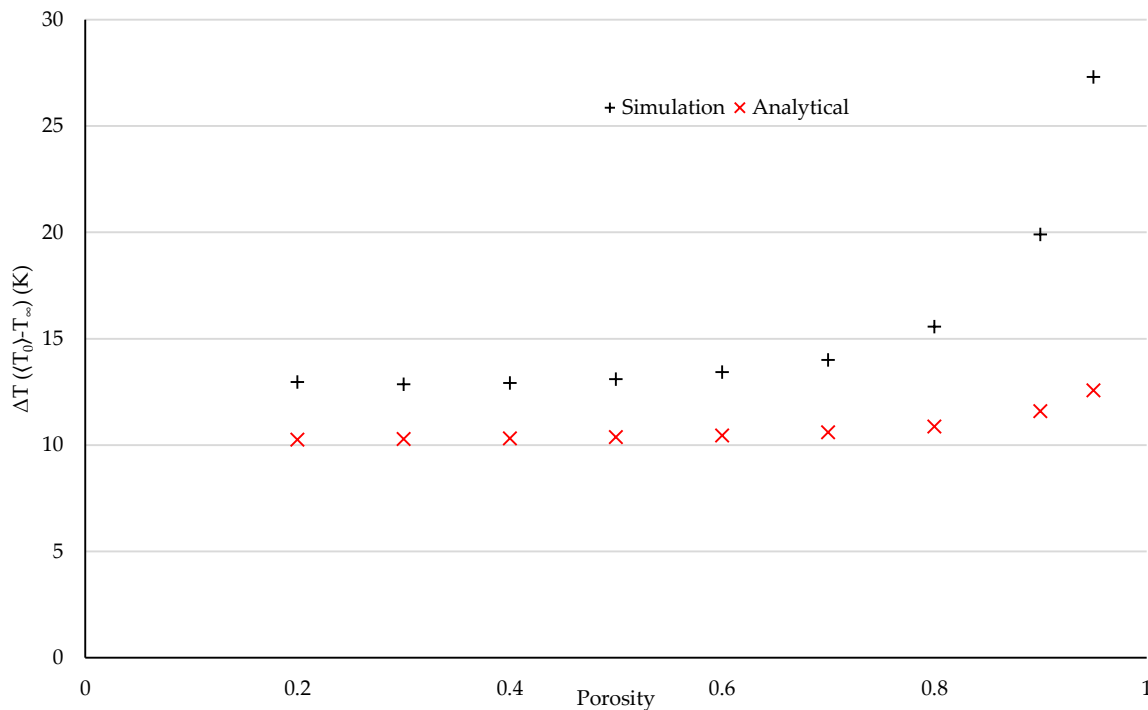


Figure 71: Effects of porosity on  $\Delta T$  for metal foams with porosities 20-95% and fibre diameter 10  $\mu\text{m}$ .

The pressure drop through the foam was also simulated and compared with the Darcy-Forchheimer model. Figure 72 shows the pressure drops between the inlet and the outlet of the metal foam for both the analytical model and the numerical simulations, on a

logarithmic scale with fibre diameter  $300\mu\text{m}$ . The results show an excellent agreement with the numerical simulations. The average percentage difference for the  $300\mu\text{m}$ ,  $155\mu\text{m}$ , and  $10\mu\text{m}$  foams were 5.83%, 2.78%, and 0.08% respectively.

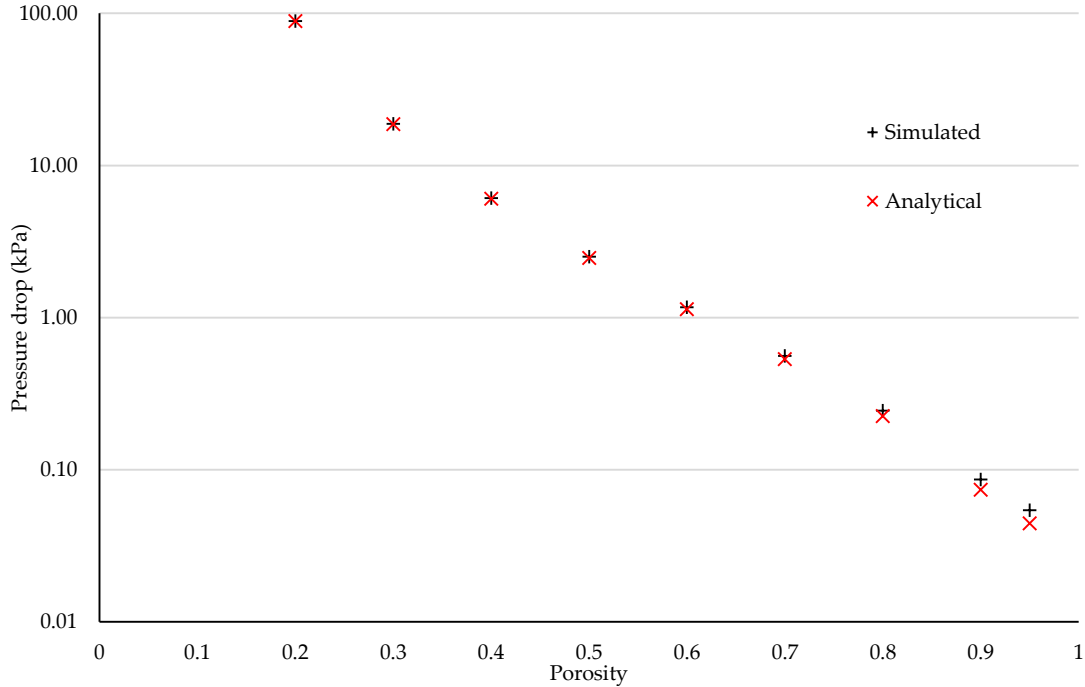


Figure 72: Effects of porosity on pressure drop for metal foam with fibre diameter  $300\mu\text{m}$ .

The results of the numerical simulations show that the proposed analytical model has a good agreement in terms of thermal behaviour, but for a limited range of foam micro geometries ( $d_f \geq 150\mu\text{m}$ ). As one of the goals of this work is to use the model to optimise the foam structure, it is important that its region of applicability is as large as possible, as it is feasible that under certain conditions, the optimal foam would have a fibre diameter approaching  $10\mu\text{m}$ . Thus, a method of improving the accuracy of the model during the optimisation procedure through the use of a Space Mapping algorithm will be explained in Chapter 3.

## 6. Conclusion

This chapter began by looking more closely at the proposed solution presented at the end of Chapter 1. It was explained that before being able to analyse the heat sink as a whole, it must first be broken down into a simplified 'case study'. This took the form of a metal foam filled channel, traversed by a coolant, with a uniform heat flux applied to the upper surface. After this, the individual heat transfer mechanisms occurring within a metal foam heat sink were outlined, and the method of reducing the overall complexity and computing time by using volume-averaged governing equations was explained. It was then shown that several fundamental parameters ( $k_{eff,s}$ ,  $h_{sf}$ ,  $K$  and  $C_2$ ) were required in order to close these equations. The ways in which these parameters are determined was discussed in length (pore-scale simulations, experimentation, analytical models) and example results were given. This review provided enough evidence to confidently conclude that the analytical approach was the most

appropriate option for this work. Several of the assumptions made by the analytical models were tested, such as the flow within the metal foam section becoming quickly fully developed. Pore-scale simulations of two different foam geometries (cube cell and tetrakaidecahedra) were carried out and it was shown that the flows dependency on its position within the porous zone becomes negligible after a small number of cell lengths.

The method of deriving an analytical model, as well as the required assumptions, was then explained. Firstly, how it is most typical used with microchannels, and then how it can be applied to metal foams. Thus two equations for the total thermal resistance were presented.

The model was then validated by comparing it to numerical simulations. The results show that for a wide range of foam porosities (20% - 90%) and fibre diameters (155 $\mu$ m - 300 $\mu$ m), the analytical model agrees well with the numerical simulations. Unfortunately, the accuracy of the model decreased when testing foams with 10  $\mu$ m fibre diameters. This is because when the local coefficient of heat transfer is too high, the assumption of constant fluid temperature in the y direction is no longer valid. As an additional means of testing the models accuracy, it was then used to replicate several experimental results found within the literature. It performed well, and captured accurately the trend of the Nusselt numbers as they varied with the Reynolds number.

In the next chapter, the drop in the models accuracy will be addressed and improved upon by using a Space Mapping algorithm. The procedure of optimising the geometry of metal foam to maximise heat transfer will then be outlined. The optimising software CADES will be used to adjust the physical properties of the foam (fibre diameter, pore diameter, porosity, pore density) to reduce the overall thermal resistance.

## 7. Bibliography

- [33] J. C. Maxwell, *Electricity and Magnetism*, London: Clarendon Press, 1873.
- [34] P. Ranut, E. Nobile and L. Mancini, "High Resolution X-Ray Microtomography-Based CFD Simulation for Characterization of Flow Permeability and Effective Thermal Conductivity of Aluminium Metal Foams," *Experimental Thermal and Fluid Science*, vol. 67, pp. 30-36, 2015.
- [35] S. A. Tassou, W. Lu and C. Y. Zhao, "Thermal Analysis on Metal-Foam Filled Heat Exchangers," *International Journal of Heat and Mass Transfer*, vol. 49, pp. 2751-2761, 2006.
- [36] B. Boyd and K. Hooman, "Air-Cooled Micro-Porous Heat Exchangers for Thermal Management of Fuel Cells," *International Communications in Heat and Mass Transfer*, vol. 39, pp. 363-367, 2012.
- [37] P. Jiang, Z. Ren and B. Wang, "Numerical Simulation of Forced Convection Heat Transfer in Porous Plate Channels Using Thermal Equilibrium and Non Thermal Equilibrium Models," *Numerical Heat Transfer*, vol. 35, n° 11, pp. 99-113, 1999.
- [38] H. Darcy, *Recherches Experimentales Relatives au Mouvement de l'Eau dans les Tuyaux*, Mallet-Bachelier, 1857.
- [39] P. Forchheimer, "Wasserbewegung Durch Boden," *Zver auf Deutsch*, vol. 45, pp. 1782-1788, 1901.
- [40] S. Pinson, "Architected Materials for Transpiration Cooling : Application to Combustion Chambers," *Universite Grenoble Alpes, Grenoble*, 2016.

- [41] V. V. Calmidi and R. L. Mahajan, "The Effective Thermal Conductivity of High Porosity Fibrous Metal Foams," *Journal of Heat Transfer*, vol. 121, pp. 466-471, 1999.
- [42] Y. Yao, H. Wu and Z. Liu, "A New Prediction Model for the Effective Thermal Conductivity of High Porosity Open-Cell Metal Foams," *International Journal of Thermal Sciences*, vol. 97, pp. 56-67, 2016.
- [43] X. Xiao, P. Zhang and M. Li, "Effective Thermal Conductivity of Open-Cell Metal Foams Impregnated with Pure Paraffin for Latent Heat Storage," *International Journal for Thermal Sciences*, vol. 81, pp. 94-105, 2014.
- [44] E. Sadeghi, S. Hsieh and M. Bahrami, "Thermal Conductivity and Contact Resistance of Metal Foams," *Journal of Physics D: Applied Physics*, vol. 44, pp. 1-7, 2011.
- [45] M. S. Phanikumar and R. L. Mahajan, "Non-Darcy Natural Convection in High Porosity Metal Foams," *International Journal of Heat and Mass Transfer*, vol. 45, pp. 3781-3793, 2002.
- [46] E. Solorzano, J. A. Reglero, M. A. Rodriguez-Perez, D. Lehmkus, M. Wichmann and J. A. de Saja, "An Experimental Study on the Thermal Conductivity of Aluminium Foams by Using the Transient Plane Source Method," *International Journal of Heat and Mass Transfer*, vol. 51, pp. 6259-6267, 2008.
- [47] M. Zafari, M. Panjepour, M. D. Emami and M. Meratian, "Microtomography-Based Numerical Simulation of Fluid Flow and Heat Transfer in Open Cell Metal Foams," *Applied Thermal Engineering*, vol. 80, pp. 347-354, 2015.
- [48] M. Wang and N. Pan, "Modeling and Prediction of the Effective Thermal Conductivity of Random Open-Cell Porous Foams," *International Journal of Heat and Mass Transfer*, vol. 51, pp. 1325-1331, 2008.
- [49] O. Wiener, "The Theory of Mixtures for Fields with Constant Currents," *Akademie der Wissenschaften.*, pp. 32-507, 1912.
- [50] X. Yang, J. Bai, H. Yan, J. Kuang, T. Lu and T. Kim, "An Analytical Unit Cell Model for the Effective Thermal Conductivity of High Porosity Metal Foams," *Transport In Porous Media*, vol. 102, pp. 403-426, 2014.
- [51] P. G. Collishaw and J. R. G. Evans, "An Assessment of Expressions for the Apparent Thermal Conductivity of Cellular Materials," *Journal of Material Sciences*, vol. 29, pp. 486-498, 1994.
- [52] Z. Wu, C. Caliot, G. Flamant and Z. Wang, "Numerical Simulation of Convective Heat Transfer Between Airflow and Ceramic Foams to Optimise Volumetric Solar Air Receiver Performances," *International Journal of Heat and Mass Transfer*, vol. 54, pp. 1527-1537, 2011.
- [53] Z. Nie, Y. Lin and Q. Tong, "Numerical Investigation of Pressure Drop and Heat Transfer Through Open Cell Foams with 3D Laguerre-Voronoi Model," *International Journal of Heat and Mass Transfer*, vol. 113, pp. 819-839, 2017.
- [54] S. Kakac, R. K. Shah and W. Aung, *Handbook of Single-Phase Convective Heat Transfer*, New York: Wiley, 1987.
- [55] V. V. Calmidi, "Transport Phenomena in High Porosity Fibrous Metal Foam," 1998.
- [56] A. Inayat, M. Klumpp, M. Lammermann, H. Freund and W. Schwieger, "Development of a New Pressure Drop Correlation for Open-Cell Foams Based Completely on Theoretical Grounds: Taking into Account Strut Shape and Geometric Tortuosity," *Chemical Engineering Journal*, 2015.

- [57] C. L. Tien and S. M. Kuo, "Analysis of Forced Convection in Microstructures for Electronic System Cooling," *Proceedings of the International Symposium Cooling Technology for Electronics Equipment*, Honolulu, 1987.
- [58] D. Liu and S. V. Garimella, "Analysis and Optimization of the Thermal Performance of Microchannel Heat Sinks," *International Journal for Numerical Methods in Heat and Fluid Flow*, vol. 15, n° 11, pp. 7-26, 2005.
- [59] T. M. Harms, M. J. Kazmierczak and G. F. M., "Developing Convective Heat Transfer in Deep Rectangular Microchannels," *International Journal of Heat and Fluid Flow*, vol. 20, pp. 149-157, 1999.
- [60] G. Hetsroni, M. Gurevich and R. Rozenblit, "Metal Foam Heat Sink for Transmission Window," *International Journal of Heat and Mass Transfer*, vol. 48, pp. 3793-3803, 2005.
- [61] J. Noh, K. Lee and C. Lee, "Pressure Loss and Forced Convective Heat Transfer in an Annulus Filled with Aluminium Foam," *International Communications in Heat and Mass Transfer*, vol. 33, pp. 434-444, 2006.
- [62] A. M. Bayomy, M. Z. Saghir and T. Yousefi, "Electronic Cooling Using Water Flow in Aluminum Metal Foam Heat Sink: Experimental and Numerical Approach," *International Journal of thermal Sciences*, vol. 109, pp. 182-200, 2016.



---

# CHAPTER 3

---

## OPTIMISATION OF METAL FOAM MICRO GEOMETRY USING THE ANALYTICAL MODEL

---

### Table of Contents

1. INTRODUCTION.....	80
2. OPTIMISATION.....	80
2.1 CADES PROCEDURE .....	80
2.2 OPTIMISED FOAM .....	82
3. SPACE MAPPING .....	90
3.1 INTRODUCTION.....	90
3.2 SM ALGORITHM.....	90
3.3 APPLICATION OF SM ALGORITHM.....	91
3.4 VALIDATION OF SM ALGORITHM .....	92
4. FOAM/MICROCHANNEL COMPARISONS .....	94
5. CONCLUSIONS.....	96

## 1. Introduction

In this chapter, the procedure of optimising the geometry of metal foam to maximise heat transfer is outlined. It is shown that by using the optimising software CADES, the defining characteristics of foam (fibre diameter, pore diameter, porosity, pore density) can be adjusted in order to reduce the overall thermal resistance. This is achieved using the series of equations discussed in Chapter 2. Also shown in the previous chapter was the fact that the model loses accuracy under certain conditions. This issue is addressed by using the Space Mapping (SM) methodology, which is intended specifically to be applied to the optimisation of engineering models. By using this technique, the accuracy of the thermal resistance, calculated by the analytical model, is greatly increased. Following this, the optimised metal foam performance is directly compared with the performance of optimised microchannel heat sinks that have been tested under comparable conditions. As laid out in Chapter 2, microchannels have been used as a benchmark with which to judge the efficacy of metal foams as a power electronics heat sink.

## 2. Optimisation

Optimisation of both analytical models (metal foam and microchannel) was achieved using the software CADES (Component Architecture for the Design of Engineering Systems). This program was developed for dimensioning and optimising an unlimited variety of physical systems or phenomena.

### 2.1 CADES procedure

The results of the optimisation process are heavily dependent on the input parameters (heat flux, available hydraulic power, pressure loss etc.), and hence will differ from application to application. This means that no universal optimised foam/microchannel that has a consistently minimal thermal resistance exists. It was therefore necessary to define ranges or fixed values for many of the parameters contained within the analytical models. In the case of the metal foams heat sink, three variables were chosen to have a restricted range: pressure drop  $\Delta p$ , porosity  $\varepsilon$ , and fibre diameter  $d_f$ , and three for the microchannel heat sink as well: pressure drop  $\Delta p$ , channel width  $w_c$ , and fin width  $w_f$  (Table 4). For both the foam and the microchannels, two of the variables define the geometry of the heat sinks ( $\varepsilon$  and  $d_f$ ,  $w_c$  and  $w_f$ ). The limits given to these variables are in line with current fabrication techniques and constraints. The third is a hydraulic parameter required to limit the rate of heat transfer that could be achieved simply by increasing the flowrate indefinitely. On occasion, one or more of these variables may also be constrained with a prescribed value for the purpose of analysing the impact of the others, but in each case this will be made clear when the results are displayed.

The remaining parameters are split into two groups: the input parameters whose values are required prior to the optimisation process (Table 5), and the output parameters, who are unconstrained and are calculated during optimisation (Table 6). As with the validation process, a volumetric flowrate of  $3.25 \times 10^{-6} m^3 \cdot s^{-1}$  ( $u_{in} = 0.65 m \cdot s^{-1}$ ) was chosen, corresponding to an increase in fluid temperature of 20K when using a heat flux of 100 W. CADES then uses an SQP (Gradient Sequential Quadratic Programming) optimiser to

find the solutions to every equation that corresponds to a minimised total thermal resistance  $R_{tot}$ . This is an iterative method for constrained nonlinear optimization. Though a powerful tool, capable of handling any degree of non-linearity, even within the constraints, it has the disadvantages of needing to incorporate several derivatives. As these will likely need to be worked analytically in advance of iterating to a solution, SQP can become quite cumbersome for large problems with many variables or constraints.

TABLE 4:

Foam and microchannel variables

Symbols	Foam Variables	
$\Delta p$	Pressure drop	0 – 50 kPa
$d_f$	Fibre diameter	$\geq 10 \mu m$
$\varepsilon$	Porosity	0.4 – 0.95
Symbols	Microchannel Variables	
$\Delta p$	Pressure drop	0 – 50 kPa
$w_c$	Channel width	$\geq 100 \mu m / 10 \mu m$
$w_f$	Fin width	$\geq 100 \mu m / 10 \mu m$

TABLE 5:

Foam and microchannel input values

Symbols	Hydraulic Input Values	
$Q$	Volumetric flowrate	$3.25 \times 10^{-6} m^3 \cdot s^{-1}$
$\rho$	Fluid density	$760 kg \cdot m^{-3}$
$\mu$	Fluid dynamic viscosity	$0.00152 Pa \cdot s$
Symbols	Thermal Input Values	
$T_\infty$	Fluid inlet temperature	300 K
$C_p$	Fluid specific heat capacity	$2010 J \cdot kg^{-1} \cdot K^{-1}$
$k_f$	Fluid thermal conductivity	$0.15 W \cdot m^{-1} \cdot K^{-1}$
$k_s$	Solid thermal conductivity	$387.6 W \cdot m^{-1} \cdot K^{-1}$
$\Phi_0$	Heat flux	100 W

TABLE 6:

Foam and microchannel output values

Symbols	Hydraulic Output Parameters	
$Re$	Reynolds number	–
$C_2$	Inertial coefficient	$m^{-1}$
Symbols	Thermal Output Parameters	
$\langle T_0 \rangle$	Average temp. at base of fins	K
$\langle T_0 \rangle_{fo}$	Average temp. at base of foam	K
$R_{tot}$	Microchannel thermal resistance	K/W
$R_{tot,fo}$	Foam thermal resistance	K/W
$k_{eff,s}$	Effective solid thermal conductivity	$W \cdot m^{-1} \cdot K^{-1}$
$h_{sf}$	Interfacial heat transfer coefficient	$W \cdot m^{-2} \cdot K^{-1}$
Symbols	Foam Output Parameters	

$A_{sf}$	Specific surface area	$m^{-1}$
$d_p$	Pore size	$m$
$K$	Permeability	$m^2$
$D_{h,fo}$	Foam hydraulic diameter	$m$
$\tau$	Tortuosity	–
Symbols	Microchannel Output Parameters	
$\alpha$	Fin aspect ratio	–
$N$	Number of channels	–
$D_h$	Microchannel hydraulic diameter	$m$

## 2.2 Optimised Foam

In order to attain a preliminary idea of the thermal and hydraulic behaviour of the various metal foam geometries, an initial series of optimisations were carried out where both the porosity and pressure drop were constrained. Thus the first porosity within its given range (40%) was chosen, and the foam was optimised at every pressure drop within its range (0 – 50 kPa). The process was then repeated at intervals 5% porosity, up to 95%, and only the fibre diameter was left to vary freely. From this, a series of Pareto curves plotting thermal resistance against pressure drop for each porosity was extracted from the results. An example of this for a 90% porosity foam can be seen in Figure 71. The graph shows that as the pressure drop increases, the overall thermal resistance is reduced. Though on the face of it, this is an expected result, it must be remembered that the fluid flowrate is constant throughout, so any reduction in thermal resistance is achieved purely through the manipulation of the foam geometry.

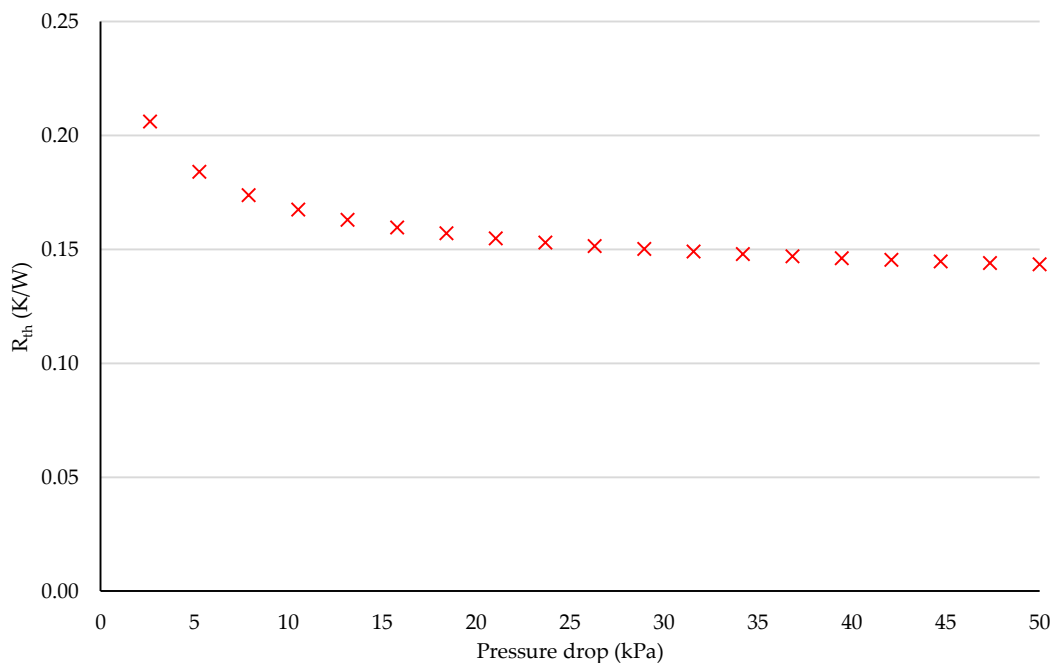


Figure 71: Minimised thermal resistance for metal foam with 90% porosity, an imposed heat flux of 100 W and a flowrate of  $3.25 \times 10^{-6} m^3 \cdot s^{-1}$ .

Understanding the relationship between the thermal and hydraulic behaviour of metal foam and its geometry is an important aspect of this project. To do so, the fibre diameters,

pore sizes, permeabilities, specific surface areas and interfacial heat transfer coefficients corresponding with the thermal resistances shown in Figure are compared in Figure 72.

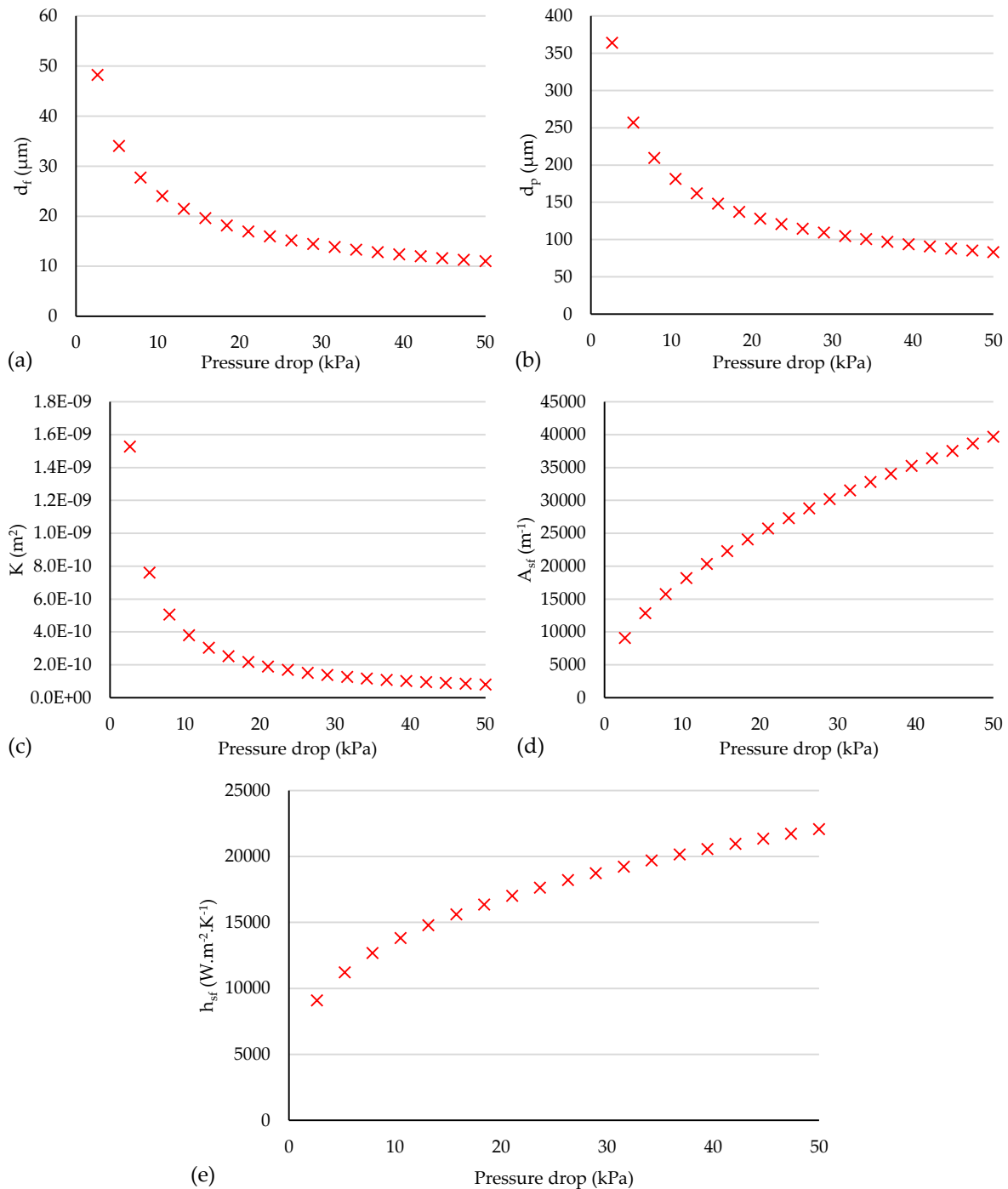


Figure 72: Results of optimised foam with 90% porosity, an imposed heat flux of 100 W and a flowrate of  $3.25 \times 10^{-6} \text{m}^3 \cdot \text{s}^{-1}$  showing pressure drop against (a) fibre diameter, (b) pore size, (c) permeability, (d) specific surface area, and (e) interfacial heat transfer coefficient.

By studying the results in Figure 72, it can be seen that when the imposed pressure drop is increased whilst maintaining the flowrate constant, CADES reduces the fibre diameter, which in turn reduces the pore diameter (see equation (2)). This has several effects that explain the results seen in Figure . Firstly, it reduces the permeability of the foam, which generates the

increased pressure drop. Secondly, it increases both the specific surface area and the interfacial heat transfer coefficient, which accounts for the improved thermal behaviour (see equation (2.22) introduced in chapter 2, and equation (1.2), introduced in chapter 1).

$$\frac{h_{sf}d}{k_f} = \begin{cases} 0.76Re_d^{0.4}Pr^{0.37}, & (1 \leq Re_d \leq 40) \\ 0.52Re_d^{0.5}Pr^{0.37}, & (40 \leq Re_d \leq 10^3) \\ 0.26Re_d^{0.6}Pr^{0.37}, & (10^3 \leq Re_d \leq 10^5) \end{cases} \quad d = (1 - e^{-(1-\varepsilon)/0.04})d_f \quad (2.22)$$

$$A_{sf} \text{ (m}^{-1}\text{)} = \frac{3\pi d_f \left(1 - e^{-\frac{(1-\varepsilon)}{0.04}}\right)}{(0.59d_p)^2} \quad (1.2)$$

This is confirmed by looking at equation (2.56) for  $R_{tot,fo}$ , introduced in the previous chapter, with the  $m_{fo}$  term expanded:

$$R_{tot,fo} = \frac{1}{2\rho C_p Q} + \frac{1}{\sqrt{h_{sf}A_{sf}k_{eff,s}} A \tanh H \sqrt{h_{sf}A_{sf}/k_{eff,s}}} \quad (2.56)$$

The first term on the right hand side of equation (2.2.3) is constant due to the constant flowrate. In the second term  $A$  and  $H$  relate to the external dimensions of the heat sink, so remain constant, as well as  $k_{eff,s}$  due to the fixed porosity. Thus, for a fixed porosity and flowrate, the reduction in  $R_{tot,fo}$  is only caused by the increase in  $h_{sf}$  and  $A_{sf}$ . These two parameters can be combined to produce a term for the volumetric heat transfer coefficient:

$$h_v = h_{sf}A_{sf} \quad (3.63)$$

$h_v$  can then be plotted against the pressure drop, this is shown in Figure 73.

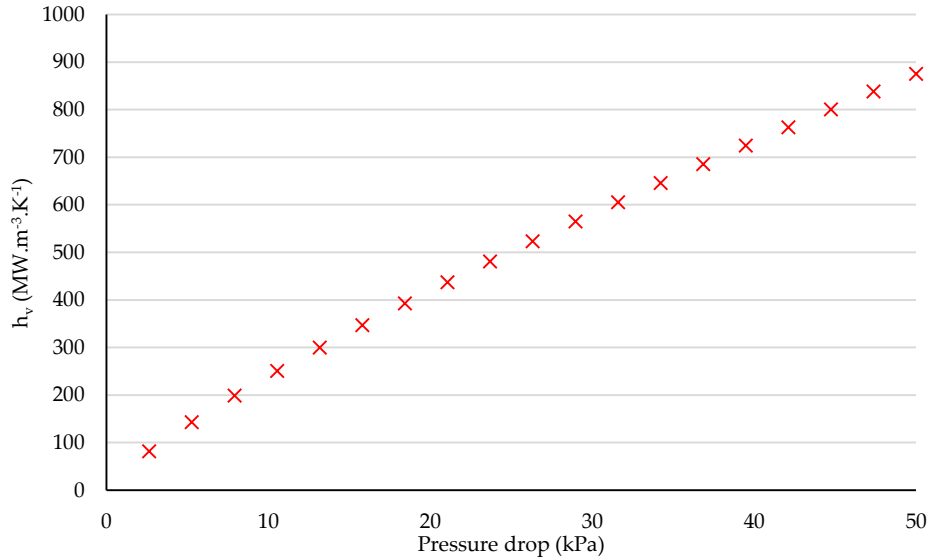


Figure 73: Volumetric heat transfer coefficient as a function of pressure drop for optimised foams with 90% porosity, an imposed heat flux of 100 W and a flow rate of  $3.25 \times 10^{-6} \text{m}^3 \cdot \text{s}^{-1}$ .

These results explain the foams thermal and hydraulic behaviour for a fixed porosity, however the effect of varying the porosity must also be analysed. In order to see clearly how

performance varies with porosity, MATLAB was used to combine the thermal resistance results for each porosity into a single 3D surface plot, which can be seen in Figure 74.

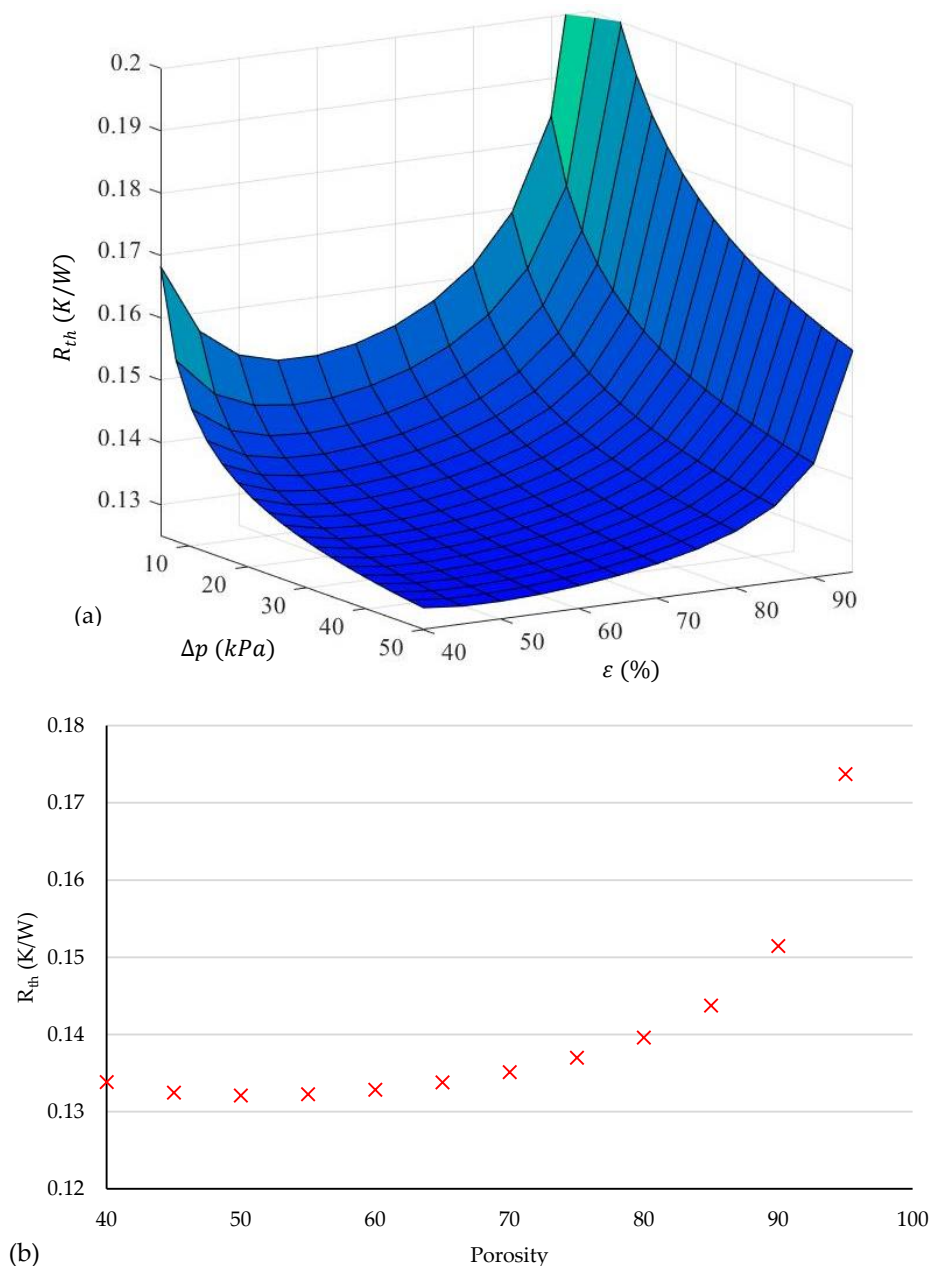


Figure 74: Minimised thermal resistance for metal foams with porosities ranging from 40% to 95% an imposed heat flux of 100 W and a flowrate of  $3.25 \times 10^{-6} \text{m}^3 \cdot \text{s}^{-1}$  (a), and thermal resistance values at a constant pressure loss of 25kPa (b).

Figure 74 shows that when looking along a line of constant pressure drop, there is an optimum porosity that minimises the overall thermal resistance. Once again it is advantageous to understand which of the foams physical variables contribute to this behaviour. Thus, the fibre diameters, pore sizes, specific surface areas, interfacial heat transfer coefficients and effective solid thermal conductivities corresponding with the thermal resistances shown in Figure 74 will be compared (Figure 75). A pressure drop of 25 kPa was chosen as it is in the centre of the tested range.

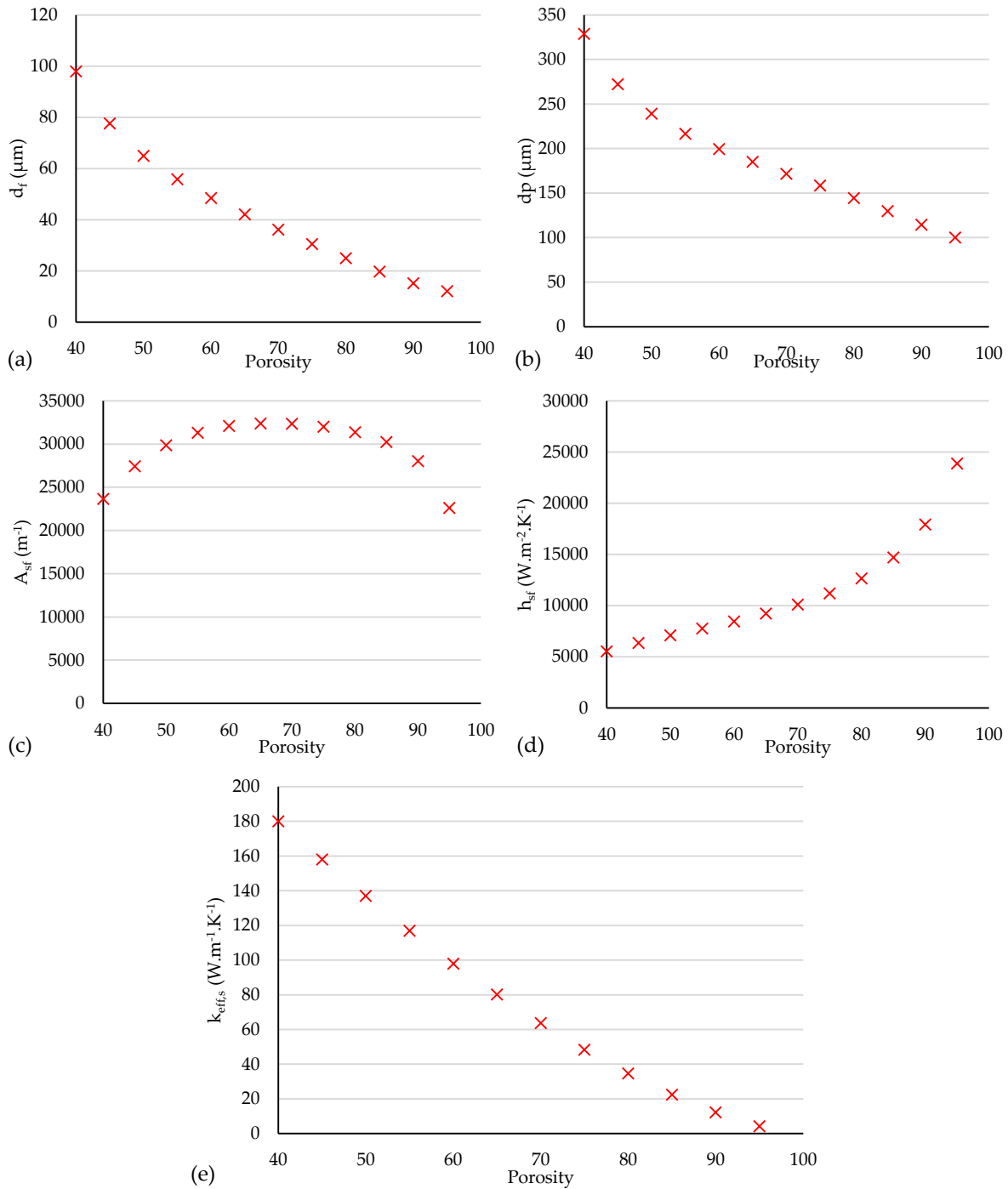


Figure 75: Results of optimised foam with 25kPa pressure drop, an imposed heat flux of 100 W and a flowrate of  $3.25 \times 10^{-6} \text{m}^3 \cdot \text{s}^{-1}$  showing porosity against (a) fibre diameter, (b) pore size, (c) specific surface area, (d) interfacial heat transfer coefficient, and (e) effective solid thermal conductivity.

In the previous example,  $d_f$  was adjusted such that the pressure loss across the foam was increased, whilst maintaining a constant porosity. In this example,  $d_f$  is varied in such a way as to keep the pressure loss constant, whilst the porosity increases. As before, by decreasing  $d_f$ ,  $d_p$  is also decreased. However, in this case the combination of a decreasing porosity, fibre diameter and pore diameter results in parabolic specific surface area, with its maximum at roughly 70% porosity.  $h_{sf}$  also increases, similarly to the previous example, due

to the reducing fibre diameter (see equation (2.22)). The added variable in this example is  $k_{eff,s}$ , which decreases with increasing porosity. Again, the volumetric heat transfer coefficient can be plotted (Figure 76) using equation (3.63), and even though  $A_{sf}$  decreases with porosities above 70%, the volumetric heat transfer coefficient increases at a fairly constant rate.

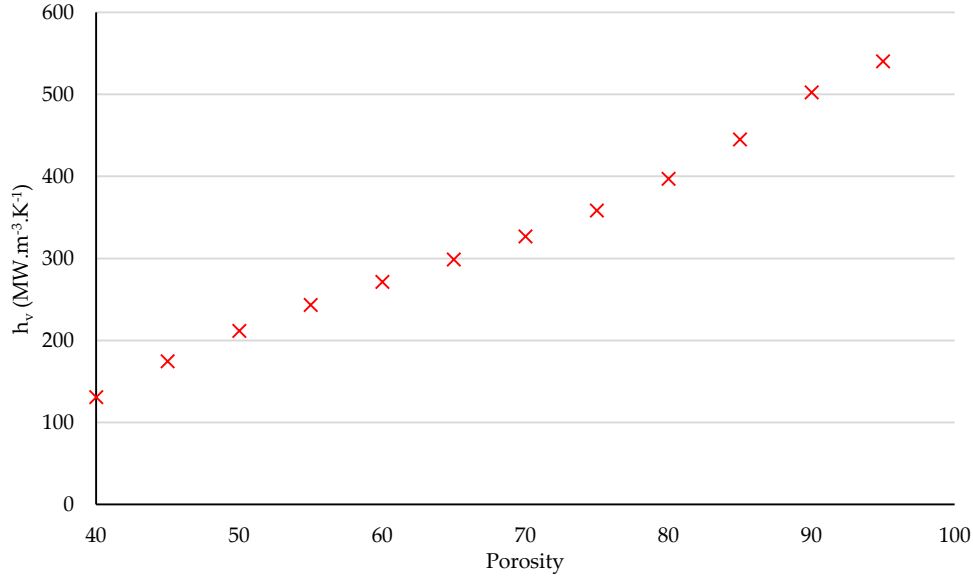


Figure 76: Volumetric heat transfer coefficient as a function of pressure drop for optimised foams with 25kPa pressure drop, an imposed heat flux of 100 W and a flowrate of  $3.25 \times 10^{-6} \text{m}^3 \cdot \text{s}^{-1}$ .

Therefore, the parabolic nature of the results shown in Figure 74 can be explained by the combination of an increasing  $h_v$  and decreasing  $k_{eff,s}$ . This can be understood by looking again at equation (2.56), specifically the term  $\sqrt{h_{sf}A_{sf}k_{eff,s}}$  as the variation of  $\tanh H\sqrt{h_{sf}A_{sf}/k_{eff,s}}$  is negligible in comparison. How  $\sqrt{h_{sf}A_{sf}k_{eff,s}}$  varies with porosity can be seen in Figure 77.

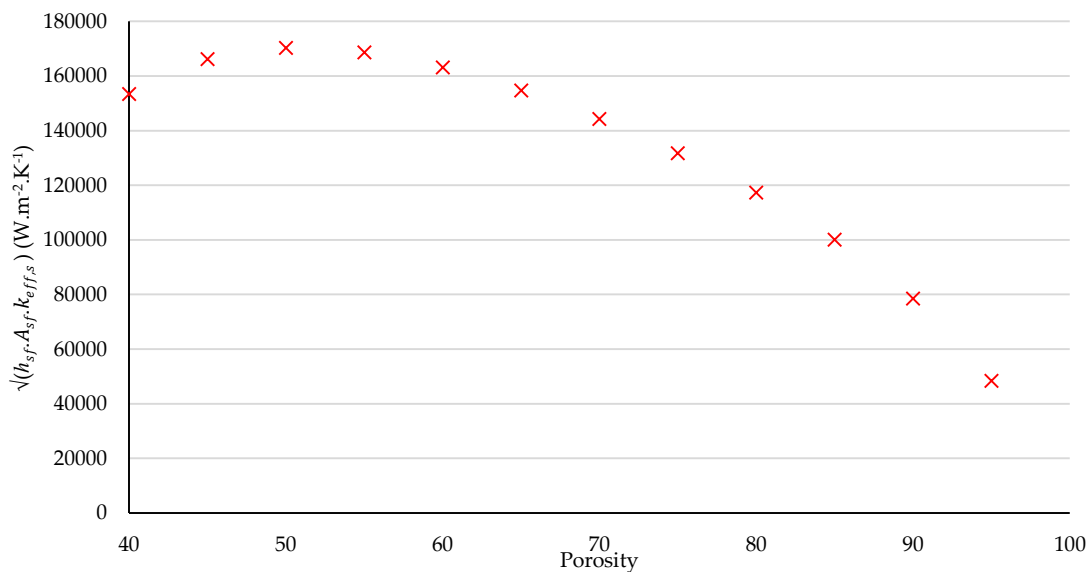


Figure 77: Effects of porosity on  $\sqrt{h_{sf}A_{sf}k_{eff,s}}$  for optimised foams with 25kPa pressure drop, an imposed heat flux of 100 W and a flowrate of  $3.25 \times 10^{-6} \text{m}^3 \cdot \text{s}^{-1}$ .

Figure 77 shows that an optimum exists as a result of the combination of  $h_{sf}$ ,  $A_{sf}$  and  $k_{eff,s}$ . In terms of heat transfer mechanisms, depending on the porosity there is a predominance over heat transfer by conduction or heat transfer by convection. At low porosities, conduction is responsible for a higher proportion of the overall heat transfer, which would result in a nearly uniform temperature across the entire heat exchange surface and a higher foam efficiency,  $\eta_{fo}$ . At high porosities, conduction decreases and convection becomes the mainly contributor to heat transfer. Thus the temperature of the foam surface will no longer be uniform, and  $\eta_{fo}$  will be reduced. This is shown in Figure 78.

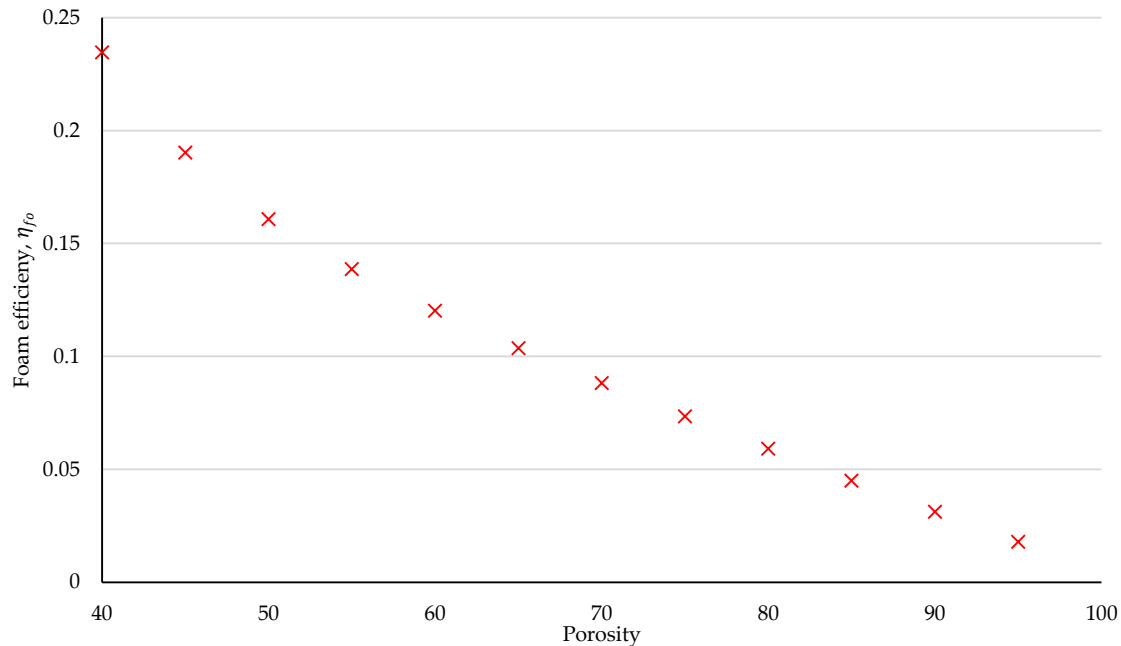


Figure 78: Effects of porosity on foam efficiency with a 25kPa pressure drop, an imposed heat flux of 100 W and a flowrate of  $3.25 \times 10^{-6} \text{m}^3 \cdot \text{s}^{-1}$ .

As conduction and convection heat transfer occur simultaneously (i.e. neither reaches zero at any porosity that is not 0% or 100%), the optimum porosity is the point where the combination of the two is at a maximum.

Thus far, results have been attained by varying three parameters. Multiple optimisations were carried out by imposing values of  $\Delta p$  and  $\varepsilon$  within their ranges, and  $d_f$  was modified freely. In a practical setting, this method could be used when a selection of different metal foams is already available, and the user wishes to determine which would perform better for their specific needs. However, in the case where the foam will be manufactured new, the porosity can be treated in the same way as the fibre diameter. Both would vary freely within their ranges and thus, a single optimised foam will be generated for each pressure loss. The results of this can be seen in Figure 79.

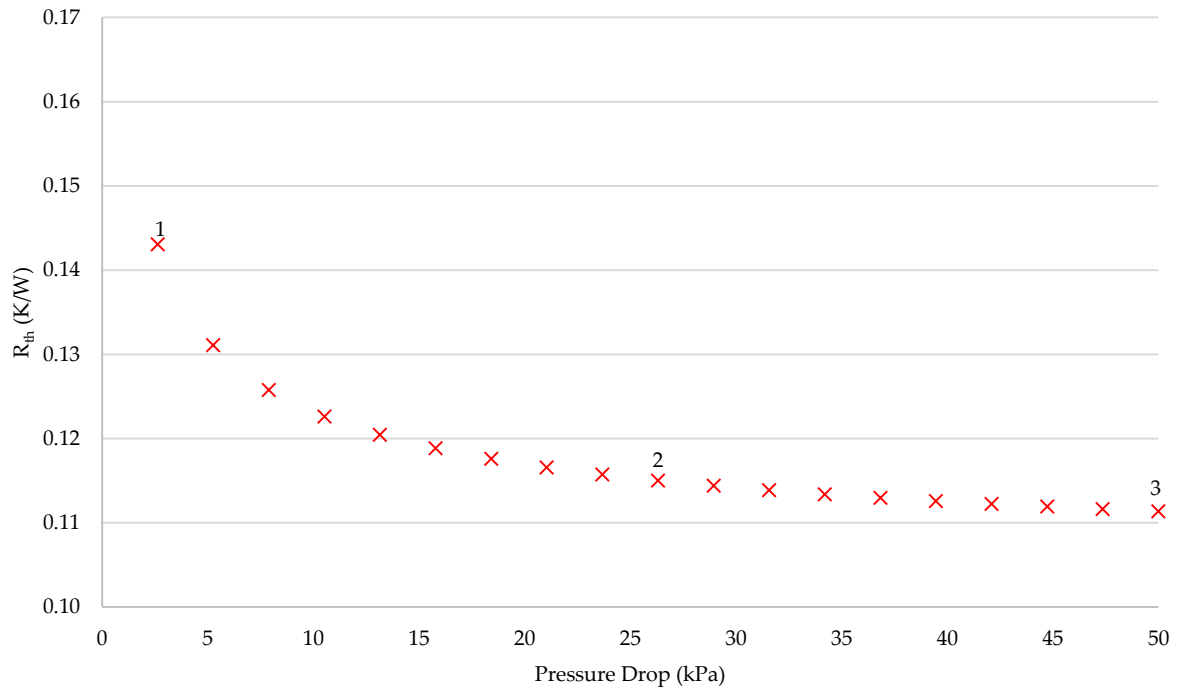


Figure 79: Minimised thermal resistance for metal foam with free varying porosity and fibre diameter, an imposed heat flux of  $100 \text{ W}$  and a flowrate of  $3.25 \times 10^{-6} \text{ m}^3 \cdot \text{s}^{-1}$ .

The results shown in Figure 79 correspond to a series of unique foam geometries, whose details are readily available after the optimisation process. Also, as can be seen in Table 7, depending on the imposed constraints, metal foams optimised for heat transfer can have a range of porosities outside of what can be found commercially. Three example foams, at pressure losses of 2.63kPa, 26.31kPa, and 50kPa have been showcased to highlight this point. The information in Table 7 can be used to manufacture the foam best suited for the individual situation. Comparisons with commercially available foams can also made, and the properties of several of the most common industry foams can be seen in Table 8.

TABLE 7:

Properties of selected foams

Properties	Foam 1	Foam 2	Foam 3
Porosity	61.2%	50.6%	47.9%
Fibre diameter	0.17 mm	0.06 mm	0.05 mm
Pore diameter	0.71 mm	0.24 mm	0.17 mm
$\Delta P$ drop	2.63 kPa	26.31 kPa	50 kPa
$R_{th}$	0.143 K/W	0.115 K/W	0.111 K/W

TABLE 8:

Comparison between industry foams

Properties	Replicated Foam	MetaFoam®	Porvair®	Versarien®	Duocel®
Porosity	75-85%	88 – 94.1%	>90%	63%	68 – 91%
Material	Al	Cu	Cu	Cu	Cu/Al

It is interesting to note that the majority of metal foams proposed by the industry have porosities far higher than what has been calculated as optimal within this work. As has been shown in Chapter 1, they are fabricated using lost carbonate sintering, replication, vapour deposition and investment casting. Though these methods provide a good amount of control over porosity, fibre diameter and pore size, very few different porosities can be bought commercially. This work shows that for heat transfer purposes, a larger range of foam porosities is required within the industry. Powder sintering, the space holder method or lost carbonate sintering (used to fabricate Versarien® foam) would be ideal solutions; each method is inexpensive and can produce low porosity foams *en masse*.

As previously outlined in Chapter 2, the model proposed in this work suffers a drop in accuracy at the lower limits of the tested fibre diameter. It was shown that when the interfacial coefficient of heat transfer becomes too high, the model no longer aligns with the results calculated numerically, though the general tendencies are still followed. Thus, to overcome this problem, and increase the model's accuracy, a process known as output Space Mapping (SM) will be applied.

## 3. Space Mapping

### 3.1 Introduction

SM is the process of replacing a computationally expensive, fine model (numerical simulations), with a fast, course, surrogate (analytical model) that has been iteratively improved using the fine models results [63]. It is often used as a means of reducing the required time at the design phase. SM-based algorithms are typically broken down into four steps [64]:

- Course model simulation.
- Comparison of results with fine model.
- Updating course model.
- Re-simulation of the course model.

Output SM involves a simple transformation of the surrogate models outputs so that they are aligned as closely as possible to the fine model. It does not, in fact, require any re-writing of the course model.

### 3.2 SM algorithm

The procedure begins at iteration  $i$  from a vector of initial input values ( $x$ ) (porosity, fibre diameter). A first optimisation is then performed using only the course model. The results are defined as the vector  $c_i(x)$  and are obtained for the optimal inputs vector ( $x$ ).  $c_i(x)$

is then compared with the results vector from the fine model  $f(x)$  using the same optimal inputs vector  $x$ . The adjustment required between the course and fine model is defined as [65]:

$$\theta_i = \frac{f(x)}{c_i(x)} \quad (3.64)$$

where  $\theta_i$  is the transformation. Hence, if the outputs of the course mode were multiplied by this ratio, then the new results would coincide with the results of the fine model. Thus, only the outputs of the course model are adjusted, whilst the actual writing of the model is left unaltered. So  $\theta_i$  is calculated from the results of iteration  $i$ , and is used to determine the new values of the course model, at  $i + 1$ . Thus  $c_i(x)$  is replaced by  $c_{i+1}(x)$ :

$$c_{i+1}(x) = \theta_i c_i(x) = \frac{f(x)}{c_i(x)} c_i(x) \quad (3.65)$$

This process can then be repeated as needed to improve the values of the course model.

### 3.3 Application of SM algorithm

In order to improve the accuracy of the results shown in Figure 79, a series of numerical simulations were carried out periodically to ascertain reference 'fine model' results. The foams simulated were the three shown in Table 7, this can be seen in Figure 80.

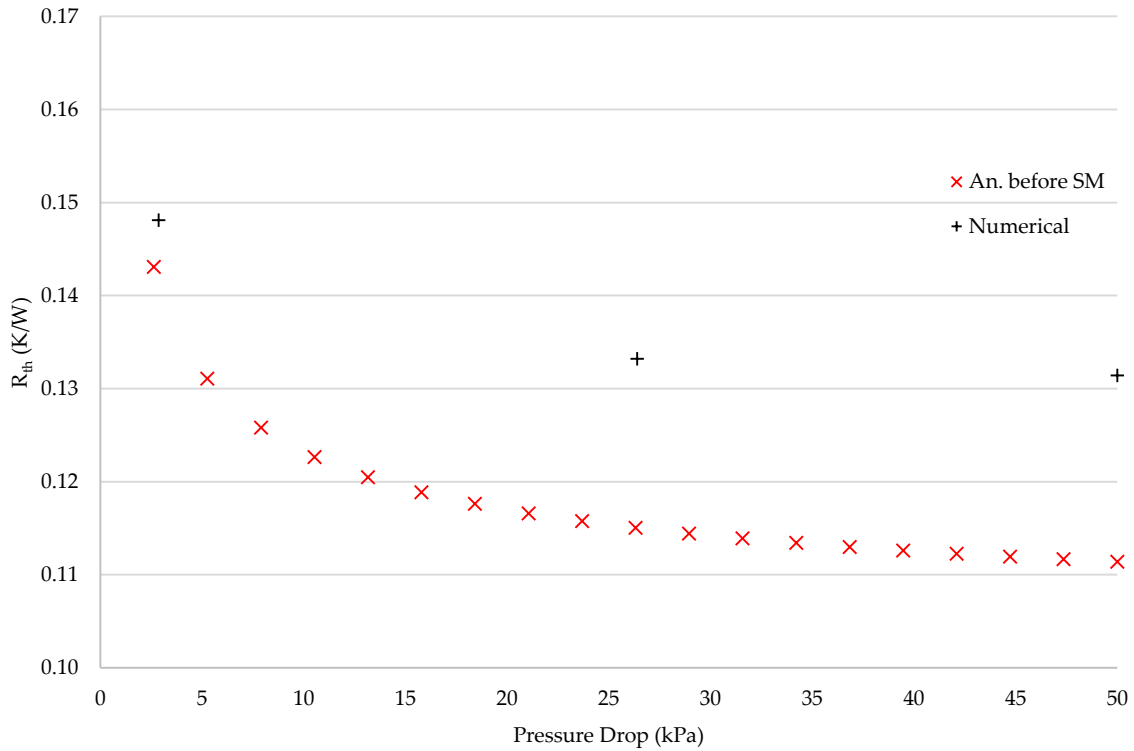


Figure 80: Comparison of thermal resistance between analytical and numerical results.

If equation (3.64) was applied to the results shown in Figure 80, a different value for  $\theta$  would be calculated at each point. In order to determine a single function that can effectively transform the analytical results across the entire range of pressure drops, a power law regression was used to determine the equation of the closest fitting lines of each set of results. These were  $R_{th} = 0.1494p^{-0.079}$  and  $R_{th} = 0.1547p^{-0.043}$  for the analytical and numerical

results respectively. Then by using equation (3.65) a pressure dependant transformation function can be ascertained:

$$\theta = 1.04p^{0.036} \quad (3.66)$$

$\theta$  is applied to equation (2.56) as follows:

$$R'_{tot,fo} = R_{tot,fo}\theta = \left( \frac{1}{2\rho C_p Q} + \frac{1}{k_{eff,s} m_{fo} A \tanh m_{fo} H} \right) \theta \quad (3.67)$$

The optimisation process is then repeated, this time minimising  $R'_{tot,fo}$ , instead of  $R_{tot,fo}$ , which would generate a new, more accurate Pareto curve. This process can be repeated as many times as is necessary to reach the required accuracy. The results after one SM iteration are shown in Figure 81. The graph shows a reduction in the average error of the calculated total thermal resistance from 10.76% to 1.74%. In this work, only a single iteration was required, as further iterations offered negligible improvements to the overall accuracy.

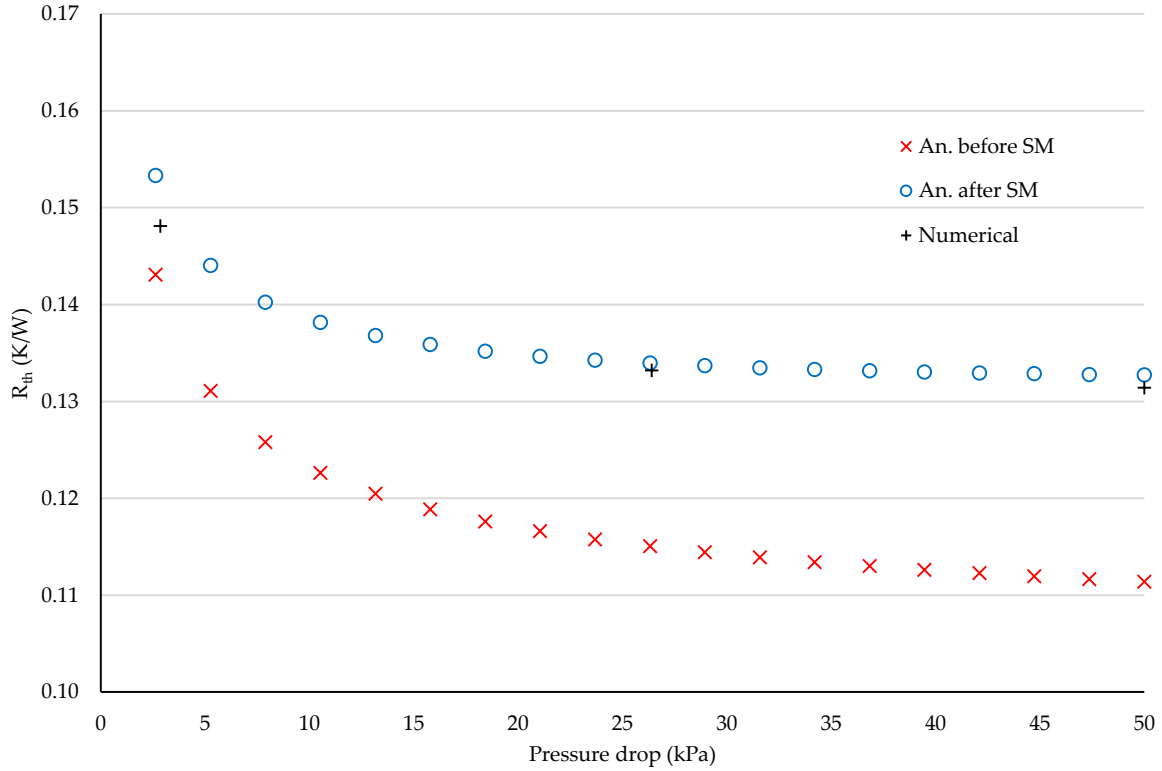


Figure 81: Optimisation results before and after SM procedure and reference numerical results.

### 3.4 Validation of SM algorithm

Two important assumptions have been made during the SM process that need to be validated. The first is presuming that the results shown in Figure 79 align well with the simulations. The assumption is that even if the analytical model has a lower accuracy at the lowest values of  $d_f$ , it still follows the thermal trends. Thus the configuration of  $d_f$ ,  $d_p$  and  $\varepsilon$  that produces analytically a minimum  $R_{th}$  for a given pressure drop, also produces the minimum  $R_{th}$  in reality. To verify that each value of  $R_{th}$  in Figure 79 is a minimum, foam 2 from Table 7 was tested. Keeping the pressure loss constant, the porosity was slightly increased and lowered, generating four new unique foams that should, in theory, perform less

well than foam 2. Properties for each foam can be seen in Table 9. The thermal resistance of all the foams was then calculated numerically, the results of which can be seen in Figure 82.

TABLE 9:

Properties of new foams to validate SM algorithm

Properties	Foam 2--	Foam 2-	Foam 2	Foam 2+	Foam 2++
Porosity	46%	49%	50.6%	52%	54%
Fibre diameter	0.074 mm	0.067 mm	0.064 mm	0.061 mm	0.058 mm
Pore diameter	0.264 mm	0.244 mm	0.236 mm	0.228 mm	0.221 mm

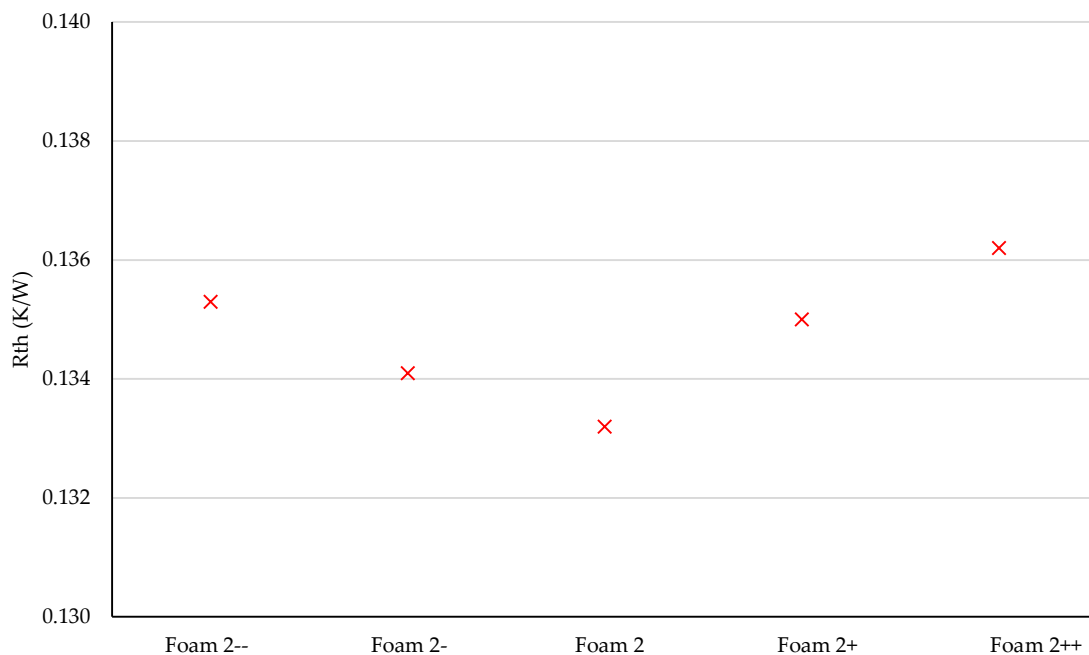


Figure 82: Thermal resistance of three foams with an imposed heat flux of 100 W, a flowrate of  $3.25 \times 10^{-6} \text{m}^3 \cdot \text{s}^{-1}$  and a pressure drop of 26.31 kPa.

The results show clearly that foam 2, generated by CADES using the analytical model proposed by this work, performs better than the variations. This suggests that the analytical model accurately predicts the thermal trends as the parameters of metal foam are varied. Thus an optimal foam generated by CADES using the analytical model will always have a minimum thermal resistance for the given inputs.

The second assumption made was that only three points are required to accurately represent the Pareto curve of the numerical simulations (Figure 80). Clearly more points would generate a more accurate curve, but would also require more simulation time, defeating the objective of an efficient analytical model. Thus, the assumption was tested by adding two additional numerical simulation points and calculating if there was a sizeable increase in accuracy or not. Using a power law regression again, a new equation of the closest fitting line of the numerical simulations was determined,  $R_{th} = 0.153p^{-0.041}$ . Applying this function to the analytical model gives the results shown in Figure 83. Using the additional

numerical simulations decreased the average errors between the thermal resistances from 1.74% to 0.96%. Though the results have improved, the difference is small and does not warrant the additional computing time required, especially when an average error of 1.74% is already sufficiently small.

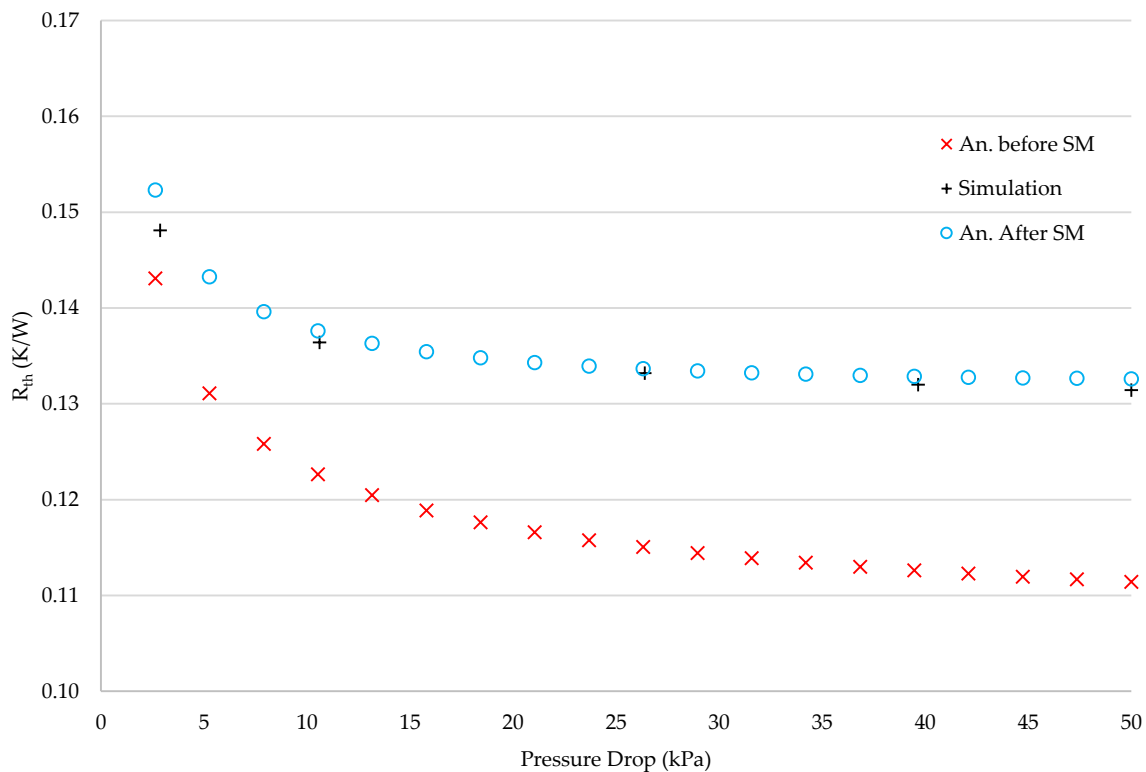


Figure 83: Optimisation results before and after SM procedure and reference numerical results, using additional points of comparison.

## 4. Foam/Microchannel Comparisons

Optimisation of the microchannel model was performed in the same way as for the metal foam model. Initially the channel width and fin width were both constrained to a minimum of 100 $\mu$ m as this value conforms to commonly available microchannels. The results showed that the thermal resistance would decrease with increasing pressure loss (as expected) until roughly 10kPa, beyond which the performance would steeply decline. It was discovered that during the optimisation process, the increased pressure drop was achieved by decreasing both the fin width and the channel width (thus increasing the number of channels). However, once the 100 $\mu$ m limit was reached, the only way to increase the pressure drop further was to increase the fin width, and thus decrease the number of channels. Pressure loss was increased, but as the heat exchange surface area was lowered, it was to the detriment of performance. Thus, a second optimisation was performed, this time extending the minimum fin and channel widths to 10 $\mu$ m. This time, thanks to the loosened constraints the fin and channel widths continuously decreased, and the number of channels continuously increased. It was deemed important to compare the metal foam performance with a microchannel that has reached a true optimum. This is however, somewhat unrealistic, as microchannels with fin widths of

10 $\mu\text{m}$  are uncommon and expensive, and require specialised manufacturing techniques to produce. The results of the microchannel optimisation process can be seen in Figure 84.

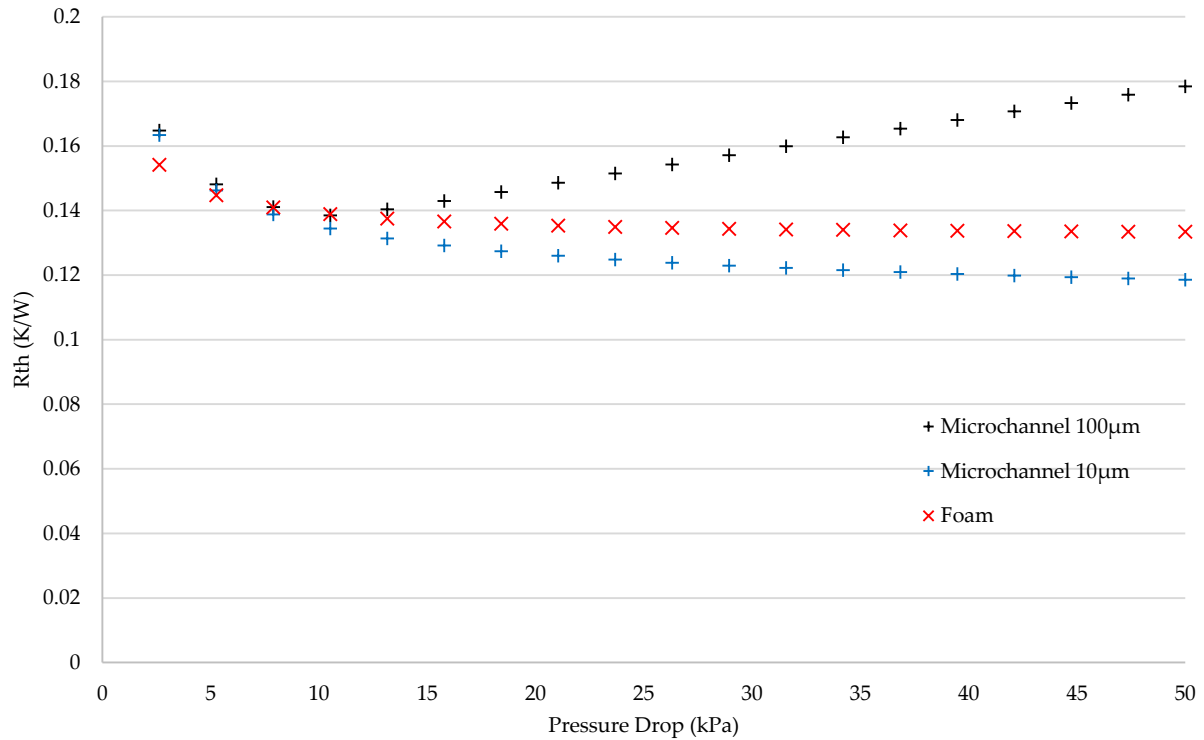


Figure 84: Minimised thermal resistance of metal foam and microchannel heat sinks with flowrate of  $3.25 \times 10^{-6} \text{m}^3 \cdot \text{s}^{-1}$ .

The results in Figure 84 show that at low pressures (<10 kPa), the thermal resistances of each heat sink are very similar. Above this value, the thermal resistance of the microchannels limited to 100 $\mu\text{m}$  are greater than the value of the metal foams. The microchannels limited to 10 $\mu\text{m}$  performed consistently better than the metal foam, having a 6.6% lower thermal resistance on average. As before, a selection of microchannels have been chosen at pressure losses of 2.63kPa, 26.31kPa and 50kPa for both the channels constrained to 100 $\mu\text{m}$  and of 10 $\mu\text{m}$ . Important parameters of each are shown in Table 10.

TABLE 10:

Properties of selected microchannels

Properties	100 $\mu\text{m}$			10 $\mu\text{m}$		
	1	2	3	1	2	3
Fin width	0.1mm	0.45mm	0.94mm	0.07mm	0.02mm	0.02mm
Channel width	0.17mm	0.1mm	0.1mm	0.16mm	0.05mm	0.04mm
No. of channels	37	18	10	58	128	177
$\Delta P$ drop	2.63kPa	26.31kPa	50kPa	2.63kPa	26.31kPa	50kPa

$R_{th}$	0.163K/W	0.154K/W	0.177K/W	0.161K/W	0.123K/W	0.118K/W
----------	----------	----------	----------	----------	----------	----------

The information in Table 10 highlights the problems that arose during the optimisation process. Initially the thermal resistance of the 100 $\mu$ m channels decreases when the pressure loss is increased (as is expected), but above 10 kPa the performance begins to drop, and the  $R_{th}$  value is larger at 50kPa than at 2.63kPa. This is because 10 kPa is the maximum pressure loss that the 100 $\mu$ m channels can generate whilst still increasing the surface exchange area. Pressure drops higher than this are achieved by reducing the number of channels, hence decreasing the surface exchange area and increasing the thermal resistance. To confirm this is the case, another test was performed with an increased flowrate. It is assumed that if the fluid flowrate were increased high enough (increasing the pressure drop), the constraints on the fin and channel width would be made irrelevant, and the results of both of the microchannels would coincide with one another. To test this, the flowrate was set to  $5 \times 10^{-5} m^3/s$  ( $u_{in} = 1m/s$ ) and the optimisation procedure was run again.

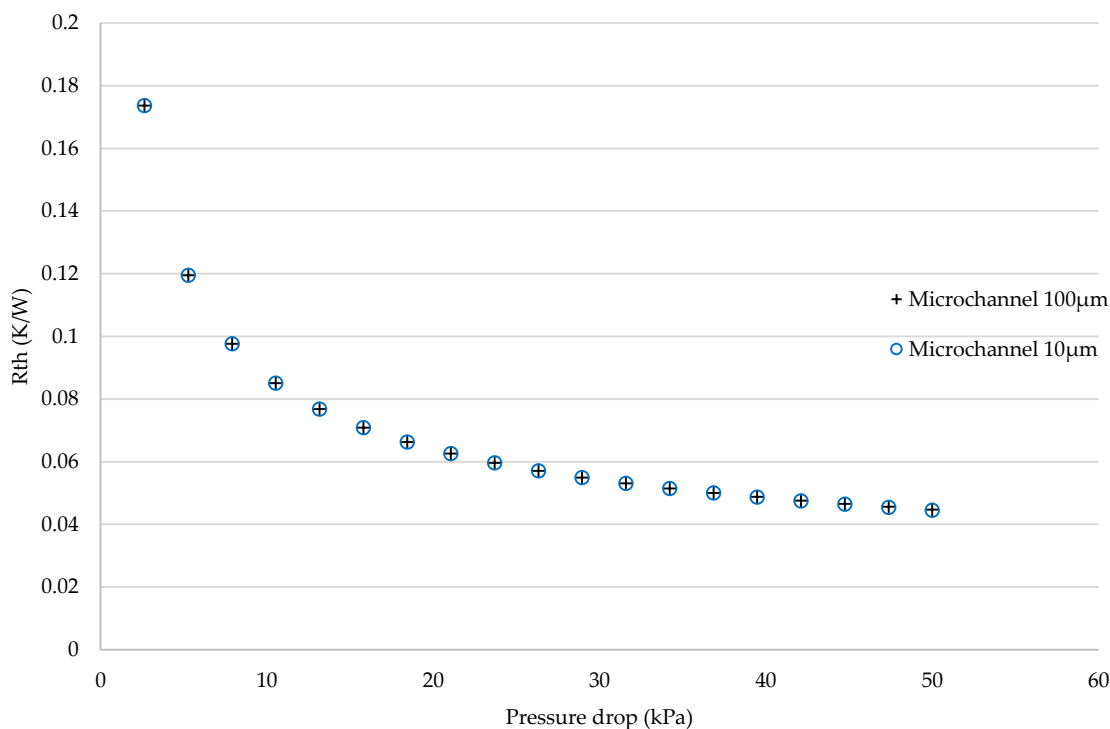


Figure 85: Minimised thermal resistance of microchannel heat sinks with flowrate of  $5 \times 10^{-5} m^3 \cdot s^{-1}$ .

As predicted, the results of the two differently constrained microchannels line up exactly. This is because at such an elevated flowrate, the optimum fin and channel widths are larger than 100 $\mu$ m in each case.

## 5. Conclusions

In this chapter, the analytical model outlined in Chapter 2 has been successfully used to optimise the geometry of metal foam in order to maximise heat transfer performance. This

is a validation of one of the aims of the present work, which was to show that the classic methodology for optimising microchannel heat sinks could be applied to metal foams. All that it required to generate an optimised foam is information regarding the operating conditions of the heat sink, such as which metal will be used, which fluid, the available pumping power, etc. The analytical model will then provide all the necessary data to fabricate the unique metal foam (fibre diameter, pore diameter, porosity, pore density). Following this, the issue of the loss of accuracy of the models results at elevated values of  $h_{sf}$  was addressed. By applying an SM algorithm, which calculated a transformation function  $\theta$ , to minimise the discrepancies between the analytical and numerical results, overall errors were reduced from 10.76% to 1.74%. Finally, the results were compared with the optimisation of microchannel heat sinks. The microchannel optimisation was performed twice, first with the channel width and fin width constrained to a minimum of  $100\mu\text{m}$  (common industry standard), then secondly with a minimum reduced to  $10\mu\text{m}$ . The results showed that when the constraints applied to the microchannels were loosened, they had consistently lower thermal resistances than the metal foam, however there are several important points that must be noted. Firstly, as previously mentioned, though by no means impossible to fabricate, microchannels having a fin width of  $10\mu\text{m}$  are uncommon and expensive, as they have very large form factors ( $>100$ ). Thus, specialised manufacturing techniques are required. Therefore, though they were shown to have a reduced thermal resistance, when compared with metal foams, in a real world application they may fall outside of financial and/or manufacturing constraints. In contrast, there are several, inexpensive fabrication methods (power sintering, space holder, lost carbonate sintering) that could produce the optimised metal foams.

In the final chapter of this project, the design and assembly of a new test bench will be presented, having applications in thermodynamics and fluid mechanics beyond the use within the present work. The fabrication of the test section, and metal foam and microchannel samples will also be outlined. Finally, the experimental results will be discussed and compared to the previously shown analytical and numerical work.

## 6. Bibliography

- [63] L. Encica, J. Paulides and E. Lomonova, "Space-Mapping Optimization in Electromechanics: An Overview of Algorithms and Applications," *The International Journal for Computation and Mathematics in Electrical and Electronic Engineering*, vol. 28, n° 15, pp. 1216-1225, 2009.
- [64] J. W. Bandler, Q. S. Cheng, S. A. Dakroury, A. S. Mohamed, M. H. Bakr, K. Maden and J. Sondergaard, "Space Mapping: The State of the Art," *IEEE Transactions on Microwave Theory*, vol. 52, n° 11, pp. 337-361, 2004.
- [65] S. Vivier, D. Lemoine and G. Friedrich, "Fast Optimization of an IPMSM with Space Mapping Technique," *2011 IEEE Energy Conversion Congress and Exposition*, Phoenix, 2011.



---

# CHAPTER 4

---

## EXPERIMENTAL VALIDATION AND RESULTS ANALYSIS

---

### Table of Contents

<b>1. INTRODUCTION.....</b>	<b>101</b>
<b>2. EXPERIMENTAL SETUP .....</b>	<b>101</b>
2.1 TEST LOOP.....	101
2.2 EXPERIMENTAL CONTROLS.....	104
2.2.1 Coolant flow.....	104
2.2.2 Coolant inlet temperature .....	104
2.2.3 Internal vacuum pressure .....	104
2.3 EXPERIMENTAL MEASUREMENTS .....	104
2.3.1 Temperatures .....	104
2.3.2 Pressure loss.....	104
2.3.3 Flow rate .....	105
2.3.4 Data logger .....	105
2.4 EXPERIMENTAL PROCEDURE .....	105
<b>3. HEAT SINKS .....</b>	<b>106</b>
3.1 MICROCHANNEL SAMPLE .....	108
3.2 METAL FOAM SAMPLES .....	108
3.2.1 Cutting foam samples.....	108
3.2.2 X-ray microtomography.....	109
3.2.3 Attaching copper foam to copper plate.....	111
<b>4. TEST SECTION.....</b>	<b>112</b>
4.1 FULLY DEVELOPED FLOW .....	115
4.2 ENSURING TEST SECTION IS WATERTIGHT .....	118
<b>5. EXPERIMENTAL RESULTS .....</b>	<b>121</b>
5.1 MEASURING INTERFACE THERMAL RESISTANCE.....	121
5.1.1 Interface thermal resistance test .....	121
5.1.2 Interface thermal resistance results.....	124
5.2 TIME REQUIRED TO REACH THERMAL STABILITY .....	125
5.3 MICROCHANNEL RESULTS.....	126
5.4 METAL FOAM RESULTS .....	129
5.5 POTENTIAL ERRORS ANALYSIS .....	132

6. CONCLUSION ..... 134

## 1. Introduction

Thus far, this work has remained largely theoretical. In chapter 2 an analytical model was derived that can predict the thermal and hydraulic performances of metal foam heat sinks with various internal geometries. In that same chapter the model was validated with numerical simulations. However, it was also explained that Fluent is unable to solve the full fluid and solid energy equations on a large scale due to the complexity of foam, and as such volume averaged versions of the equations are used instead. This calls into question the results of the simulations, and by definition the results of the analytical model as well, and thus it was decided that an experimental test bench will be developed that can measure the thermal and hydraulic performances of various heat sinks (metal foam and microchannel). This chapter therefore begins by describing the test bench that was developed and the components that comprise it. This is followed by a look at the heat sinks that were fabricated for testing as well as the test section that houses them. The experimental results are then presented and compared with the predictions of the analytical model, and finally the conclusions that can be drawn from the results are explained.

## 2. Experimental Setup

### 2.1 Test loop

The test loop is a closed system that incorporates a multitude of components to test the thermal and hydraulic characteristics of a small heat sink with an imposed heat flux of  $\Phi_0$ , being traversed by a liquid coolant. When designing the test loop it was important to be cognisant of which parameters needed to be measured, as this dictates many of the design decisions. In chapter 3 the overall thermal resistance  $R_{tot}$  was used to draw distinctions between the metal foam and microchannel heat sinks, and was minimised during the optimisation process with respect to  $\Delta p$ , the pressure drop. Recalling from chapter 2:

$$R_{tot} = (\langle T_0 \rangle - T_\infty) / \Phi_0 \quad (2.42)$$

where  $T_\infty$  is the fluid temperature at the inlet and  $\langle T_0 \rangle$  is the average solid temperature at the base of the foam/microchannels. It is expected some amount of the imposed heat flux will be lost to the atmosphere. The methods employed to limit this will be explained later in the chapter, however it can already be stated that the actual heat flux that passes through the heat sink and into the fluid must be measured. Recalling from chapter 2 again:

$$\Phi_0 = \rho C_p Q (T_f(L) - T_\infty) \quad (2.39)$$

where  $\rho$ ,  $C_p$ ,  $Q$  and  $T_f(L)$  are the fluid density, specific heat, volumetric flow rate and temperature at the outlet of the heat sink respectively. Thus, in order to make comparisons with the analytical model and numerical simulations, the test loop must be able to measure  $\langle T_0 \rangle$ ,  $T_\infty$ ,  $T_f(L)$ ,  $Q$  and  $\Delta p$ . Figure shows a schematic diagram of the test loop, and Figure 89 shows a photo of the assembled test loop.

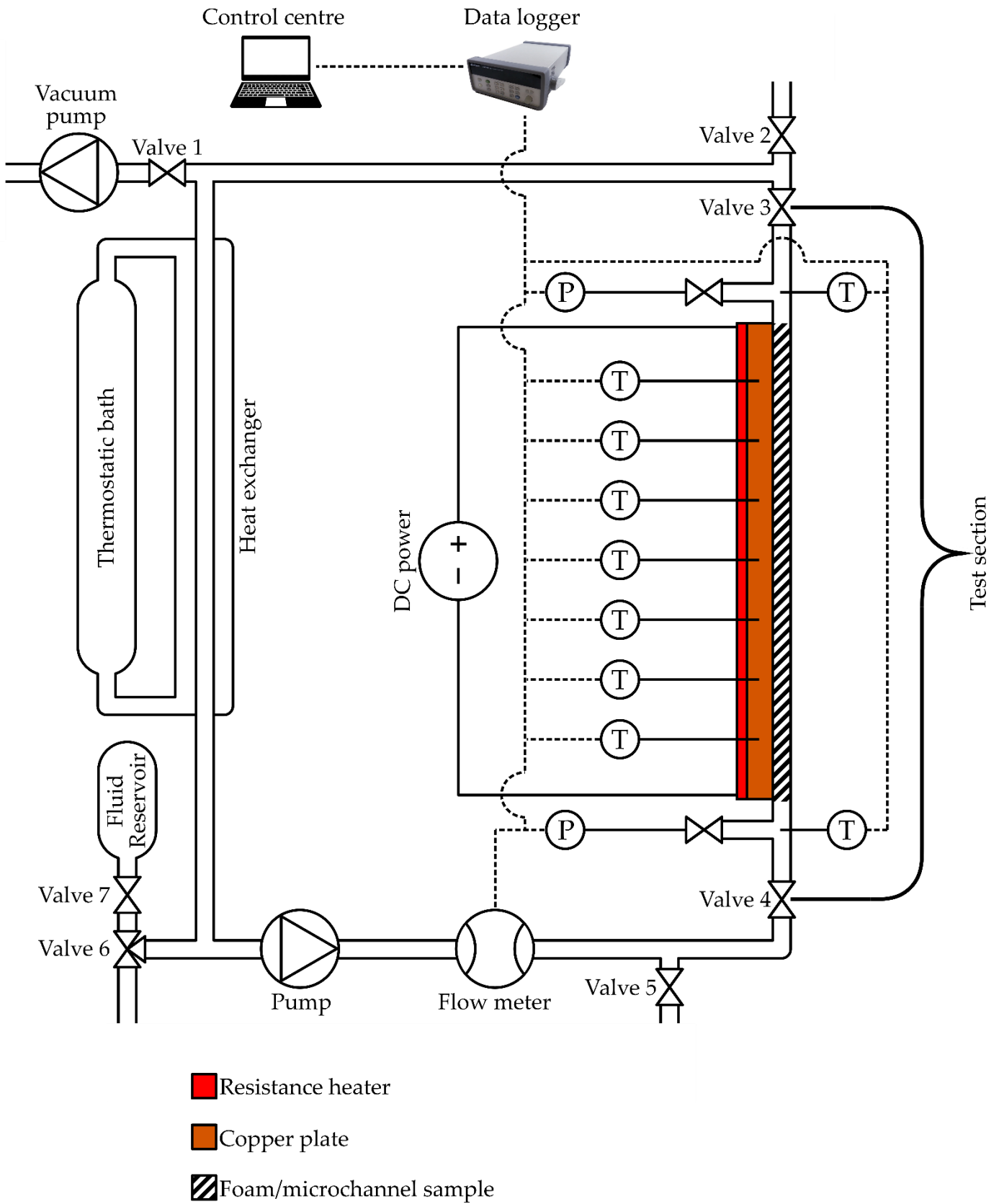


Figure 88: Schematic representation of test loop.



Figure 89: Assembled test loop.

The different elements of this setup are the following:

- |   |   |
|---|---|
| 1a./1b. Vacuum pump and pressure sensor.    | 8. Valve 5: purges test loop.                     |
| 2. Valve 1: isolates loop from pump.        | 9a/9b. Flow meter and digital display.            |
| 3. Valve 2: removes air bubbles.            | 10. Flow pump.                                    |
| 4a/4b. Valve 3 and 4: isolates test section | 11. Fluid reservoir.                              |
| 5. Test section.                            | 12a./12b. Valve 6 and 7: fills loop with coolant. |
| 6. Pressure sensor.                         | 13a/13b. Fluid cooler and heat sink.              |
| 7. Resistance heater power source.          | 14. Data logger.                                  |

Between valves 3 and 4 is a detachable portion of the loop where test sections of various sizes can be placed. It is for this reason that the experiment will continue to be used beyond the scope of the current work.

## 2.2 Experimental controls

The setup shown in Figure and Figure 89 uses several actuators that control critical functions and allow the experiment to run.

### 2.2.1 Coolant flow

To generate a constant flow rate of the coolant, an Ismatec MCP-Z gear pump was used. This is a calibrateable dispensing pump, with memory for storing up to four sets of operating parameters. It has an operating range of 1-7020 ml.min<sup>-1</sup>.

### 2.2.2 Coolant inlet temperature

To keep the coolant at a constant inlet temperature the Huber CC-415 Circulator Bath was used. This is a heating and cooling machine with an operating temperature range of -40°C to 120°C, a heating capacity of 1.3 kW to 1.6 kW, and a cooling capacity of 1.2 kW to 0.05 kW. An external sensor, measuring the fluid temperature just before entering the heat sink, controls the bath regulation in order to monitor the inlet temperature of the test section.

### 2.2.3 Internal vacuum pressure

When filling the test loop (see Appendix), first the internal pressure is lowered. This was achieved using an Edwards XDS5 dry scroll vacuum pump, which is designed for pumping condensable vapours and uses materials selected for a wide range of laboratory wet chemistry applications. It has an ultimate vacuum of  $6 \times 10^{-2}$  mbar.

## 2.3 Experimental measurements

Several different kinds of sensors were used in order to measure  $\langle T_0 \rangle$ ,  $T_\infty$ ,  $T_f(L)$ ,  $Q$  and  $\Delta p$ . These are all shown in Figure and Figure 89 and will now be described in detail.

### 2.3.1 Temperatures

To measure the fluid temperature at the inlet and the outlet,  $T_\infty$  and  $T_f(L)$ , Type K thermocouples (Nickel-Chromium / Nickel-Alumel) were placed into the flow just before and just after the heat sink. Type K thermocouples (Nickel-Chromium / Nickel-Alumel) are the most common type of thermocouple. They are inexpensive, accurate, reliable, and have a wide temperature range.

To measure the average temperature at the base of the metal foam/microchannels,  $\langle T_0 \rangle$ , Type T thermocouples (Copper/Constantan) were embedded into the copper plates that they were attached to. Type T thermocouples are very stable and are often found in laboratory environments.

Both types of thermocouples have suitable temperature ranges and accuracies to be used interchangeably to measure either the fluid or solid regions of the experiment. Therefore, other factors were used to decide which to use for each task.

### 2.3.2 Pressure loss

The pressure loss across the heat sinks was measured using a Deltabar S PMD75 differential pressure sensor. It has a piezo-resistive sensor and welded metallic membrane that is used in all industries for continuous measurement in liquids, vapours and gases. It is

sold as having good reliability and repeatability, with an accuracy of 0.05% and a pressure range of -50kPa to 50kPa. As during the theoretical analysis section of this project, the applied pressure drop never exceeded 50kPa, the Deltabar was deemed suitable.

### 2.3.3 Flow rate

To measure the coolant flow rate a Micro Motion™ CMFS015 Coriolis flow meter was used, in conjunction with a Micro Motion™ 1700 flow transmitter. A Coriolis flow meter relies on a practical application of the Coriolis Effect, where a vibration of the flow tube is induced as the fluid passes through. Sensors monitor this vibration and analyse changes in frequency, phase shift, and amplitude. At zero flow, the two tubes vibrate in phase with each other. When flow is introduced, the Coriolis Effect causes the tubes to twist, resulting in a phase shift. The time difference between the phases of the vibrations is measured and is directly proportional to the mass flow rate. The volume flow rate can also be calculated from the measured mass flow rate and density. Information on the flow meter accuracy and repeatability, provided from the manufacturer, can be seen in Table 12.

TABLE 12:

Parameters of Coriolis flow meter

Performance specification	CMFS015
Flow rate range	0 – 330 $kg \cdot h^{-1}$
Mass/volume flow accuracy	$\pm 0.10\%$ of rate
Mass/volume flow repeatability	0.05% of rate
Density accuracy	$\pm 0.0005g/m^3$ ( $\pm 0.5kg \cdot m^{-3}$ )
Density repeatability	$\pm 0.0002g/m^3$ ( $\pm 0.2kg \cdot m^{-3}$ )

### 2.3.4 Data logger

To record the results during an experiment, all thermocouples were connected to a Keysight 34972A data logger, which is capable of monitoring multiple channels over extended periods of time. It offers  $6\frac{1}{2}$  digits of resolution and 0.004% dcV accuracy. It was paired with a 20-channel relay multiplexer and was programmed to make 100 temperature readings at a rate of one reading per three seconds. Thus, an average temperature for each thermocouple could be calculated, with small anomalies having a negligible impact.

## 2.4 Experimental procedure

The following is an account of each of the steps required to run a typical experiment. Information regarding filling and purging the test loop can be found in the Appendix.

Running an experiment:

- Flow rate is controlled using the pump in conjunction with the flow meter. The rpm of the pump is selected and the flow meter gives a reading in kg/h. In such a way, the rpm can be slowly increased/decreased until the desired flow rate is reached.

- The power source for the resistance heater is set to a voltage of 54.77V and a current of 1.83A. As the resistance heater has a resistance of 30  $\Omega$ , this corresponds to a power of 100W.
- The thermostatic bath is programmed to cool the hot fluid that comes from the heat sink down to 300K, thus maintaining a constant fluid inlet temperature.
- The data logger records the solid and fluid temperatures and displays them in real-time on the computer.
- The real-time temperature readings indicate when the system has stabilised each time the flow rate is adjusted.
- A period of 2 hours was required for the system to stabilise. The determination of this time is described later in this chapter.
- The seven solid temperatures and two fluid temperatures are then averaged, giving an experimental value for  $\langle T_0 \rangle$  and  $\langle T_f \rangle$ .
- The pressure sensor then provides the corresponding value for  $\Delta p$ .

### 3. Heat Sinks

Two heat sinks were fabricated for use within this work, one using microchannels, and the another using metal foam. In both cases the samples had the same outer dimensions,  $10\text{ mm} \times 5\text{ mm} \times 40\text{ mm}$  for the foam/microchannel portion, attached to a copper plate  $10\text{ mm} \times 2\text{ mm} \times 40\text{ mm}$ . The thickness of the copper plate was dictated by two factors, the first being that it needed to be as thin as possible to limit heat transferring laterally along its length. Lateral heat transfer would mean the density of the flux passing into the fluid would be dependent on the position along the heat sinks length, and would mean that the fluid temperature would not increase linearly, as has been assumed. The second factor is the need to measure the temperature at the base of the metal foam/microchannels. As was previously mentioned, thermocouples were embedded into the plate. Ideally they would be placed at the interface, however this was not possible to achieve without either compromising the connection between the two parts, or disturbing the fluid flow. By looking at similar experiments carried out within the literature [66] [32] [67], the agreed upon solution is to move the thermocouples away from this boundary region, and embed them into the metal plate. To do this, 1mm holes needed to be cut into the plate, which restricted its minimum thickness to 2mm. The holes were evenly spaced 5 mm apart from one another, and were cut on alternate sides of the plate. This is because their presence creates an additional resistance to lateral heat transfer, which therefore needed to be symmetrical. The even spacing means that an average temperature can be calculated, and also means that the temperature profile along the length of the heat sink can be analysed. A diagram of this can be seen in Figure 90.

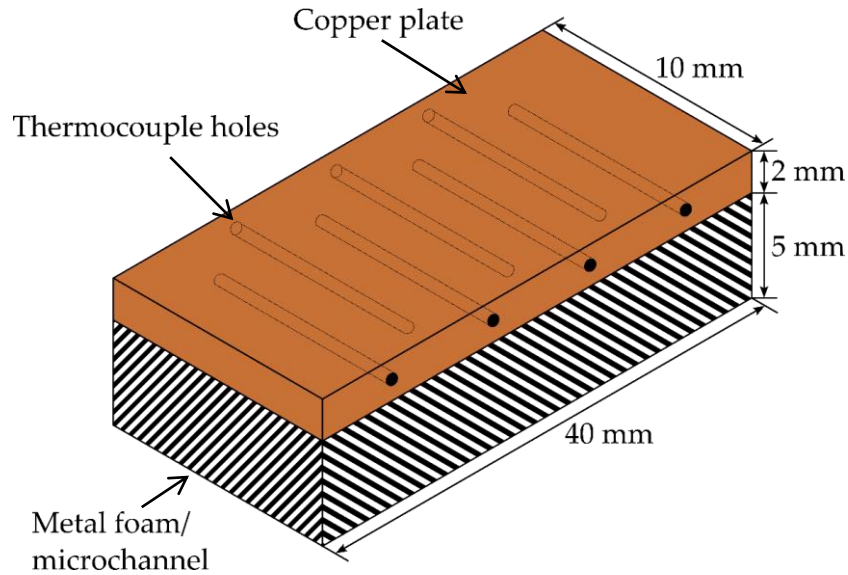


Figure 90: Diagram of heat sink sample attached to copper plate.

As can be seen in Figure 90, the thermocouple holes are cut to overlap one another, but not pass right through the plate. Each hole is 7.5mm in length. Placing the thermocouples away from the boundary between the foam/microchannels and the metal plate relies on the assumption that the temperature variation across the thickness of the plate is negligible. When using the equation for heat transfer by conduction with a power of 100W, the calculated temperature difference from the edge of the plate to its centre (thermocouple location) was roughly 0.5K. When comparing this to the expected increase in value of  $\langle T_0 \rangle_{fo}$ , calculated numerically in chapter 2 (10K – 90K), the discrepancy created by the location of the thermocouples can be neglected. To complete the samples, a resistance heater from Captec company was then attached to the top of the copper plate to provide 100W of power to the heat sinks. This is an ultra-thin (0.5 mm) flexible copper plate, electrically insulated on one side by a layer of Kapton. The heated section has the same dimensions as the surface of the heat sinks (10 mm × 40mm), and it has a resistance of 30 Ohms. The normal max temperature of the heater is 120°C, however when compressed between two solid surfaces, this increases to 200°C, well within the anticipated maximum temperature during an experiment. An advantage of this heater is that its resistance is independent of temperature, thus supplied voltage and current need not be adjusted during an experiment to keep the power output constant.

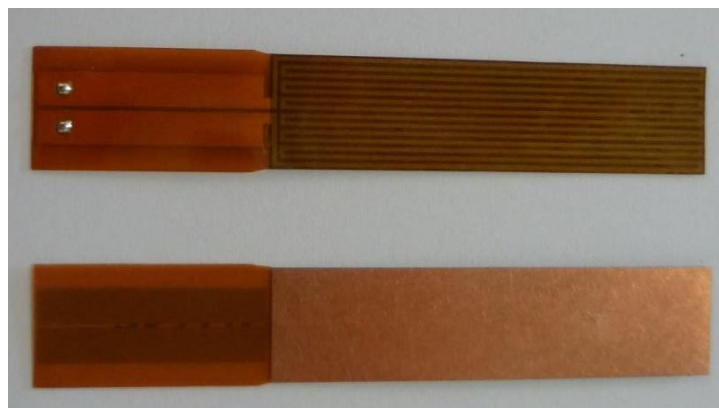


Figure 91: Captec resistance heater.

### 3.1 Microchannel sample

The microchannel sample was machined from a single solid piece of copper in the G2Elab workshop, and as such there was no need to attach it to a separate plate of copper. It has four channels, a fin width  $w_f = 1.5 \text{ mm}$ , a channel width  $w_c = 1 \text{ mm}$ , and a channel aspect ratio  $\alpha = 5$ . Constraints in the available manufacturing techniques restricted how small the channels could be made. It is therefore a minichannel, rather than a microchannel. A diagram of the sample can be seen in Figure 92.

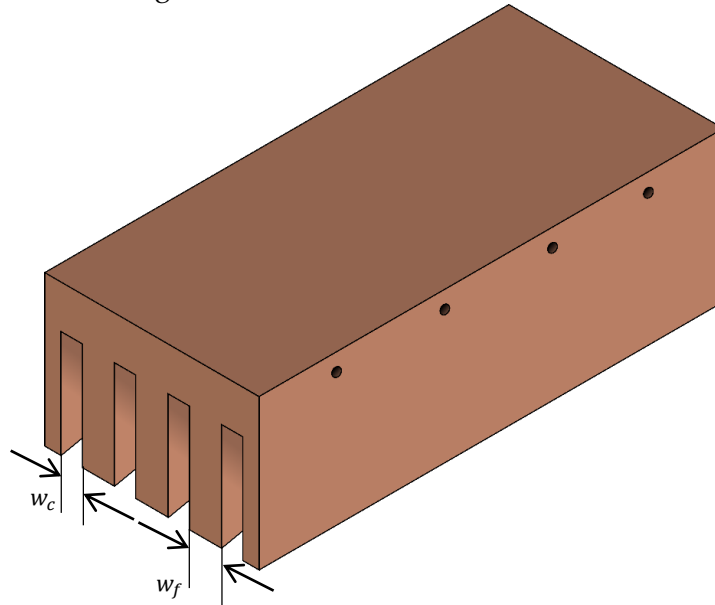


Figure 92: Microchannel sample.

### 3.2 Metal foam samples

Two different foams samples were purchased, the Duocel™ and Versarien™ copper foams discussed in chapter 1. Unfortunately, due to time constraints, only the Duocel™ foam was tested upon. As the details of the foams provided by the manufacturers were somewhat lacking (porosity and pore density), it was necessary to measure at least the fibre diameter. This would allow the other parameters (pore size, permeability and specific surface area) to be calculated. It was decided that x-ray microtomography ( $\mu\text{CT}$ ) would be used on small samples of foam to make these measurements. It was therefore first necessary to cut the Duocel™ foam, which is sold in sheets, into smaller samples.

#### 3.2.1 Cutting foam samples

Cutting the metal presented a problem. Using typical machine methods, such as saw blades, caused the ends of the foam fibres to bend and deform as they were cut, thus changing the microstructure in an irregular fashion. Thus, it was decided to use electrical discharge machining (EDM). This is a metal fabrication process that removes material from the work piece by using a series of rapidly recurring current discharges between two electrodes [68]. The advantage of this method is that it is capable of cutting through metal without the direct application of a force, thus the metal foam fibres are undisturbed.

### 3.2.2 X-ray microtomography

Once the foam had been cut into appropriately sized samples, they could be used in the  $\mu$ CT process. This is a method of taking cross-section images of a solid object, without destroying the original source. Imaging software (ImageJ) is then used to combine the 'stack' of individual images (~1300) into a virtual 3D model of the object, which can then be mathematically analysed and measured in a variety of ways. The dimensions of the section of foam that would be tested are constrained by the required quality of the images. For the current purposes, a maximum voxel size of  $6\mu\text{m}$  was allowed. This corresponding to a source object of size  $4\text{ mm} \times 4\text{ mm} \times 5\text{ mm}$ . The resulting 3D image of the Duocel™ foam from the  $\mu$ CT process can be seen in Figure 93.

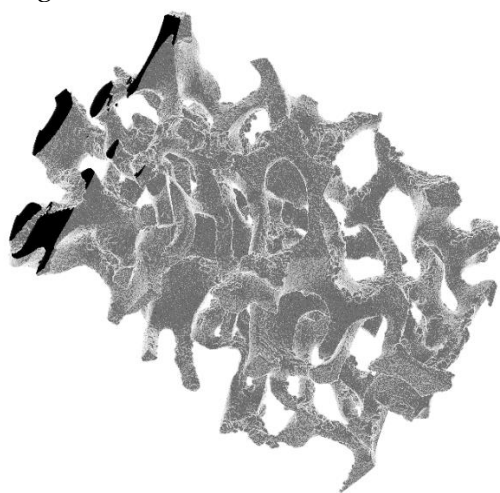


Figure 93: 3D image of Duocel™ copper 91% porosity foam.

The first step in measuring the foam properties is to convert each image into binary. This is so that the imaging software knows where the limits of the solid foam surface are. An example of this process is shown in Figure 94, where the porosity is black and the solid phase is white.

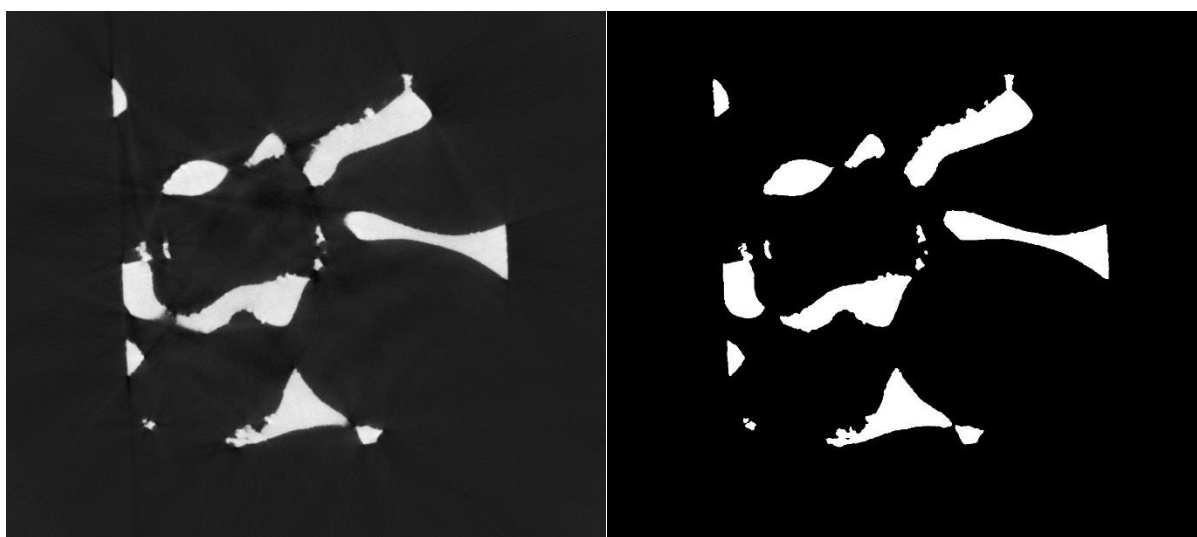


Figure 94: Standard 8-bit slice (left) of Duocel™ foam and the same image converted into binary (right)

Finally, a plugin called 'local thickness' is used to measure the average diameter of the foam fibres. To do this, circles are grown throughout the solid (white) portion of each images. They are grown to the maximum possible size, whilst being contained within the solid phase. Thus, the diameter of the circle corresponds to the diameter of the foam fibre at that point, this can be seen in Figure 95.

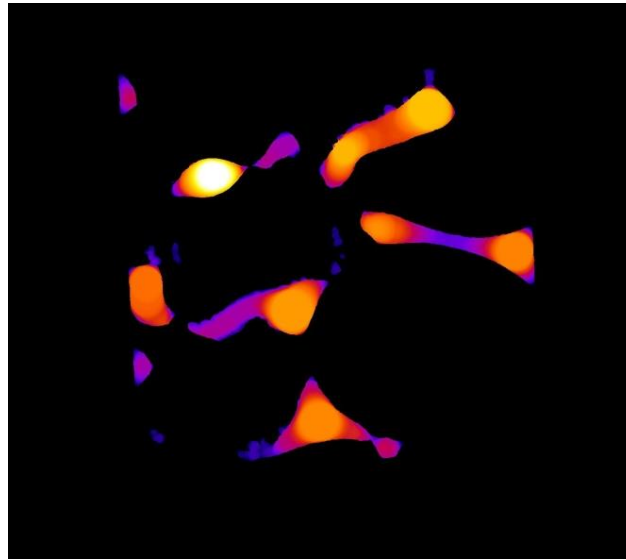


Figure 95: Circles grown within solid part of image. 'Hotter' colours represent the largest diameters.

This process is carried out at every position for each image and the results are made into a histogram of fibre diameters, which can be seen in Figure 96.

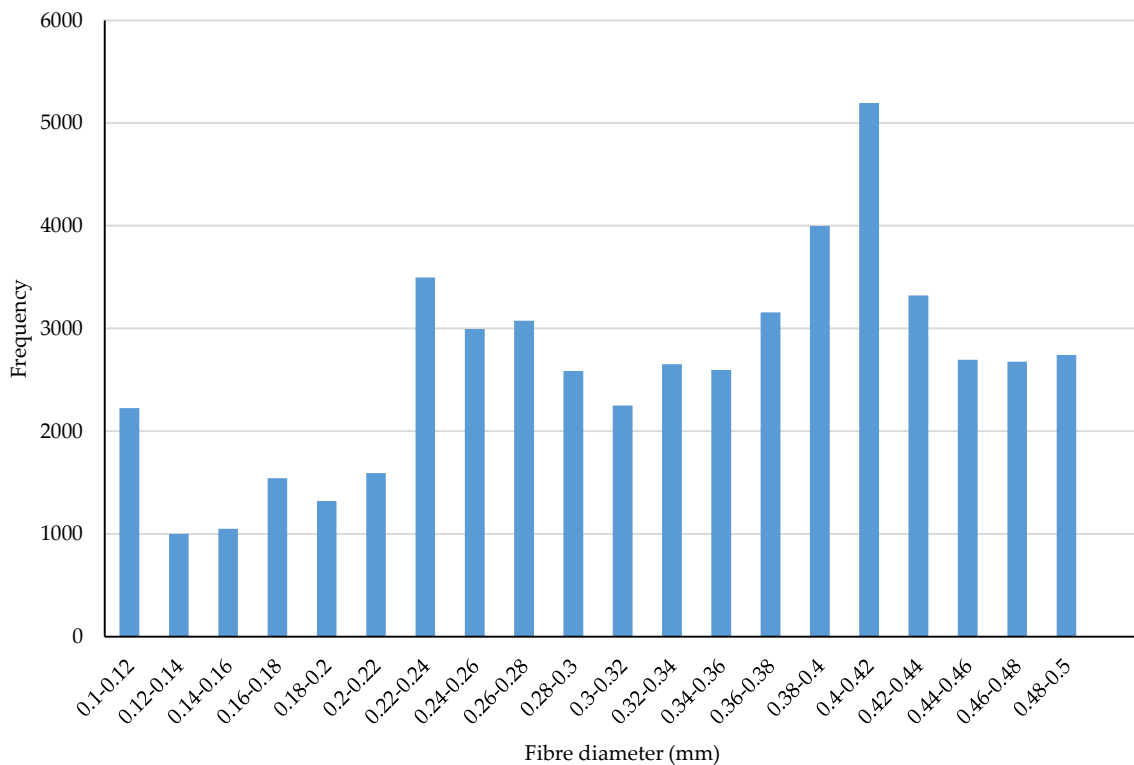


Figure 96: Histogram of fibre diameters of Duocel™ 91% porosity copper foam.

From the data shown in Figure 96 an average fibre diameter of 0.33 mm was calculated, which was then used to find the remaining parameters shown Table 13.

TABLE 13:

Duocel™ foam parameters	
Parameter	Duocel™
Porosity $\varepsilon$	0.91
Fibre diameter $d_f$	0.33 mm
Pore size $d_p$	2.55 mm
Specific surface area $A_{sf}$	1220 m <sup>-1</sup>
Permeability $K$	7.93 × 10 <sup>-8</sup> m <sup>2</sup>

Once the Duocel™ foam had been characterised, it was then attached to a copper plate, thus completing the heat sink.

### 3.2.3 Attaching copper foam to copper plate

The foam and plate were attached by brazing them together using a SAC305 brazing paste. The paste was applied to the surface of the copper plate, the foam was put in place, and the two were compressed together using the system shown in Figure 97.

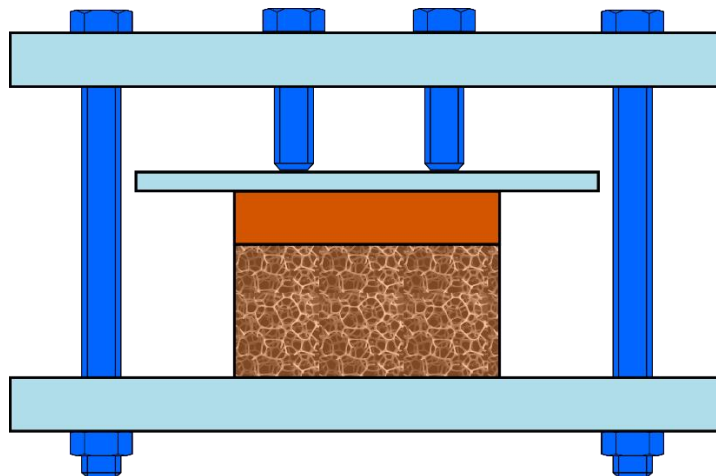


Figure 97: Device used to compress copper plate and copper foam together.

The entire assembly was then placed into a brazing oven, which first applies a vacuum before heating. The sample underwent the following temperature profile:

- A ramp of 63.33°C/min until a temperature of 210°C was reached. This is relatively slow for brazing but allows the solvents to evaporate and to avoid thermal shocks,
- 210°C maintained for 6 min to allow each of the components to reach the same temperature,

- A ramp of  $6.67^{\circ}\text{C}/\text{min}$  until a temperature of  $270^{\circ}\text{C}$  was reached. This is to achieve a temperature higher than that of the fusion point of the paste,
- A slope of  $24^{\circ}\text{C}/\text{min}$  until room temperature was reached.

This method produced an excellent connection between the copper cubes and foam that did not break even when large forces were applied. As such, it was also the chosen method for attaching the resistance heater to the copper plate. It is important to note that, as with any interface, there is an associated thermal resistance. Later on in this chapter, there is a description of the tests carried out to characterise this resistance.

## 4. Test Section

A custom-made test section was designed and manufactured for this experiment. Before the design phase began, the principle requirements and constraints were listed, so as to provide a basis for the initial concepts; they are as follows:

- Must contain a rectangular channel of cross-section 5mm by 10mm.
- Channel must be long enough that the flow is fully developed before entering sample.
- Must house the foam/microchannel sample and heat source.
- Must house thermocouples and pressure sensors.
- Must fit within the test loop.
- Must be watertight.
- Must be as thermally insulated as possible.

With these constraints in mind, it was decided that a channel of the required dimensions would be cut into a solid block of Teflon. Teflon was chosen for its low thermal conductivity ( $0.25 \text{ Wm}^{-1}\text{K}^{-1}$ ), which would help to insulate the heat sink from the exterior environment. A second piece of Teflon would then be placed on top of the first as a cover, creating the roof of the channel. These two pieces were compressed together between two plates of aluminium, which would in turn be bolted together. The foam or microchannel sample and resistance heater would then fit into the Teflon channel. Schematic diagrams of the test section can be seen in Figure 98 and Figure 99. They show a to-scale, front and side view of the test section. Two holes were drilled into the front and back of the channel, allowing the test section to be connected to the test loop. Four more holes were drilled into the base of the channel, two for the thermocouples and two for the pressure sensor to measure the fluid temperature and pressure respectively at the inlet and outlet of the heat sink. Seven holes were drilled into the sides of the cover; these align with those drilled into the copper plate and are for the thermocouples used to measure the solid temperature. Finally, a last hole was drilled into the top of the cover for wires that power the resistance heater.

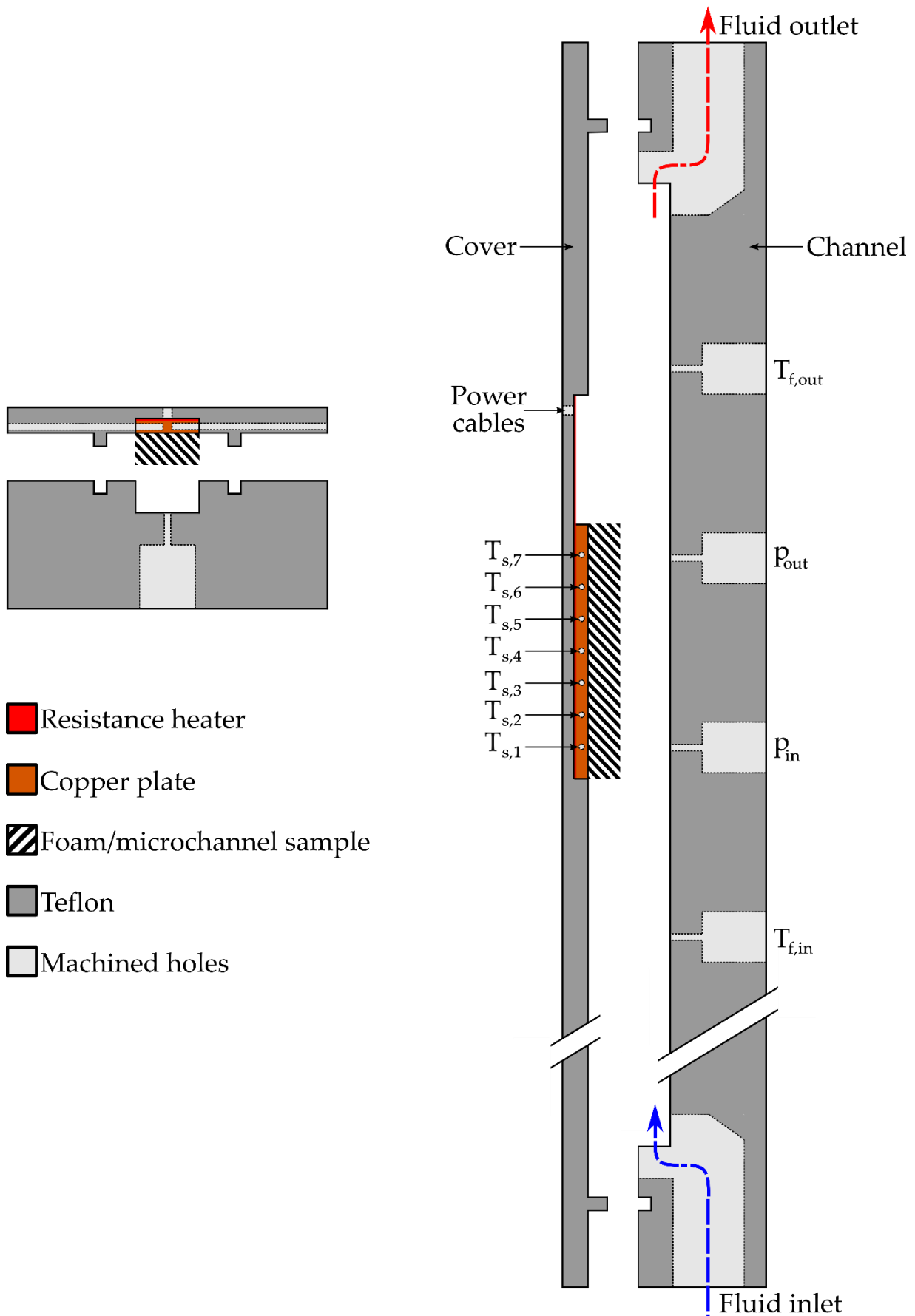


Figure 98: Front (left) and side (right) plan of experimental test section.

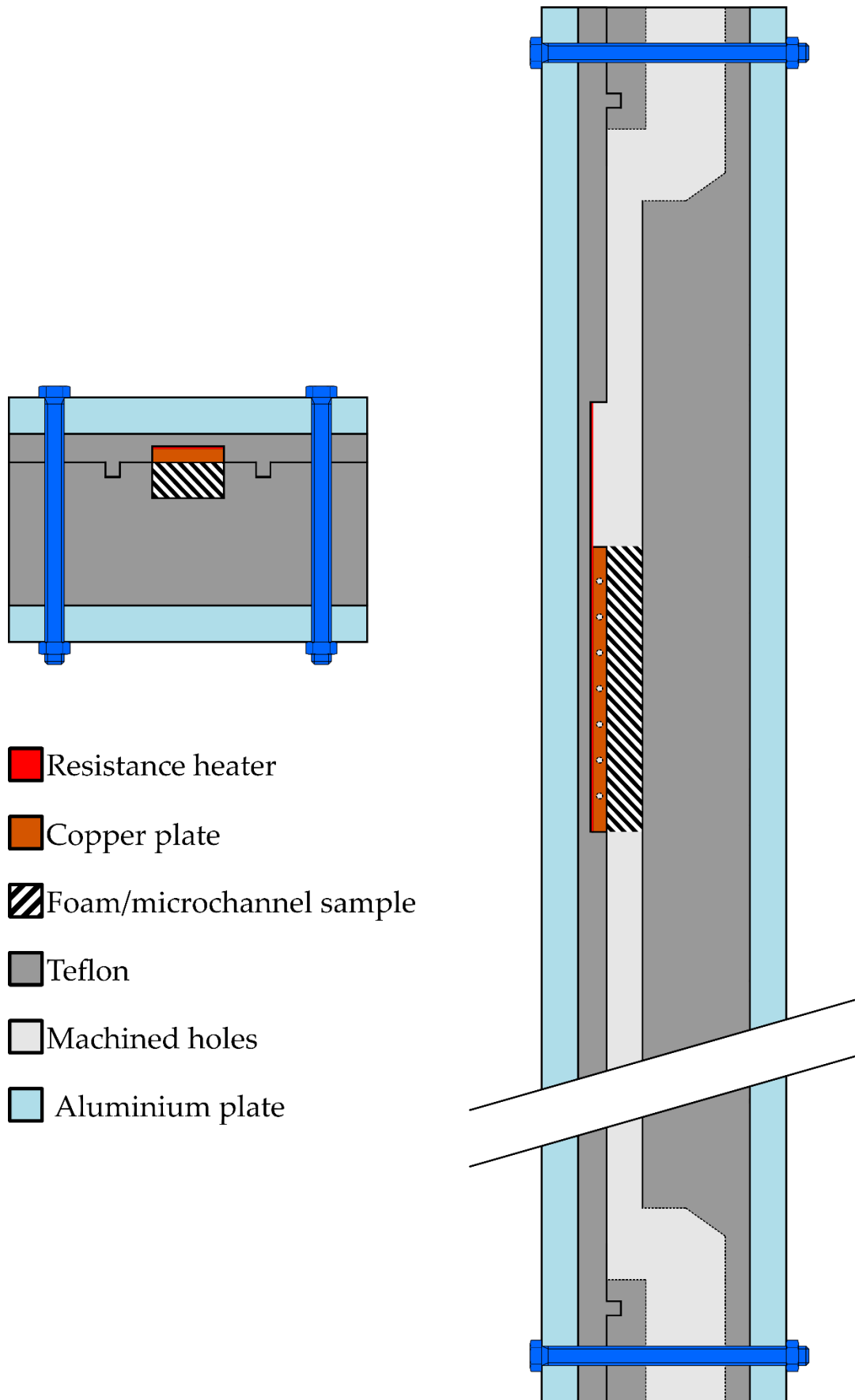


Figure 99: Method of closing test section from the front (left) and the side (right).

The two constraints that required the most attention were the need for the channel to be sufficiently long, such that the fluid becomes fully developed, and the need for the test section to be watertight. How these two issues were overcome is explained next.

#### 4.1 Fully developed flow

It is important that the fluid flow within the channel, prior to entering the foam, reach a hydrodynamically fully developed state. This is to avoid any erroneous results caused by an unstable flow. When the fluid first enters the channel, it is comprised of two distinct regions: the boundary layer, where viscous effects and velocity changes are significant, and the inviscid core, where they are negligible. As the fluid moves along the length of the channel, the boundary layers thickness increases from zero, until it eventually reaches the centre of the channel, becoming the only flow region [69]. After this point, the velocity profile is fully developed, and no longer changes with respect to the length of the channel, thus the following is true:

$$\frac{\partial u(r, z)}{\partial z} = 0 \quad (4.68)$$

where  $r$  is the rotational flow direction and  $z$  is the direction along the length of the channel. An example of how flow develops along the length of a channel can be seen in Figure 100 [69].

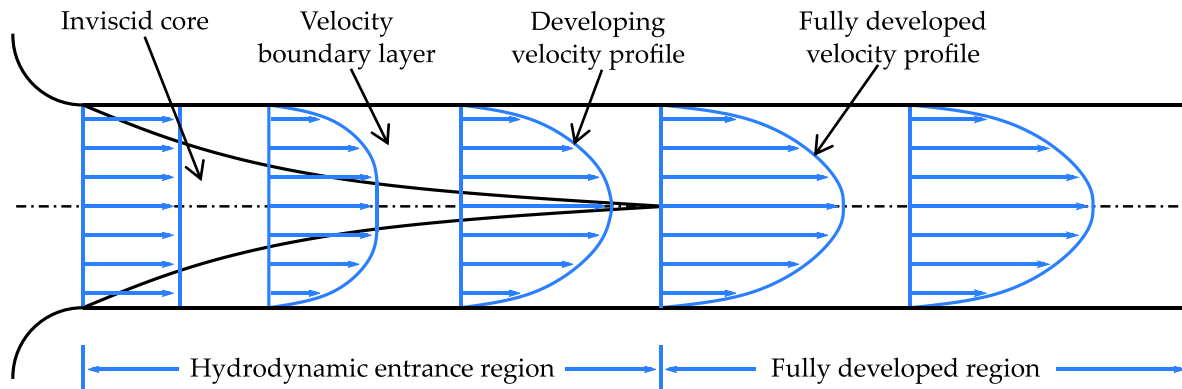


Figure 100: Developing velocity profile within channel [69].

Typically, the hydrodynamic entrance length of laminar fluid flow in a non-circular channel can be usually calculated using the following equation:

$$L_h = 0.05ReD_h \quad (4.69)$$

However, as there were other factors that would perturb the fluid, equation (4.69) could not be used. The first factor is the fact that the fluid would flow from the circular pipes of the test loop, to the rectangular channel of the test section. In addition, as can be seen in Figure 98, the path from the entrance of the test section to the rectangular channel undergoes two 90-degree bends. Therefore, to accurately determine the fluid entrance length, simulations were carried out on the flow path, with constant fluid inlet velocity. The geometry that was simulated can be seen in Figure 101.

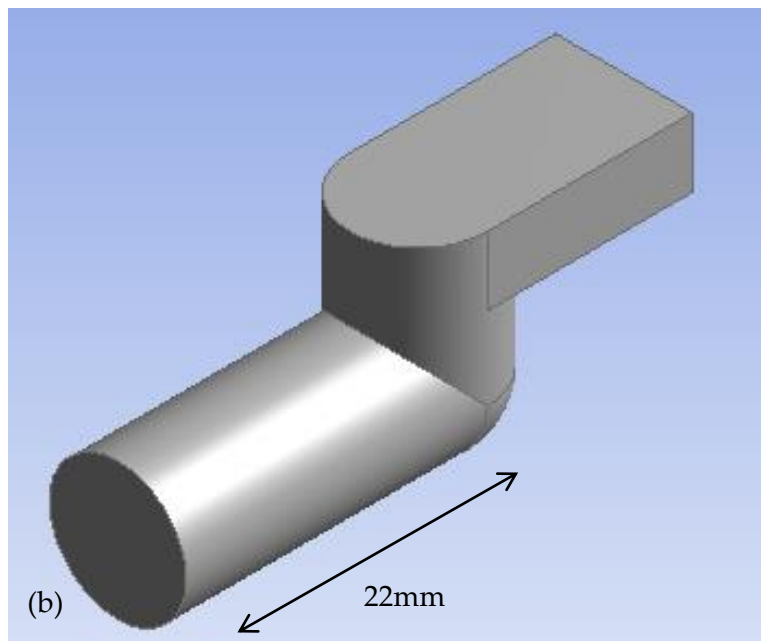
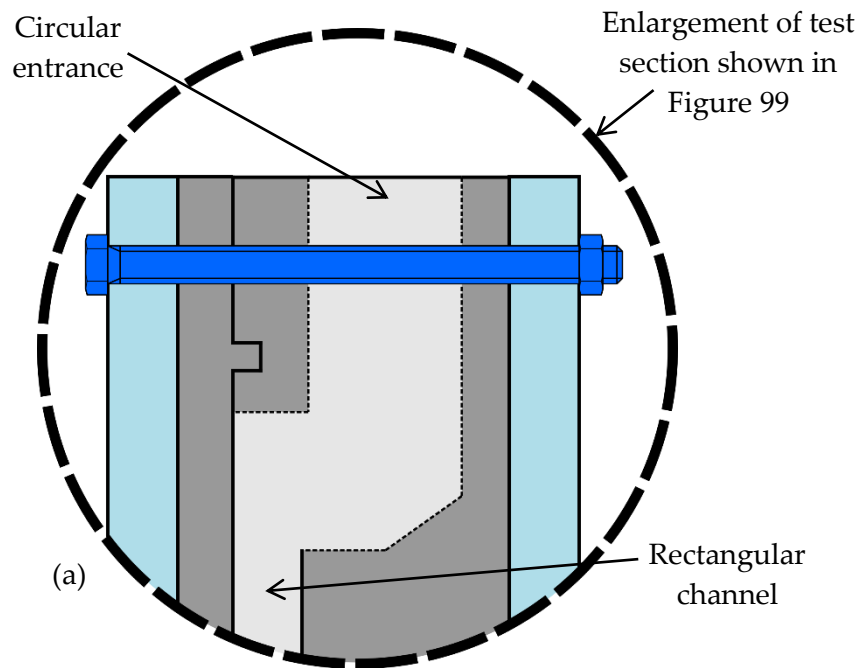


Figure 101: Enlargement of the test section to show flow path (a), and simulated geometry to calculate entrance length (b).

Figure 101 shows an offset circular pipe and rectangular channel connected together. When simulated, the rectangular channel continues much further than shown in Figure 101. A fluid flow rate was calculated that corresponded to a velocity through the foam of  $0.5 \text{ m} \cdot \text{s}^{-1}$  ( $9 \times 10^{-6} \text{ m}^3 \cdot \text{s}^{-1}$ ), the maximum that was expected during experimentation. Water was the chosen fluid as it would have a higher Reynolds number than Paratherm™ for the same flow rate, thus increasing the size of the entrance length. Figure 102 shows the rate of change of the fluid velocity  $\partial u_z / \partial z$  with respect to its position along the length of the channel  $z$ .

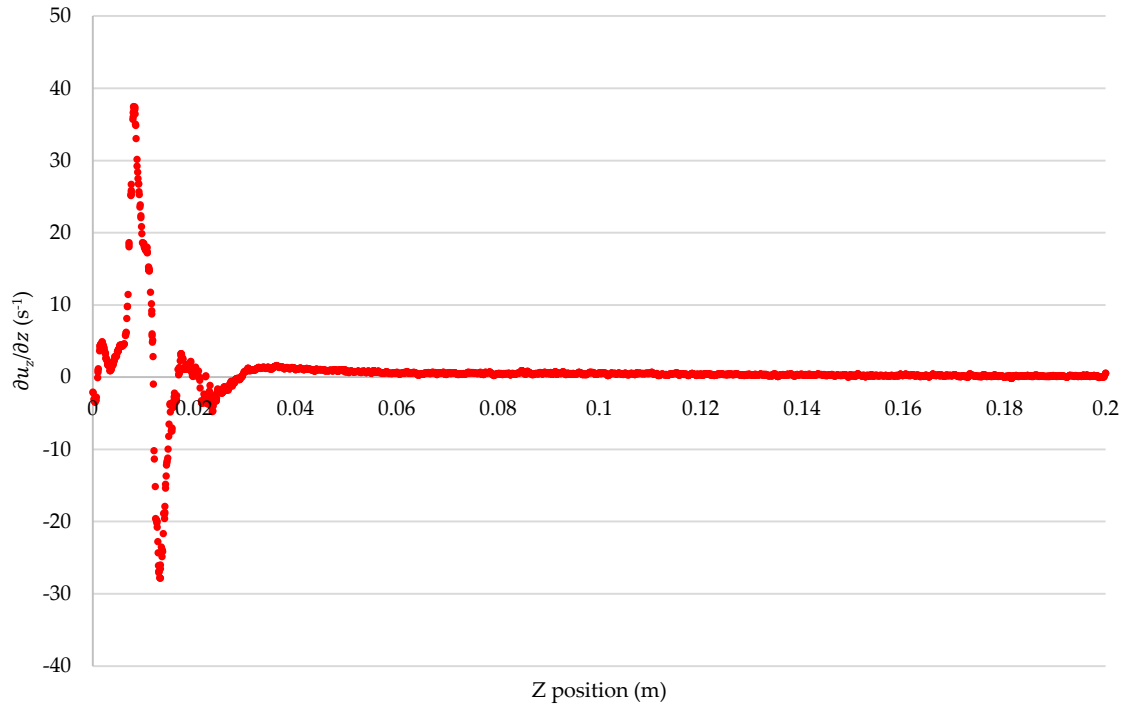


Figure 102: Rate of change of the fluid velocity with respect to its  $z$  position with a flow rate of  $9 \times 10^{-6} \text{ m}^3 \cdot \text{s}^{-1}$ .

At  $z = 0$  the fluid enters the circular pipe. The rectangular channel begins at  $z = 22\text{mm}$ . As was expected, initially the fluid is highly perturbed as it passes through the two bends. Once entering the rectangular channel however, it quickly settles down and  $\partial u_z / \partial z$  tends towards zero. By reducing the scale of Figure 102 and eliminating noise by averaging the values of  $\partial u_z / \partial z$  every  $1 \text{ mm}$ , the behaviour of the fluid can be more easily analysed. This can be seen in Figure 103.

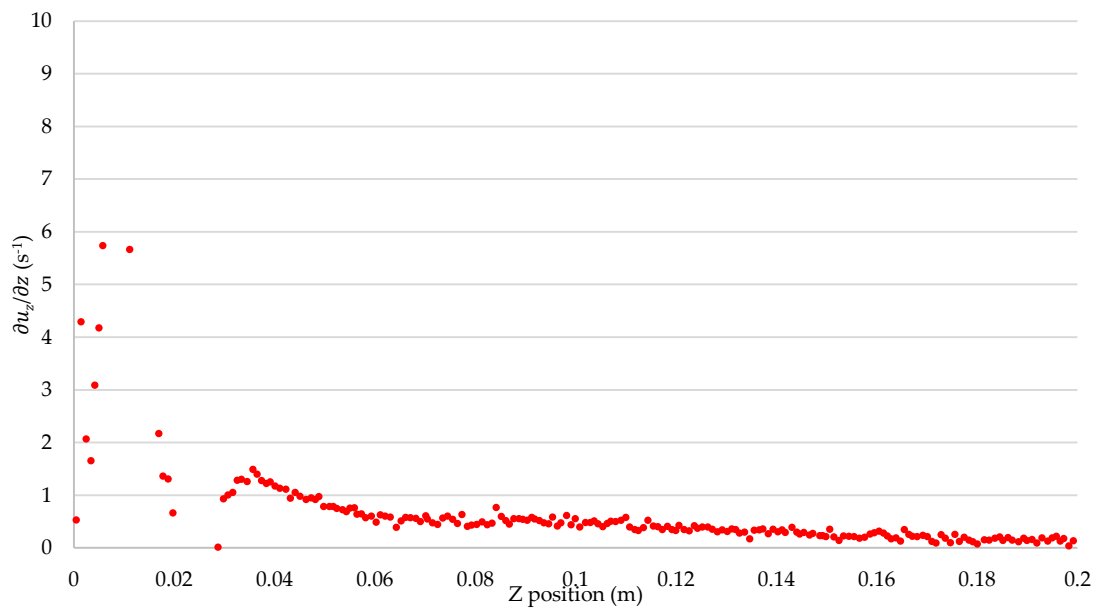


Figure 103: Rate of change of the fluid velocity with respect to its  $z$  position with a flow rate of  $9 \times 10^{-6} \text{ m}^3 \cdot \text{s}^{-1}$  at a reduced scale.

From 160 mm onwards, the average value of  $\partial u_z / \partial z$  stops noticeably decreasing and becomes stable and flat. Thus, the fluid can be considered fully developed. The length the channel could therefore be determined, being the sum of the inlet (160 mm), the heat sink (40 mm), and the outlet (50mm) outlet, thus 250 mm in total. The outlet length was calculated by the general rule that it be five times the width of the channel, which avoids any outlet effects travelling upstream into the heatsinks. The outer dimensions of the test section were designed around the length of the channel at its centre.

## 4.2 Ensuring test section is watertight

Maintaining a completely sealed test section was a difficult criterion to achieve, in large part due to the choice of material. Though Teflon makes an excellent thermal insulator, it is also a relatively soft plastic, prone to bending, twisting and warping when put under stress. This meant that there were several locations that had an increased risk of leaking. The largest of these was along the interface between the channel and the cover. To improve this region, an 'O-ring' was machined into the cover, and a corresponding groove into the channel. An example of this can be seen in Figure 104.

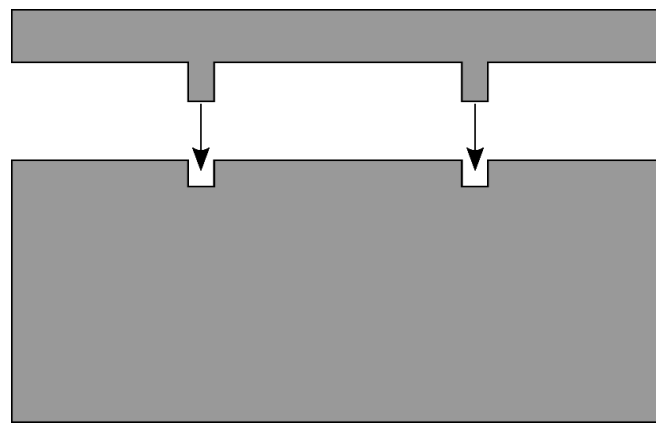


Figure 104: Section view of Teflon O-ring.

Much like a typical rubber O-ring, when the two parts of the test section are compressed together, the male ring fits into the female groove. As Teflon is soft and malleable, the ring was given a height of 3mm, whilst the groove only had a depth of 2mm, thus when compressed, the ring will be forced against the bottom and sides of the groove, increasing the quality of the seal. It was initially decided that the channel and cover would be held together directly using nuts and bolts. However, even when using large washers, if the bolts were tightened too much, the Teflon would deform, as is illustrated in Figure 105.

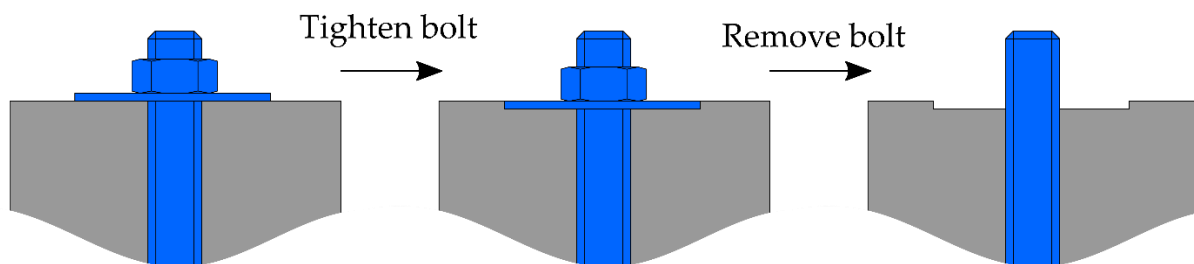


Figure 105: Deformation of Teflon surface when nuts are over tightened.

It was for this reason that two aluminium plates were used to compress the Teflon channel and cover together, rather than bolting the Teflon directly. This spreads the pressure across the whole top and bottom surface of the test section and eliminates the risk of deformation.

Other locations prone to leaking were the threaded holes that either connected the test section to the test loop, or were used to connect thermocouples or pressure sensors. Again, the use of Teflon meant that the typical sealing methods could not be used. If the test section had instead been made of a metal, such as aluminium, it would have sufficed to simply wrap the male threads in Teflon tape, and then tighten the connectors until a seal was achieved. However, screwing a connector too tightly into Teflon would certainly cause the threading to break. Thus, specialised connectors were required that could create a seal without applying too great a force. The ideal solution was Swagelok connectors that contained an integrated rubber O-ring. These could be tightened by hand, without the need for any tools, and produced a water tight seal. Unfortunately, as the available connectors did not have the correct sized output, a series of intermediary connections were required to make them fit. This information can be seen in the Appendix. For the wires used to power the resistance heater, one single multi-wire vacuum feed through was used. As this connector was screwed directly into the outer aluminium plate, an integrated O-ring was not necessary. Finally, when fitting the solid thermocouples into the side of the test section, a small bead of silicon was used to ensure a good seal.

The final design was then converted into a 3D model, such that the Teflon parts could then be machined using computer aided manufacturing (CAM). The 3D model can be seen in Figure 106.

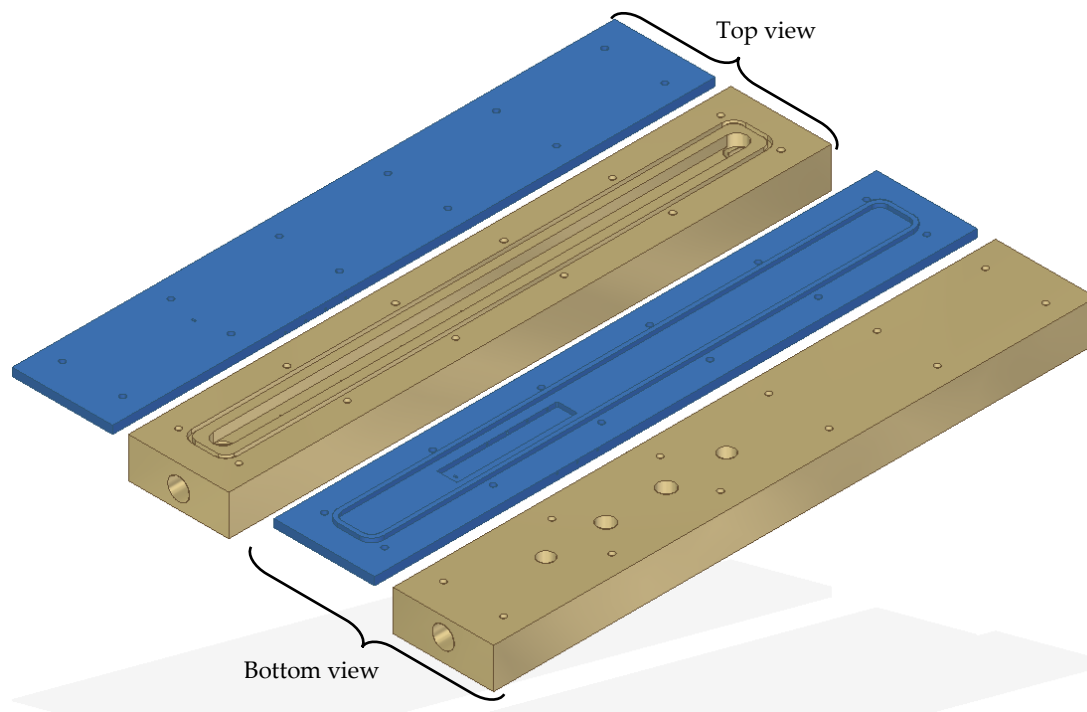


Figure 106: 3D model of both sides of Teflon cover and channel.

Figure 107 shows when all the components of the test section, as well as the connectors, are assembled together.

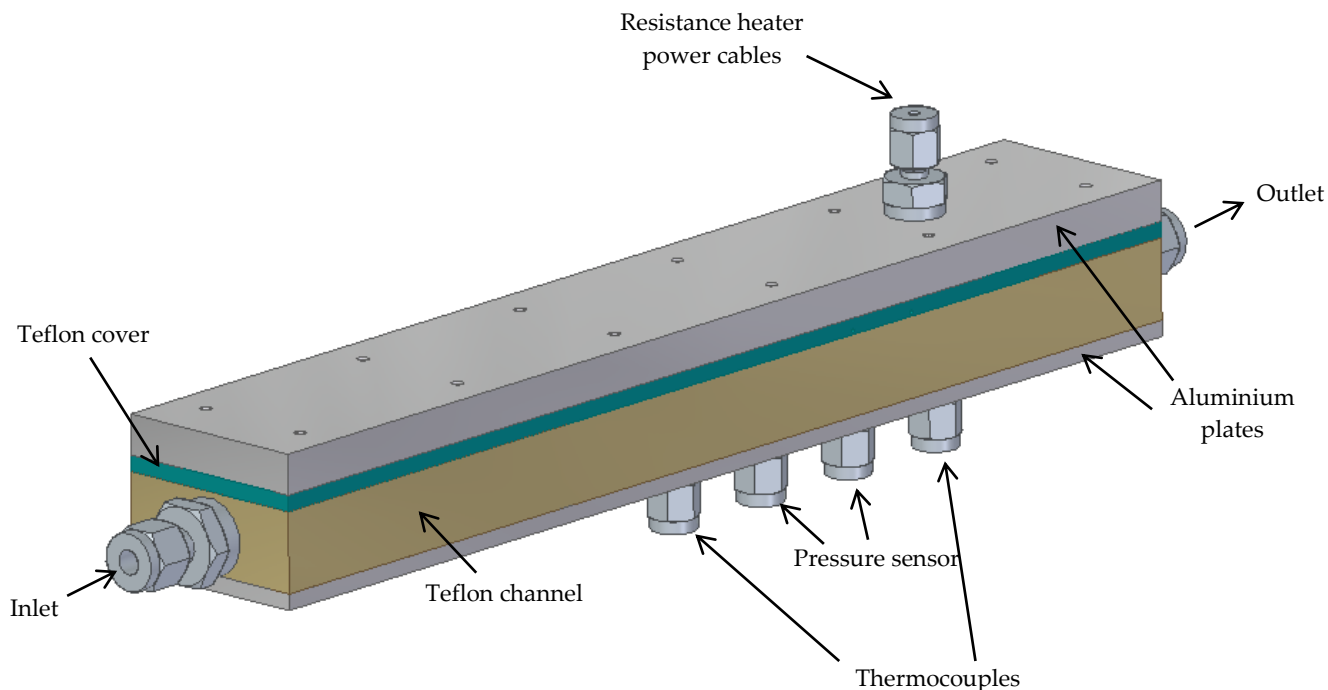


Figure 107: Assembled test section and connectors.

Finally, Figure 108 shows an internal slice of the test section, displaying clearly how the thermocouples are placed inside the copper plate, and how the pressure sensor reaches the fluid.

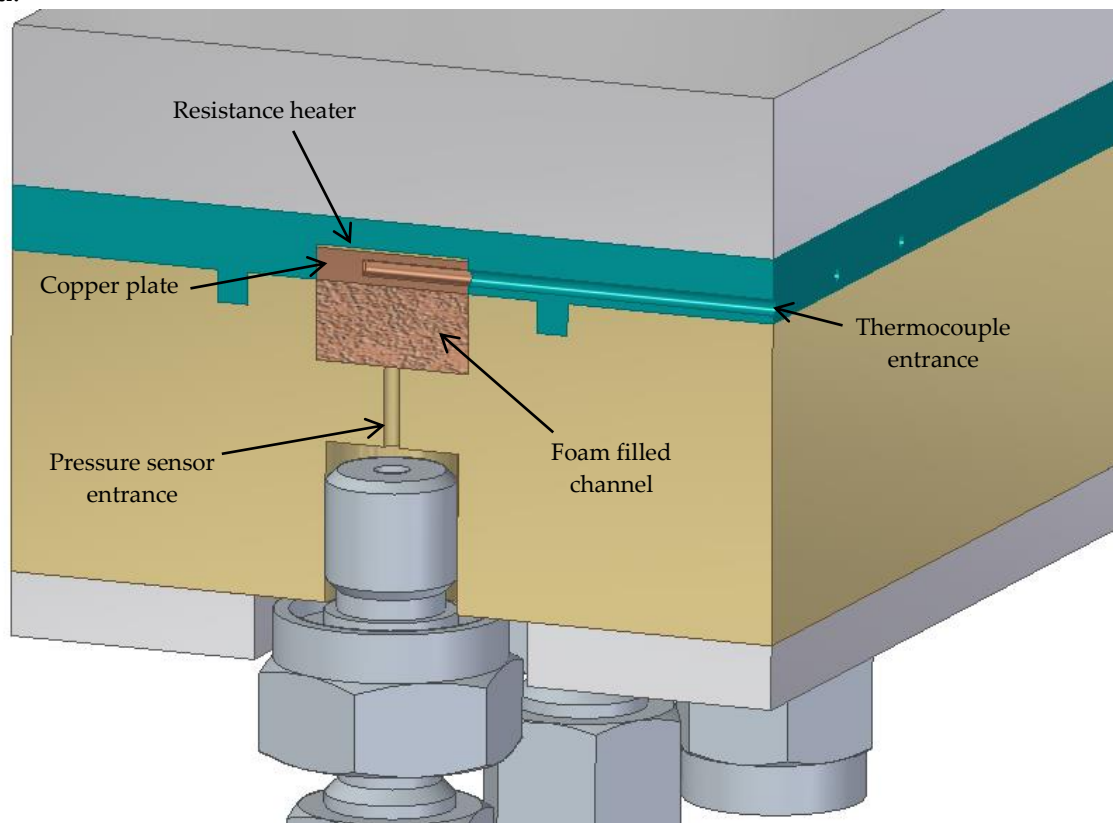


Figure 108: Internal slice of test section.

## 5. Experimental Results

Before commencing testing of the two heat sinks, a series of preliminary tests were carried out. The first set of tests was to estimate the value of the thermal resistance at the interface between the metal foam and the copper plate. The second, carried out using the microchannel heat sink installed within the test loop, was to determine the required time for the experiment to reach thermal stability.

### 5.1 Measuring interface thermal resistance

A crucial part of this project was how to attach the metal foams to the copper plate in a way that minimises the associated thermal resistance at the interface. It was therefore necessary to determine whether the thermal resistance in this case was negligible or not when compared to the overall thermal resistance of the heat sink.

#### 5.1.1 Interface thermal resistance test

The obvious concern is that the flat face of the metal foam samples has a low surface area, reducing the physical contact between them and the copper plate. Fortunately, there were no mechanical constraints imposed for the experiments, so it was possible to concentrate solely on the thermal connection between the two pieces. It was decided that the two pieces would be brazed together, thus the additional thermal resistance at the interface was heavily dependent on the intermediary material used and the heat treatment applied. Directly measuring thermal resistance can be a difficult task. A temperature difference must be imposed across the sample, whilst making sure that the entire setup is completely thermally insulated, to avoid inaccuracies in the results. To avoid this, it was decided that the electrical resistance of the interface would be measured instead. This means that the heat transfer by convection is ignored, and only conduction through the solid phase is considered. It also relies on the assumption that thermal and electrical resistances are linked, and that a minimum electrical resistance would correspond with a minimum thermal resistance. This assumption can be justified by looking at the relationship between the thermal and electrical conductivities of metals. It is based upon the fact that heat and electrical transport both involve the free electrons in the metal. When temperature increases the velocity of free electrons increases which results in an increase in thermal conductivity. Contrary to this, electrical conductivity decreases with increasing particle velocity due to the increased collisions between electrons. This means that the ratio of thermal to electrical conductivity depends upon the average velocity squared, which is proportional to the kinetic temperature. The relationship, known as the Wiedemann Franz law, can be seen in equation (4.70) [70]:

$$\frac{k}{\sigma} = LT \quad (4.70)$$

where  $k$  is the thermal conductivity,  $\sigma$  is the electrical conductivity,  $T$  is the temperature and  $L$  is the Lorenz number:

$$L = 2.44 \times 10^{-8} W \Omega K^{-2} \quad (4.71)$$

Thus, at a constant temperature, thermal and electrical conductivities of metals are proportional, and as thermal and electrical resistances are simply their reciprocals, they too are proportional with each other. The next step was then to isolate the electrical resistance of

just the interface. One way to do this would be to measure the total electrical resistance of the plate, interface and foam using four-terminal sensing, as can be seen in Figure 109.

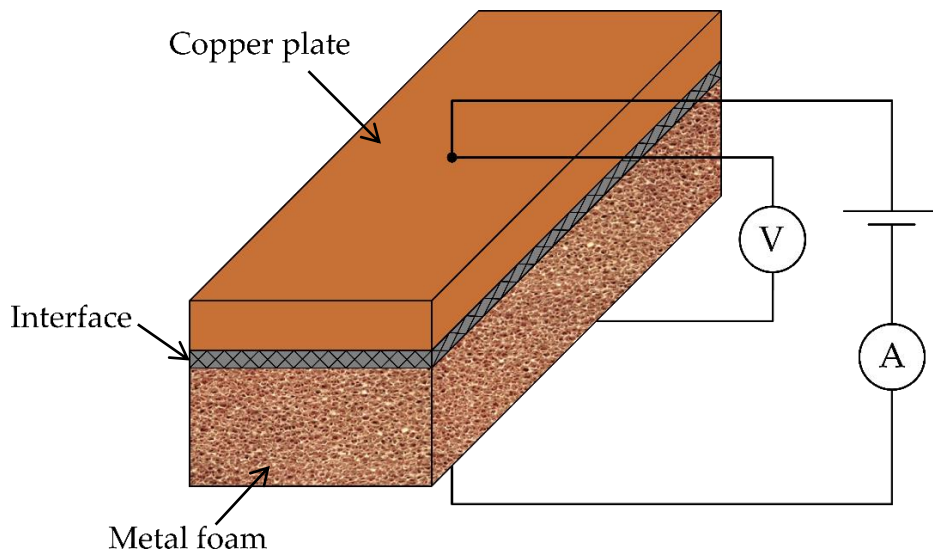


Figure 109: 4-terminal sensing of electrical resistance of copper plate, interface and metal foam.

In the system shown in Figure 109 a current is applied through the sample and the voltage is measured. With these two values the overall resistance can then be calculated. As the three regions are in series with one another, it can be written:

$$R_{elec,total} = R_{elec,plate} + R_{elec,interface} + R_{elec,foam} \quad (4.72)$$

The problem with equation (4.72) is that the electrical resistance of the foam is very difficult to measure experimentally, and is highly dependent on the location of the probe. Also, as the thickness of the copper plate is very small, the equipotential lines emanating from the charge point do not have enough space to evenly diffuse before reaching the interface. With these factors in mind, the test was reworked; the revised design can be seen in Figure 110.

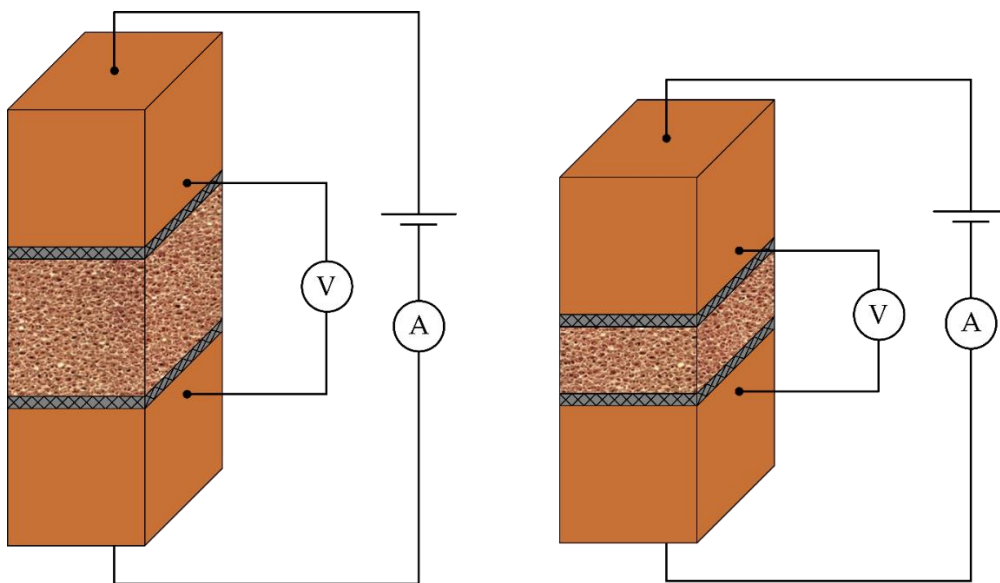


Figure 110: Modified 4-terminal sensing to improve precision.

In Figure 110, the flat plate of copper has been replaced with 10 mm × 10 mm × 10 mm copper cubes. As mentioned, this is so that the equipotential lines are able to become flat and perpendicular to the flow direction, before reaching the interface. This guarantees that the current passes through the interface evenly, as can be seen in Figure 111.

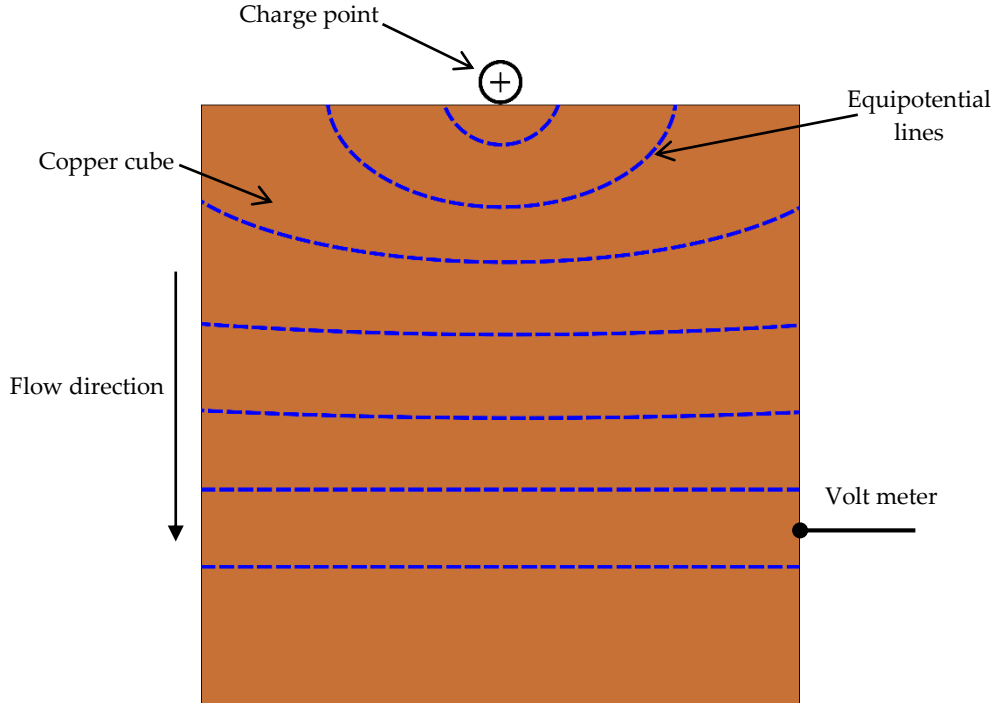


Figure 111: Lines of equipotential travelling through a copper cube.

Figure 110 also shows that copper cubes were attached to each side of the foam, and that two samples were made, one with a thickness of 5 mm, and the other with a thickness of 3 mm. This means that the following set of equations can be written:

$$R_{elec,tot 1} = 2R_{elec,interface} + 5R_{elec,foam} \quad (4.73)$$

$$R_{elec,tot 2} = 2R_{elec,interface} + 3R_{elec,foam} \quad (4.74)$$

Thus by multiplying equation (4.73) by three and equation (4.74) by five, then subtracting  $R_{elec,tot 1}$  from  $R_{elec,tot 2}$ , an equation can be written for  $R_{elec,interface}$ :

$$R_{elec,interface} = \frac{5}{4}R_{elec,tot 2} - \frac{3}{4}R_{elec,tot 1} \quad (4.75)$$

Once the electrical resistance of the interface has been calculated, the electrical conductivity  $\sigma$  can be found using:

$$\sigma_{interface} = \frac{t}{R_{elec,interface}A} \quad (4.76)$$

where  $t$  is the thickness of the interface layer, and  $A$  is the surface area. Then the Wiedemann Franz law can be used to calculate the thermal conductivity, and finally the thermal resistance is given by:

$$R_{th,interface} = \frac{t}{k_{interface}A} \quad (4.77)$$

### 5.1.2 Interface thermal resistance results

In total five samples were made for both the 5 mm and 3 mm thickness foams, so that an average could be calculated. A current of 10 A was applied to each and the electrical resistance was calculated. The results can be seen in Table 14.

TABLE 14:

Interface electrical resistance

Sample	5mm thickness resistance ( $\Omega$ )	3mm thickness resistance ( $\Omega$ )
1	$3.8 \times 10^{-5}$	$3.2 \times 10^{-5}$
2	$4.3 \times 10^{-5}$	$2.8 \times 10^{-5}$
3	$4.6 \times 10^{-5}$	$3.2 \times 10^{-5}$
4	$4.0 \times 10^{-5}$	$3.2 \times 10^{-5}$
5	$4.1 \times 10^{-5}$	$3.3 \times 10^{-5}$

By averaging the results shown in Table 14 and using equation (4.75) the electrical resistance of the interface was calculated to be  $6.3 \times 10^{-6} \Omega$ . Using the Wiedemann Franz law the thermal resistance was then found to be 0.86 K/W, for a surface area of 1 cm<sup>2</sup>. As the surface area associated with the heat sink is 4 cm<sup>2</sup>, this value must be divided by four, giving a value of  $R_{th,interface} = 0.215$  K/W. This value can then be put back into equation (4.73) in order to calculate the electrical resistance of the foam  $R_{elec,foam}$ :

$$R_{elec,foam} = \frac{1}{5} R_{elec,tot} - \frac{2}{5} R_{elec,interface} \quad (4.78)$$

In the same way that the Wiedemann Franz law was used to calculate the thermal conductivity of the interface, it can also be used to calculate the effective thermal conductivity of the foam  $k_{eff,s}$ . Thus, these measurements also provide an experimental validation of the analytical model chosen in chapter 2 to calculate  $k_{eff,s}$ . The Bruggemann model, revised by Collishaw and Evans [51] gives a value of 10.47 W.m<sup>-1</sup>.K<sup>-1</sup> for the 91% porosity Duocel™ foam, and the electrical resistance measurements gives 14.35 W.m<sup>-1</sup>.K<sup>-1</sup>. The two methods show a reasonable accordance with one another. However, when the analytical  $k_{eff,s}$  is used in equation (4.73) or (4.74), the interface thermal resistance varied significantly,  $R_{th,interface} = 0.109$  K/W. Therefore, the potential sources of error that can occur during testing must be considered. Firstly, the ten samples were brazed in two separate batches, according to the foam thickness. Though in each case the same temperature profile was used, it cannot be ruled out that the brazing process produced a different thermal resistance each time. Secondly, there may be slight inaccuracies in the thickness of the foam between each sample, which may account for the minor differences in the measured electrical resistance. By taking into account these potential errors, a range of possible values for the interface thermal resistance was calculated. These results can be seen in Table 15, alongside the associated effective thermal conductivities.

The minimum and maximum values of  $R_{th,interface}$  were calculated by taking the extreme values of the measured resistances shown in Table 14.

TABLE 15:

Range of potential interface thermal resistances

Sample	$R_{th,interface}$ (K/W)	$k_{eff,s}$ ( $W \cdot m^{-1} \cdot K^{-1}$ )
Min. measured resistance	0.035	9.76
Measurement using analytical $k_{eff}$	0.109	10.47
Average measured measurement	0.215	14.35
Max. measured resistance	0.377	29.28

As it is difficult to assess at this moment which of the measured thermal resistances is the most accurate, when the analytically calculated thermal resistance of the foam heat sink will be compared to the experimental results, it will first be done without incorporating an interface resistance. After this, the different interface resistances will be analysed by making comparisons with the experimental results.

## 5.2 Time required to reach thermal stability

To ensure the accuracy of the measurements, it was necessary to determine the time required for the experimental setup to reach thermal stability. This was achieved by running an experiment at a constant flow rate using the microchannel heat sink and an imposed heat flux of 100 W. Measurements were taken every 30 min for a total of 150 min, and the total heat flux passing into the fluid was then calculated ( $\Phi_0 = \rho C_p Q \Delta T_f$ ). The results can be seen in Figure 112.

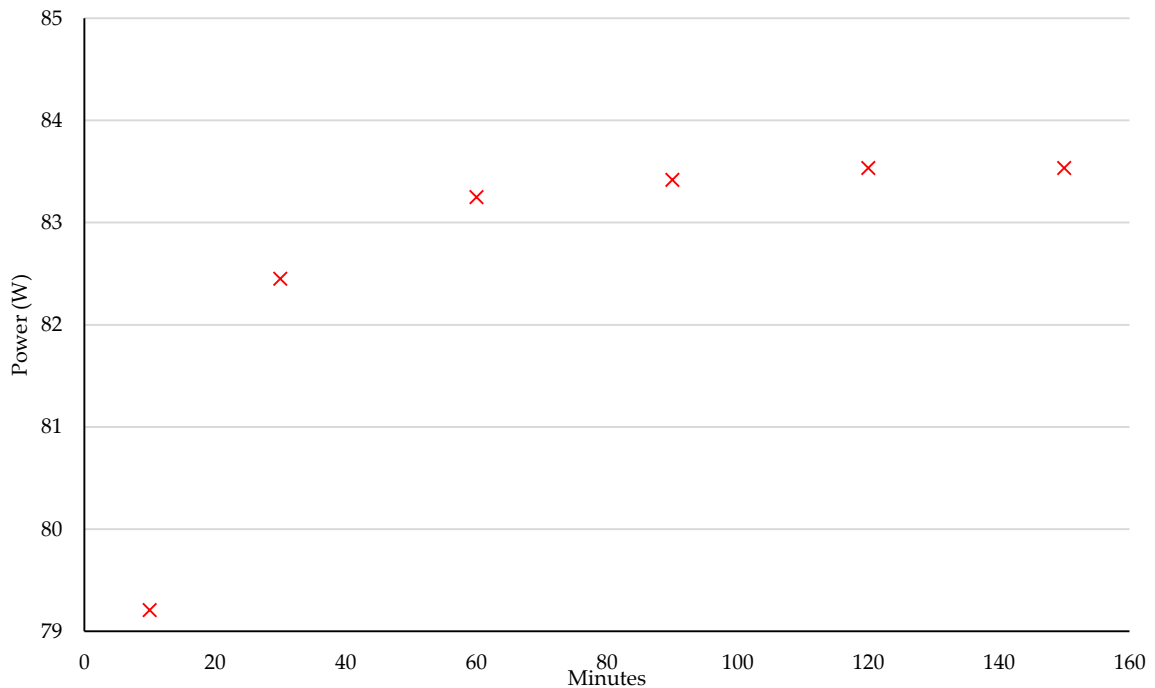


Figure 112: Total power passing into the coolant at 30-minute intervals.

The results show that a minimum of two hours was required for the experiment to reach thermal stability.

### 5.3 Microchannel results

Once the required wait time had been evaluated, the experiment was repeated with the microchannel for a range of flow rates. In chapter 3, the optimisation process was carried out at a constant flow rate that corresponded to a fluid temperature increase of 20K when a 100W heat flux is applied ( $3.67 \times 10^{-6} \text{ m}^3 \cdot \text{s}^{-1}$ ). Results were displayed as thermal resistance against pressure loss and each point on the graphs represented a different foam/microchannel geometry. As there were only two heat sinks to be tested upon, it was necessary to vary the flow rate in order to have enough points to make comparisons. The flow rate ranged from  $2 \times 10^{-6} \text{ m}^3 \cdot \text{s}^{-1}$  to  $9 \times 10^{-6} \text{ m}^3 \cdot \text{s}^{-1}$ . This was chosen as it generates enough of a difference in thermal and hydraulic performance to be measurable, it includes the flow rate that corresponds to a fluid temperature increase of 20K, and it remains in the laminar flow regime, with a maximum Reynolds number of 375.

This experiment had two functions, the first being to validate the experimental setup. As the microchannel analytical model used within this work is well known within the scientific literature, it was used to ensure the accuracy of the experiment. As such, where possible, the analytical results are provided alongside the experimental results. The second function was to provide benchmark results with which to compare with the metal foam heat sink, as was done in chapter 3. It should be noted that though effort was made to thermally insulate the experiment, thermal losses were still suffered. Thus the analytical results were calculated using the measured heat flux, as opposed to the imposed 100W. The measured heat flux at each flow rate can be seen in Figure 113.

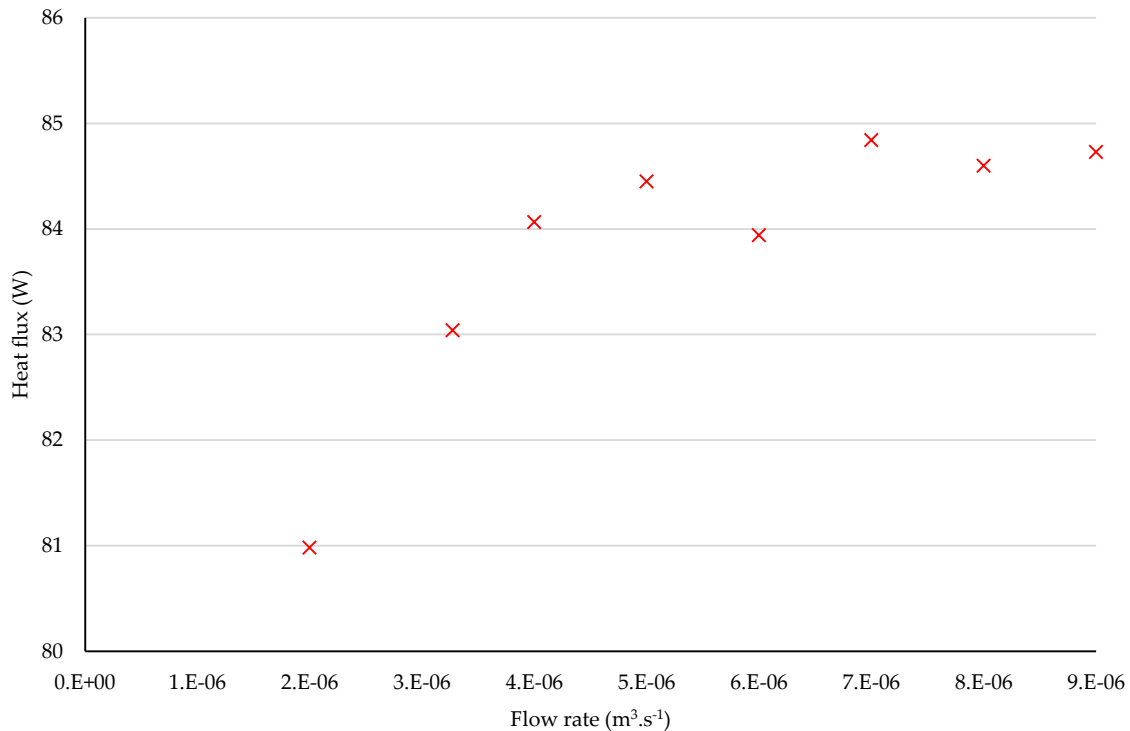


Figure 113: The effects of flow rate on the thermal losses of a microchannel heat sink with an imposed heat flux of 100W.

The results show that thermal losses tend to increase with decreasing flow rate. This corresponds with the expected behaviour, as at lower flow rates the overall maximum temperature of the heat sink and the coolant is increased. The results of the microchannel heat sink can be seen in Figure 114.

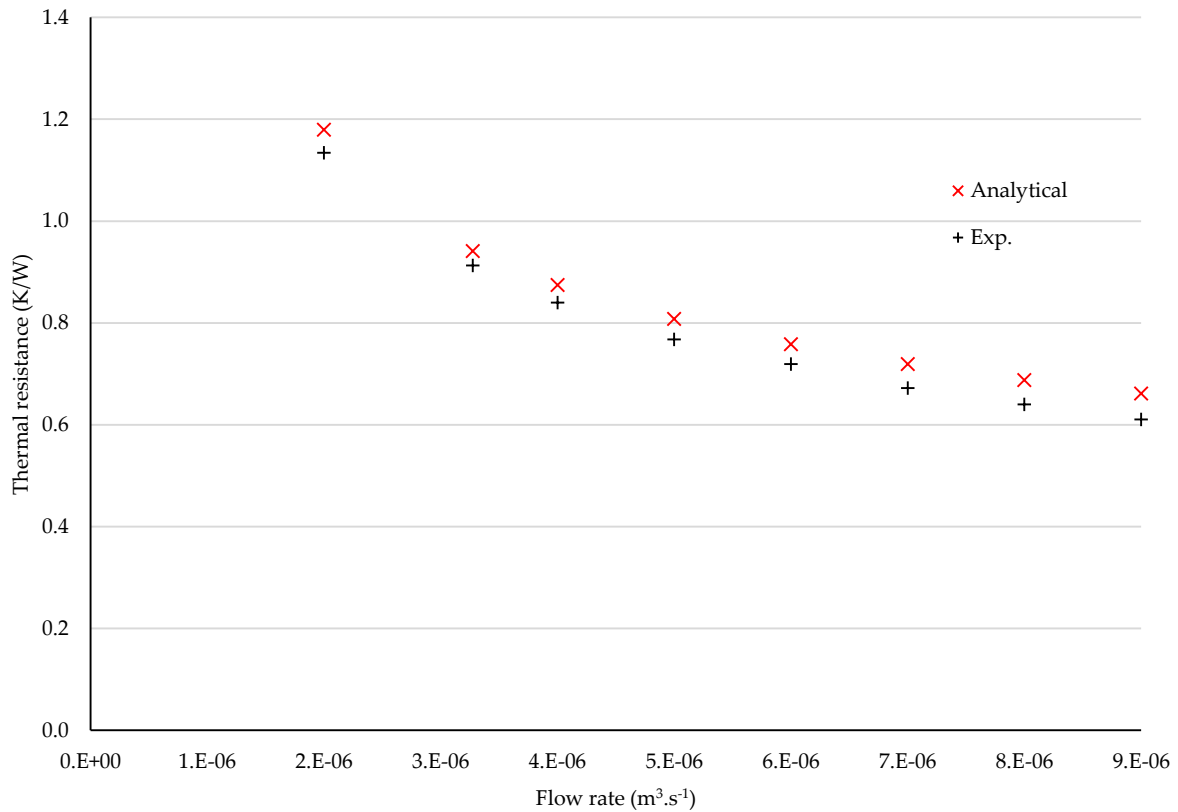


Figure 114: The effects of flow rate on  $R_{th}$  of microchannels with an imposed heat flux of 100W.

The figures show an excellent agreement between the experimental and analytical results, with an average deviation in value of only 5.6%. It is also interesting to analyse the temperature profile along the length of the heat sink. As mentioned previously in this chapter, the copper plate portion of each heat sink was made as thin as possible in order to avoid lateral heat transfer, parallel to the fluid flow. Figure 115 shows the temperature profile ( $T_0 - T_\infty$ ) as a function of the position along the length of the heat sink ( $z$ ). If there was no lateral heat transfer, then the temperature along the heat sink would increase linearly. The results show a small decline in the rate of the temperature increase, thus lateral heat transfer was unfortunately not completely avoided. This may well have had an effect on measured thermal resistance of the heat sink, but further analysis is required to know more.

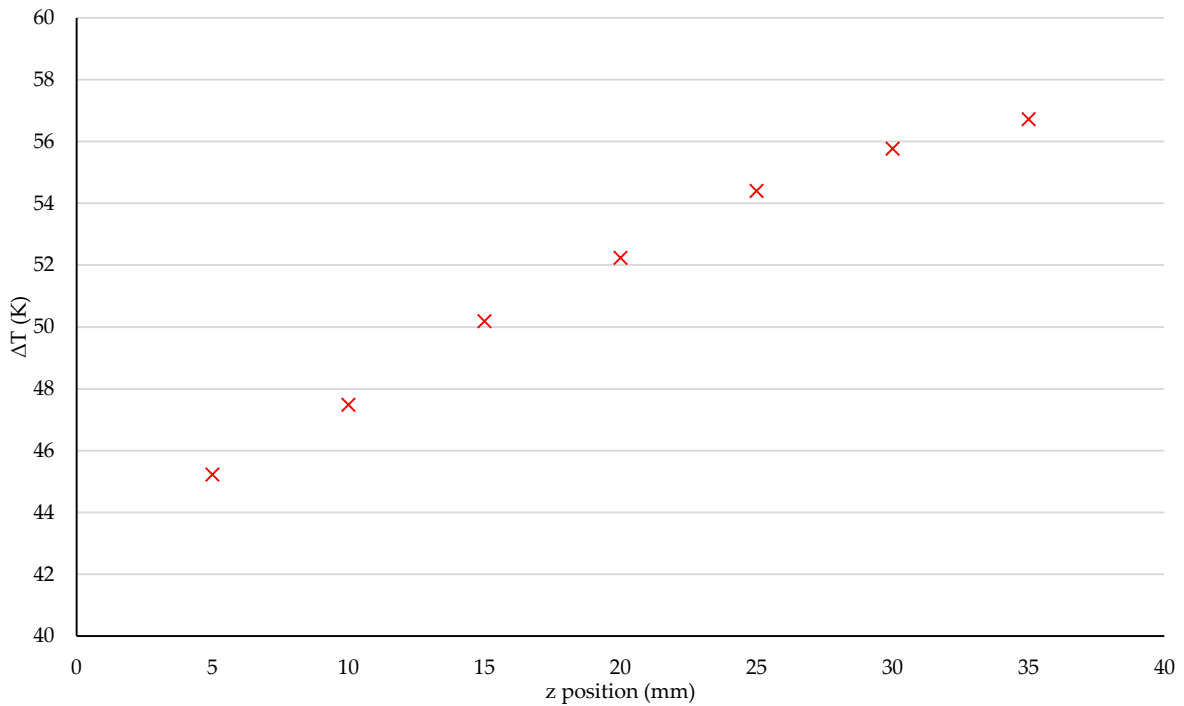


Figure 115: Temperature profile along the length of a microchannel heat sink with a fluid flow rate of  $9 \times 10^{-6} \text{ m}^3 \cdot \text{s}^{-1}$  and an imposed heat flux of  $100 \text{ W}$ .

Finally, the hydraulic performance of the heat sink was also tested. The pressure difference was measured across the microchannels at the same range of flow rates, and the results were converted into a pressure gradient. This can be seen in Figure 116.

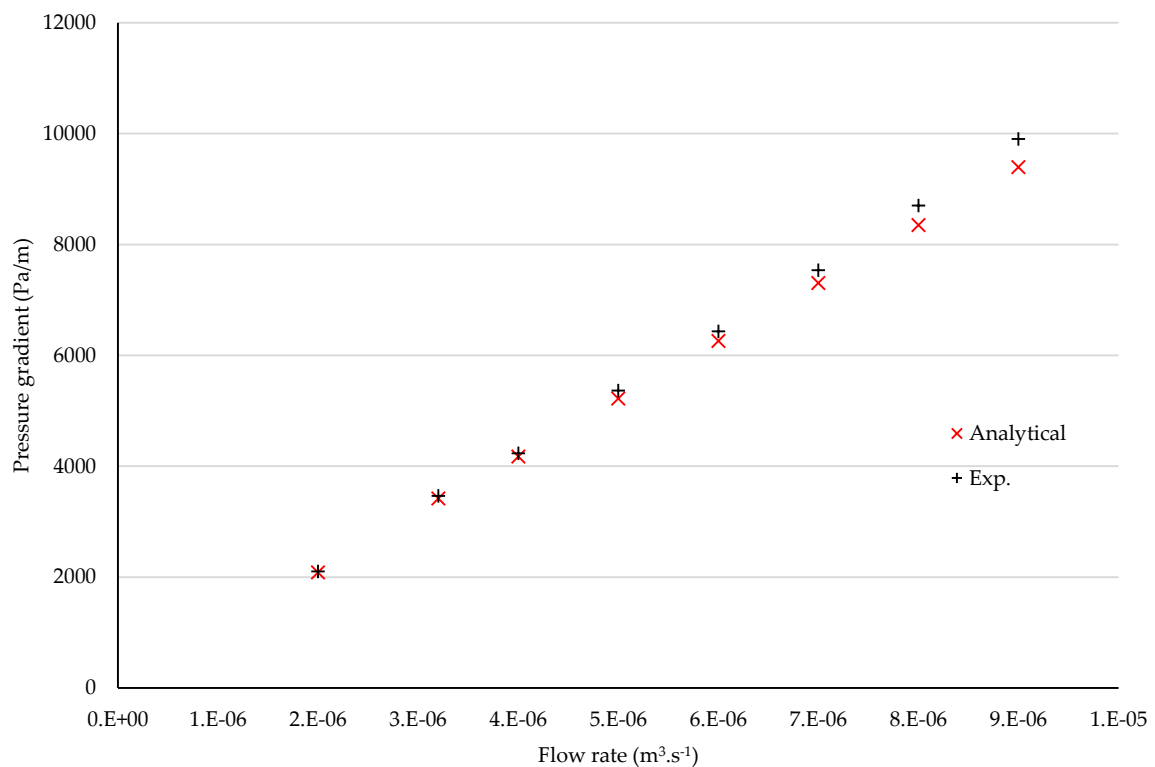


Figure 116: The effects of flow rate on pressure gradient of a microchannel heat sink.

The results show that analytical model predicts very well the pressure gradient across the microchannel heat sink, with an average deviation in results of only 2.7%. As mentioned previously, the microchannel analytical model used within this work is well known within the scientific literature, and has already been validated experimentally. It is therefore reasonable to rely on the model being accurate, and as the experimental results match very closely, it can be reasonably concluded that the test loop, its components and the test section are able to accurately measure thermal and hydraulic performances.

## 5.4 Metal foam results

After completing the experiments with the microchannel channel heat sink, it was replaced with the metal foam heat sink. Experiments were then repeated under the same conditions. This second set of experiments has a single purpose, to further validate the metal foam analytical model and simulations. One noticeable difference between the two sets of experiments was that when the heat sinks were replaced and the test section was disassembled and reassembled, the amount of insulation used was increased. This was in reaction to the heat loss results shown in Figure 113 and as such the heat loss during the metal foam experiments was expected to be lower. These results can be seen in Figure 117, and to aid comparisons the previous results using the microchannel heat sink have been superimposed.

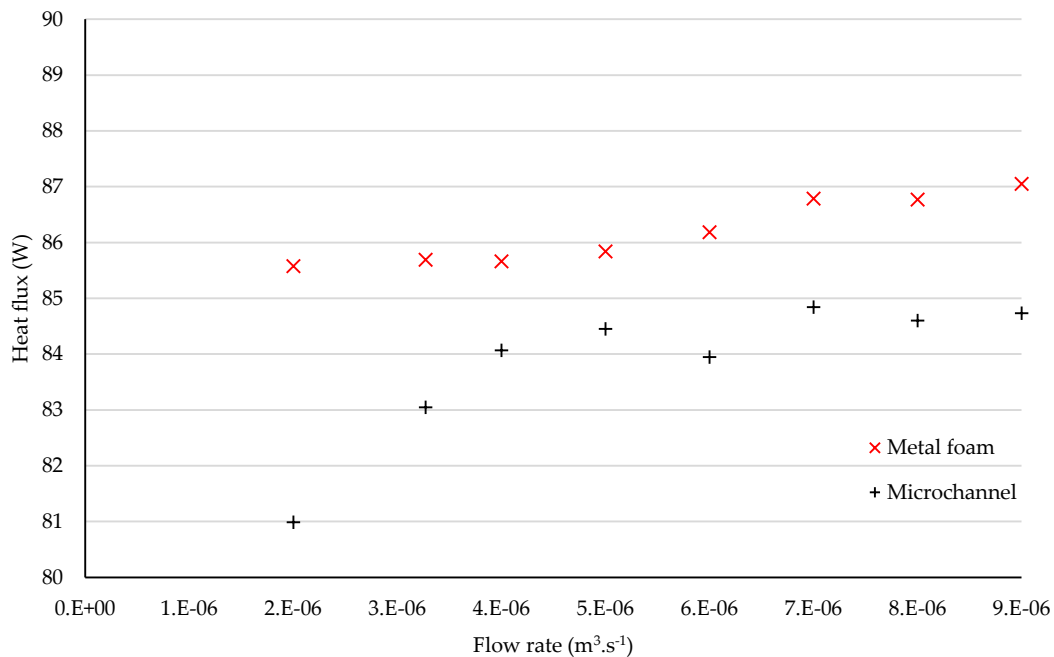


Figure 117: The effects of flow rate on the thermal losses of a metal foam and microchannel heat sink with an imposed heat flux of 100W.

The results in Figure 117 show a decrease in heat loss during the metal foam experiments when compared to the microchannel experiments. The amount of heat loss was also less affected by the change in flow rate, with a total difference of only 1.5W between the maximum and minimum flow rates. For the microchannel experiments the difference in heat flux loss across the same range of flow rates was more than double at 3.8W. This suggests that the effectiveness of the thermal insulation was improved between the two sets of experiments.

It could also be explained by an improvement in heat transfer by the coolant thanks to the foam, which would also result in a reduction in thermal losses. Following this, the total thermal resistance was measured and compared with the analytical model and numerical simulations, which can be seen in Figure 118. As a reminder, neither the analytical model nor the numerical results incorporate an interface resistance at this stage. Also, the analytical and numerical results were calculated using the measured heat flux (100 W – losses). At a first look the analytical and experimental results appear in good agreement with one another, deviating on average by 8.5%. However, there are potential sources of error that will be discussed later. As with the microchannels it was also deemed important to assess the temperature increase along the length of the metal foam heat sink. These results (Figure 119) show a far more linear increase in temperature. A trend line was included to highlight how little the results deviate. The difference in behaviour between the microchannel and metal foam heat sinks is likely attributed to their geometries. In both cases the heat flux was applied to one side of a copper plate measuring 10 mm × 40 mm × 2 mm. However, in the case of the microchannels, there were also five copper fins running parallel to the fluid flow direction. It is likely that, as well as moving vertically down, as was intended, heat was also able to transfer laterally along the fins. These straight lines of solid copper clearly do not exist within the metal foam heat sinks and thus heat could only move vertically downwards.

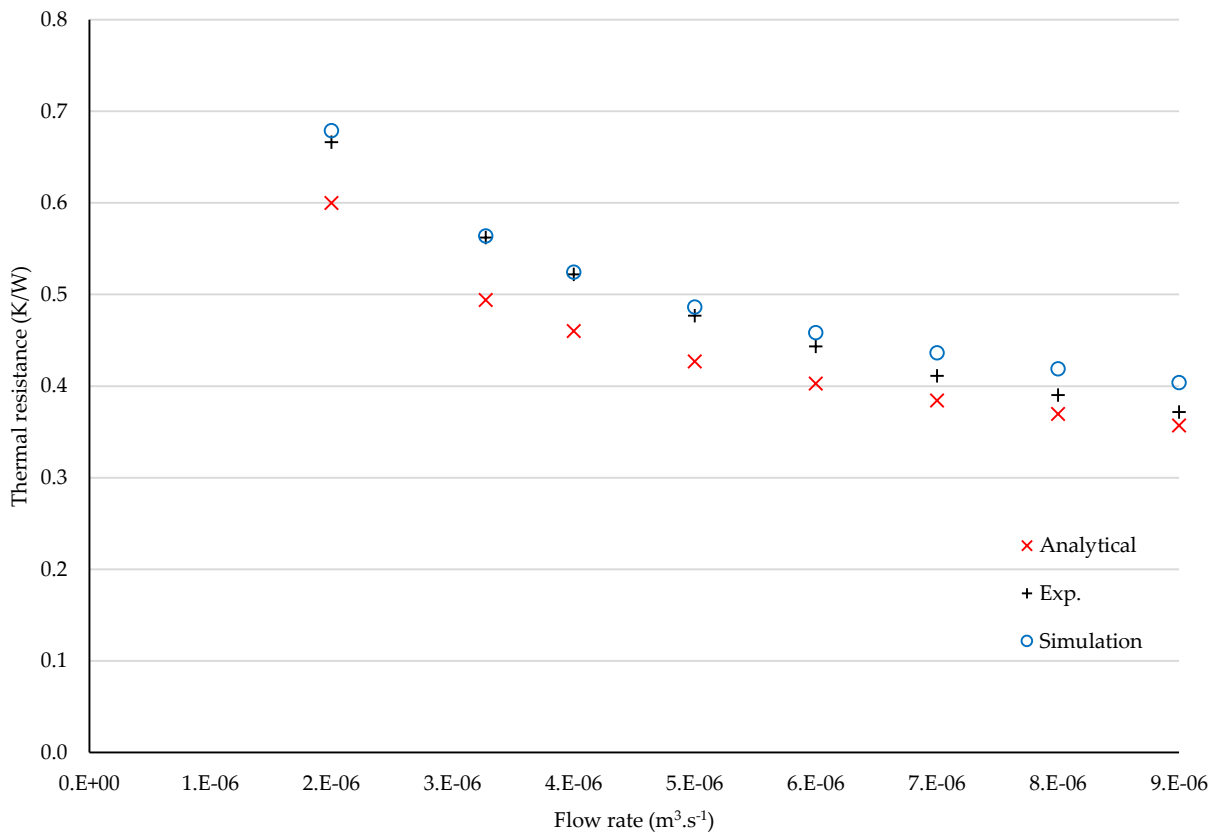


Figure 118: The effects of flow rate on  $R_{th}$  of metal foam with an imposed heat flux of 100W, and  $k_{eff,s}$  of  $10.47 \text{ W.m}^{-1}.K^{-1}$ . Analytical/numerical  $R_{th}$  was calculated using measured heat flux (100 W – losses).

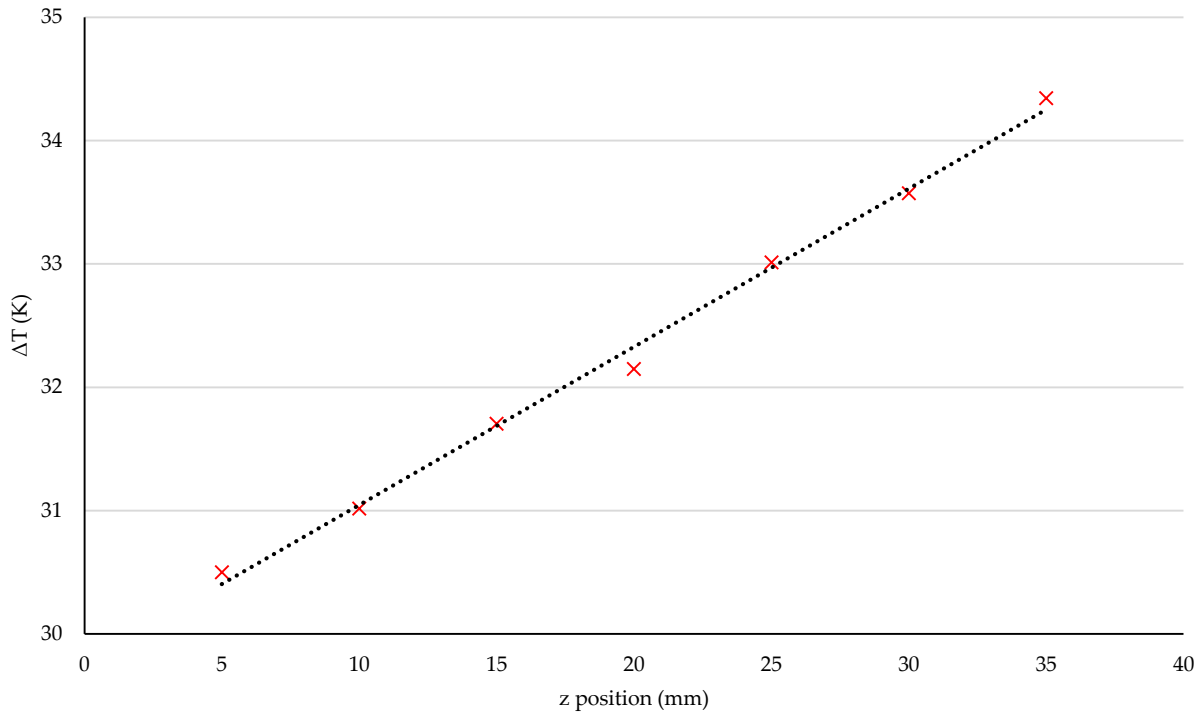


Figure 119: Experimental temperature profile along the length of a metal foam heat sink with a fluid flow rate of  $9 \times 10^{-6} \text{ m}^3 \cdot \text{s}^{-1}$  and an imposed heat flux of 100W.

Finally, the hydraulic performance of the metal foam heat sink was also tested. As before, the pressure difference was measured and later converted into a pressure gradient. The results can be seen in Figure 120.

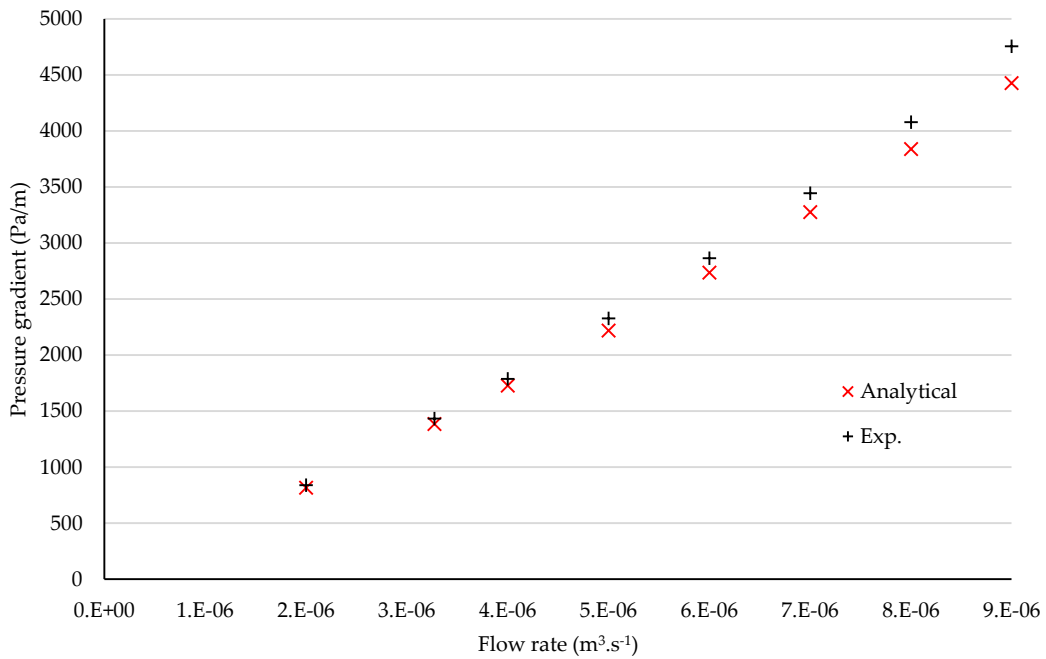


Figure 120: The effects of flow rate on pressure gradient of a metal foam heat sink.

A very good agreement between the experimental and analytical results was found, with an average deviation between the two of 4.5%.

## 5.5 Potential errors analysis

It is important to address and attempt to explain the potential sources of error that may exist within this works experimentation. Firstly, then sensors used have accuracy ratings provided by the manufacturer.  $\pm 0.75\%$  of the measured values for the Type T and type K thermocouples, and  $\pm 0.1\%$  of the measured values for the Micro Motion™ flow rate meter. These are used to create error bars for both the experimental and analytical results, as the analytical results were calculated using the measured heat flux. In order to assess the contribution to the overall errors each of the limitations of the sensors have, this work uses the law of propagation of errors. Moffat [71] showed that when a function contains several independent variables, each with their own accuracies, the overall error of the function is calculated by a root-sum-square method. The function in question is the thermal resistance:

$$R_{th} = \frac{\langle T_0 \rangle - T_\infty}{C_p \dot{m} (T_f - T_\infty)} \quad (4.79)$$

In equation (4.79) there are four variables with associated errors,  $\langle T_0 \rangle$ ,  $T_\infty$ ,  $T_f$  and  $\dot{m}$ . The errors in the calculated thermal resistance are thus:

$$\delta R_{th} = \sqrt{\left(\frac{\partial R_{th}}{\partial \langle T_0 \rangle} \delta \langle T_0 \rangle\right)^2 + \left(\frac{\partial R_{th}}{\partial T_\infty} \delta T_\infty\right)^2 + \left(\frac{\partial R_{th}}{\partial \dot{m}} \delta \dot{m}\right)^2 + \left(\frac{\partial R_{th}}{\partial T_f} \delta T_f\right)^2} \quad (4.80)$$

where  $\delta$  represents the absolute error of each parameter.

$$\delta R_{th} = \sqrt{\left(\frac{R_{th} \delta \langle T_0 \rangle}{\langle T_0 \rangle - T_\infty}\right)^2 + \left(\frac{R_{th} \delta T_\infty}{(T_f - T_\infty)} - \frac{\delta T_\infty}{C_p \dot{m} (T_f - T_\infty)}\right)^2 + \left(\frac{-R_{th} \delta \dot{m}}{\dot{m}}\right)^2 + \left(\frac{-R_{th} \delta T_f}{(T_f - T_\infty)}\right)^2} \quad (4.81)$$

The errors calculated using equation (4.81) were applied to the thermal resistances measured experimentally and calculated analytically. The error bars calculated from this method are relatively small, the results can be seen in Figure 121.

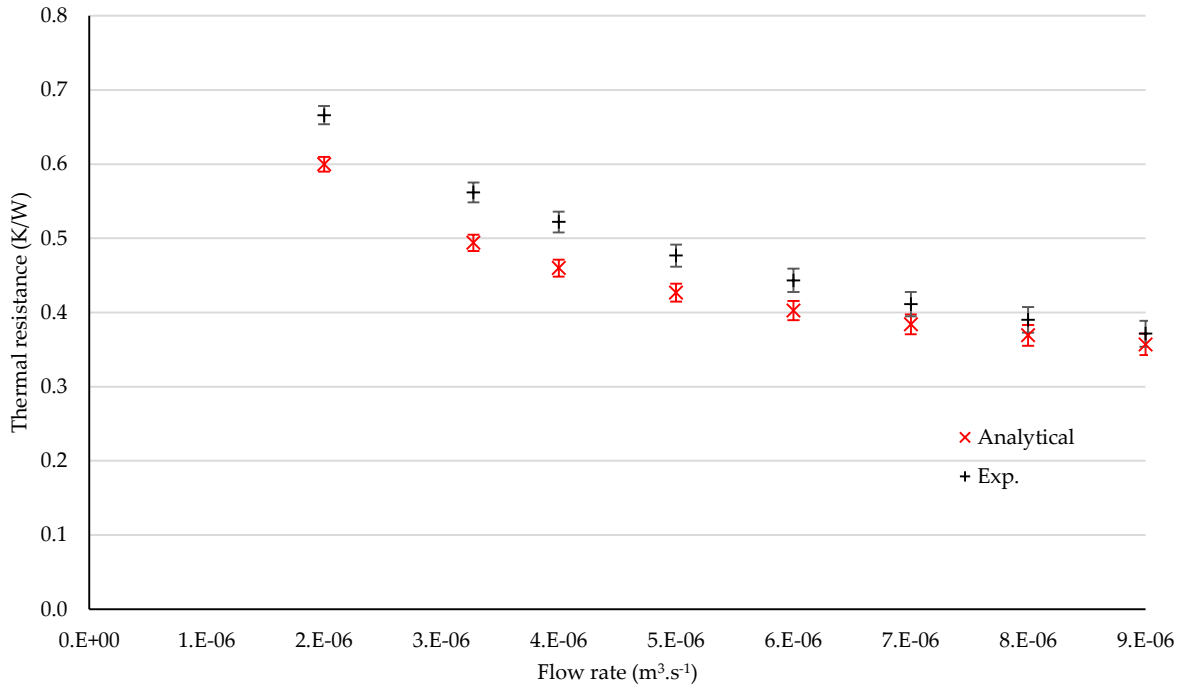


Figure 121: The effects of flow rate on  $R_{th}$  of metal foam with an imposed heat flux of 100W, and  $k_{eff,s}$  of  $10.47 \text{ W.m}^{-1}.\text{K}^{-1}$ , with errors bars.

The next important point to be discussed is the thermal losses that were recorded during the experiments. 100W was imposed on the heat sink via the resistance heat, and using the measurements of the temperature of the coolant and the inlet and outlet it was found that 14.5W to 12.9W were lost, dependant on the flow rate. To account for this, the measured heat flux was used in the analytical model, though this assumed that all losses occurred prior to entering the heat sink. In reality, some losses could have occurred after the heat sink, as conduction through the metal pipes of the heat loop. Thus the losses are actually between 0W and the measured value. To show this, the results from Figure 118 are repeated in Figure 122, this time with an additional set of results where all thermal losses are ignored.

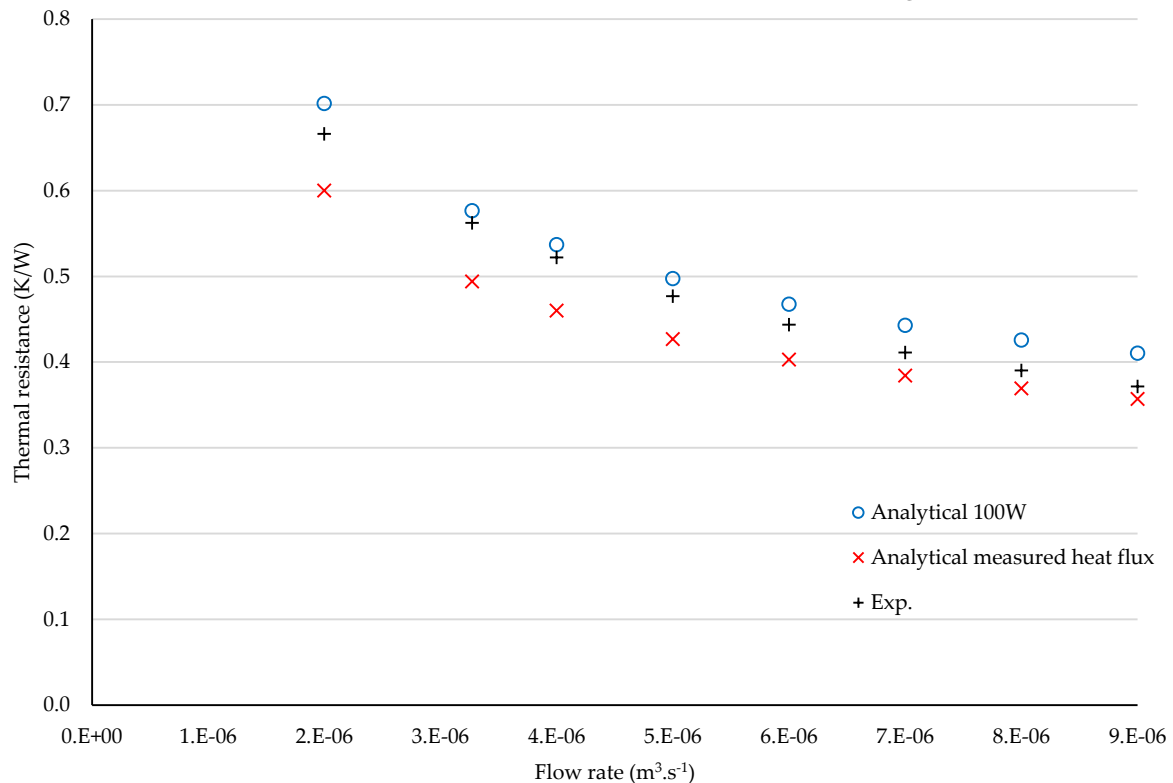


Figure 122: The effects of flow rate on  $R_{th}$  of metal foam with an imposed heat flux of 100W. Results are shown with measured heat flux, and with neglected heat losses.

Finally, the thermal resistance associated with the interface between the metal foam and the copper plate must be addressed. Each of the possible values shown in Table 15 were added to the analytical model in series, the results of which can be seen in Figure 123. In each case, the associated effective thermal resistances were also used. The results show a significant range in the total thermal resistance when applying the various methods of calculating the interface resistance. The average deviations from the experimental results for the 'Min.', 'Analytical  $k_{eff}$ ', 'Average' and 'Max.' results are 3.83%, 14.16%, 26.27% and 43.33% respectively. This highlights the need for further work to be carried out so as to:

- determine precisely the value of this resistance;
- improve the brazing process such that it can be assured that the resistance between samples is the same.

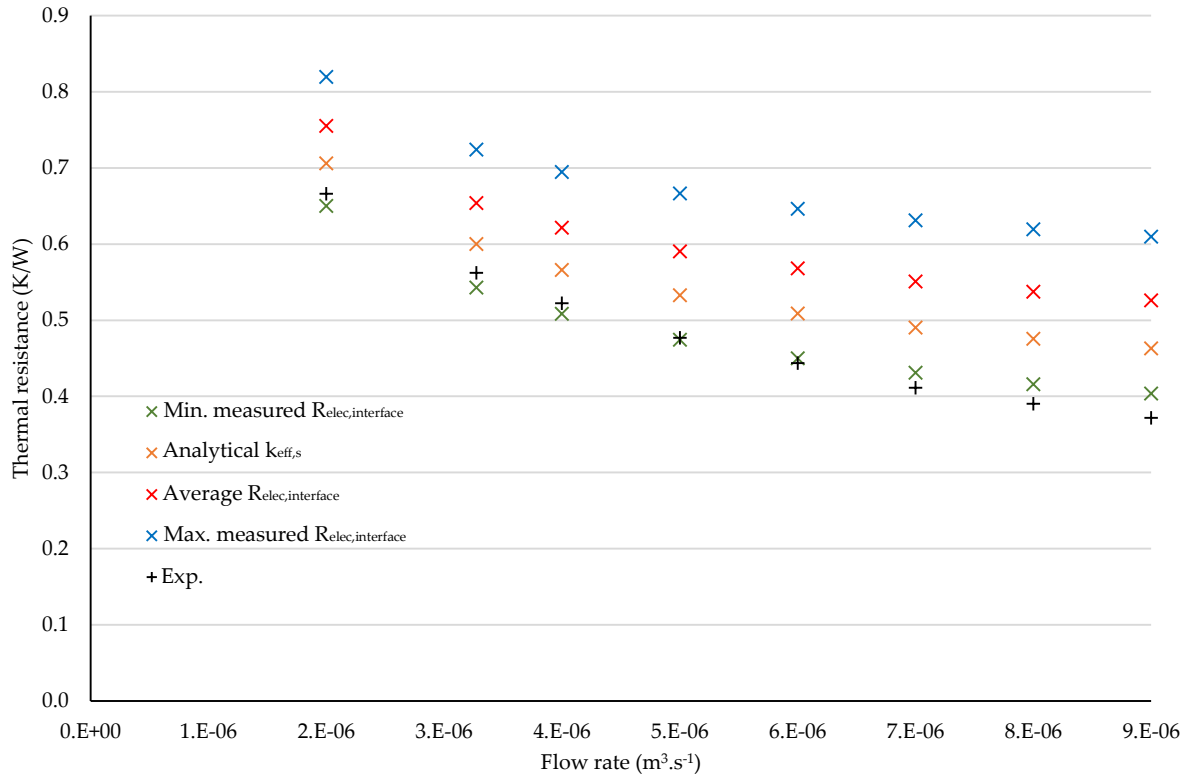


Figure 123: The effects of flow rate on  $R_{th}$  of metal foam with an imposed heat flux of 100W with various methods of calculating the interface resistance.

## 6. Conclusion

In this chapter the need for experimental results was explained and the test loop developed during this work was described in detail. The individual components were introduced and the procedure for running a typical experimental was laid out. As well as describing the work that has been carried out for this project, this also acts as a guide for future work, as the scope of applications of the test loop is very broad. Next the process of constructing two heat sinks was described, one using microchannels and the second using metal foam. In the section the physical parameters of each heat sinks were presented, providing the basis for the analytical calculations. Following this the designing of the test section was described. Being the physical link between the heat sinks and the test loop, the test section was imposed with constraints from the beginning. It was required to house a heat sink, nine thermocouples, two pressure sensors, and a resistance heater as well as fitting within the test loop and remaining watertight. The design decisions that made all of this achievable were laid out in detail, such that a second test section could be constructed in the future if necessary.

After fully describing the experimental setup, the results of the preliminary testing were presented. The time required for the experiment to reach thermal stability was first determined. It was found that when an input parameter was changed (i.e., the flow rate), it was necessary to wait at least two hours before results could be recorded. This was followed by attempts to determine the thermal resistance of the interface between the metal foam sample and the copper plate by measuring the electrical resistance. Four thermal resistances

were presented that corresponded to the maximum, minimum and average measured electrical resistance, and the resistance found from using the analytically calculated  $k_{eff,s}$ . The resistances were 0.377 K/W, 0.035 K/W, 0.215 K/W and 0.109 K/W respectively. It was concluded that further testing is required to validate the measurements of the thermal resistances.

This was then followed by the results of the experimentation proper. The first set of experiments were performed on the microchannel heat sink as a means of validating the experimental setup. The results showed a deviation from the analytical model in thermal and hydraulic performances of 5.6% and 2.7% respectively. This was deemed sufficiently small as to verify the accuracy of the experimental measurements. However, the results also made clear the need to improve the thermal insulation applied to the test loop and test section as heat losses of up to 19 W were measured. Effort was made to more efficiently insulate the second set of experiments, and though the heat loss was reduced, there was still room for further improvement. Finally, it was seen that heat was able to transfer laterally along the length of the heat sink, even though this was taken into consideration during its design phase.

Following this, tests were then carried out under the same conditions on the metal foam heat sink. When the interface resistance was neglected a deviation from the analytical model in thermal and hydraulic performances of 8.7% and 4.5% respectively was seen. When the four interface resistances were included, the average deviation from the experimental results were 3.83 %, 14.16 %, 26.27 % and 43.33 % for the 'Min.', 'Analytical  $k_{eff}$ ', 'Average' and 'Max.' respectively. The results also showed a very linear increase in solid temperature along the length of the heat sink, which was contrary to the microchannel results. It was deemed likely that the physical structure of the metal foam provided a certain level of resistance against lateral heat transfer, which would generate a linear temperature profile consistent with the assumption of a unidirectional imposed heat flux.

## 7. Bibliography

- [66] G. G. Abadi and K. C. Kim, "Experimental Heat Transfer and Pressure Drop in a Metal-Foam-Filled Tube Heat Exchanger," *Experimental Thermal and Fluid Science*, vol. 82, pp. 42-49, 2017.
- [67] V. V. Calmidi and R. L. Mahajan, "Forced Convection in High Porosity Metal Foams," *Journal of Heat Transfer*, vol. 122, pp. 557-565, 2000.
- [68] E. C. Jameson, *Electrical Discharge Machining*, Society of Manufacturing Engineers, 2001.
- [69] Y. A. Cimbala and J. M. Cengel, *Fluid Mechanics : Fundamentals and Applications* (1st ed.), Boston: McGraw-Hill Higher Education, 2006.
- [70] W. Jones and N. H. March, *Theoretical Solid State Physics*, Courier Dover Publications, 1985.
- [71] R. J. Moffat, "Describing the Uncertainties on Experimental Results," *Experimental Thermal and Fluid Science*, vol. 1, pp. 3-17, 1988.
- [72] "Emerson Global," [En ligne]. Available: [www.emerson.com](http://www.emerson.com). [Accessed 17<sup>th</sup> September 2020].

- 
- [73] X. Ma, A. J. Peyton and Y. Y. Zhao, "Eddy Current Measurements of Electrical Conductivity and Magnetic Permeability of Porous Metals," *NDT & E International*, vol. 39, pp. 562-568, 2006.
- [74] S. Kang, "Advanced Cooling for Power Electronics," *International Conference on Integrated Power Electronics Systems (CIPS)*, 2012.
- [75] S. Baskaya, M. Sivrioglu and M. Ozek, "Parametric Study of Horizontal Natural Convection Heat Transfer from Horizontal Rectangular Fins," *International Journal of Thermal Science*, vol. 39, pp. 797-805, 2000.
- [76] A. Bhunia and C. L. Chen, "On the Scalability of Liquid Microjet Array Impingement Cooling for Large Area Systems," *Journal of Heat Transfer*, vol. 133, n° 16, 2011.
- [77] M. G. Khan and A. Fartaj, "A review on Microchannel Heat Exchangers and Potential Applications," *International Journal of Energy Research*, vol. 35, pp. 553-582, 2010.
- [78] M. R. Pais, L. C. Chow and E. T. Mahefkey, "Surface Roughness and its Effects on the Heat Transfer Mechanism in Spray Cooling," *Journal of Heat Transfer*, vol. 114, n° 11, pp. 211-219, 1992.
- [79] J. C. Y. Koh and A. Fortini, "Prediction of Thermal Conductivity and Electrical Resistivity of Porous Metallic Materials," *International Journal of Heat and Mass Transfer*, vol. 16, n° 111, pp. 2013-2012, 1973.
- [80] O. Wiener, "The Theory of Mixtures for fields with Constant Currents," *Akademie der Wissenschaften.*, pp. 32-507, 1912.
- [81] P. Ranut, E. Nobile and L. Mancini, "High Resolution Microtomography-Based CFD Simulation of Flow and Heat Transfer in Aluminum Metal Foams," *Applied Thermal Engineering*, 2013.
- [82] A. L. Loeb, "Thermal conductivity: VIII, a Theory of Thermal Conductivity of Porous Materials," *Journal of the American Ceramic Society*, vol. 37, n° 12, pp. 96-99, 1954.
- [83] G. B. Abadi and K. C. Kim, "Experimental Heat Transfer and Pressure Drop in a Metal-Filled Tube Heat Exchanger," *Experimental Thermal and Fluid Science*, vol. 82, pp. 42-49, 2017.
- [84] C. Chen, "Forced Convection Heat Transfer in Microchannel Heat Sinks," *International Journal of Heat and Mass Transfer*, vol. 50, pp. 2182-2189, 2007.

---

---

# GENERAL CONCLUSIONS

---

---

## Aims

This project sought to provide a solution to the problem of modern PE packaging by offering a compact and efficient cooling strategy, using metal foam as a novel heat sink within a forced-convection liquid cooling environment. These was to be achieved by completing the following aims:

- Develop an analytical model capable of predicting the thermal and hydraulic performance of flow through a metal foam heat sink.
- Compare the model with numerical simulations/literature results.
- Use the model to optimise the internal geometry of the metal foam to maximise heat transfer for a given pressure loss.
- Compare the performance of the optimised foam with that of optimised microchannels.
- Fabricate a test bench in order to validate the model experimentally.

The problematic could be broken down into three main parts:

## Analytical model

The first part of the work focused on the development of an analytical model capable of predicting the thermal and hydraulic performance of flow through a metal foam heat sink. This was achieved by following the same approach as is commonly used with microchannel heat sinks. By simplifying the governing equations, the system was reduced down to a network of thermal resistances in series. To validate the model, it was first compared with numerical simulations using the porous media model supplied by Ansys FLUENT. Simulations were carried out for a wide range of porosities (20 % - 90 %) and fibre diameters (10  $\mu\text{m}$  – 300  $\mu\text{m}$ ), with the other foam parameters being calculated as a function of these two. For the majority of the studied range, the analytical and numerical results were in good agreement with one another when predicting thermal behaviour. However, at the lower limit of the tested fibre diameters a greater deviation between the numerical and analytical thermal resistances was calculated. The hydraulic results did not show this same behaviour, and were in good agreement throughout the entire range of tested foams. This was to be expected as the model to calculate the pressure did not rely so heavily on assumptions.

In order to seek further validation, the model was used to replicate several experimental results found within the literature. It performed well, and captured accurately the trend of the Nusselt numbers as they varied with the Reynolds number. It also closely reproduced the pressure gradient as a function of the fluid inlet velocity of two different approaches from the literature.

## Optimisation

The second part of this work was to implement the analytical model into the optimisation software CADES. This involves defining all parameters within the model as either inputs (requiring a fixed value or range of values), outputs (able to vary freely), or as the function to be minimised. A series of parametric optimisations were carried out exploring a range of porosities (40% - 95%), fibre diameters ( $10^{-3}\text{m}$  -  $10^{-6}\text{m}$ ) and pressure drops (0 - 50 kPa), with a fixed volumetric flowrate of  $3.25 \times 10^{-6} \text{ m}^3\cdot\text{s}^{-1}$ . In each case, the total thermal resistance was minimised. The results showed that for a given flowrate there is an optimum porosity, corresponding to a minimum thermal resistance. An analysis of the heat transfer mechanics determined that the optimum porosity balances heat transfer by conduction (decreases with increasing porosity) and heat transfer by convection (increases with increasing porosity). In terms of thermal parameters, this is a balance between the volumetric coefficient of heat transfer, and the effective thermal conductivity. The best performing foam from the optimisation process had a porosity of 47.9 % ( $\Delta p = 50 \text{ kPa}$ ). This highlights the need for a wider range of foam porosities to be available commercially. The accuracy of the results was improved by applying a space mapping algorithm, which minimised the discrepancies between the analytical and numerical results, reducing the overall errors 10.76% to 1.74%. The results were then compared with optimised microchannels under two different constraints. The first had a minimum channel width and fin width of  $100\mu\text{m}$  as this value conforms to commonly available microchannels, and the second had a minimum channel width and fin width of  $10\mu\text{m}$ . The metal foams performance sat in between the two microchannels, which had thermal resistances of 0.155 K/W and 0.109 K/W for the  $100\mu\text{m}$  and  $10\mu\text{m}$  microchannels respectively. This however, does not take into consideration the differences in the cost of manufacturing. A microchannel with a fin width of  $10\mu\text{m}$  has a very large form factor ( $>100$ ), and it requires specialised manufacturing techniques that are expensive. In contrast, there are several, inexpensive fabrication methods (power sintering, space holder, lost carbonate sintering) that could produce the optimised metal foams. It must also be noted however that when fabricating a heat sink from metal foam, an additional thermal resistance is created at the interface between the foam and substrate, which does not exist in the case of microchannel.

## Experimentation

The final part of this work was to develop an experimental test bench that can measure the thermal and hydraulic performances of various heat sinks (metal foam and microchannel). This was carried out as a way of validating the first two parts of this project, which relied on several critical assumptions. A test loop, test section and two example heat sinks were designed and fabricated. The microchannel heat sink was tested upon first as a means of validated in the experimental setup. A good agreement was found, both thermal and hydraulically, between the experimental results and the chosen analytical model. Following this, the metal foam heat sink was then tested. At this point in time it is not possible to assess how well the proposed analytical model performed, as the experimentation process highlighted several uncertainties. Instead, an analysis of these aspects was presented, the most impactful being the importance of the interface thermal resistance between the metal foam and the copper plate it was attached to. Several different values for the interface thermal

resistance were determined experimentally, and were added to the analytical model in series, along with the associated effective thermal conductivities. The resulting overall thermal resistance of the heat sink was then compared with the experimental results. It was seen that the interface resistance has a significantly impact on the overall thermal resistance. Were more time available, further tests would have been carried out, first to verify the measurements of the interface resistance, then to determine if it could be minimised by using a different joining technique.

## **Future work**

At the end of this work it is clear that there are still several unanswered questions, that unfortunately there was not enough time to address. The next step is to improve the robustness of the results by testing more heat sinks, particularly using different types of metal foams. It was intended to construct a third heat sink using a different type of foam, namely the one produced by Versarien™. It would also be great interest to fabricate one of the optimised foams in-house. The SIMaP laboratory has a wealth of experience in metal powder sintering, and this will have provided an additional set of experimental results. Finally, it was one of the principle aims of this project to ‘propose a solution to the problem of modern PE packaging by offering a compact and efficient cooling strategy’. It is therefore the role of the next PhD student to construct a prototype PE module that can, by utilising the steps made in this work, integrate a metal foam heat sink.



---

---

# APPENDIX

---

## Process to fill/purge test loop

Initial valve positions:

- Valves 1, 3 and 4 are set to the open position, connecting the entire test loop and test section to the vacuum pump.
- Valves 2, 5 and 7 are left in the closed position, thus the test loop is watertight and isolated from the reservoir.
- Finally, valve 6 is set so it is open between the reservoir and the atmosphere.

Filling the test loop:

- The vacuum pump and vacuum pressure sensor are switched on.
- A pressure of at least  $2 \times 10^{-1}$  mbar within the test loop is waited for. This was shown to be sufficiently low to aspirate coolant throughout the test loop.
- When the required pressure is reached, valve 1 is opened, isolating the test loop from the vacuum pump.
- In quick succession, valve 7 is opened, draining out a small amount of coolant, but also filling the region between valve 6 and 7, and then valve 6 is set to be open between the reservoir and the test loop. This technique reduces the possibility of air bubbles entering the test loop.
- When the coolant level in the reservoir level stabilises, valve 7 is closed.
- Valve 2 is used to remove unwanted gas bubbles from the test loop.

Purging the test loop:

- When either the fluid or the sample needs to be changed, the test loop must be purged.
- To remove coolant from the test loop, valve 2 and 5 are opened.
- Compressed air is applied at valve 2 to further expel coolant stuck within the loop.
- As it is very difficult to remove all the coolant, the vacuum pump is then left running, typically through the night, to degas the rest.

## Test section connections

*Inlet/outlet → test loop*

Swagelok connector SS-400-1-OR	Swagelok connector SS-8M0-R-4	8mm inox tube
		

*Test section → pressure sensor*

Swagelok SS-400-1-OR	Swagelok SS-401-PC	Swagelok SS-400-7-2RG	Liquifit connector	6 mm polyamide tube
				

*Test section → fluid thermocouples*

Swagelok SS-400-1-OR	Swagelok SS-401-PC	Swagelok SS-400-7-2RG	TC Direct vacuum feed through
			

## Preparing samples

The copper cubes and foams samples needed to be properly cleaned before each attempt to attach them together. It is important to remove grease and oxide layers on the samples so as to improve the quality of the thermal connection. The samples were placed into five beakers, one after the other, containing various liquids. The different liquids and the times taken for each step can be seen in Table 16.

TABLE 16

Beaker	Liquid	Duration (min)
1	Ethanol ( $C_2H_5OH$ )	2
2	DI water ( $H_2O$ )	2
3	Diluted sulphuric acid ( $H_2SO_4$ )	3
4	DI water ( $H_2O$ )	2
5	Acetone ( $C_3H_6O$ )	2

---

## Abstract

Several decades ago, power electronics (PE) emerged as an important discipline in the world of electrical engineering. Thanks to regular technological advancements, namely the use of "wide band gap" materials for semiconductors, PE devices have become more compact and efficient, but this has unfortunately resulted in a less efficient thermal management. Thus, as a collaborated effort between the G2Elab, LEGI and SIMAP laboratories of Univ. Grenoble Alpes, this work has studied the use of metal foam as a novel heat sink used in a forced-convection cooling system that can be integrated into PE modules for superior cooling. Metal foams are lightweight, have low densities, high specific surface areas, an open-celled structure and good thermal properties. They are typically categorised by their porosity ( $\epsilon$ ), their pore density (PPI, pores per inch) and by the diameter of the solid fibres ( $d_f$ ). The advantages to heat transfer arise from the possibility of an increased specific surface area over other heat sinks, such as microchannels, and from the tortuous structure of metal foam that generates flow turbulence and improves convective transfers within the coolant. Thermal performances of metal foam based heat sinks were modelled by developing an analytical model that considered them as a network of resistances in series. This was achieved by simplifying the LTNE equations that govern energy transfer through the solid and fluid phases. The model was initially compared with numerical simulations and experimental results from the scientific literature, where it performed well. As an additional level of validation, a thermo-hydraulic test bench, as well as a test section, were designed and assembled in-house. After a validation of the experimental means on a microchannel heat sink, the characterization of thermo-hydraulic performances of a novel heat sink integrating metal foams was carried out. Analytical and experimental results agreed well with each other, with an average deviation of the thermal resistance of less than 10%. The model was then used to optimise the foams physical properties in order to produce a heat sink that maximises thermal performances whilst minimising the required hydraulic power. The results show that for a pressure drop of 50kPa, the thermal resistance of a metal foam heat sink is 0.127 K/W. Metal foams are thus a viable heat sink material and the model proposed in this work can be used as a quick and inexpensive means of optimisation.

## Résumé

Il y a plusieurs décennies, l'électronique de puissance (PE) est devenue une discipline importante dans le monde de l'électrotechnique. Grâce aux progrès technologiques réguliers, à savoir l'utilisation de matériaux à "wide band gap" pour les semi-conducteurs, les dispositifs PE sont devenus plus compacts et efficaces, mais cela a malheureusement entraîné une gestion thermique réduite. Ainsi, dans le cadre d'un effort collaboratif entre G2Elab, LEGI et SIMAP, ce travail a étudié l'utilisation de la mousse métallique comme nouvel échangeur de chaleur utilisé dans un système de refroidissement à convection forcée qui peut être intégré dans des modules PE pour un refroidissement supérieur. Les mousses métalliques sont légères, ont de faibles densités, des surfaces spécifiques élevées, une structure à cellules ouvertes et de bonnes propriétés thermiques. Ils sont typiquement classés par leur porosité ( $\epsilon$ ), leur densité de pores (PPI, pores par pouce) et par le diamètre des fibres solides ( $d_g$ ). Les avantages du transfert de chaleur proviennent de la possibilité d'une surface spécifique accrue par rapport à d'autres échangeurs de chaleur, tels que des micro canaux, et de la microstructure tortueuse qui génère des turbulences d'écoulement et améliore les transferts de convection dans le fluide de refroidissement. Les performances thermiques ont été modélisées en développant un modèle analytique qui considérait les échangeurs de chaleur comme un réseau de résistances en série. Ceci a été réalisé en simplifiant les équations LTNE qui régissent le transfert d'énergie à travers les phases solide et fluide. Le modèle a été initialement comparé aux simulations numériques et aux résultats expérimentaux de la littérature scientifique, où il a bien fonctionné. Comme niveau supplémentaire de validation, un banc d'essai expérimental a été conçu et assemblé in-house. Les performances thermiques ont été vérifiées en utilisant des thermocouples pour mesurer le profil de température des phases solide et fluide, et les propriétés hydrauliques ont été trouvées en mesurant la chute de pression à travers les échangeurs de chaleur. Les résultats analytiques et expérimentaux concordaient bien les uns avec les autres, s'écartant en moyenne de moins de 10%. Le modèle a ensuite été utilisé pour optimiser les propriétés physiques des mousses afin de produire un échangeur de chaleur qui maximise les performances thermiques tout en minimisant la puissance hydraulique requise. Les résultats montrent que pour une perte de charge de 50 kPa, la résistance thermique d'un échangeur de chaleur en mousse métallique est de 0,127 K/W. Les mousses métalliques sont donc un matériau d'échangeur de chaleur viable et le modèle proposé dans ce travail peut être utilisé comme un moyen rapide et peu coûteux d'optimisation des performances.